DISSERTATION

PRECIPITATION AND EROSION DYNAMICS IN THE RIO PUERCO BASIN

Submitted by

Peter Molnár

Civil Engineering Department

In partial fulfillment of the requirements

for the Degree of Doctor of Philosophy

Colorado State University

Fort Collins, Colorado

Spring 2001

UMI Number: 3013853

Bell & Howell Information and Learning Company
300 North Zeeb Road
P.O. Box 1346
Ann Arbor, MI 48106-1346

COLORADO STATE UNIVERSITY

December 8, 2000

WE HEREBY RECOMMEND THAT THE DISSERTATION PREPARED UNDER OUR SUPERVISION BY PETER MOLNÁR ENTITLED "PRECIPITATION AND EROSION DYNAMICS IN THE RIO PUERCO BASIN" BE ACCEPTED AS FULFILLING IN PART REQUIREMENTS FOR THE DEGREE OF DOCTOR OF PHILOSOPHY.

Committee on Graduate Work

____

____

____

____

____
Adviser

____
Department Head

ABSTRACT OF DISSERTATION

PRECIPITATION AND EROSION DYNAMICS IN THE RIO PUERCO BASIN

River basins in arid and semiarid regions, with highly erodible land surface and highly variable precipitation, are susceptible to dramatic watershed and channel erosion. In these environments, even small changes in mean climate can produce a large response in the erosion dynamics. To predict the direction and magnitude of future channel adjustment, it is necessary to understand the processes of erosion and deposition in ephemeral streams and the role of spatial and temporal variability in rainfall and runoff. That is the objective of this study. A modeling analysis of precipitation and erosion dynamics is conducted on the Rio Puerco Basin, New Mexico.

Annual, monthly and daily rainfall and runoff data are analyzed for trends in the recent record (1948-1997). Analyses at the annual timescale show a statistically significant increasing trend in Rio Puerco precipitation. This trend is connected with large scale climate patterns and anomalies in the Northern Pacific. Analyses at finer temporal scales show that the increase in precipitation is a result of rising non-summer rainfall, and identify substantial shifts in the daily distributions of both rainfall and runoff. It is postulated that changes in runoff are related to recent alluviation in the Rio Puerco stream system and to vegetation changes in the Basin.

The spatial and temporal variability in daily rainfall is investigated by the discrete random cascade theory using radar and climate station data. A rainfall modeling system is developed that disaggregates regional annual rainfall into a sequence of daily stochastic rainfall fields, while preserving important statistical properties at all spatial and temporal scales involved. A conceptual lumped rainfall-runoff model transforms spatially distributed rainfall into daily streamflow on a subbasin scale.

A new channel erosion model ERMO is developed and applied to the Rio Puerco main stream. The model is used to analyze channel change in long-term simulations, with special emphasis placed on the role of transmission losses. Modeling with stochastic rainfall shows the importance of external climate factors (average regional precipitation, spatial distribution and magnitude of rainfall, etc.) and internal channel characteristics (tributary confluences, distribution of channel width, infiltration into the streambed, etc.) on the erosion dynamics. It is determined that although aggradation is the dominant process in the Rio Puerco main stream in the long term, short term variability is caused mostly by rapid degradation during wet years. Particular attention is given to general trends in channel change under a changing climate. It is found that moving towards a wetter and more extreme climate generally brings more stream-wide degradation and an intensification of both maximum erosion and deposition rates.

Peter Molnár
Civil Engineering Department
Colorado State University
Fort Collins, CO 80523
Spring 2001

ACKNOWLEDGEMENTS

This research was largely supported by the U.S. Geological Survey Grant 1434-CR-97-AG00025. The support is gratefully acknowledged. In particular, thanks are due to Ray Watts and Milan Pavich from the U.S. Geological Survey for their encouragement and perseverance in managing the project.

Numerous people helped in many ways in the course of the investigations. Thanks are due to all: especially to Jeremy Franz and Scott Francis who assisted me in the fieldwork, to Mike Murphy and the ARS in Fort Collins for the soil texture laboratory analyses, to Rolf Hertenstein and his colleagues from CSU Atmospheric Sciences Department for arranging and supplying NOWrad ™ rainfall data, to my fellow graduate students in the Hydrology Group for insightful discussions. Thanks are also due to John Elliott and Allen Gellis from the U.S. Geological Survey for sharing their data and their extensive knowledge of the Rio Puerco Basin during the course of this study.

I am most grateful to my academic advisor Jorge Ramirez, for his unending support, encouragement and friendship, and to my graduate committee members: Ellen Wohl, Ray Watts, Roger Smith and Jose Salas.

Finally, I thank my wife, Darcy, and daughter, Monika, for their patience. You have been a source of inspiration.

AUTOBIOGRAPHY

Peter Molnár

DIPL.ENG., 1992, SLOVAK TECHNICAL UNIVERSITY

Water Resources Management and Hydraulic Engineering (Faculty of Civil Engineering)

M.S., 1996, COLORADO STATE UNIVERSITY

Hydrologic Science and Engineering (Civil Engineering Department)

PH.D., 2001, COLORADO STATE UNIVERSITY

Water Resources, Hydrologic and Environmental Sciences (Civil Engineering Department)

TABLE OF CONTENTS

1 Introduction

The effects of climate variability and change on small - regional and large watershed - scales are receiving considerable interest in recent years (e.g., IPCC 1995). There is evidence that both natural environmental change and human activity result in significant perturbations of water and sediment fluxes from drainage basins at varying timescales. These perturbations can cause dramatic changes in watershed characteristics, often with widespread effects on human habitat (e.g., NRC 1991). Erosion - at the hillslope and channel scale - invariably accompanies most watershed changes. Therefore scientific investigations of precipitation and erosion dynamics in a changing environment should be an important element of successful land and water resources management.

Arid and semiarid regions of the world are especially susceptible to dramatic and widespread erosion, because of high erodibility of the land surface and often high variability in precipitation. In these environments, even small changes in mean climate can produce relatively large changes in the frequency of rainfall events. In order to anticipate the direction and magnitude of channel changes in the future, it is necessary to understand well the physical processes of erosion and deposition in river systems and the role of the spatial and temporal distribution of driving forces of erosion - rainfall and runoff. That is the objective of this study. The subject of study is the Rio Puerco Basin, located in New Mexico in the semiarid region of the U.S. Southwest (Figure 1.1).

The main contributions of this study to the field of hydrology are (*a*) the development of a new channel erosion model designed to simulate long-term channel change in an ephemeral stream driven by spatially and temporally variable rainfall; and (*b*) the development of a new approach to the stochastic modeling of channel erosion dynamics in a changing climate.

The main tasks in this study are: (1) To provide a description of the Rio Puerco precipitation, streamflow and sediment data, and delineate the river network and subbasins from digital terrain data (Chapter 2). (2) To analyze trends in Rio Puerco rainfall and runoff data, and examine the connection between these trends and recent watershed and channel changes (Chapter 3). (3) To analyze the spatial and temporal variability in precipitation in the region using the discrete random cascade theory, and develop a rainfall modeling system for the generation of stochastic rainfall fields (Chapter 4). (4) To develop a channel erosion model for long-term (100-year) simulation of channel dynamics in the Rio Puerco main stream, and to quantify the effects of external climate factors (e.g., average regional precipitation, spatial and temporal distribution of daily rainfall, rainfall magnitude) and internal channel characteristics (e.g., tributary confluences, distribution of channel width, infiltration into the streambed) on the erosion dynamics (Chapter 5). Chapter 6 discusses the main results and conclusions are presented in Chapter 7.

In this introductory Chapter 1, a historical review of the causes of channel degradation observed in the U.S. Southwest is presented in Section 1.1 and a process-based model of channel degradation is discussed in Section 1.2. A general outline of investigations in this study and their goals are presented in Section 1.3.

For clarity, tables and figures are presented at the end of each chapter. Scientific notation is defined separately for every chapter. The notation of the original authors is preserved wherever possible. For instance, W denotes the cascade generator for the random cascade model in Chapter 4 and the width of the channel in the channel erosion model in Chapter 5. Such duplications are few and they do not affect the important parameters and variables in this study.

1.1 Arroyo Formation in the U.S. Southwest

The U.S. Southwest is a semiarid region with widespread characteristic channel features - *arroyos* - deeply entrenched ephemeral channels with vertical banks and highly variable width (e.g., Bryan 1928a, Peterson 1950) that have undergone periodic erosion and filling in the past (e.g., Cooke and Reeves 1976). The most recent, and geographically widespread, period of rapid entrenchment in the U.S. Southwest was initiated towards the end of the 19th Century, with emphasis placed on the period 1880-1900 in New Mexico (e.g., Bryan 1925, 1928a, 1928b, Cooke and Reeves 1976). This section reviews the hypothesized causes of arroyo formation and their observational foundation.

The question of arroyo formation has historically been approached from two different perspectives. The first perspective concentrated on searching for possible causes of entrenchment - mostly changes in the watershed and climatic environment - without much emphasis on the processes of erosion themselves. The second perspective focused on a better understanding of the processes of channel and watershed erosion. The causes of arroyo formation were then linked to this understanding. Historically, the first perspective was adopted by early observers of arroyo formation. Their interest in arroyo existence was initiated by massive trenching and the social impacts it had on the population of the region. Two hypotheses of arroyo formation were proposed: (1) land-use change, and (2) climate change. The second perspective naturally evolved as the scientific knowledge and records of observations increased. This process-based viewpoint stressed the role of (3) natural temporal and spatial variability in driving forces of erosion, and (4) intrinsic, threshold-dependent channel response in arroyo formation and evolution.

The reader is reminded that the above formalization of the hypotheses of arroyo formation is somewhat arbitrary. The hypotheses are not exclusive: in reality many researchers invoke more than one hypothesis in their explanation of arroyo formation. Nevertheless, for the purposes of reviewing arroyo causes, the above definition is sufficient. The historical review focuses on the U.S. Southwest in general, and New Mexico in particular.

1.1.1 LAND-USE CHANGE

The foundation for this hypothesis lies in the depletion of vegetation by human alterations of the watershed environment, and the resulting increase in hillslope and channel runoff leading to erosion. Overgrazing, due to the introduction of large numbers of livestock (mainly cattle) to the U.S. Southwest by settlers in the 1860s, is stated to be the main cause of vegetation depletion (Rich 1911, Duce 1918, Bailey 1935). Under the land-use change hypothesis, human control of vegetation is considered to be more significant (because it potentially operates on a shorter timescale and therefore can produce rapid response) than climatic controls (Bryan 1928b, Thornthwaite et al. 1942, Antevs 1952, 1954). The most serious opposition to the hypothesis of land-use change lies in the fact that earlier Spanish settlers also introduced large amounts of livestock (mainly sheep) to the U.S. Southwest at the end of the 16th Century and appreciable erosion apparently did not occur (e.g., Bryan 1928a, Cooke and Reeves 1976). There was also an earlier cattle boom in the dry period 1790-1820 without reports of accentuated erosion. However, this fact does not invalidate the hypothesis of land use change. It is likely that the dramatic increase in cattle numbers in the 1860s did play a role in vegetation and surface runoff alteration, although possibly not as marked a role as originally proposed.

1.1.2 Climate Change

Archaeological, botanical, and geological evidence in the U.S. Southwest suggests that periods of erosion and sedimentation occurred in prehistoric times when human influence was very unlikely (Bryan 1940, Tuan 1966, Cooke and Reeves 1976, Shepherd 1978, Euler et al. 1979, Thornes 1994, Grissino-Meyer 1995, and others). Trenching was therefore attributed (at least partially) to changes in available moisture. However, two opposing views emerged. The more popular one in the U.S. Southwest was that an overall decrease in moisture, a shift towards drier conditions, would cause entrenchment by depleting the vegetative cover and increasing the erosive power of surface runoff (Bryan 1925, 1928a, 1928b, 1940, Antevs 1952). The opposing view suggested that increased humidity would re-vegetate watersheds and thus decrease sediment production from the hillslopes. This, together with increased runoff, would cause rapid entrenchment in the channels (Huntington 1914, Tuan 1966). In both cases, overgrazing was considered the "trigger" that could have initiated rapid channel erosion in addition to the general change in moisture. The importance of these two views (albeit opposing) lies in the recognition that precipitation, vegetation, runoff and sediment production are invariably linked to each other. However, a lack of understanding of the channel erosion process inevitably makes both views quite ambiguous (one can certainly envision both occurring in a watershed). This was also recognized by Richardson, who claimed that minimum erosion occurs in a climate just sufficient to produce a closed vegetative cover, and an increase in upstream erosion (and downstream deposition) then may result from a change towards both wetter or drier climatic conditions (Richardson 1945).

There is however a third aspect of climate change and resulting arroyo formation that deserves attention: variations in rainfall intensity. In a seminal study, Leopold showed a gradual increase in the frequency of light rains accompanied by a decrease in the frequency of high intensity rainstorms at four gaging stations in New Mexico in the period 1850-1930 (Leopold 1951). In his view this could explain arroyo cutting in the beginning of the period when less frequent light rains caused a decrease in the vegetative cover while more numerous larger storms triggered erosion. This analysis emphasized not only the importance of large events in ephemeral channel adjustment, but also that sequences of events may play an important role in this adjustment.

1.1.3 Natural Variability

This process-based hypothesis of arroyo formation concentrates on the natural temporal and spatial randomness of meteorological and geomorphological features of river systems in arid environments. The underlying assumption is that the cutting and filling of arroyos is part of the natural behavior of ephemeral river systems. The hypothesis builds on the recognition of the importance of rainfall distribution in arroyo formation (Leopold 1951). Under the hypothesis of natural variability in driving forces of erosion it is argued that the temporal variability in frequency and magnitude of rainfall and runoff may lead to significant channel change in arid regions where a fine balance exists between aggradation and degradation (e.g., Gregory 1917, Schumm 1973, Balling and Wells 1990). Arroyo entrenchment represents an intensification of normal channel gullying initiated by intense rainfall events resulting in intense floods. Ample field evidence supports the importance of floods in arroyo evolution (Thornthwaite et al. 1942, Tuan 1966, Bull 1979).

In addition to the temporal distribution, the wide spatial distribution of rainfall will create localized runoff events that will result in differential erosion of the streambed and cross-cutting (Dellenbaugh 1912). This is especially pertinent to the U.S. Southwest, where intense summer rainstorms are extremely localized and may affect very small areas of the watersheds. Discontinuities in the longitudinal profiles at tributaries and headcut migration are common expressions of differential flows through the drainage network (Thornes 1977, 1994). In addition, variability in the supply of sediment to the streams greatly affects local stream erosion and deposition (Leopold et al. 1966) and the spatial distribution of vegetation may also play a role in the erosion dynamics (Graf 1979).

In my view, the hypothesis of the temporal and spatial variability in driving forces of erosion is essential to the explanation of channel aggradation and degradation in ephemeral streams in semiarid regions.

1.1.4 INTERNAL ADJUSTMENT

All previous hypotheses deal with external environmental controls on arroyo formation. The hypothesis of intrinsic geomorphic thresholds addresses the internal behavior and adjustment of channel systems essentially independent of environmental controls. It was brought forward by Schumm and Hadley, who observed that trenching of valley fills is commonly associated with a steepening of the gradient of the valley fill (Schumm and Hadley 1957). They also recognized that in ephemeral streams in arid regions losses to evaporation and mainly infiltration result in deposition of sediment on the channel bed that could build up the channel slope to a critical level and trigger incision. Lateral migration and changes in channel pattern may also add to the threshold behavior and cause local erosion. Although this theory was applied generally to small watersheds (e.g., Patton and Schumm 1975), there is no reason to believe that the processes would be different on a larger scale. The original definition of threshold-dependent processes was linked with exceeding a critical slope, but similar arguments can be made for threshold behavior based on the concepts of stream power (Bull 1979) and shear stress (Graf 1979).

The importance of the hypothesis of intrinsic geomorphic thresholds lies in the recognition that natural processes of water and sediment transport in a stream system may be sufficient to explain periodic aggradation and degradation of the streambed and the complexity of observed drainage response (Schumm 1973, 1980). This is true especially for ephemeral streams in arid regions, where there is high spatial variability in streamflow. Although there is experimental evidence for the hypothesis of intrinsic thresholds (Schumm and Khan 1972), it remains a matter of debate whether it alone can explain the rapid erosion rates of the recent arroyo trenching period in the U.S. Southwest.

1.1.5 Observations

There are two fundamental principles that lead to arroyo initiation: increased erodibility of the valley floor, and increased erosiveness of flow (Peterson 1950, Cooke and Reeves 1976). Erodibility is determined by properties of the valley and channel materials, and their degree of stability. Erosiveness is a function of hydraulic, channel and sediment transport variables. However, there are numerous ways by which these two conditions for arroyo initiation can be reached.

Field evidence suggests that the most recent period of channel entrenchment in the U.S. Southwest was initially intermittent along most valley floors, and only later was consolidated into more continuous arroyos (e.g., Thornthwaite et al. 1942, Leopold and Miller 1956, Tuan 1966, Cooke and Reeves 1976). There is strong evidence that local valley floor changes (creation of roads, irrigation ditches, canals and embankments) often provided the centers for the initiation of rapid channel erosion in Southwestern Arizona (Cooke and Reeves 1967). It has been documented that high magnitude floods as well as features locally constricting flow cause rapid erosion in affected channel sections (Gregory 1917, Melton 1965). In ephemeral streams, channel sections below tributaries are subject to large variability in streamflow and mainly sediment supply, and are prone to localized erosion or deposition (Leopold et al. 1966, Thornes 1977, 1994).

Overall, the hypothesis of arroyo formation, invoking temporal and spatial variability in driving forces of erosion, seems most convincing in the explanation of intermittent arroyo initiation. Once initiated, arroyos seem to gradually become deeper and wider driven by discharges of different magnitudes, and eventually attain a fairly stable condition (e.g., Leopold and Miller 1956). These internal changes are at the core of the hypothesis of intrinsic geomorphic thresholds in arroyo formation and development.

The above local changes are generally instrumental in arroyo initiation. However, evidence was also found of regional changes in climate and vegetation in Southern Arizona that may have promoted subsequent arroyo development (Cooke and Reeves 1976). Changes in rainfall intensity observed by Leopold (1951) in New Mexico were also found to occur in Arizona. Furthermore, there seems to be a pattern of drought years followed by an unusually wet year during which erosion is more likely (Cooke and Reeves 1976). The arguments for the hypothesis of land use change seem the weakest, as the regional correlation between arroyo formation and the cattle boom is in many cases not as good as previously thought. There is, however, quite convincing evidence for gradual vegetation change and/or variability in some regions of the U.S. Southwest in the last century (Antevs 1954, Branson and Janicki 1986).

A conclusion from observations of arroyos is that similar arroyo forms and behavior are present in different areas of the U.S. Southwest as a result of different combinations of initial conditions and environmental changes.

In the Rio Puerco Basin, it is argued that accelerated erosion began between 1880 and 1900, and was initially intermittent but quickly progressed (Bryan 1928a). It is argued that this latest entrenchment episode is part of a cyclic process of erosion and deposition in the watershed. There is evidence that discontinuous gullies existed along the middle Rio Puerco before the 19th Century (e.g., Tuan 1966, Love 1986). It has been estimated that the pre-incision channel system contained less than 5% of the present entrenched arroyos (Bryan 1928a). Reasons for the recent entrenchment were commonly associated with cattle ranching and overgrazing, but changes in climate were also advocated (e.g., Bryan 1928a, 1928b, Antevs 1952). It is argued that presently the channel system is undergoing a period of alluviation (Tuan 1966, Elliott 1979, Elliott et al. 1999).

From the above observations, an idea of the progression and evolution of the arroyo at Rio Puerco was formed (Patton 1973, Elliott 1979, Gellis 1988). After initial rapid entrenchment, the arroyo widens as a result of lateral shifts of the channel, channel bank slumping, and passage of large floods. In later stages, an inner floodplain is created inside the arroyo (sometimes with permanent vegetation establishing itself), and the channel is constrained again. Processes of erosion and filling periodically continue within the arroyo (caused by variability in sediment delivery and storage). There are many identifiable terraces within the Rio Puerco arroyo system that support this theory (e.g., Love 1986).

1.2 Foundations for Channel Modeling

What makes ephemeral streams in arid regions susceptible to the observed high rates of channel erosion and filling? There are at least four features that stand out: (1) the ephemeral and intermittent nature of flows, (2) asynchronicity of flows through the drainage network because of localized runoff events, (3) transmission losses into the streambed and loss of sediment transporting capacity, and (4) highly erodible surface materials and resulting extremely high sediment loads (Thornes 1994).

The framework for erosion modeling in this study builds on the process-oriented hypotheses of arroyo formation and on the specific features of ephemeral streams. In the development of the channel erosion model three characteristics stand out as most essential.

First is the spatial and temporal variability of rainfall and runoff throughout the river network, as this naturally creates conditions for differential erosion and aggradation of the streambed, in particular at tributary confluences (e.g., Bryan 1928a, Dellenbaugh 1912, Mosley 1976, Thornes 1977, Miller and Wells 1986). Often this is where channel entrenchment is initiated, and gradual channel changes progress upstream and downstream from here. The process can occur at a very fast rate, because of the hydraulic and sediment characteristics in channels with mobile beds (loose sandy material is present in most valley fills where arroyos are forming).

Second is the role of large floods, which have been shown to initiate significant trenching in ephemeral channels because of their great erosive power (e.g., Leopold 1951, Schumm and Hadley 1957, Tuan 1966, Schumm 1973, Finley and Gustavson 1983, Balling and Wells 1990). The temporal distribution, frequency, and the spatial distribution of floods will be of great importance to channel erosion and arroyo formation.

Third is the role of transmission losses by infiltration into the streambed. There exists an inherent threshold process in the channel system where the capacity of the flow to transport sediment varies spatially, producing local erosion or deposition, with a significant factor being transmission losses (Schumm and Hadley 1957). Deposition caused by transmission losses is generally a persistent but slow process.

The channel erosion model in this study is built on these process-based foundations of arroyo formation and evolution.

1.3 Outline of Investigations

The investigations in this study are organized into three topics: current trends in hydroclimate, rainfall analysis and channel erosion modeling.

1.3.1 Current Trends in Hydroclimate

Chapter 3 addresses current trends in hydroclimate in the Rio Puerco Basin. Annual, monthly and daily rainfall and runoff data are analyzed by the nonparametric Mann-Kendall test for trend in order to identify trends in the recent instrumental records. Analyses at the annual timescale show a statistically significant increasing trend in Rio Puerco precipitation, but not streamflow. Trends in annual precipitation are also connected with large scale climate anomalies in the Northern Pacific. Analyses at the monthly timescale show that the increase is due to rising non-summer rainfall. At the daily timescale, substantial shifts in the distributions of both rainfall and runoff are found, which indicate that progressive changes in the conveyance of the Rio Puerco main stream have occurred since 1948, causing a significant decrease in extreme runoff events. Trend analyses are investigated in the context of geomorphological changes in the river system. Chapter 3 provides a data-based foundation for and evidence of channel changes in the Rio Puerco main stream in the recent period.

1.3.2 Rainfall Analysis

Chapter 4 addresses precipitation dynamics in the Rio Puerco Basin. Using radar and climate station data, the spatial and temporal distributions of daily rainfall totals are investigated by the discrete random cascade model. Parameters of the model are estimated for both spatial and temporal rainfall and related to large scale regional and seasonal precipitation. The goal of this investigation is to develop a rainfall modeling system that will disaggregate a regional annual rain rate into a sequence of spatial daily rainfall fields while preserving important statistical properties at all spatial and temporal scales involved. A part of the rainfall modeling system is a conceptual lumped rainfall-runoff model that transforms generated spatially distributed rainfall into daily streamflow on a subbasin scale. The rainfall modeling system is successfully calibrated and tested with available data. Chapter 4 provides a complete analysis of the spatial distribution of daily rainfall in the Rio Puerco Basin and develops the mathematical foundation for the generation of subbasin runoff for the Rio Puerco channel erosion modeling.

1.3.3 Channel Erosion Modeling

Chapter 5 addresses erosion dynamics in the Rio Puerco Basin. A new channel erosion model, ERMO, is developed here for simulating long-term channel change in ephemeral streams under spatially and temporally variable runoff. Sediment rating curves are calibrated and used to determine the transport capacity-driven sediment transport in the Rio Puerco main stream. The ERMO model is used to analyze the longitudinal and cross-sectional erosion profiles in long-term simulations. Most active areas are found in the vicinity of tributary confluences with the main stream. It is determined that although aggradation is the dominant process in the Rio Puerco main stream in the long term, short term variability is caused mostly by rapid degradation in wet years. The influence of streamflow magnitude and infiltration into the streambed on maximum deposition and erosion depths is analyzed. Investigations of a changing climate on channel dynamics are also conducted. It is found that moving towards a wetter climate generally brings more stream-wide degradation and an intensification of both maximum erosion and deposition rates. Examples of short-term analyses with another channel erosion model, GRAD, developed here emphasize the dynamic nature of channel change, in particular the role played by the spatial and temporal variability in runoff at tributary confluences. Chapter 5 provides a new modeling approach to long-term behavior of ephemeral streams. It quantifies channel erosion and deposition in the Rio Puerco main stream and points to the primary processes and determining factors in the erosion dynamics.

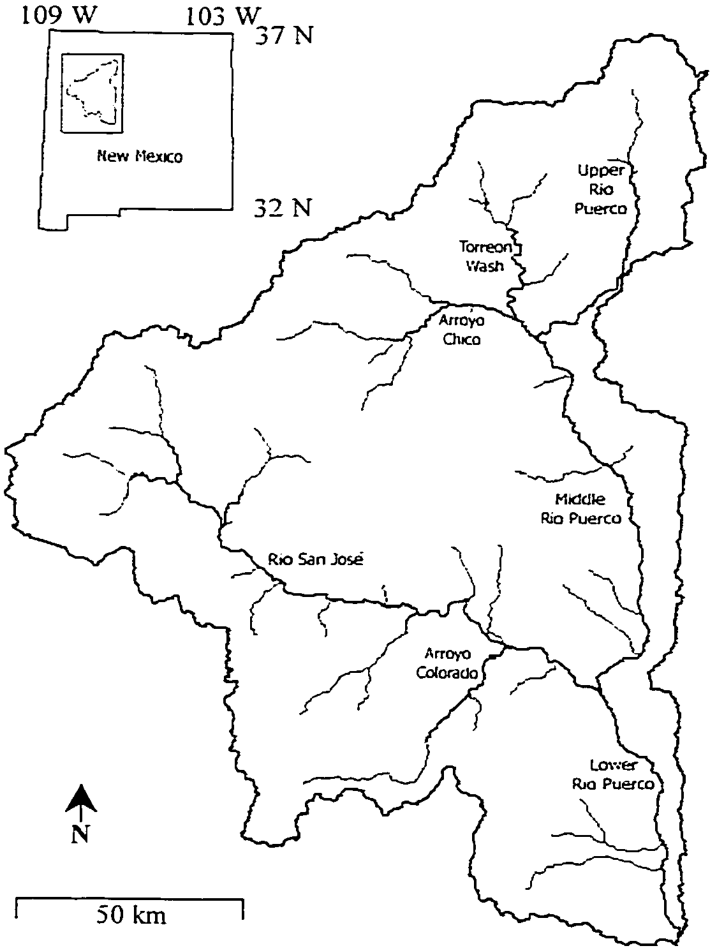

Figure 1.1. Location of the Rio Puerco Basin in New Mexico.

2 Rio Puerco Basin and Data

This Chapter gives a description of the Rio Puerco Basin and of the hydroclimatic, geographic and sediment data used in further investigations. The Basin is subdivided into smaller hydrologic units based on analyses with digital terrain data (Section 2.2). These subbasins will be used in rainfall-runoff modeling in Chapter 4 and erosion modeling in Chapter 5. Some topological properties of the extracted Rio Puerco river network are presented. Rainfall and runoff data sources and basic descriptive statistics on annual, monthly and daily timescales are presented (Sections 2.3 and 2.4). Regional flood frequency analysis is conducted on peak and annual maximum flow data (Section 2.5). Also reported are field measurements of infiltration rates in the Rio Puerco streambed and analyses of sediment texture (Section 2.6).

2.1 Basin Description

The Rio Puerco is a major tributary of the Rio Grande west of Albuquerque, in northwestern New Mexico. It drains an area of approximately 16,000 km^2 (Figure 2.1). The northeastern boundary of the watershed lies in the Sierra Nacimiento and San Pedro Mountains. In the west and southwest are the San Mateo Mountains and the Malpais, a broad plateau capped with basaltic lava. The watershed valley is covered by Tertiary and Upper Cretaceous sandstone and shale, which are very easily eroded when exposed.

Modern streams in the Rio Puerco Basin are cutting into the most recent valley floodplain deposits composed predominantly of silt and sand (Bryan and McCann 1937, 1938, Wright 1946, Love 1986). Vegetation consists mostly of grassland and pinyon juniper woodland, with some sagebrush and forest. The climate of the region is semiarid (Thornthwaite et al. 1942, Antevs 1954). Average annual precipitation ranges from about 180 mm in the south to 600 mm in the mountains. Three quarters of the Basin receive less than 350 mm (Dortignac 1960, Heath 1983). Elevations in the basin range from 1437 m at the outlet to 3445 m at Mount Taylor (about 2160 m at the Rio Puerco headwaters near Cuba). The Rio Puerco Basin is essentially undeveloped, moderately grazed and very sparsely populated.

The Rio Puerco consists of five main hydrologic units: the Arroyo Chico watershed, the Rio San Jose watershed and the Rio Puerco main stream which consists of the Upper (upstream of the confluence with Arroyo Chico), Middle (between Arroyo Chico and Rio San Jose tributaries) and Lower (downstream of the Rio San Jose confluence) Rio Puerco watersheds (Figure 2.2). The Rio Puerco main stream is approximately 240 km long. The river network is characterized by ephemeral and intermittent flow conditions, with high transmission losses as a result of infiltration. The Rio Puerco carries large amounts of suspended sediment (e.g., Bryan 1928a, Nordin 1963). Large variability in streamflow, together with great sediment transporting capacity and availability, make the fluvial system susceptible to rapid channel changes.

2.2 Subbasin and River Network Analyses

The geographical analyses reported here were conducted on a 1-degree digital elevation model (DEM) of the Rio Puerco region obtained from the USGS EROS Data Center (edcwww.cr.usgs.gov). The 1-degree DEM provides coverage in 1×1 degree blocks (1:250,000 scale maps). The Rio Puerco Basin covers 6 of these maps (Shiprock E, Gallup E, Saint Johns E, Aztec W, Albuquerque W, Socorro W). The spatial resolution of 1-degree DEMs is 3 arcseconds (which is about 77 meters at Albuquerque longitude and latitude). The data are produced by the Defense Mapping Agency from cartographic and photographic sources and are gridded based on the World Geodetic System 1984 standard UTM projection.

The original 3-arcsec scale DEM for the Rio Puerco region was averaged onto a Δx=Δy=500 meter grid, with elevations rounded off to 1 meter (Figure 2.1). This spatial scale is sufficient for the analyses in this study, especially with regard to the rainfall radar data scale (Chapter 4). The Rio Puerco Basin was extracted from the regional DEM by computing drainage directions and contributing drainage area using the D8 method; i.e., assigning flow in the steepest direction to one of the cell's 8 neighbors (O'Callaghan and Mark 1984). A constant drainage area threshold A_t=50 km^2 was used to determine the extent of the drainage network. All computation were performed with the geographic information system GRASS (blacklandgrass.brc.tamus.edu). The extracted Rio Puerco Basin and river network are shown in Figure 2.2.

2.2.1 Subbasin Properties

A further step in the characterization of the Rio Puerco was to delineate subbasins for the purposes of rainfall-runoff and erosion modeling. A drainage area threshold of 100 km^2 was used to identify so-called *tributary subbasins*; i.e., basins that contain a single tributary with drainage area greater than 100 km^2. The remaining areas were termed *main stream subbasins*; i.e., basins that are assumed to drain directly into the main stream. The latter may contain tributaries that drain areas less than 100 km^2. Figure 2.3 shows 25 delineated subbasins in the Rio Puerco watershed: there are 13 tributary subbasins and 12 main stream subbasins.

Note that only the area downstream of the Malpais junction is considered to contribute to the Rio San Jose. The Malpais volcanic region is a closed basin that does not drain directly to the Rio San Jose, and the upstream reaches of the Rio San Jose are substantially affected by the withdrawals of water from Bluewater reservoir. Therefore it is assumed that the natural hydrology of the Rio San Jose in terms of its contributions to the Rio Puerco are due to the flow regime in the Lower Rio San Jose (Subbasin 4 in Figure 2.3).

Drainage areas, average elevations, slopes and other properties for main stream subbasins are listed in Table 2.1, and for the tributary subbasins in Table 2.2. The total delineated area (Figure 2.3) of the 25 Rio Puerco subbasins is 13,057 km^2. (Including the Upper Rio San Jose watershed the total drainage area was 15,987 km^2.) The two largest tributaries are Rio San Jose (Subbasin 4): A=3,922 km^2 and the Arroyo Chico (Subbasin 10): A=3,592 km^2. Compared to the main stream subbasins, the tributary subbasins have a higher average elevation (2020 m compared to 1842 m) and steeper hillslopes (0.062

m/m compared to 0.055 m/m). The hypsometric curve for the Rio Puerco (25 subbasins) is shown in Figure 2.4. The type of the curve is indicative of an approximate equilibrium between aggradation and degradation basin-wide, or moderate basin activity (e.g., Bras 1990, p.585-6). Half of the area in the Rio Puerco has a relative elevation less than 0.28.

An important factor in the subbasin rainfall-runoff transformation is the infiltrability of soils. To parametrize this factor on a subbasin scale, data from the STASGO Database of the Natural Resources Conservation Service (NRCS) were used. The soil infiltrability parameter F is defined as the area fraction of low and very low infiltration soils in each subbasin (Tables 2.1 and 2.2). Permeable soils (low F) are generally along the main stream, whereas areas of low permeability are mostly in Upper Rio Puerco Basin and in tributary subbasins below the Mount Taylor massif.

2.2.2 River Network

The DEM-extracted river network was compared with the drainage network from 1:250,000 topographic maps of the Basin. The location of the streams matched well. Naturally, the ephemeral nature of the streams could not be captured by the DEM analysis. The elevation profile and increase in drainage area along the main stream are shown in Figure 2.5. From the outlet to the mouth of tributary Subbasin 13, the main stream is 214.7 kilometers long. The elevation profile is gradual, without major breaks in slope. Table 2.1 gives some properties of the main stream subbasin channel sections. The average length of the main stream reaches was 17.9 km, average channel bed slope was 0.003 m/m and sinuosity (defined by the ratio of along-channel length and straight-line length) was 1.09. The low sinuosity is an artifact of the DEM-extraction technique and true values of sinuosity in the Rio Puerco are higher. Some channel properties of tributary channels are given in Table 2.2.

A variety of geomorphological properties can be used to describe individual forms of drainage networks. For illustration, let us look at Horton's laws on the DEM-extracted river network. The river network is ordered according to Strahler, where channels that originate at a source are defined as first order streams, and when two streams of order ω join a stream of order $\omega+1$ is created. Horton's laws relate the number of streams of a given order N_ω, stream area A_ω and stream length L_ω to stream order as:

$$\begin{aligned} N_\omega &= R_B^{\,\Omega-\omega} \\ A_\omega &= R_A^{\,\omega-1} A_1 \\ L_\omega &= R_L^{\,\omega-1} L_1 \end{aligned} \tag{2.1}$$

where R_B is the bifurcation ratio, R_A is the stream area ratio and R_L is the stream length ratio. The highest order of the Rio Puerco DEM-extracted network is Ω=8. Figure 2.6 shows the Rio Puerco estimated network ratios: R_B=4.1, R_A=4.6 and R_L=2.1. These values are all within ranges normally observed in perennial river networks (e.g., Bras 1990).

Based on Horton's laws, it can be concluded that the Rio Puerco drainage network extracted from the DEM is not distinguishable in its structure from an average perennial river network. However, observations show that the structure of the actual dissected arroyo network may be rather different. This difference cannot be captured by DEM analyses and a different approach to the topological description of ephemeral stream structure may be needed.

2.3 PRECIPITATION

Climate records for the Rio Puerco region were obtained from the National Climatic Data Center (NCDC) databases (TD3200) of the National Oceanic and Atmospheric Administration (NOAA). The National Weather Service (NWS) cooperative network of precipitation gaging stations was queried for stations lying within a quadrangle that covered the entire Basin (including a buffer zone up to 0.5 degrees of longitude and latitude). Within this quadrangle, 18 stations were identified that were in operation in 1997 and had sufficiently long records (at least 30 years). The locations of these stations are shown in Figure 2.7 and station details are listed in Table 2.3. Of these stations, only 4 were located directly inside the Rio Puerco watershed (Cuba, Torreon, Grants and Laguna). The Rio Puerco Basin lies in three New Mexico NOAA climatic divisions: Northern Mountains (NM-02), Southwestern Mountains (NM-04) and Central Valley (NM-05).

Monthly precipitation for all stations was obtained from NCDC Online Climate Data (www.ncdc.noaa.gov/ol/climate/climatedata.html). These data were verified and extended with monthly precipitation data sets from the Western Regional Climate Center (WRCC) Database (www.wrcc.dri.edu/summary/climsmnm.html) and with the NCDC Summary of the Day CD-ROM Database. A base record period starting in 1948 (or beginning of record) was chosen for most analyses. Annual precipitation totals were computed from monthly data at all sites.

The analysis of long-term climatic division precipitation on a monthly and annual basis for the period 1895-1997 was conducted on data from the NCDC Online Climate Database (www.ncdc.noaa.gov/onlineprod/drought/ftppage.html). The divisional monthly data are based on the NCDC digital database TD9640. For issues of data quality, the reader is referred to the respective web pages of the data providers. Data quality is generally fair to good. Precipitation records were used without erroneous data that did not pass the (standard) NWS quality check.

2.3.1 Annual

Climatic divisions in which the Rio Puerco Basin lies are diverse. Highest precipitation occurs in the Northern Mountains (NM-02) climatic division that contains the San Pedro and Sierra Nacimiento mountains to the northeast of the basin, the Upper Rio Puerco watershed, and most of the Arroyo Chico watershed. It is also the region with the highest mean elevation and lowest mean air temperature. From the 103-year divisional climate record (1895-1997), mean annual precipitation in this climatic division is 418 mm. Moderate precipitation occurs in the Southwestern Mountains (NM-04) climatic division that contains the Rio San Jose watershed, Zuni Mountains, the Malpais and much of western New Mexico. Mean annual precipitation in this division is 332 mm. Lowest precipitation occurs in the Central Valley (NM-05) climatic division in the Rio Grande basin of central New Mexico. This division also contains the Middle and Lower Rio Puerco watersheds and the Mount Taylor massif. Mean annual precipitation in this division is 239 mm. Generally, mean annual precipitation correlates well with station elevation (Figure 2.8).

Mean annual precipitation in the Rio Puerco Basin was estimated by the Thiessen polygon method. Station weights ρ are listed together with station mean annual precipitation in Table 2.4. Of the 18 precipitation gaging stations analyzed, 14 stations had areas of influence inside the watershed (i.e., $\rho > 0$). The estimated mean annual precipitation in the Rio Puerco Basin from the period 1948-1997 was 267 mm.

Snowfall in the Rio Puerco Basin, especially in the Northern Mountains, can be significant. Mean annual snowfall totals for all stations are also listed in Table 2.4. Maximum snowfall is at Wolf Canyon, with an average of 3,178 mm per year. Snowfall is important for spring snowmelt runoff contributions to the Upper Rio Puerco watershed.

2.3.2 MONTHLY

Precipitation seasonality is influenced mostly by the summer monsoon that brings moisture from the Gulf of Mexico and the eastern Pacific to the U.S. Southwest region (e.g., Hirschboeck 1987, Webb and Betancourt 1990, Gershunov and Barnett 1998). This is evident in Figure 2.9, which shows the seasonal distribution of mean monthly precipitation computed from gaging station data grouped by climatic division (Table 2.5).

Precipitation peaks in August, with a well-defined beginning of the summer monsoon period in July. On the average, the winter (January-March) and spring (April-June) seasons contribute 16% of precipitation to the annual total, summer (July-September) contributes 46% and fall (October-December) 22%. Precipitation is highest in the northern portion of the Rio Puerco Basin (NM-02), whereas the central and southern portions (NM-05, NM-04) receive less rainfall throughout the year. Mean monthly precipitation in the peak month of August ranged from 44 mm in the Central Valley to 69 mm in the Northern Mountains division. However, maximum recorded monthly totals at individual gages were considerably greater (see Table 2.4).

2.3.3 Daily

Daily precipitation totals are extremely variable throughout the Basin. Maximum recorded 1-day events for all analyzed stations are listed in Table 2.4. Socorro, south of the basin, rated highest, with 92 mm recorded in one day (on July 30, 1976). Four other stations recorded events larger than 70 mm: Wolf Canyon, Chaco Canyon, Jemez Springs and Laguna. An interesting fact is that the distinction between the wet and dry seasons is not so obvious for 24-hour extreme rainfall. In fact, rainfall events larger than 30 mm occurred throughout the non-winter months. The correlation of 24-hour maximum recorded precipitation amounts with station elevation is not as good as for mean annual rainfall (Figure 2.8).

In other studies of extreme events, NOAA reports estimates of 6- and 24-hour precipitation amounts with given return periods for New Mexico (NOAA Atlas). According to these estimates, the 100-year 24-hour precipitation amount ranges from about 65 mm to 75 mm in the lower lying portions of the Basin, up to 105 mm in the San Pedro Mountains, and 95 mm on Mount Taylor.

In further investigations, daily precipitation data are organized on a water year basis to facilitate comparisons with streamflow analyses.

2.4 Streamflow

Altogether there were 20 streamflow gaging stations (continuous and partial record gages) active in the Rio Puerco Basin at different times during the last 70 years. Data from 12 of these stations with sufficiently long and reliable records are used in this study. Of these stations, 6 report daily streamflow and peak flow (continuous record gages) and

6 report only peak flow (partial record - crest stage gages). The continuous gages are automatic gages that record stage every 15 minutes from which daily averages of stage and discharge are computed. Crest stage gages are commonly read only after known major floods. The Bernardo gage (3530) is also a real-time gage which transmits stage information every 3 hours to the New Mexico USGS District Office in Albuquerque via the GOES data collection system, and it can be viewed online at wwwdnmalb.cr.usgs.gov. Streamflow gage locations are plotted in Figure 2.10 and basic information is given in Table 2.6 (throughout this study, gages are generally referred to by their 4-digit identification number from Table 2.6).

This study relies mostly on data from 4 *main stations* with continuous records of daily streamflow at the outlets of main Rio Puerco subbasins and the watershed as a whole: Rio Puerco above Arroyo Chico (3340), Arroyo Chico (3405), Rio San Jose at Correo (3515) and Rio Puerco near Bernardo (3530). Only three of these gages are currently in operation. Daily and peak streamflow data were obtained from the USGS National Water Information System (NWIS) Database. Monthly and annual totals were computed from daily data.

In addition to analyses for the complete periods of record (Table 2.7), comparisons between streamflow records were conducted on a *common record* spanning 35 years between 1952 and 1986 at the 4 main stations. Analyses with daily precipitation and streamflow data in this study are organized on a water year basis (the water year begins on October 1 and ends on September 31 of the water year).

Since 1951 there have been no notable dams or irrigation diversions on the main stream of the Rio Puerco or any of its tributaries (with the exception of Bluewater Dam in the headwaters of the Rio San Jose Basin upstream of Grants). Although analyzed streamflow records suffer from errors induced by high suspended sediment concentrations and extreme flow variability common in ephemeral streams, they are largely free of anthropogenic effects within the watershed. The quality of streamflow data is reported to be generally poor (USGS Water Resources Data). Occasionally, flow has to be estimated because of faulty gages. This estimation, commonly done by regional streamflow regression models, inspecting high-water marks or analyzing precipitation records (Waltemeyer 1998, personal communication), introduces error and bias into the data. Although the author did his best to ensure the highest possible data quality (e.g., random data quality checks were conducted on raw 15-minute streamflow data), subsequent results are only as precise as available daily records allow.

2.4.1 Annual

Estimates of mean annual runoff observed at Rio Puerco streamflow gages are listed in Table 2.7. Highest runoff volume is generated on the average in the Arroyo Chico and Upper and Middle Rio Puerco watersheds. Rio San Jose, which drains an area almost twice the size of Arroyo Chico, contributes only about half the volume of Arroyo Chico because of upstream water use (Bluewater Lake) and the extreme permeability of the Rio San Jose Basin. Average annual discharge from the Rio Puerco Basin at Bernardo is about 38.4 mil m^3/yr (1941-1997). Inter-annual variability is fairly consistent at main gages. The Rio San Jose near Grants gage (3435) has lower variability because discharges are influenced by springs and reservoir releases from Bluewater Dam upstream.

Minimum annual infiltration losses in the Middle and Lower Rio Puerco reaches were estimated by subtracting observed streamflow at Bernardo from observations at Rio Puerco above Arroyo Chico, Arroyo Chico and San Jose at Correo (4 main stations). The annual streamflow loss (ASL) obtained in this manner is a minimum estimate of annual infiltration into the streambed, because it does not account for all ungaged tributary contributions. Average ASL is 4.02 mil. m^3/yr (from the common record), but variability is large. Stochastic simulations conducted in this study in Chapter 5 (that account for tributary inflows) show that the average annual infiltration loss along the entire main stream of the Rio Puerco is much larger. The length of the main stream between Arroyo Chico and the outlet is approximately 185 km, which gives us an estimated minimum infiltration loss of 21.8 m^3 per meter of channel per year. This figure corresponds with infiltration measurements of Heath (1983) on the Lower Rio Puerco and of the author's own field measurements of infiltration into the streambed.

2.4.2 Monthly

The monthly distribution of mean streamflow volumes at the main gages is shown in Figure 2.11. On the average, most runoff occurs between July and September (about 60%). The fall and winter seasons each contribute only 11.5% of the total annual runoff. August is commonly the month with the highest observed runoff. In the Upper Rio Puerco watershed (3340), monthly runoff peaks in May, because of snowmelt and baseflow runoff from the mountainous regions in the northern and northeastern sections of the watershed. The average spring runoff contribution to annual runoff at gage 3340 was 42%, whereas the summer season contribution was only 32%. At the same time, these contributions were 5% in the spring and 73% in the summer for Arroyo Chico (3405). At the outlet of the Basin, average monthly runoff in the high flow month of August was 14.4 mil. m^3, which is 38% of the annual total.

Descriptive statistics for monthly streamflow at the Rio Puerco main stations are given in Table 2.8. The variability in monthly streamflow volumes is large at all stations, which is typical of ephemeral streams (the monthly coefficient of variation is generally greater than 1). Also reported is P_0, the probability of zero total streamflow in a given month. The parameter P_0 is a good measure of seasonal aridity in the Rio Puerco Basin. Interestingly, the probability of zero monthly runoff at the outlet of the Rio Puerco watershed at Bernardo (3530) is generally much higher than for upstream areas, especially in the low flow period November-April (P_0 varied between 0.49 and 0.86 for these months). It is clear that in this period losses resulting from infiltration in the Rio Puerco main stream on a monthly basis are often sufficient to eliminate all channel flow before it reaches the Basin outlet.

2.4.3 Daily

Rio Puerco daily streamflow series are intermittent, with a probability that there will be no flow on a given day and a continuous distribution of streamflow magnitudes on days with flow. Flow duration curves capture this intermittency and variability. The flow duration curve is essentially a cumulative frequency curve that shows the probability that in the studied period a given streamflow value was equaled or exceeded. Flow duration curves for the common period of record for the four main gaging stations constructed by the total period method are shown in Figure 2.12. Class intervals were computed according to the method originally suggested by Searcy (1959).

Several observations can be made from this figure. First, although the Arroyo Chico (3405) and Rio Puerco above Arroyo Chico (3340) gages are very close to each other, there are considerable differences between their flow duration curves. Although flows less than about 1.5 m^3/s are more frequent in the Upper Rio Puerco Basin (spring season contributions), larger flows are more frequent in the Arroyo Chico Basin (summer season contributions). Second, the Rio San Jose at Correo (3515) gage shows less variability in daily streamflow (with a large percentage of flows concentrated in the range 0.1-0.3 m^3/s). This is likely the result of reservoir and spring-influenced water supplies upstream and the geologic nature of the Rio San Jose watershed. Third, although the Bernardo (3530) gage measures the outflow of the whole Rio Puerco Basin, overall it is much drier than the upstream gages. The probability of zero flow on a day in the 35 years of the common record was p_o=0.43 for 3340, p_o=0.43 for 3405, p_o=0.52 for 3515 and p_o=0.69 for 3530. However, at the same time, flows above 0.4 m^3/s were most frequent at the Bernardo gage.

Analyses in Chapter 3 will look at the shifts in the distribution of daily streamflow and examine changes in the quantiles of these distributions. Extreme runoff events are of great importance in the Rio Puerco river system because of their large erosive power and high sediment transporting capacity. For this reason, a flood frequency analysis was conducted on annual maximum daily flows and annual peak flows.

2.5 Flood Frequency Analysis

The largest recorded flood at the Arroyo Chico gage was on September 12, 1972, at 431 m^3/s. At the Rio Puerco above Arroyo Chico gage, the largest flood on record was on July 29, 1967, at 197 m^3/s. The record of observations at Bernardo is longer and the maximum flood there was estimated at about 911 m^3/s on September 23, 1929 (Heath 1983).

The magnitude and frequency of extreme runoff events in the Rio Puerco watershed are examined in this section by conducting a regional flood frequency analysis on annual instantaneous peak flow and annual maximum daily flow data at all streamflow gaging stations with records longer than 20 years. Flood quantiles with given recurrence intervals are estimated, together with their confidence bounds. In general, frequency analyses consist of the following steps: (1) choice of distribution model, (2) estimation of distribution parameters from data, (3) quantile computation and error estimation.

2.5.1 GEV Distribution

It has been argued that the physical origin of random variables such as annual maximum events suggests that their distribution is likely to be one of several extreme value types (e.g., Stedinger et al. 1993). The generalized extreme value (GEV) distributions have been widely used in flood frequency analysis with very good results (e.g., Chowdhury et al. 1991, Hosking and Wallis 1997).

In its general form, the GEV is a parametric distribution with 3 parameters. The cumulative distribution function (cdf) of the GEV distribution can be written as:

$$F(x) = \exp\left\{-\left[1 - \frac{\kappa(x-\xi)}{\alpha}\right]^{1/\kappa}\right\} \qquad \kappa \neq 0 \tag{2.2}$$

$$F(x) = \exp\left\{-\exp\left[-\frac{x-\xi}{\alpha}\right]\right\} \qquad \kappa = 0 \tag{2.3}$$

where ξ is the location parameter, α is the scale parameter and κ is the shape parameter of the distribution. There are three types of GEV distributions. For $\kappa=0$, the GEV distribution becomes Type I, also known as the Gumbel distribution, where x is not bounded. For $\kappa>0$, the GEV probability distribution function (pdf) has an upper bound at $\xi+\alpha/\kappa$ and corresponds to the GEV Type III distribution (this is typically not the type applicable to flood data). For $\kappa<0$, the GEV pdf has a lower bound at $\xi+\alpha/\kappa$ and corresponds to the GEV Type II distribution (this is the most common type used in flood frequency analysis).

Quantiles (i.e., annual extreme streamflows with an exceedance probability $q=1-p$) of the GEV distribution can easily be computed by inverting Equations (2.2) and (2.3) to obtain:

$$x_p = \xi + \frac{\alpha}{\kappa}\{1-[-\ln(F(x))]^{\kappa}\} = \xi + \frac{\alpha}{\kappa}\{1-[-\ln(p)]^{\kappa}\} \tag{2.4}$$

$$x_p = \xi - \alpha\ln[-\ln(F(x))] = \xi - \alpha\ln[-\ln(p)] \tag{2.5}$$

where p is the non-exceedance probability (or cumulative probability) of the quantile x_p.

There are several methods by which the parameters of the GEV distribution may be estimated from flood data. The L-moment method developed by Hosking (1990) was chosen here. The advantage of the L-moment method is that it doesn't involve power transformations of data, so the L-moments are nearly unbiased and not affected by outliers (e.g., Chowdhury et al. 1991, Stedinger et al. 1993, Hosking and Wallis 1997).

Also important for GEV parameter estimation are the dimensionless L-moment ratios - coefficients of variation τ_2, skewness τ_3 and kurtosis τ_4 - which are analogous to their product moment equivalents.

Extreme runoff events in the Rio Puerco are generally created by summer convective high-intensity rainfall events, and therefore they can be assumed to come from a single population, which justifies the use of a single distribution model for flood frequency analysis.

2.5.2 Regional Parameter Estimation

Regional flood frequency estimation is the preferred approach to flood frequency analysis mainly because short records bias at-site analyses (e.g., Lettenmaier et al. 1987, Hosking and Wallis 1988, Potter and Lettenmaier 1990, Hosking and Wallis 1997). The concept underlying regionalization is that distributions of floods at sites in a region are the same except for some scale parameters that reflect the size, rainfall, runoff and other characteristics of each basin.

For heterogeneous regions with some sites with longer records, the advised regionalization method has been to estimate a regional shape parameter for a chosen regional distribution model and then to estimate the remaining parameters of at-site distributions from at-site data (Lettenmaier et al. 1987, Potter and Lettenmaier 1990, Stedinger et al. 1993). This is the approach chosen here, with the following steps: (1) Regional second and third L-moments are computed from at-site moment estimates $\hat{\lambda}_j$ by record length weighting:

$$\hat{\lambda}_j^r = \sum_{k=1}^{K} n_k \hat{\lambda}_j \Big/ \sum_{k=1}^{K} n_k \qquad j = 2, 3 \tag{2.6}$$

There are K sites in the region, each with a record length n_k. A regional L-moment skewness coefficient is then estimated as:

$$\hat{\tau}_3^r = \frac{\hat{\lambda}_3^r}{\hat{\lambda}_2^r} \tag{2.7}$$

(2) A regional GEV distribution shape parameter κ^r is computed by iteratively solving

$$\frac{\hat{\tau}_3^r + 3}{2} = \frac{1 - 3^{-\hat{\kappa}^r}}{1 - 2^{-\hat{\kappa}^r}} \tag{2.8}$$

The shape parameter is the only regional parameter of the GEV model common at all stations. (3) Using κ^r, at-site estimates of the scale and location parameters of the GEV distribution are computed from:

$$\hat{\alpha} = \frac{\hat{\kappa}^r \hat{\lambda}_2}{(1 - 2^{-\hat{\kappa}^r})\Gamma(1 + \hat{\kappa}^r)} \tag{2.9}$$

$$\hat{\xi} = \hat{\lambda}_1 - \frac{\hat{\alpha}}{\hat{\kappa}^r}[1 - \Gamma(1 + \hat{\kappa}^r)] \tag{2.10}$$

where $\Gamma(.)$ is the gamma function. The estimated GEV distributions at each site are then based on at-site estimates of ξ and α, and a regional estimate of κ.

This regional flood frequency method does not assume that flood series at a site, when scaled by the mean, are homogeneous, but rather that only the skewness at each site can be represented by a regional average. Lettenmaier et al. (1987) provided an exhaustive Monte Carlo analysis of the effects of heterogeneity on different regionalization procedures. They conclude that for regions with the coefficient of variation greater than 0.5, the above GEV regionalization procedure is the preferred method for flood quantile estimation (in the Rio Puerco, the average product moment coefficient of variation for peak flows was 0.9 and 0.86 for annual maxima).

Results of the Rio Puerco regional GEV flood frequency analysis are listed in Table 2.9. Asymptotically, most quantile estimators $\hat{x}_p$ are normally distributed. It follows that if $\hat{x}_p$ has a variance $\mathrm{Var}(\hat{x}_p)$, then an approximate 100(1-α)% confidence interval is:

$$\hat{x}_p \pm Z_{1-\alpha/2}\sqrt{\mathrm{Var}(\hat{x}_p)} \qquad (2.11)$$

where $Z_{1-\alpha/2}$ is the value of the standard normal distribution with a probability of exceedance of $\alpha/2$. The sampling variances $\mathrm{Var}(\hat{x}_p)$ in Table 2.9 are computed according to Lu and Stedinger (1992). Corrections to the confidence bounds as a result of intersite dependence were not conducted (Hosking and Wallis 1988). The estimated regional GEV shape parameters are: κ^r=-0.256 for peak flows and κ^r=-0.207 for maximum daily flows. These values represent GEV models with thick tails, which are very typical for flood flows in semi-arid and arid regions (Farquahrson et al. 1992).

The final question remaining is whether the proposed regional distribution is consistent with available at-site data. Various goodness-of-fit tests address this issue.

2.5.3 Results

The question of distribution appropriateness in flood frequency analyses contains two inseparable parts. First is the question whether the chosen distribution model is a good model for the true distribution from which our sample is drawn (accepting that the true model will never be known with certainty). Second is the question whether the proposed regional distribution model fits our at-site data satisfactorily.

The first question is difficult to answer. Many types of distribution models have been used in regional flood frequency analyses, and the choice between them is somewhat arbitrary. However, the GEV family of models has been found appropriate for flood data, and it has been argued that the problem of distribution misspecification can be to some degree diminished if a robust parameter estimation technique is used, such as the L-moment method (Landwehr et al. 1980). Furthermore, plots of L-moments against each other (L-moment diagrams) can be very useful for identifying which families of distributions are consistent with data from a region (e.g., Vogel et al. 1992, Vogel and Wilson 1996).

Hosking and Wallis (1993) suggest a measure of discordancy by plotting L-moment skewness, kurtosis and coefficient of variation against each other and flagging sites that plot far from the center of the points. The skewness-variation L-moment plot for the Rio Puerco gages is shown in Figure 2.13 (top). Note that the L-moment spread is greater for peak flows than for maximum daily flows. For peak flows, station 3485 stands out with high skewness and coefficient of variation. This crest stage gage (with questionable data) was not used in determining the (shape) parameter of the regional GEV distribution model. Another L-moment diagram, the skewness-kurtosis plot, is very useful for determining whether the GEV family of models is good for given at-site samples in a region. There is a one-to-one relationship between GEV model skewness and kurtosis, which is also plotted in Figure 2.13 (bottom). Although formal definitions of a goodness-of-fit for the L-moment diagram have been proposed by Hosking and Wallis (1993), here it suffices to conclude from visual inspection that the GEV model is consistent with Rio Puerco at-site data.

The second question can be tackled by goodness-of-fit tests, which determine whether departure of the data from a model is statistically significant, or whether it is due to expected sample-to-sample variability. Two goodness-of-fit tests were used to test whether the shape parameter κ of the at-site distribution (or the at-site L-moment skewness τ_3) equals that of the regional GEV distribution κ^r (or the regional average L-moment skewness τ_3^r): the probability plot correlation (PPC) test (e.g., Filliben 1975) and the L-skewness (LS) test (e.g., Hosking 1990). All Rio Puerco stations were found to conform to the regional distribution ($\kappa = \kappa^r$) at the α=0.01 significance level, except the Encinal Creek gage (3485) for peak flows in the PPC test. In the LS test the most severe departure was again found at Encinal Creek (3485) for peak flows, significant at α=0.05. Both the PPC and the LS test are especially good for detecting departure for thick-tailed GEV alternatives κ<0 (which was the Rio Puerco studied case).

An example of the probability plot and the fitted regional GEV model for the Bernardo gage is shown in Figure 2.14. The probability axis is plotted in logarithmic scale in order to accentuate the tail of the distributions.

The Water Resources Council (WRC) standard method for flood frequency analysis used in the U.S., the Log Pearson Type III distribution, was found to be inferior to the regional GEV method (e.g., Potter and Lettenmaier 1990). In general, quantiles computed using the log Pearson Type III model with low discharge threshold and zero generalized skewness adjustments by Waltemeyer (1996) for some Rio Puerco stations (using data up to 1993) underestimate the regional GEV quantile results in this study, especially for higher return periods.

2.6 CHANNEL PROPERTIES

Sediment properties play an important role in the erosion dynamics. In terms of the water balance and routing in ephemeral streams, streambed infiltration is crucial. Sediment transport is affected by particle size and distribution. In this section, results of field measurements of infiltration and analyses of sediment texture in the Rio Puerco are reported.

2.6.1 STREAMBED INFILTRATION

Streamflow losses resulting from infiltration during runoff events in the Rio Puerco outweigh evaporative losses, and are an important element in the water balance. Rio Puerco is a losing stream; i.e., in contrast to perennial rivers, discharge generally decreases in the downstream direction. In the context of losses during the conveyance of water, we are interested in evaluating the steady-state infiltration rate f into the streambed.

In June 1997 a field experiment was carried out in which the in-situ infiltration rate of soils in the Rio Puerco streambed was measured at seven cross sections. The measurement sites were distributed throughout the Rio Puerco main stream and on the Arroyo Chico (about 3 km upstream of the confluence) and their locations are shown in Figure 2.15. Infiltration was measured using a single ring infiltrometer with diameter 25 cm (inserted into the substrate to a depth of at least 10 cm) (e.g., Bouwer 1986, Daniel 1988). Water for the infiltration tests was clear with temperature ranging between 22-25 °C (at-site sediment laden water could not be used, because the stream was dry at most sites). A constant head range (4-5 cm) was maintained in the infiltrometer and the time for the drop in head was measured. The duration of every measurement was approximately 1 hour. Infiltration stabilized after the initial period to the steady-state infiltration rate f.

Cylinder infiltrometers measure in-situ infiltration rates for inundated soils; i.e., the field-saturated hydraulic conductivity of the alluvium. Issues that may complicate the extrapolation of these point measurements into a Rio Puerco stream-wide infiltration rate are (1) two-dimensional subsurface flow; (2) high suspended sediment concentrations; (3) restricting subsurface silt-clay layers (Bouwer 1986). However, ring infiltrometer tests are advantageous in cases where many measurements need to be taken and where the substrate has high permeability (Daniel 1988).

The infiltration rate f was determined at 2-6 points evenly distributed across the main channel at each cross section and at 1-2 points in the floodplain. An example of the measurements at the Junkyard section is shown in Figure 2.16. The estimated steady-state infiltration rate is listed as an average for the channel segment and the floodplain segment at all cross sections in Table 2.10 and shown in Figure 2.17. The data exhibit wide variability, with a basin-wide average of about f=31 cm/hr in the streambed and f=28 cm/hr in the floodplain. These values are high and indicative of the loose sandy alluvium in the Rio Puerco stream system. It is noteworthy that because the streambed and floodplain generally both consist of the same sediment material, the infiltration values for the streambed and floodplain did not show any appreciable differences.

Heath measured hydraulic conductivities in the Lower Rio Puerco reach, and found the average surface rate to be about 65 cm/hr (range between 9 and 138 cm/hr) (Heath

1983). In Tijeras Arroyo, in New Mexico, Thomas estimated infiltration rates to be between 2.9 and 38.2 cm/hr (Thomas 1995).

The effect of water storage in the alluvium on effective infiltration rates is impossible to estimate in the field. It is argued that although groundwater levels are generally low in the Rio Puerco Basin, occurrence of perched groundwater tables is possible (Heath 1983). Furthermore, in ephemeral streams, infiltration rates depend on the antecedent moisture condition of the channel alluvium (e.g., Keppel and Renard 1962) and on the suspended sediment concentration in the flow (e.g., Matlock 1965). Crust and soil sealing effects that are often observed to decrease infiltration on hillslopes (e.g., Mualem and Assouline 1996) operate in a similar manner on the channel bed (e.g., Nordin 1963).

2.6.2 Sediment Texture

Soil sediment samples were taken at each of the infiltrometer sites described in the preceding section with a standard soil core sampler. In addition, at 6 of the 7 cross sections a 200 g surface soil sample and a subsurface soil sample were taken at a single location in the center of the streambed. The subsurface soil sample was taken at a depth of about 0.25 m. The purpose of these latter samples was to evaluate the layering and armoring (if present) in the most recent layer of flood deposits.

Textural analyses of the soil samples were conducted at the Agricultural Research Service (ARS) Laboratory in Fort Collins. Soil samples were oven dried and the particle size distribution between the three main size classes (sand, silt, clay) was analyzed by the simplified hydrometer method (Gee and Bauder 1979). This method quantifies the primary particle sizes by their settling rates in an aqueous solution using a hydrometer type ASTM 152H. The classes of these primary particles are: clay <0.002 mm, silt 0.002-0.05 mm, sand 0.05-2 mm. Pretreatment for the removal of soluble salts, organic matter, carbonates and iron oxides was not necessary. The simplified hydrometer method has a detection limit of 2% for all classes and is generally reproducible to within ±8%. The procedure requires a 40 g dried soil sample to which 100 ml of calgon dispersing solution is added and mixed on a horizontal shaker for about 16 hours. The suspension is then brought to a volume of 1 liter by deionized water, put into a sedimentation cylinder and stirred. Temperature corrections are made and hydrometer readings are taken at 40 sec (sand) and 2 hours (clay), and the relative sizes of the particle classes are determined.

Altogether there were 33 samples analyzes at the infiltrometer sites: 22 from the channel streambed and 11 from the floodplain. There were 12 additional samples (6 surface and 6 subsurface) analyzed for the vertical distribution of sediment in the streambed. The results are in Table 2.11. The sediment is remarkably homogeneous, containing on the average over 90% of sand. The floodplain sediments seemed to be generally finer (there were fewer samples taken on the floodplain). This is likely a result of increased (vegetation) roughness and fine sediment settling in the floodplain after the passage of larger floods that inundate these areas. Other analyses of bed material particle size distribution in the Rio Puerco stream system also showed largely sandy material: D_{50}=0.07 mm (Nordin, 1963) and D_{50}=0.11 mm (Elliott 1979) in the downstream reaches and D_{50}=0.22 mm in the upstream reaches (Elliott 1979).

Based on the laboratory analyses, finding of previous researchers and data from the USGS NWIS Database, the Rio Puerco bed material in this study is assumed to be homogeneous sand with representative particle sizes D_{50}=0.125 mm, D_{10}=0.0625 mm and D_{90}=0.325 mm.

Another interesting result of the textural analysis is that there are insignificant differences in the texture of the surface and subsurface sediments in the streamline of the Rio Puerco analyzed cross sections. This is an indication of the homogeneity of bed sediments transported through the Rio Puerco stream system. It also raises doubts about the importance of armoring of the streambed in the Rio Puerco on long-term channel change. It remains true that a silty layer is deposited in the streambed in waning flow which effectively armors the bed. Our excavations in the streambed showed intermittent layers, 1-2 cm thick, of silt and clay in the streambed. However, this remains a short-term phenomenon, and the silty layer is promptly eroded or covered with sediment on the passage of the next runoff event.

Table 2.1. Rio Puerco main stream subbasin and channel properties: drainage area A, average elevation E, basin average slope S_b (average slope is computed from a 3×3 cell neighborhood around each cell), basin soil infiltrability parameter F (average fraction of area with low and very low infiltration soils), along-channel reach length L, sinuosity s, and channel reach slope S_{ch}.

No.	A [km^2]	E [m]	S_b [m/m]	F	L [km]	s	S_{ch} [m/m]
1*	147.8	1515.5	0.0358	0.10	17.2	1.047	0.0015
2*	322.3	1562.5	0.0341	0.12	23.1	1.092	0.0019
3*	266.3	1604.1	0.0357	0.17	23.3	1.089	0.0019
4*	257.5	1643.5	0.0393	0.10	23.1	1.188	0.0023
5*	358.0	1730.5	0.0402	0.12	21.2	1.026	0.0026
6*	219.5	1776.9	0.0399	0.24	12.0	1.102	0.0032
7*	137.3	1842.7	0.0685	0.30	16.1	1.051	0.0031
8*	181.8	1944.9	0.0868	0.17	10.6	1.115	0.0018
9*	200.8	2051.3	0.0746	0.17	10.0	1.066	0.0038
10*	256.5	1944.7	0.0494	0.18	32.5	1.146	0.0045
11*	216.0	2154.5	0.0801	0.28	16.7	1.074	0.0052
12*	115.5	2327.4	0.0775	0.18	9.1	1.068	0.0041

* Main stream subbasins are denoted with a star superscript in Figure 2.3.

Table 2.2. Rio Puerco tributary subbasin and channel properties: drainage area A, average elevation E, basin average slope S_b (as in Table 2.1), basin soil infiltrability parameter F (as in Table 2.1), bed slope S_{tr} (average slope in the reach 5 km upstream from the tributary mouth), channel width W (estimated or measured width at the tributary mouth), and the distance X of the tributary confluence from the Rio Puerco outlet.

No.	Name	A [km^2]	E [m]	S_b [m/m]	F	S_{tr} [m/m]	W [m]	X [km]
1	Coyote Draw	764.0	1786.5	0.0544	0.32	0.0083	10	7.7
2	Arroyo Comanche	245.0	1740.1	0.0451	0.10	0.0079	10	17.2
3	Hidden Mnt. Arroyo	177.0	1711.7	0.0623	0.22	0.0049	8	51.7
4	Rio San Jose (DS)	3921.5	2037.6	0.0638	0.22	0.0057	10	63.5
5	Can. de los Apaches	266.3	1801.9	0.0504	0.25	0.0046	10	76.4
6	Can. del Ojo	200.5	1788.1	0.0435	0.20	0.0064	10	86.6
7	Arroyo Cuervo	161.5	1885.0	0.0611	0.20	0.0083	8	119.8
8	Salado Creek	345.3	2113.4	0.0748	0.40	0.0101	10	122.3
9	Canyon Tapia	138.5	2323.7	0.0727	0.27	0.0097	8	146.4
10	Arroyo Chico	3591.8	2116.9	0.0464	0.31	0.0036	15	156.4
11	Arroyo Hondo	113.3	2396.5	0.1107	0.42	0.0088	6	205.6
12	Arroyo Chijuilla	169.5	2168.9	0.0424	0.58	0.0057	6	207.2
13	Rio Puerco (US)	284.0	2388.7	0.0760	0.60	0.0104	15 *	214.7

* This is the Rio Puerco main stream width at the outlet of Subbasin 13.

Table 2.3. NWS cooperative network gaging station information for selected sites in and around the Rio Puerco watershed used in this study (records ending in 1997 are used in most analyses). H is station elevation.

Station name	COOP ID	County	Climatic division **	Lat. (N) [deg:min]	Lon. (W) [deg:min]	H [m]	Record since (years)
Chaco Canyon Nat. Monum.	291647	San Juan	NM-01	36:02	107:55	1881.8	1948 (51)
El Morro Nat. Monum.	292785	Cibola	NM-01	35:03	108:21	2202.8	1948 (51)
Lybrook	295290	Rio Arriba	NM-01	36:14	107:34	2179.3	1951 (48)
Mcgaffey 5 SE	295560	McKinley	NM-01	35:20	108:27	2438.4	1949 (50)
Star Lake	298524	McKinley	NM-01	35:56	107:28	2022.3	1953 (46)
Otis	296465	San Juan	NM-01	36:19	107:52	2097.0	1957 (42)
Cuba *	292241	Sandoval	NM-02	36:01	106:58	2147.3	1948 (51)
Jemez Springs	294369	Sandoval	NM-02	35:46	106:41	1909.0	1948 (51)
Torreon Navajo Mission *	299031	Sandoval	NM-02	35:48	107:11	2042.2	1961 (38)
Wolf Canyon	299820	Sandoval	NM-02	35:57	106:45	2505.5	1952 (47)
Grants-Milan Munic. Airp. *	293682	Cibola	NM-04	35:10	107:54	1987.3	1953 (46)
Quemado	297180	Catron	NM-04	34:20	108:31	2090.9	1948 (51)
Augustine 2 E	290640	Socorro	NM-04	34:05	107:37	2133.6	1948 (51)
Bernardo	290915	Socorro	NM-05	34:25	106:50	1443.2	1962 (37)
Laguna *	294719	Cibola	NM-05	35:02	107:22	1773.3	1948 (51)
Los Lunas 3 SSW	295150	Valencia	NM-05	34:46	106:45	1475.2	1957 (42)
Socorro	298387	Socorro	NM-05	34:04	106:53	1397.5	1948 (51)
Albuquerque Int. Airp.	290234	Bernalillo	NM-05	35:03	106:36	1618.5	1948 (51)

* Stations located within the Rio Puerco watershed boundary.
** Climatic divisions are:
NM-01 Northwestern Plateau
NM-02 Northern Mountains
NM-04 Southwestern Mountains
NM-05 Central Valley

Table 2.4. Mean annual precipitation P, maximum monthly precipitation $P_{\mathrm{mon}\ max}$, maximum 1-day rainfall extremes $P_{24\mathrm{hr}\ max}$, mean annual snowfall R and Thiessen weights ρ for analyzed precipitation stations (statistics computed for periods of record in Table 2.3).

Station name	ρ	P [mm]	$P_{\mathrm{mon}\ max}$ [mm] (in month)	$P_{24\mathrm{hr}\ max}$ [mm]	R [mm]
Chaco Canyon Nat. Monument	0.0020	228	149 (OCT)	71	386
El Morro Nat. Monument	0.0090	351	195 (AUG)	64	1113
Lybrook	0	287	166 (AUG)	54	704
Mcgaffey 5 SE	0.0515	481	173 (OCT)	66	1397
Star Lake	0.0813	234	113 (AUG)	47	485
Otis	0	257	119 (OCT)	51	752
Cuba *	0.0535	323	135 (AUG)	52	648
Jemez Springs	0.0066	439	179 (AUG)	71	787
Torreon Navajo Mission *	0.1453	259	118 (AUG)	48	511
Wolf Canyon	0.0051	586	180 (JUL)	85	3178
Grants-Milan Munic. Airport *	0.2136	273	119 (OCT)	49	323
Quemado	0	256	168 (AUG)	53	594
Augustine 2 E	0.0015	299	180 (AUG)	51	267
Bernardo	0.0596	212	141 (AUG)	57	91
Laguna *	0.2851	238	124 (JUL)	73	282
Los Lunas 3 SSW	0.0566	231	116 (OCT)	61	107
Socorro	0	220	161 (AUG)	92	173
Albuquerque Int. Airport	0.0293	219	85 (JUL)	49	259

* Stations located within the Rio Puerco watershed boundary.

Table 2.5. Mean monthly precipitation in millimeters at analyzed Rio Puerco precipitation stations, summarized by climatic divisions from climate summaries (for periods of record in Table 2.3).

Station name	JAN	FEB	MAR	APR	MAY	JUN	JUL	AUG	SEP	OCT	NOV	DEC
Chaco Canyon	12.4	12.7	14.0	12.2	15.5	12.2	30.0	32.8	28.7	24.9	16.8	15.0
El Morro	27.7	21.8	28.7	18.8	15.7	15.0	50.3	66.3	35.8	28.2	20.8	25.1
Lybrook	18.3	15.2	18.3	12.4	14.7	13.7	33.0	52.3	31.0	26.4	18.3	18.3
Mcgaffey	45.0	37.1	46.0	27.9	20.6	16.5	61.5	69.1	40.1	37.6	37.3	37.8
Star Lake	11.1	9.9	11.9	11.9	14.5	14.0	34.8	47.2	29.0	22.4	15.2	12.7
Otis	14.2	12.2	16.8	13.0	14.7	17.8	36.8	45.5	26.2	27.7	17.8	14.5
Mean (NM-01)	21.5	18.2	22.6	16.0	16.0	14.9	41.1	52.2	31.8	27.9	21.0	20.6
Cuba	21.8	16.8	22.1	17.0	20.1	20.1	52.6	57.7	35.3	28.4	20.1	17.0
Jemez Springs	27.4	22.1	26.2	22.9	27.2	27.4	67.1	79.2	40.6	38.1	27.2	24.1
Torreon	13.7	11.4	14.7	13.5	18.0	15.2	38.1	47.0	33.3	24.4	18.3	13.7
Wolf Canyon	46.5	40.6	47.8	31.5	32.8	30.5	86.4	92.2	47.2	44.5	41.1	39.1
Mean (NM-02)	27.4	22.7	27.7	21.2	24.5	23.3	61.0	69.0	39.1	33.8	26.7	23.5
Grants-Milan	13.0	11.2	13.5	11.4	14.7	14.7	43.9	52.6	34.8	27.9	14.5	16.8
Quemado	12.2	13.7	16.0	9.4	9.1	10.9	52.1	56.6	28.4	23.9	12.4	13.0
Augustine	10.7	9.7	11.2	6.9	13.2	13.5	56.1	65.5	40.1	29.7	10.2	13.7
Mean (NM-04)	11.9	11.5	13.5	9.2	12.4	13.0	50.7	58.3	34.5	27.2	12.4	14.5
Bernardo	7.1	7.6	7.1	8.1	11.9	13.5	33.8	41.7	33.8	23.9	9.4	12.2
Laguna	10.7	9.9	10.4	9.4	15.7	12.4	43.2	47.8	32.3	26.9	8.6	12.7
Los Lunas	8.9	10.7	11.9	11.2	12.7	14.5	31.5	45.0	30.2	27.9	11.9	13.7
Socorro	8.3	9.6	8.7	9.1	11.3	15.4	36.4	47.6	34.9	26.5	9.9	14.6
Albuquerque	10.4	11.1	13.2	11.8	13.6	14.8	34.7	38.8	24.1	22.3	12.0	12.9
Mean (NM-05)	9.1	9.8	10.3	9.9	13.0	14.1	35.9	44.2	31.1	25.5	10.4	13.2

Table 2.6. Rio Puerco USGS streamflow gaging station information. A is contributing drainage area as reported in the USGS Water Resources Data and USGS NWIS Database. H is station elevation.

Station name	Station number *	Watershed	Lat. (N) [deg:min]	Lon. (W) [deg:min]	H [m]	A [km^2]
DAILY & PEAK FLOW						
Rio Puerco above Arroyo Chico	08 **3340** 00	Upper R. P.	35:36	107:10	1813.3	1088
Arroyo Chico	08 **3405** 00	Arr. Chico	35:36	107:11	1804.7	3600
Rio San Jose near Grants	08 **3435** 00	San Jose	35:04	107:45	1910.9	3030
Rio San Jose at Correo	08 **3515** 00	San Jose	34:58	107:11	1668.7	6553
Rio Puerco at Rio Puerco	08 **3525** 00	Lower R. P.	34:48	106:59	1526.6	14141
Rio Puerco near Bernardo	08 **3530** 00	Lower R. P.	34:25	106:51	1439.4	16110
PEAK FLOW						
San Pablo Creek near Cuba	08 **3327** 00	Upper R. P.	35:57	106:57	2075.7	33.2
San Mateo Creek n. San Mateo	08 **3426** 00	San Jose	35:21	107:47	2072.6	196
Arroyo Colorado near Correo	08 **3514** 00	San Jose	34:58	107:14	1691.6	1132
Grants Canyon at Grants	08 **3431** 00	San Jose	35:09	107:50	1966.0	33.7
Encinal Creek n. Casa Blanca	08 **3485** 00	San Jose	35:09	107:28	2026.9	16.0
Rio Paguate bl. Jackpile Mine	08 **3498** 00	San Jose	35:07	107:20	1773.9	277

* Only numbers in bold are used in this study for station identification.

Table 2.7. Record lengths at the analyzed Rio Puerco streamflow gaging stations and average annual runoff $\underline{Q}$ for the complete and common (1952-1986) records - the term in parentheses is the coefficient of variation of the estimate.

Station name	No.	Record period (length) for daily flow	Record period (length) for peak flow **	$\underline{Q}$ complete [mil m^3/yr]	$\underline{Q}$ common [mil m^3/yr]
DAILY & PEAK FLOW					
R.P. above A. Chico*	3340	1952 – 1997 (46)	1952 - 1996 (45)	12.92 (0.69)	12.17 (0.74)
Arroyo Chico	3405	1944 – 1986 (43)	1944 - 1986 (43)	18.77 (0.63)	19.07 (0.63)
R.S.J. near Grants*	3435	1937 – 1997 (61)	1937 - 1996 (60)	5.75 (0.4)	5.97 (0.35)
R.S.J. at Correo	3515	1944 – 1994 (51)	1935 - 1994 (52)	10.1 (0.75)	10.4 (0.82)
R.P. at Rio Puerco	3525	1935 – 1976 (42)	1929 - 1991 (51)	50.73 (0.72)	
R.P. near Bernardo*	3530	1941 – 1997 (57)	1940 - 1996 (57)	38.38 (0.75)	37.62 (0.75)
PEAK FLOW					
San Pablo Creek	3327		1971 - 1982 (12)		
San Mateo Creek	3426		1978 - 1982 (5)		
Arroyo Colorado	3514		1953 - 1959 (7)		
Grants Canyon	3431		1962 - 1995 (34)		
Encinal Creek	3485		1959 - 1995 (35)		
Rio Paguate	3498		1977 - 1993 (17)		

* Stations in operation in 1999.

** Because of missing data, record length may be less than that specified by record period.

Table 2.8. The mean and coefficient of variation of monthly streamflow Q_m in mil m^3 at Rio Puerco main gages for the common period of record (1952-1986). P_0 is the probability of zero monthly flow.

Station	JAN	FEB	MAR	APR	MAY	JUN	JUL	AUG	SEP	OCT	NOV	DEC
3340												
Q_m	0.14	0.77	1.31	1.35	2.81	1.0	1.13	1.87	0.88	0.63	0.18	0.1
CV(Q_m)	2.39	1.77	1.84	1.34	1.28	1.6	1.1	1.01	1.58	2.72	1.94	1.82
P_0	0.23	0.09	0.11	0.03	0.11	0.2	0.03	0.03	0.14	0.26	0.26	0.17
3405												
Q_m	0.23	0.96	1.07	0.37	0.21	0.39	3.18	7.35	3.37	1.51	0.27	0.16
CV(Q_m)	2.13	2.59	2.19	2.65	1.33	1.95	1.26	1.18	1.28	1.58	1.38	1.86
P_0	0.11	0.11	0.11	0.2	0.2	0.26	0	0	0.06	0.14	0.17	0.17
3515												
Q_m	0.3	0.34	0.41	0.51	0.29	0.16	1.31	3.81	1.65	1.24	0.21	0.19
CV(Q_m)	0.73	0.67	1.42	2.7	2.32	2.83	1.84	1.56	1.33	1.84	1.36	1.11
P_0	0.11	0.14	0.17	0.26	0.54	0.63	0.06	0	0.2	0.26	0.26	0.2
3530												
Q_m	0.1	0.8	1.52	1.12	1.99	1.03	5.36	14.38	6.98	3.76	0.48	0.09
CV(Q_m)	3.03	2.42	2.26	2.34	1.69	1.41	1.45	1.23	1.46	1.87	2.43	4.13
P_0	0.71	0.63	0.49	0.49	0.17	0.26	0.03	0	0.06	0.34	0.57	0.86

Table 2.9. Rio Puerco at-site product moments (and other descriptive statistics), regional GEV parameter estimators and flood quantiles Q_p in [m^3/s] with return periods $T = 5$, 10, 25, 50, 100 years, and 80% confidence intervals. The estimated regional shape parameters are κ^r=-0.256 for peak flows and κ^r =-0.207 for annual maxima. Quantiles are reported with three significant digits.

Station	3340	3405	3525	3530	3435	3515	3431	3485
PEAK FLOW								
Mean [m^3/s]	61.59	138.19	242.27	118.34	7.79	63.47	9.00	8.57
Std. Dev. [m^3/s]	40.85	94.08	199.12	98.99	7.94	64.30	11.10	20.97
Coeff. Var.	0.663	0.681	0.822	0.837	1.020	1.013	1.233	2.445
Coeff. Skew.	0.972	1.254	2.211	1.917	2.236	1.815	2.250	5.049
Minimum [m^3/s]	3.65	10.90	42.76	18.75	0.34	2.35	0.14	0
Maximum [m^3/s]	196.54	430.46	1067.66	532.42	39.65	311.52	43.90	122.63
n	45	43	51	57	60	52	34	35
κ^r = -0.256								
α (scale)	24.12	53.84	102.89	53.36	4.13	33.91	5.41	6.77
ξ (location)	39.59	89.09	148.44	69.67	4.03	32.54	4.06	2.40
$Q_{0.8}$ (T=5)	83.7 ± 14.9	188 ± 34	337 ± 60	167 ± 29	11.6 ± 2.2	94.6 ± 19.5	14.0 ± 3.9	14.8 ± 4.8
$Q_{0.9}$ (T=10)	113 ± 23	253 ± 52	462 ± 91	232 ± 45	16.6 ± 3.4	136 ± 30	20.5 ± 5.9	23.0 ± 7.2
$Q_{0.96}$ (T=25)	159 ± 35	356 ± 80	658 ± 141	334 ± 69	24.5 ± 5.2	200 ± 46	30.9 ± 9.1	35.9 ± 11.2
$Q_{0.98}$ (T=50)	201 ± 47	450 ± 107	838 ± 187	427 ± 92	31.7 ± 6.9	260 ± 61	40.3 ± 12.1	47.8 ± 14.9
$Q_{0.99}$ (T=100)	251 ± 60	562 ± 138	1051 ± 242	538 ± 119	40.2 ± 9.0	330 ± 79	51.6 ± 15.6	61.8 ± 19.3
ANN. MAX.								
Mean [m^3/s]	13.78	37.66	84.27	54.34	2.46	20.04		
Std. Dev. [m^3/s]	10.61	25.95	57.19	41.42	2.97	21.00		
Coeff. Var.	0.770	0.689	0.679	0.762	1.211	1.048		
Coeff. Skew.	1.974	1.332	0.930	1.188	2.410	2.671		
Minimum [m^3/s]	1.19	5.04	16.71	9.09	0.20	0.79		
Maximum [m^3/s]	56.64	122.63	232.22	169.35	15.24	116.11		
n	46	43	42	57	61	51		
κ^r = -0.207								
α (scale)	6.02	15.91	36.07	24.99	1.58	11.13		
ξ (location)	8.78	24.44	54.28	33.56	1.14	10.78		
$Q_{0.8}$ (T=5)	19.4 ± 3.3	52.4 ± 9.1	118 ± 21	77.5 ± 12.4	3.92 ± 0.76	30.4 ± 5.8		
$Q_{0.9}$ (T=10)	26.0 ± 4.9	70.0 ± 13.4	158 ± 31	105 ± 18	5.67 ± 1.12	42.7 ± 8.6		
$Q_{0.96}$ (T=25)	36.1 ± 7.4	96.6 ± 20.2	218 ± 46	147 ± 28	8.31 ± 1.68	61.3 ± 13.0		
$Q_{0.98}$ (T=50)	44.9 ± 9.6	120 ± 26	271 ± 60	184 ± 36	10.6 ± 2.2	77.6 ± 16.8		
$Q_{0.99}$ (T=100)	55.0 ± 12.1	147 ± 33	331 ± 76	226 ± 45	13.3 ± 2.8	96.3 ± 21.2		

Table 2.10. Measurment of infiltration rates at sites shown in Figure 2.15: f is the average steady-state infiltration rate.

Site	f [cm/hr]	No. of measurements	Range of f [cm/hr]
CHANNEL			
Horsefly	46.8	3	21.6 - 72
Mosquito	68.4	3	43.2 - 93.6
Arroyo Chico	3.6	3	1.8 - 5.4
Guadalupe	6.5	2	2.2 - 10.8
Junkyard	21.6	6	11.5 - 54
Hidden Lady	34.2	2	32.4 - 36
Bernardo	32.4	3	11.9 - 61.2
FLOODPLAIN			
Horsefly	28.8	1	
Mosquito	82.8	1	
Arroyo Chico	25.2	3	7.2 - 32.4
Guadalupe	3.6	1	
Junkyard	10.8	2	7.2 - 14.4
Hidden Lady	32.4	2	25.2 - 39.6
Bernardo	10.8	1	

Table 2.11. Soil textural analysis of streambed and floodplain soil samples (clay < 0.002 mm, silt 0.002 - 0.05 mm, sand 0.05 - 2 mm). Where applicable, the percentages are averages over all samples collected. Sites are shown in Figure 2.15.

Site	Sample*	Sand [%]	Silt [%]	Clay [%]	Classification (USDA)
Horsefly	CH (3)	95.0	2.5	2.5	sand
	FP (1)	87.5	5.0	7.5	loamy sand
	SURF (0)				
	SUBF (0)				
Mosquito	CH (3)	95.5	1.7	2.8	sand
	FP (1)	90.0	2.5	7.5	sand
	SURF (1)	94.1	2.5	3.4	sand
	SUBF (1)	94.1	2.5	3.4	sand
Arroyo Chico	CH (3)	93.6	2.5	3.9	sand
	FP (3)	94.2	2.5	3.3	sand
	SURF (1)	92.5	2.5	5.0	sand
	SUBF (1)	94.1	2.5	3.4	sand
Guadalupe	CH (2)	94.1	2.5	3.4	sand
	FP (1)	84.1	10.0	5.9	loamy sand
	SURF (1)	90.0	5.0	5.0	sand
	SUBF (1)	95.0	2.5	2.5	sand
Junkyard	CH (6)	90.9	3.3	5.8	sand
	FP (2)	55.0	16.3	28.7	sandy clay loam
	SURF (1)	92.5	5.0	2.5	sand
	SUBF (1)	89.1	2.5	8.4	sand
Hidden Lady	CH (2)	90.4	2.5	7.1	sand
	FP (2)	79.6	11.3	9.1	loamy sand
	SURF (1)	94.1	2.5	3.4	sand
	SUBF (1)	89.1	2.5	8.4	sand
Bernardo	CH (3)	88.0	3.3	8.7	loamy sand
	FP (1)	61.6	25.0	13.4	sandy loam
	SURF (1)	91.6	2.5	5.9	sand
	SUBF (1)	92.5	2.5	5.0	sand

* In parentheses is the number of samples.
The code is:
CH Channel sample/s
FP Floodplain sample/s
SURF Surface sample in channel
SUBF Subsurface sample (taken app. 25 cm below surface) in channel

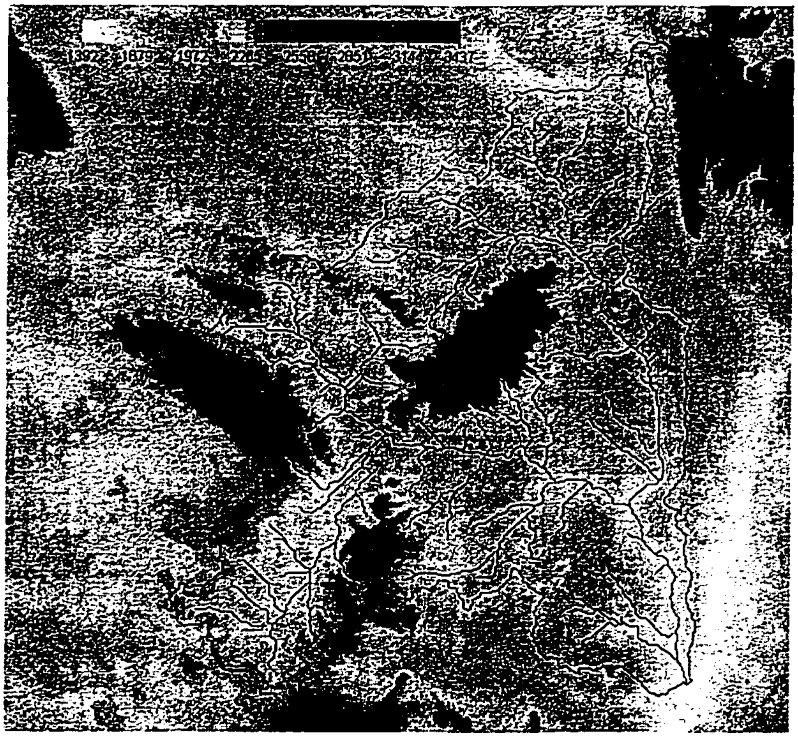

Figure 2.1. Rio Puerco Basin on a 500 meter DEM. Mt. Taylor is in the center of the Basin, the Rocky Mountain Divide follows the northwestern and western boundaries of the watershed. Rio Grande flows south in the bottom right of the figure. Elevations are in meters.

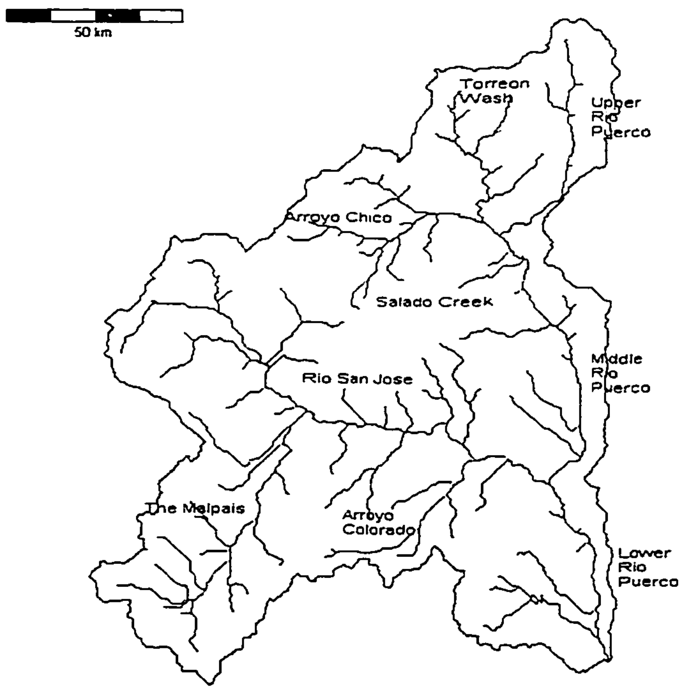

Figure 2.2. The Rio Puerco river system - main stream (divided into Upper, Middle and Lower sections) and main tributaries (Arroyo Chico and Rio San Jose).

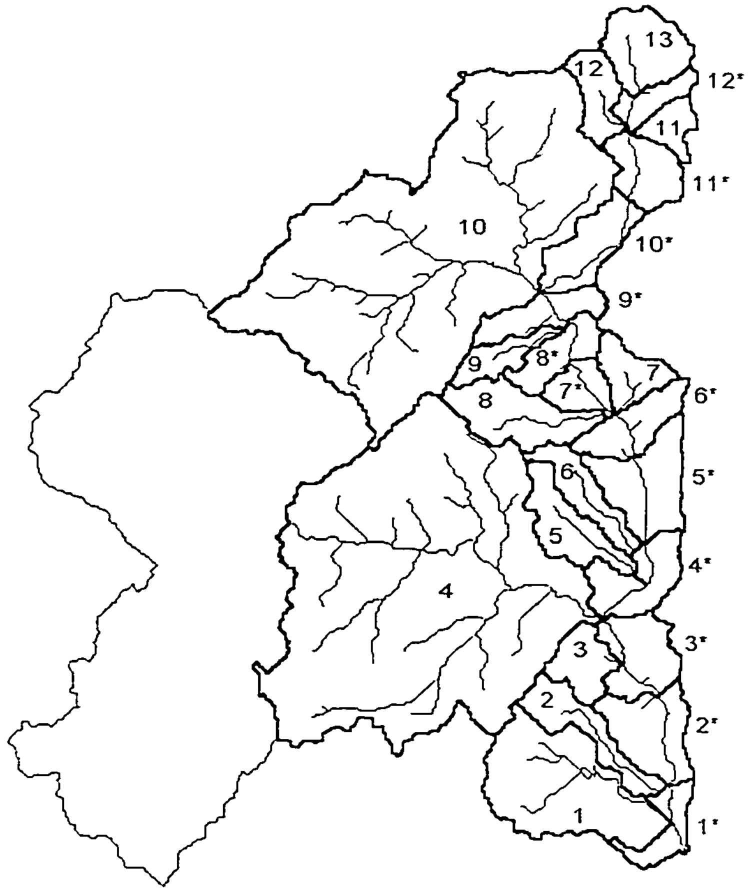

Figure 2.3. Delineation of 25 Rio Puerco subbasins in this study. There are 13 tributary subbasins (each with drainage area A>100 km^2) and 12 main stream subbasins (denoted with a star superscript).

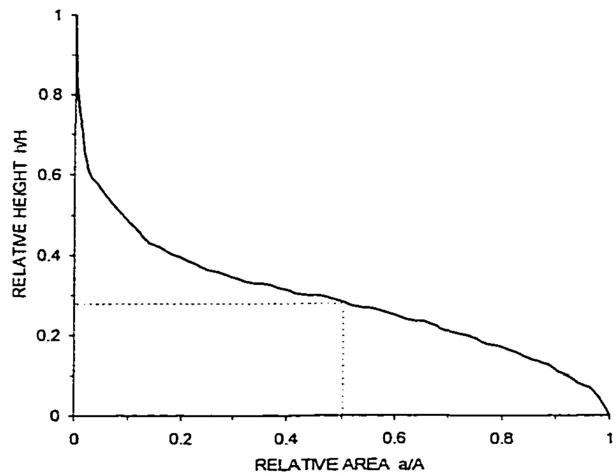

Figure 2.4. Hypsometric curve for the delineated Rio Puerco Basin in Figure 2.3.

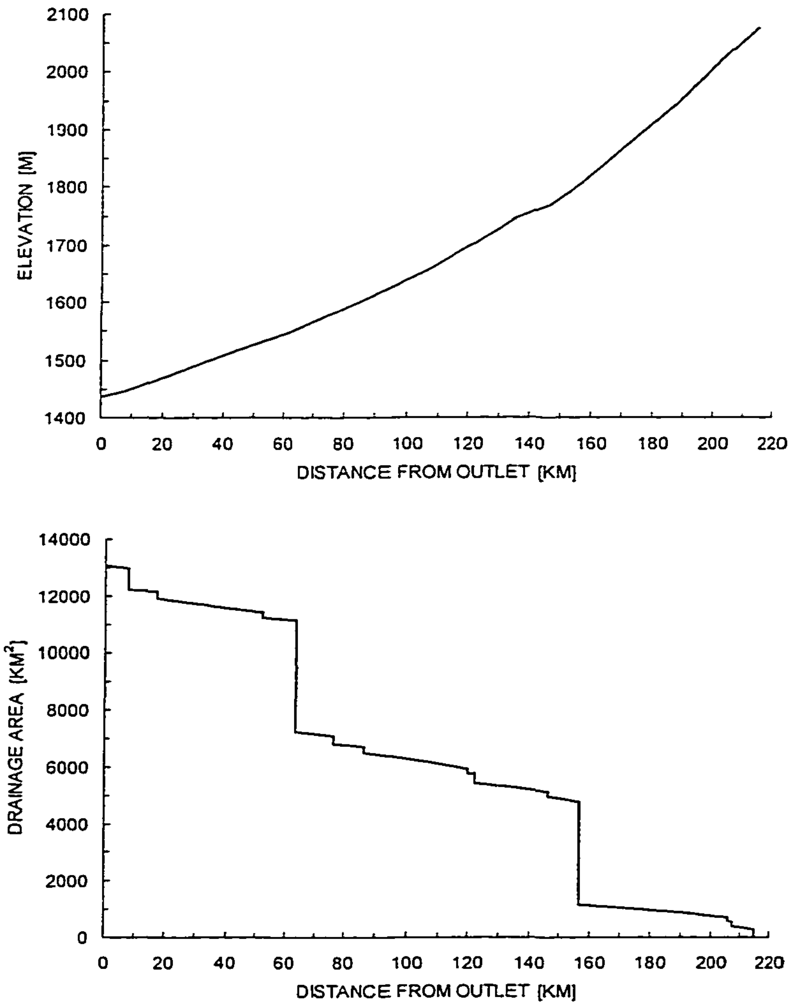

Figure 2.5. Elevation profile and drainage areas along the main stream for the delineated Rio Puerco Basin in Figure 2.3.

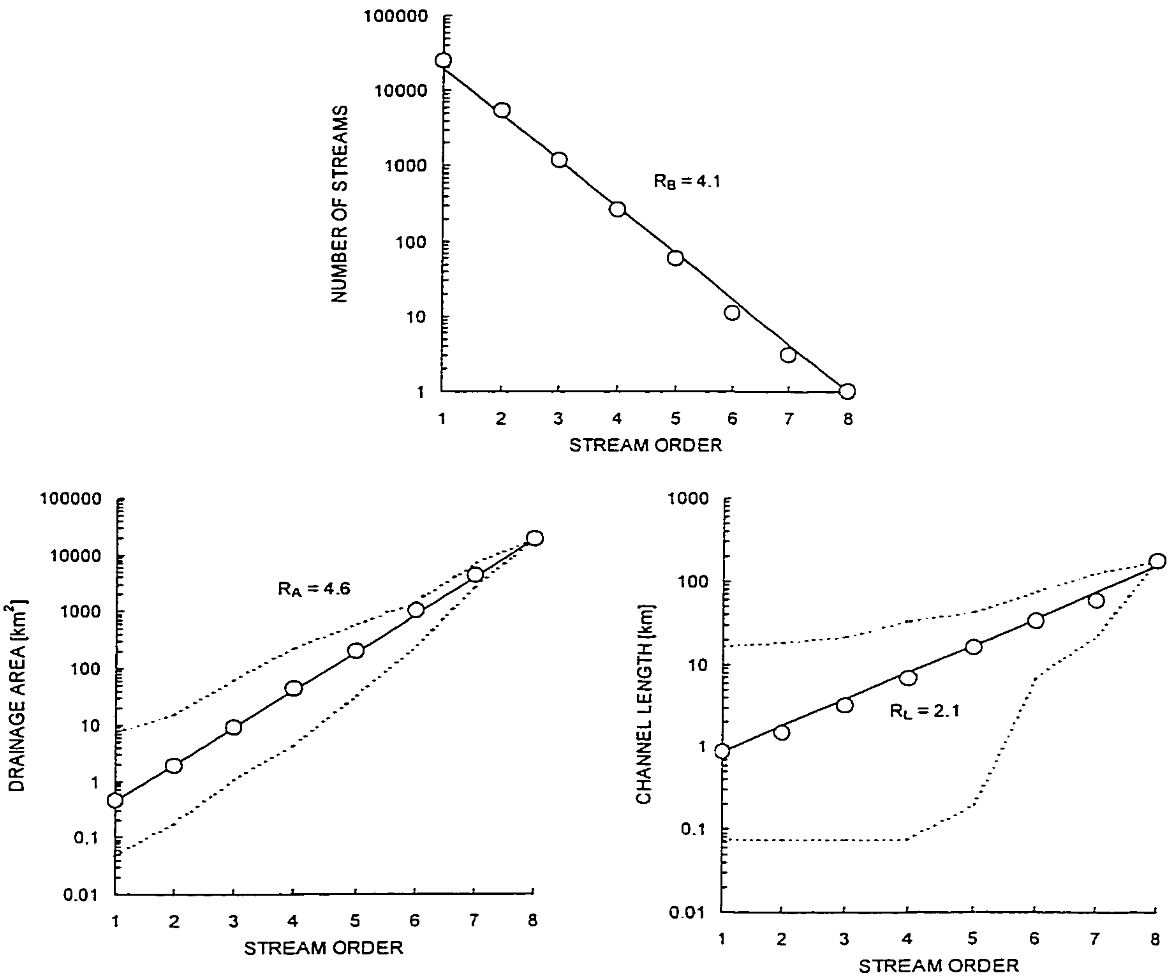

Figure 2.6. Horton's Laws for stream numbers (top), areas (bottom left) and along-channel lengths (bottom right). Dotted lines give the minimum and maximum value by stream order.

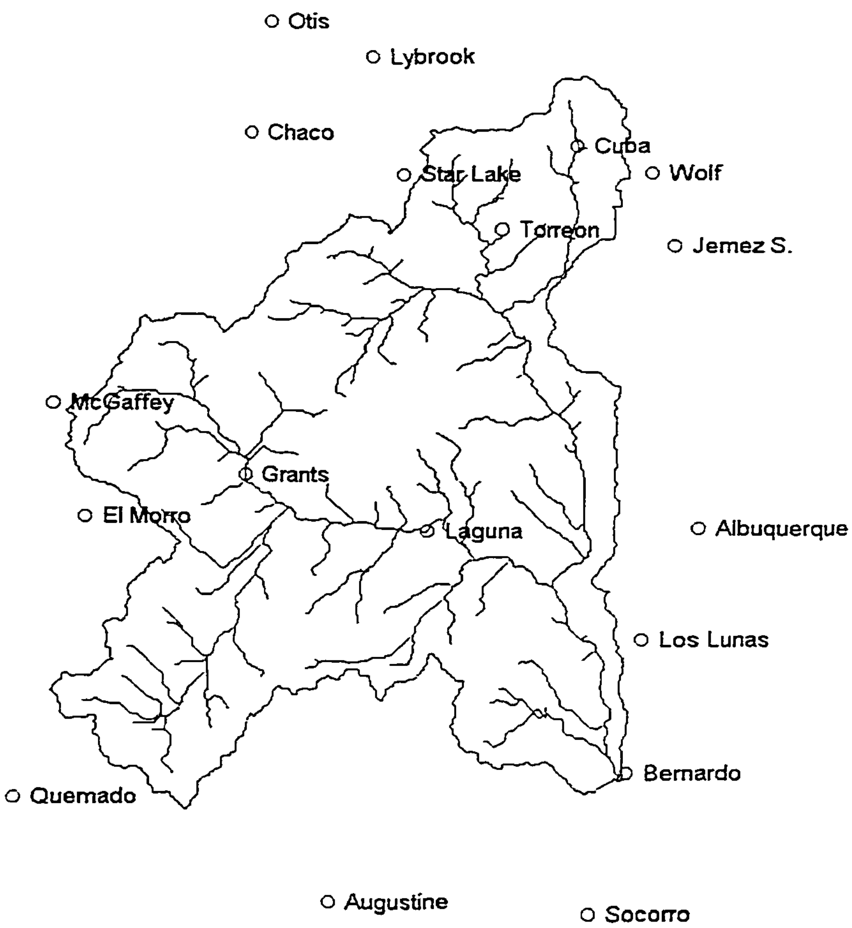

Figure 2.7. Locations of precipitation gaging stations used in this study.

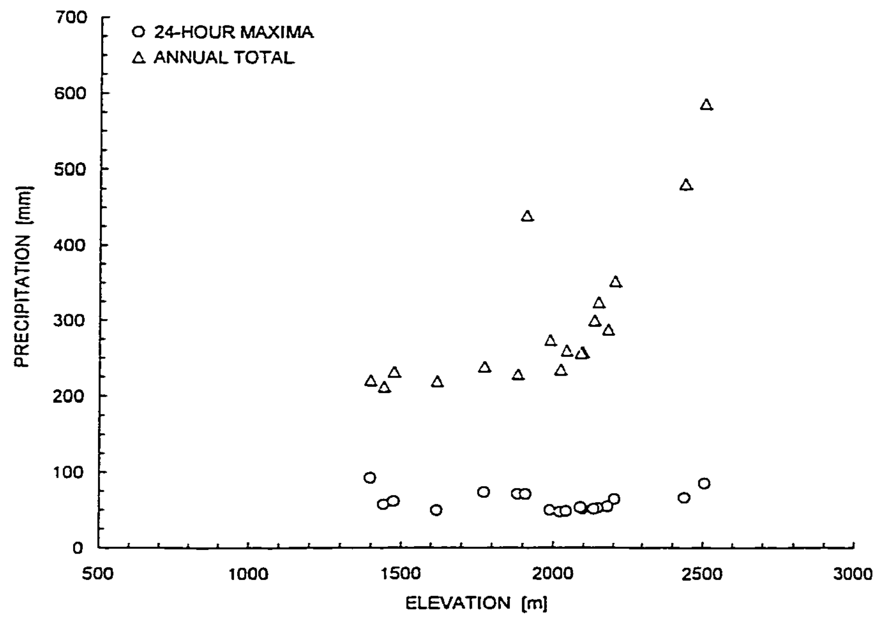

Figure 2.8. Relationship of 24-hour maximum observed rainfall and mean annual rainfall with station elevation.

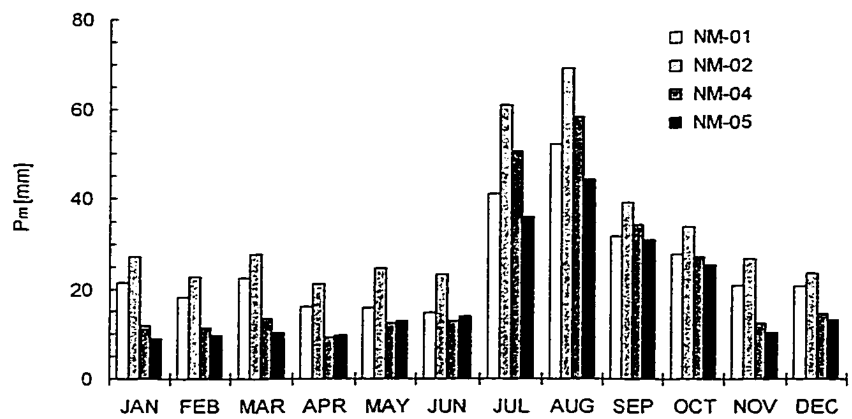

Figure 2.9. Mean monthly precipitation at Rio Puerco climate stations grouped by climatic division.

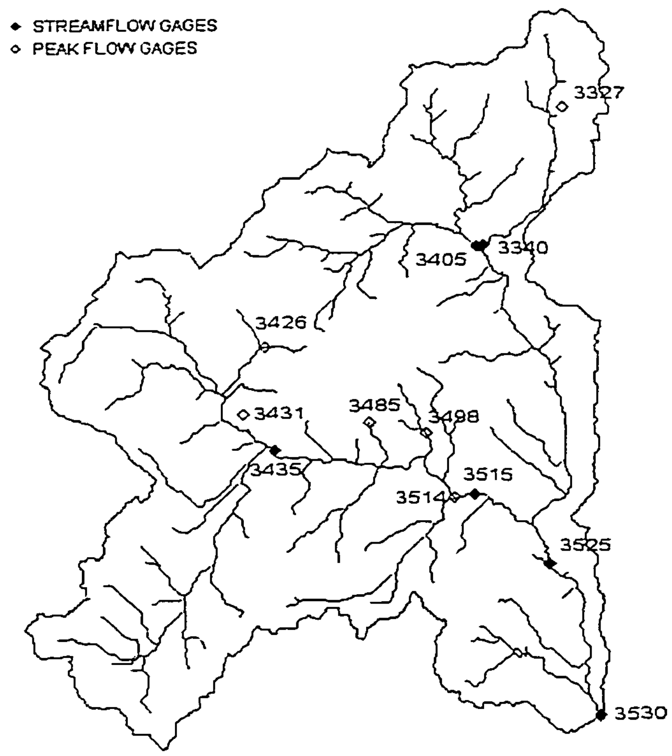

Figure 2.10. Locations of streamflow gaging stations used in this study.

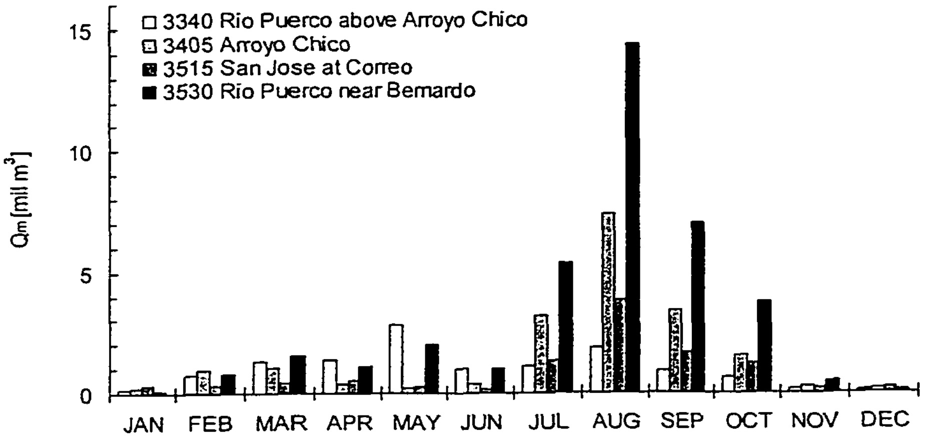

Figure 2.11. Mean monthly streamflow at the Rio Puerco main stations for the common record (1952-1986).

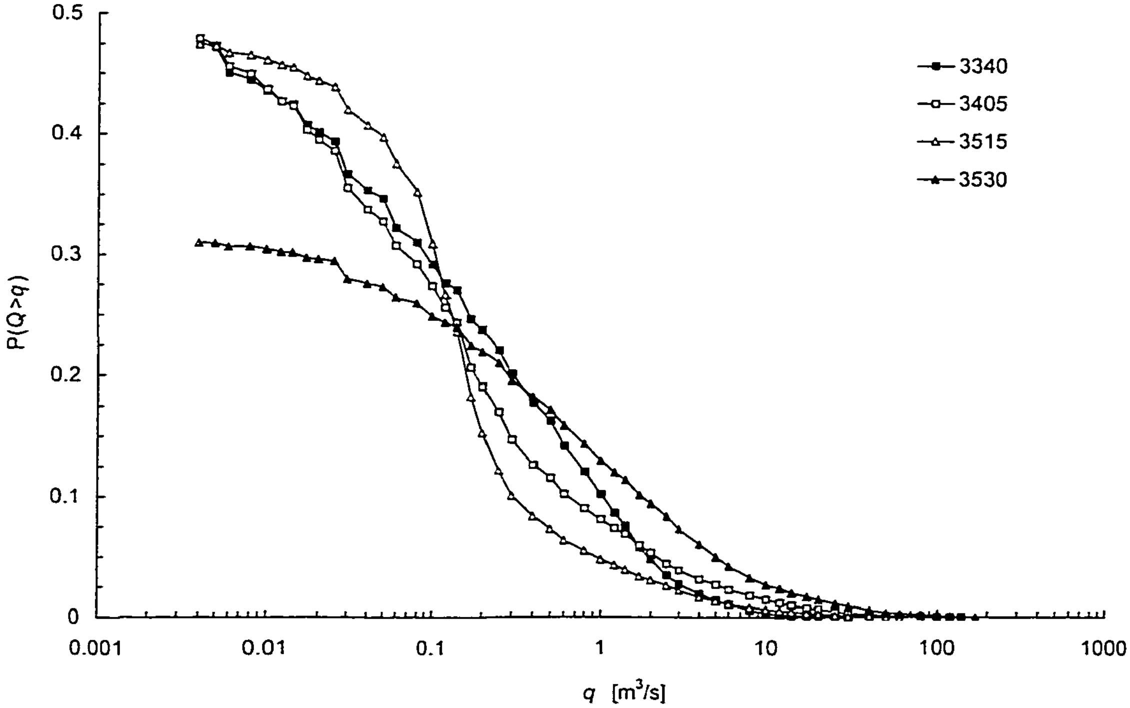

Figure 2.12. Flow duration curves constructed for the common record (1952-1986) at main gaging stations.

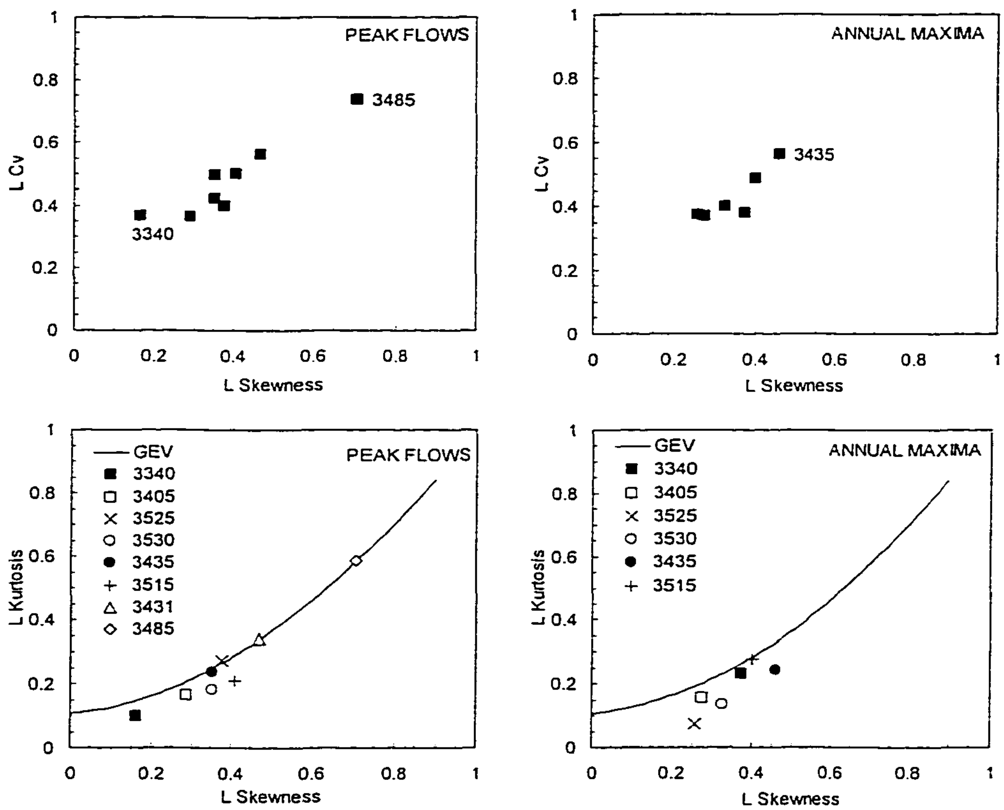

Figure 2.13. L-moment diagrams for peak (left) and annual maximum daily flows (right).

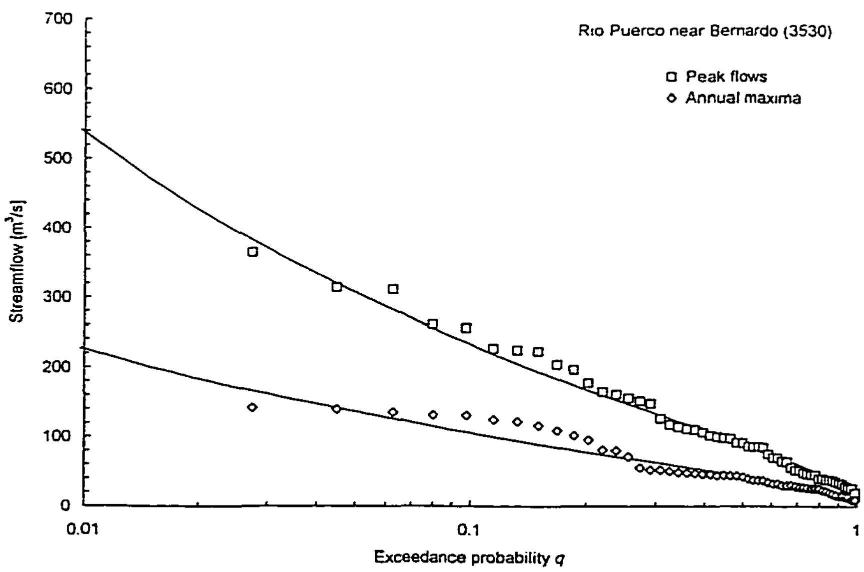

Figure 2.14. Example of empirical (points) and GEV model (line) probability plot for peak flows and annual maximum daily flow at the Bernardo (3530) gage.

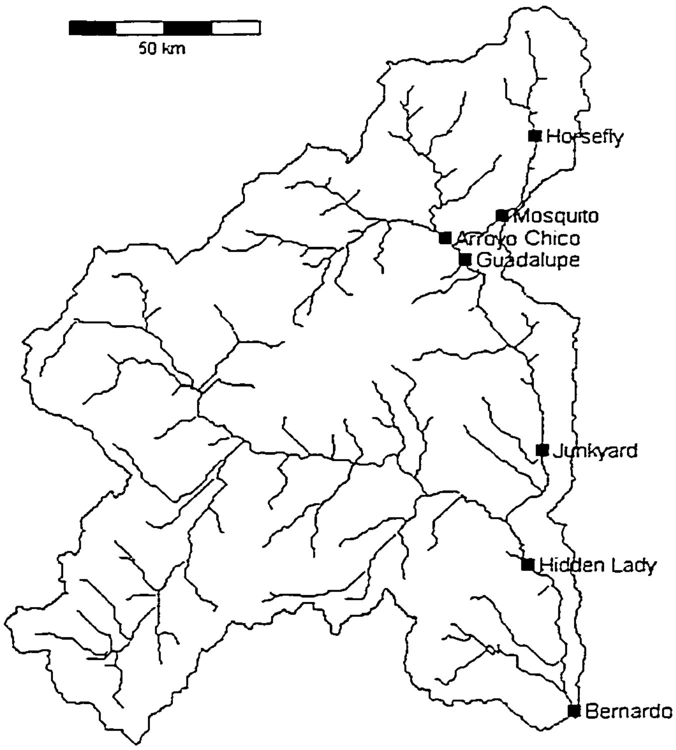

Figure 2.15. Locations of streambed and floodplain infiltration site measurements.

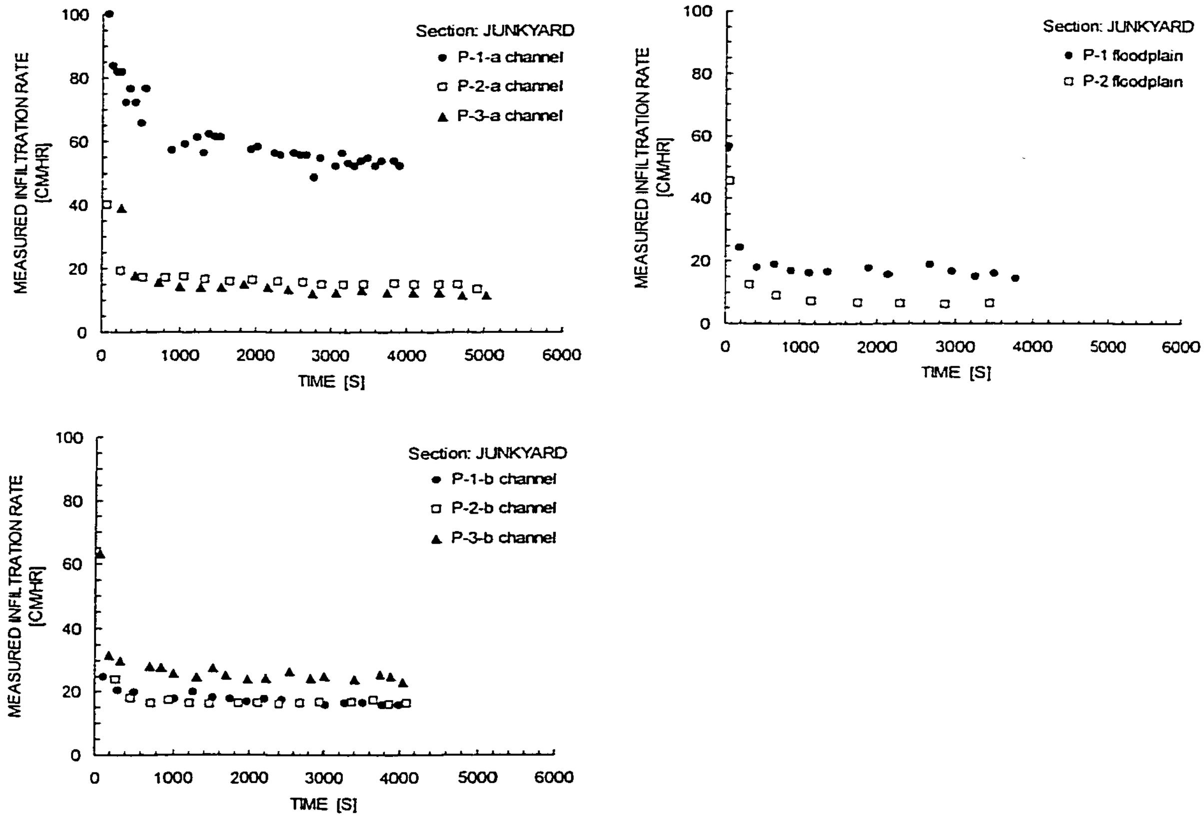

Figure 2.16. Example of measured infiltration rates in the channel (left) and floodplain (right) at the cross section Junkyard.

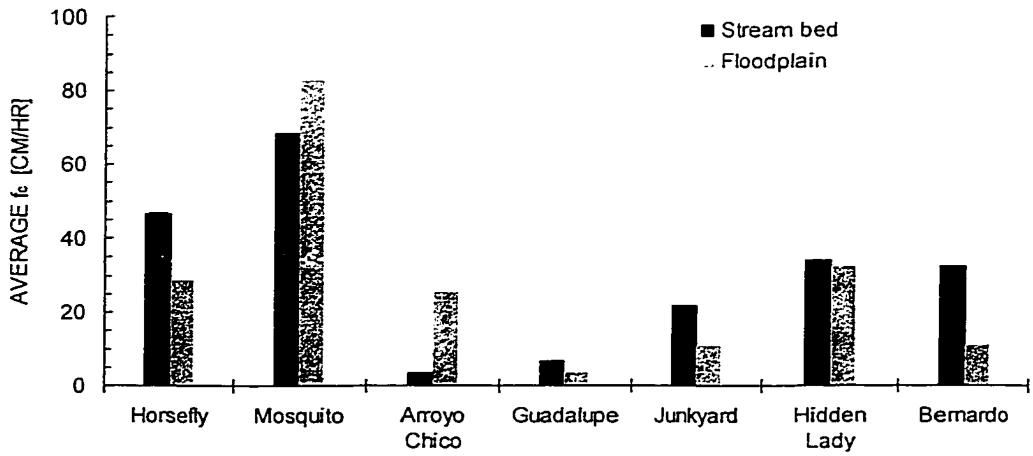

Figure 2.17. Average steady-state infiltration rates at measurement cross sections in the Rio Puerco Basin from Figure 2.15.

3 Hydroclimatic Trends

An important element of current research in climate change and variability is the analysis of trends in hydroclimatic variables from instrumental records. In the U.S., numerous large-scale analyses of hydroclimatic trends have recently been conducted on precipitation and streamflow data at different timescales (e.g., Lettenmaier et al. 1994, Karl et al. 1995, Lins 1997, Karl and Knight 1998, Lins and Slack 1999). The observed hydroclimatic variability was linked to atmospheric circulation patterns such as the Southern Oscillation (e.g., Redmond and Koch 1991, Kahya and Dracup 1993, Piechota and Dracup 1996), and also to long-term sea level pressure and temperature anomalies (Mantua et al. 1997, Zhang et al. 1997, Cayan et al. 1998, Gershunov and Barnett 1998). In this Chapter we add a watershed-based analysis of precipitation and streamflow trends in the Rio Puerco Basin, with emphasis placed on the connection between observed changes in hydroclimatology and geomorphologic adjustment of the fluvial system.

It is argued in this study that large spatial variability in rainfall and runoff, the flashy and intermittent nature of flow, highly erodible surface materials and resulting extremely high sediment loads - all these factors make ephemeral streams in semiarid regions susceptible to very high rates of channel erosion and filling (e.g., Leopold et al. 1966, Thornes 1977, 1994). Even slight climatic variations and trends in these regions may then have profound effects on the direction and magnitude of channel changes.

In this Chapter, a thorough examination of hydroclimatic data from the period 1948-1997 is conducted in order to identify seasonality, variability, trends and other properties of precipitation and streamflow on different timescales. On an annual timescale, general trends in precipitation and streamflow are examined (Section 3.2) and connections to large-scale climate anomalies in the Northern Pacific are established (Section 3.3). Monthly data analyses identify seasonality and trends in precipitation and streamflow (Section 3.4), and most importantly they show that the principal contribution to annual trends in precipitation in the Rio Puerco comes from non-summer rainfall. Most noteworthy are analyses at the daily timescale (Section 3.5), in which substantive shifts in the distributions of daily precipitation and streamflow in the Rio Puerco Basin are found.

Analyses of hydroclimatic data are explained in the context of recent geomorphologic changes in the Rio Puerco Basin. The apparent inconsistency in trends in annual maximum precipitation and streamflow events leads to the conclusion that progressive changes in vegetation and mainly hydraulic characteristics and conveyance of the channel system have occurred in the Rio Puerco Basin during the last 50 years. This conclusion is substantiated by field observations in the arroyo stream system. Periods of channel filling and erosion in the Rio Puerco Basin will continue to alternate in the future, and we can expect that the magnitude and recurrence of these processes will reflect the state of the watershed and stream system as well as large-scale and regional climate variability and change.

3.1 METHOD OF TESTING FOR TRENDS

Testing for trends in this study was conducted by the non-parametric Mann-Kendall test (Kendall 1938) which is commonly used for hydrologic data analysis (e.g., Hirsch and Slack 1984, Helsel and Hirsch 1992, Hirsch et al. 1993). It is a rank-based procedure especially suitable for non-normally distributed data, censored data, data containing outliers and non-linear trends. The null hypothesis of randomness H_0 states that the data $(x_1,\ldots, x_n)$ are a sample of n independent and identically distributed random variables. The alternative hypothesis H_1 is that the distributions of x_k and x_j are not identical for all $k, j \leq n$ with $k \neq j$. The trend test statistic S is defined as (e.g., Hirsch et al. 1993):

$$S = \sum_{k=1}^{n-1} \sum_{j=k+1}^{n} \operatorname{sgn}(x_j - x_k) \tag{3.1}$$

where sgn(.) is the sign function.

Under H_0, the distribution of S is normal in the limit as $n \to \infty$. The mean and the variance of S, considering that there may be ties in the x series, are:

$$\begin{gathered} E[S] = 0 \\ \operatorname{Var}[S] = [n(n-1)(2n+5) - \textstyle\sum_t t(t-1)(2t+5)]/18 \end{gathered} \tag{3.2}$$

where t is the length of any given tie and Σ_t denotes the summation over all ties with length t. In this study, sequential zero values of streamflow and precipitation are considered tied censored data and are included in the sum Σ_t in Equation (3.2). The normality assumption for S is found to be good even for small n ($n \approx 10$) with a correction of ± 1 and the standard normal variate is used for hypothesis testing (e.g., Hirsch et al. 1993):

$$Z = \begin{cases} \dfrac{S-1}{\sqrt{\mathrm{Var}[S]}} & \text{if} \quad S > 0 \\ 0 & \text{if} \quad S = 0 \\ \dfrac{S+1}{\sqrt{\mathrm{Var}[S]}} & \text{if} \quad S < 0 \end{cases} \tag{3.3}$$

In a two-sided test for trend, the null hypothesis is rejected at significance level α if $|Z| > Z_{(1-\alpha/2)}$, where $Z_{(1-\alpha/2)}$ is the value of the standard normal distribution with a probability of exceedance of $\alpha/2$. A positive value of Z indicates an upward trend; a negative value indicates a downward trend in the tested time series. Throughout this study, trends are identified at a significance level α=0.05, or confidence level β=1- α =0.95, unless stated otherwise.

The trend test statistic Z is used as a measure of trend magnitude, or of its significance. It is not a direct quantification of trend magnitude. In this study, we apply Mann-Kendall's trend test only to non-seasonal and independent data (such as annual streamflow or precipitation data, annual quantiles and monthly data across years, etc.) and therefore we do not include adjustments that account for seasonality and serial correlation in tested data (e.g., Hirsch and Slack 1984, Helsel and Hirsch 1992).

3.2 Annual Rainfall and Runoff

The time series of annual precipitation estimates over the Rio Puerco Basin constructed from station observations is shown in Figure 3.1. A linear trend line highlights the gradual increase in precipitation over the watershed in the studied period. The increase is quite dramatic: from an average of about 240 mm per year in the 1950s to about 340 mm in the 1990s (an increase of almost 40%). Minimum precipitation was 118 mm in 1956, maximum was 430 mm in 1997, and the coefficient of variation of the precipitation record is 0.23. Trend analyses were conducted on annual precipitation data for stations with areas of influence in the Rio Puerco Basin (see Table 2.4). Results show statistically significant increasing trends at all analyzed stations except Cuba. Other researchers have also observed increases in annual precipitation for the U.S. Southwest region in the last 50 years (e.g., Lettenmaier et al. 1994, Cayan et al. 1998, Karl and Knight 1998).

Also shown in Figure 3.1 is the long-term time series of annual precipitation in the Rio Puerco Basin constructed from climatic division records. The climatic division-derived series is obtained by weighting the annual average divisional precipitation by the area that each division covers in the Basin. Divisional records differ from Rio Puerco station-derived precipitation because they include all stations in each climatic division. It is evident from Figure 3.1 that the recent increasing trend in annual precipitation is part of a larger-scale variability in precipitation. It is noteworthy that the period of lower than average precipitation between 1895 and 1904 coincides with the beginning of the latest channel degradation period in northwestern New Mexico.

In contrast to precipitation, annual streamflow records in the Rio Puerco do not show the same significant increasing trend in recent decades. For the 35-year common period from 1952-1986 none of the studied gages in Table 2.6 exhibited a statistically significant trend in annual streamflow. In fact, three gages exhibited non-significant decreasing trends in that period (3405, 3515, 3530). Examples of the annual streamflow records at the Bernardo (3530) and the Arroyo Chico (3405) gages are shown in Figure 3.2. Inter-annual variability was fairly consistent at all gages (the coefficient of variation for the common record ranged between 0.63 and 0.82) and inter-annual storage was negligible (annual correlograms showed no significant auto-correlation at the 95% confidence level). The lack of statistically significant trends in annual streamflow series in the U.S. Southwest was also observed by Wahl (1992), Lettenmaier et al. (1994), Chiew and McMahon (1996), and others.

Streamflow records integrate precipitation on a watershed scale, including the important effects of basin properties such as geology, vegetation, drainage network development, etc. In semiarid regions, the relationship between annual precipitation and runoff is very non-linear. In the Rio Puerco Basin, the degree of linearity in this relationship was strongest in the Upper Rio Puerco and Arroyo Chico watersheds (r=0.483), which receive the highest precipitation and produce the greatest runoff per unit area (for the complete watershed r=0.122). Rio Puerco annual runoff ratios are extremely low. At best, only 2-3% of the total precipitation volume is observed as streamflow in the stream system. Therefore, it is not surprising that, on an annual timescale, trends in precipitation are dampened, or eliminated, by the infiltration-dominated rainfall-runoff process.

3.3 Large Scale Climate Anomalies

Several studies have attempted to relate the variability in hydroclimatic factors in the U.S. Southwest to large-scale atmospheric circulation patterns. On a shorter time scale, precipitation in the region has been found to correlate well with the El Nino Southern Oscillation (ENSO). The general agreement is that a wet anomaly in the Southwest is observed following a warm phase ENSO event (e.g., Redmond and Koch 1991, Piechota and Dracup 1996). Maxima in the annual precipitation record for the Rio Puerco Basin in

Figure 3.1 coincide with warm phase ENSO years (e.g., 1997, 1986, 1941, 1931). Annual streamflow in the U.S. Southwest is also correlated with ENSO events, but to a lesser degree than precipitation (e.g., Redmond and Koch 1991, Kahya and Dracup 1993).

On a longer, decadal timescale, precipitation patterns in the U.S. Southwest also are significantly correlated with sea level pressure and temperature anomalies on a global scale. Wet conditions are commonly associated with low pressure anomalies in the northern Pacific - south of the Aleutian Islands (e.g., Cayan et al. 1998, Gershunov and Barnett 1998). In particular, the Pacific Decadal Oscillation (PDO) index based on North Pacific sea surface temperature anomalies (Zhang et al. 1997, Mantua et al. 1997) correlates very well with precipitation in the Rio Puerco Basin. The annual PDO index is shown in Figure 3.3 for the period 1900-1997. The linear correlation coefficient between annual PDO and station-derived precipitation over the Rio Puerco Basin for the period 1948-1997 is r=0.552.

Positive values of PDO indicate lower sea surface temperatures and a strengthened Aleutian low pressure anomaly (Figure 3.4), which promotes a southward displacement of storm activity into the U.S. Southwest, resulting in higher precipitation (e.g., Hirschboeck 1987, Webb and Betancourt 1990, Cayan et al. 1998). The PDO anomaly has a strong winter and spring component; summer precipitation in the Rio Puerco Basin appears to be less affected. It is also noteworthy that the interdecadal variability in sea level pressure in the northern Pacific is characterized by regime shifts with a recurrence interval of about 50-70 years (Minobe 1997). Although the instrumental record is not long enough to conclusively argue for 50-70 year cycles in precipitation in the Rio

Puerco Basin (see Figure 3.1), similar cycles were found by analyzing longer tree ring chronologies in the El Malpais National Monument in the southern part of the watershed (Grissino-Meyer 1995). The importance of the connection between PDO and precipitation in the U.S. Southwest lies in the fact that the PDO climate anomaly is generally better predictable and it therefore may provide possibilities for rainfall prediction (Latif and Barnett 1994, Cayan et al. 1998).

3.4 Monthly Seasonality

Seasonality in precipitation and streamflow in the Rio Puerco Basin is important for geomorphologic adjustment in the arroyo stream system, as most notable channel changes are generally concentrated in the summer months with high rainfall and resulting runoff.

Trend analyses were conducted on monthly precipitation data, and the mean monthly trend test statistic Z for the period 1952-1986 in Rio Puerco Basin is shown in Figure 3.5. Although trends in individual months are not statistically significant, they are consistently positive in the period from September through May and negligible in the summer months of June, July and August. We conclude that in the Rio Puerco, the observed annual increase in precipitation is not caused by an increase in summer precipitation, but rather by an increase in precipitation totals in drier months. Other analyses of recent trends in precipitation in the U.S. Southwest region also report increases in fall precipitation without major changes in summer precipitation (e.g., Lettenmaier et al. 1994, Karl et al. 1995).

These results suggest that the decadal variation in the Aleutian low pressure anomaly with a strong winter and spring component may be a driving force for the observed trends in Rio Puerco precipitation in those seasons (e.g., Gershunov and Barnett 1998). Seasonal correlation analyses were conducted on a monthly basis between basin-wide precipitation and the PDO index. Correlation coefficients for the period February-May varied between r=0.27 and r=0.39, whereas correlation coefficients in remaining months were less than r=0.2.

Results of trend analyses on monthly streamflow data for the main gaging stations are shown in Figure 3.6 for the common period of record. Two important observations can be made here. First, there is a consistent (and often statistically significant) increasing trend in monthly streamflow totals for the low-flow months from November through May. Second, there is a consistent decreasing trend in monthly totals in the summer high-flow months of July and August. Most noteworthy, the decreasing trend in the maximum runoff month of August is statistically significant at 3 of the 4 main stations (except 3340). Trend analyses for the complete periods of record at each gage gave very similar results.

Seasonal trend analyses show that increasing precipitation in the fall, winter and spring seasons in the Rio Puerco generally translates into increasing runoff totals in those periods. In addition, despite negligible trends in summer precipitation totals, summer runoff has been steadily decreasing since 1950. This statistically significant reduction in wet season runoff balances runoff increases in other months and results in statistically insignificant trends in annual Rio Puerco streamflow series.

3.5 Daily Rainfall and Runoff

Analyses at the daily timescale are most interesting for understanding the complex rainfall-runoff relationship in the Rio Puerco Basin, as this is the timescale of most rainfall and runoff events. Here, shifts in the distributions of daily rainfall and runoff events are analyzed. Particular attention is given to recent trends in extreme annual rainfall and runoff events, as these are responsible for most notable channel changes in the stream system.

Daily rainfall and runoff in the Rio Puerco Basin are intermittent processes with mixed distributions. Their cumulative distribution functions $F(x)$ are:

$$\begin{gathered} F(x) = p_o \\ F(x) = p_o + (1 - p_o)G(x) \end{gathered} \tag{3.4}$$

where p_o is the probability of zero daily rainfall or runoff and $G(x)$ is the continuous cumulative distribution for positive values of x.

The importance of the intermittency parameter and the ephemeral nature of Rio Puerco streamflow are illustrated in Figure 3.7, where the probability of zero flow on a given day of the year p_o^d, d=1, ..., 365, is shown. The behavior of p_o^d reflects in general the seasonal distribution of streamflow found in monthly analyses. For instance, a winter-spring wet period and a summer wet period separated by a dry period (maximum p_o^d during days in June reached 0.8 at 3405 and 1.0 at 3515) are evident at gages 3340, 3405 and 3515. During the summer period July-August p_o^d drops dramatically at all streamflow gages. Also of interest is the prolonged dry period at the outlet of the basin (3530) in the fall and winter months. It is clear from Figure 3.7 that in this period infiltration and evaporation losses in the Rio Puerco main stream are often sufficient to eliminate all channel flow before it reaches the Basin outlet.

To find shifts in the rainfall and runoff distributions, annual empirical cumulative distributions (duration curves) $F^y(x)$ for daily precipitation and streamflow (y=1...n, where n is the number of analyzed years) were constructed. Characteristics of these distributions, such as the annual probability of zero daily precipitation or streamflow p_o^y and quantiles of $F^y(x)$ and $G^y(x)$, were then analyzed for trends across years.

3.5.1 Trends in Wetness

The annual probability of zero daily precipitation or streamflow p_o^y is used as an indicator of wetness in the basin. Mean p_o^y computed from the common record for streamflow gages ranged between 0.43 and 0.69, and for precipitation stations between 0.69 and 0.89 (see Table 3.1).

The trend statistic Z is also listed in Table 3.1. For precipitation, 11 of 14 trends in p_o^y were negative, of which 5 were statistically significant. The weighted Rio Puerco average was Z=-1.14. For streamflow, decreasing trends were statistically significant at all gages. For instance, at gages 3340 and 3405, p_o^y decreased from about 0.7 in the early 1950s to about 0.1 after 1983 (in 1983, 1984 and 1986 there were absolutely no dry days recorded at the Arroyo Chico gage).

Results show that in the period 1952-1986 there was a considerable increase in wetness in the Rio Puerco Basin both in terms of rainfall as well as runoff. The streamflow records in particular show that there is a significant basin-wide increasing trend in the number of days with observed flow in the Rio Puerco in the studied period.

3.5.2 Trends in Event Frequency, Intensity and Volume

Trend analyses were also conducted on the number of events, average event intensity and total rainfall and runoff volume in 10% (percentile) classes extracted from the continuous cumulative distribution function $G^y(x)$.

The results for precipitation in the form of a basin-averaged trend test statistic are shown in Figure 3.8. Although none of the trends are statistically significant, there is a general increase in both precipitation intensity and frequency throughout the distribution, leading to an increasing trend in precipitation volume. The increase in average precipitation intensity is highest in the 50-80% range. However, in terms of rainfall volume, the contribution of the highest percentile range to the annual total is greatest.

The results for streamflow are shown in Figure 3.9. It is clear from this figure that runoff event frequency has been increasing steadily (and significantly) throughout the distribution. However, the daily streamflow rate (event intensity) has generally been decreasing for the upper 30% of the events every year, and increasing in the lower percentile classes. As a result, streamflow volume in the studied period has generally been decreasing in the highest 10% class. Figure 3.9 illustrates well that despite only marginal trends in annual streamflow volumes, there have been substantive changes in the distributions of daily streamflow at all Rio Puerco gages in the recent record. While the stream system does seem to be getting wetter (in terms of observed runoff) in the studied period, this increase in runoff is coming from low to moderate events, and the intensity of extreme annual events is actually decreasing. Trend analyses using complete records at all precipitation and streamflow gages gave the same general results.

3.5.3 TRENDS IN ANNUAL QUANTILES

Annual streamflow and precipitation quantiles x_p^y were obtained from empirical annual cumulative distribution functions (duration curves) $F^y(x)$ for chosen non-exceedance probabilities p:

$$p = P[X \le x_p{}^y] = F^y(x_p) \tag{3.5}$$

The annual quantile x_p^y is a daily streamflow or precipitation magnitude that in a given year y was exceeded 100(1-p) percent of the time. The time series of annual quantiles x_p^y allows us to study the trends in daily flow or precipitation magnitudes with the same probability of exceedance every year.

As an example, trends in selected streamflow and precipitation quantiles are shown in Figure 3.10 and reported in Table 3.1. For precipitation, the average intensity of the annual maximum rainfall event in each year P_{max} has not been (significantly) changing during the common record (only one station showed a statistically significant increasing trend in P_{max}). At the same time, there has been a general increase in quantiles in the range $0.9<p<1$. For streamflow, the shift in the distribution was quite different. Quantiles with $p<0.95$ generally exhibited an increasing trend, whereas quantiles with $p>0.95$, including the annual maximum, exhibited a decreasing trend. The upward trend in streamflow in the period 1952-1986 is statistically significant at all stations (except 3530) for p ranging from 0.4 to 0.8 (not shown in Table 3.1). The downward trend is statistically significant for the annual maximum observed flow at all gages. Complete records gave only marginally different results. Furthermore, trend analyses of instantaneous peak flow showed the same decreasing and statistically significant trend.

For instance, mean peak discharge dropped by 51% between the periods 1952-1972 and 1973-1986 at the Arroyo Chico gage (47% at the Rio Puerco above Arroyo Chico gage).

The discrepancy between trends in annual maximum rainfall events (Karl et al. 1995, Karl and Knight 1998) and runoff events (Lins and Slack 1999) has been observed in other parts of the U.S., and it has important implications for the role of climate change in watershed adjustment. Some reasons for this discrepancy in the Rio Puerco Basin are addressed in the following discussion.

3.6 Discussion

Analyses of recent trends in precipitation and streamflow in the Rio Puerco reveal several interesting features of this Basin.

At the annual timescale, a statistically significant increasing trend in precipitation in the Basin was detected in the 1948-1997 period. This trend was not evident in streamflow data. Analyses of seasonal precipitation showed that the consistent increase in annual precipitation does not come from the summer monsoon period, but rather from an increase in precipitation in the fall and spring months promoted by a strengthened low-pressure anomaly in the northern Pacific. Monthly streamflow totals also showed consistently increasing trends in the low-flow months but a consistently decreasing trend in the high-flow months of July and August. This is even more evident in daily streamflow data in Figure 3.11, where the trend test statistic is computed for every day of the year. Here it is evident that summer daily runoff has generally decreased in the period 1952-1986.

Results at the daily timescale illustrate that the Rio Puerco Basin is getting wetter in terms of the number of rainy days and mostly in terms of the frequency of observed runoff in the stream system. For daily precipitation, increasing trends in event intensity are concentrated in the moderate rainfall intensity range, but precipitation quantiles of the highest intensity (annual maxima) remain fairly constant (with an average Basin-wide intensity of about 29 mm/day). For daily streamflow, increasing trends in event frequency are apparent across the whole range of the distribution. However, the intensity of annual maximum events is systematically and significantly decreasing at all Rio Puerco gages.

It is evident from this analysis that annual maximum precipitation events seem to be producing progressively lower annual maximum runoff events in the Rio Puerco in the last 50 years. The two most probable reasons for this are: (1) vegetation changes in the Basin that delay overland flow and increase infiltration; and (2) changes in the hydraulic characteristics of the stream system that decrease the conveyance of the channels and increase transmission losses. In the following discussion we explore field evidence for these statements in the Rio Puerco Basin.

Vegetation changes in the Rio Puerco Basin in the last 50 years are difficult to document because of large seasonal and inter-annual variability in vegetative cover and limited data. However, based on experiments and observations in a subbasin of the Arroyo Chico, Branson and Janicki (1986) argue that in the period 1958-1979 a dramatic increase in live vegetation cover took place in the Rio Puerco. They attribute this improvement mainly to increases in precipitation in this period, with a decrease in grazing intensity as a secondary cause. An increase in vegetative cover would positively affect infiltration, reduce hillslope erosion and runoff. Regarding the effects of grazing it is important to note that although irrigated agriculture was practiced in the Rio Puerco Basin together with cattle and sheep grazing in the 19th Century, almost all permanent settlements in the Upper and Middle Rio Puerco Basins were abandoned after 1880. As a result, livestock grazing in the basin has also decreased dramatically since the 1930s to a relatively stable level in recent years (BLM 1999, personal communication).

Changes in the conveyance of the Rio Puerco arroyo stream system seem to be a stronger contributor to recent trends in intense runoff events. In his detailed study, Elliott (1979) observed a distinction between upstream and downstream reaches in the Rio Puerco arroyo system. Upstream reaches generally had a large channel width-depth ratio (mean 78.3), had unstable banks, less vegetation, and a laterally shifting channel. Downstream reaches had a smaller width-depth ratio (mean 12.2), more resistant and steeper banks, dense riparian vegetation, and a more stable channel position within the floodplain. In 1935 photos, most of the stream system appeared to be similar to the upstream reach type. Between 1935 and 1979 the Lower and Middle Rio Puerco reaches have seen aggradation and stabilization of their inner floodplain and the establishment of permanent riparian vegetation. Recent surveying shows this development to be progressing upstream (Elliott 1999, personal communication). A decrease in sediment concentration at the outlet of the basin between 1948 and 1996 (Elliott et al. 1999) has also accompanied the general alluviation of the Rio Puerco stream system in that period. It can be expected that flood conveyance has decreased in those sections of the Rio Puerco where the channel is narrower and the floodplain is well vegetated. There has been a rapid expansion of salt cedar growth in the floodplain across the Rio Puerco since its introduction in 1927 (Heath 1983). The growth of riparian vegetation is also likely responsible for increasing water loss as a result of evapotranspiration and floodplain infiltration for overbank flow.

Results suggest that periods of alluviation in the Rio Puerco arroyo system may be connected with persisting wetter conditions in the basin that are favorable to vegetation recovery in conjunction with fewer high intensity rainstorms. The importance of changes in precipitation intensity for arroyo development and evolution has been emphasized in the past (e.g., Leopold 1951, Cooke and Reeves 1976, Balling and Wells 1990). Geomorphologic changes in the Rio Puerco arroyo system are continuous, with phases of alluviation followed by phases of degradation. Periodically this process seems to intensify and produce rapid entrenchment episodes that lead to arroyo formation and development. Certainly many factors can contribute to this intensification, but it is likely that climate plays a leading role. An interesting development in the possible prediction of the erosion cycles in the Rio Puerco Basin lies in their connection with persistent large-scale climate anomalies, such as the PDO discussed in this Chapter (e.g., Latif and Barnett 1994, Cayan et al. 1998).

Table 3.1. Rio Puerco mean annual probability of zero daily precipitation and streamflow p_o^y, daily discharge quantiles Q_p and precipitation quantiles P_p with p=0.9, 0.99 and the annual maximum for the common period of record (1952-1986). In brackets is the Z statistic of the trend test for each gage. The sign of Z indicates trend direction. Statistically significant trends at the 95% confidence level are set in bold and italicized. Average Z for Rio Puerco Basin precipitation is computed as $Z=\Sigma\rho_i Z_i / 14$; where Z_i is the test statistic for individual gages and ρ_i is their Thiessen weight from Table 2.4.

STREAMFLOW	p_o^y	$Q_{0.9}$ [m³/s]	$Q_{0.99}$ [m³/s]	Q_{max} [m³/s]
3340	0.43 (***-2.56***)	1.08 (1.28)	5.5 (-1.82)	13.6 (***-2.68***)
3405	0.43 (***-5.41***)	0.77 (1.61)	14.3 (***-3.61***)	36.5 (***-3.28***)
3515	0.52 (***-5.07***)	0.41 (1.19)	7.41 (***-2.07***)	21 (***-3.08***)
3530	0.69 (***-2.36***)	2.01 (0.44)	28.8 (***-2.44***)	54.2 (***-2.83***)
PRECIPITATION	p_o^y	$P_{0.9}$ [mm]	$P_{0.99}$ [mm]	P_{max} [mm]
Chaco C.	0.84 (-1.38)	1.3 (0.85)	13 (1.14)	25.3 (0.19)
El Morro	0.78 (-1.61)	2.8 (***2.71***)	16.3 (***3.1***)	29.3 (0.51)
McGaffey	0.82 (-0.91)	4.1 (***2.19***)	20.5 (1.45)	35.5 (0.44)
Star Lake [1]	0.83 (***-2.6***)	1.5 (1.92)	12.2 (0.02)	22.6 (0.45)
Cuba	0.82 (0.1)	2.4 (0.87)	18 (0.82)	29.6 (-0.6)
Jemez Spr.	0.78 (-1.53)	3.2 (1.79)	20.4 (-0.26)	33.5 (0)
Torreon [2]	0.84 (0.02)	1.6 (0.75)	14.3 (***3.25***)	29.1 (0.77)
Wolf C. [3]	0.69 (-1.11)	5 (1.87)	22.9 (1.16)	34.8 (-0.22)
Grants [4]	0.84 (***2.58***)	1.7 (***2.11***)	14.8 (1.28)	29.2 (-0.57)
Augustine	0.83 (***-2.67***)	1.5 (***2.76***)	15.8 (***2.73***)	28.8 (***3.48***)
Bernardo [5]	0.89 (-0.32)	0.4 (0.92)	15 (1.56)	28.2 (1.19)
Laguna	0.86 (***-3.78***)	1.1 (***3.58***)	14.7 (0.82)	29.3 (0.28)
Los Lunas [6]	0.88 (***-4.05***)	0.7 (***3.05***)	14.7 (0.62)	28.3 (-1.56)
Albuquerque	0.84 (***-2.76***)	1.1 (***2.83***)	12.7 (1.59)	25.1 (0.77)
RIO PUERCO	0.85 (-1.14)	1.6 (***2.26***)	15 (1.31)	28.8 (0.11)

[1] record period is water year 1954-1986 (n=33 years)
[2] record period is water year 1962-1986 (n=25 years)
[3] record period is water year 1953-1986 (n=34 years)
[4] record period is water year 1954-1986 (n=33 years)
[5] record period is water year 1963-1986 (n=24 years)
[6] record period is water year 1958-1986 (n=29 years)

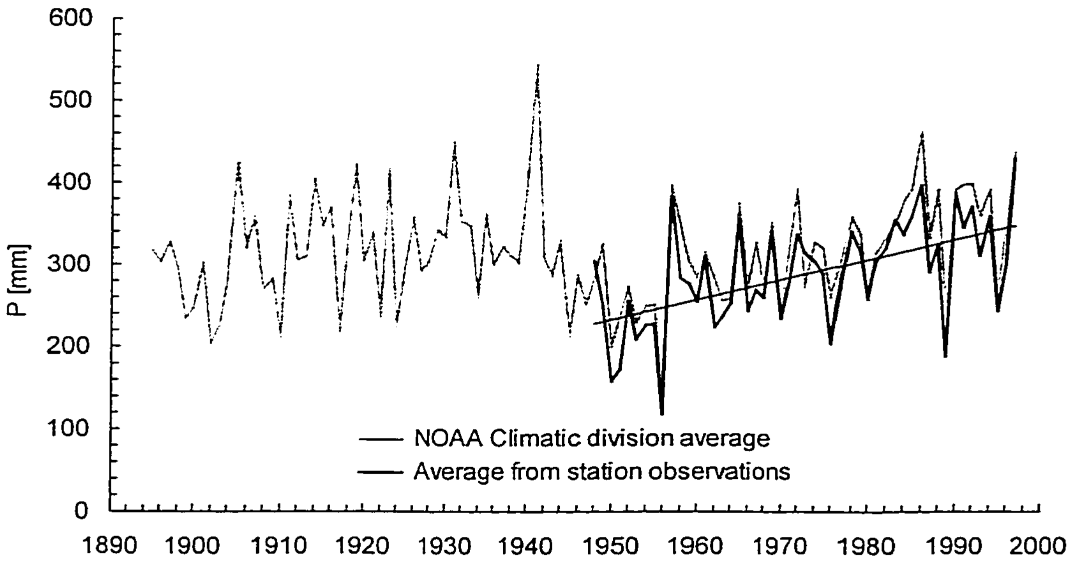

Figure 3.1. Time series of annual precipitation P over the Rio Puerco Basin from station observations (1948-1997) with linear trend; and from climatic division data (1895-1997).

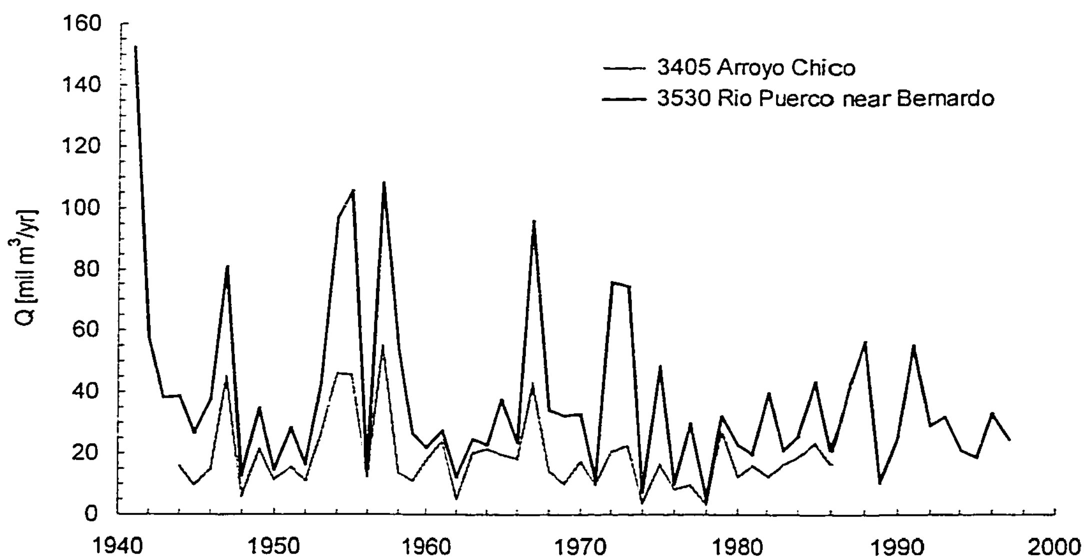

Figure 3.2. Time series of annual streamflow at gages 3530 (Bernardo) and 3405 (Arroyo Chico) for complete records.

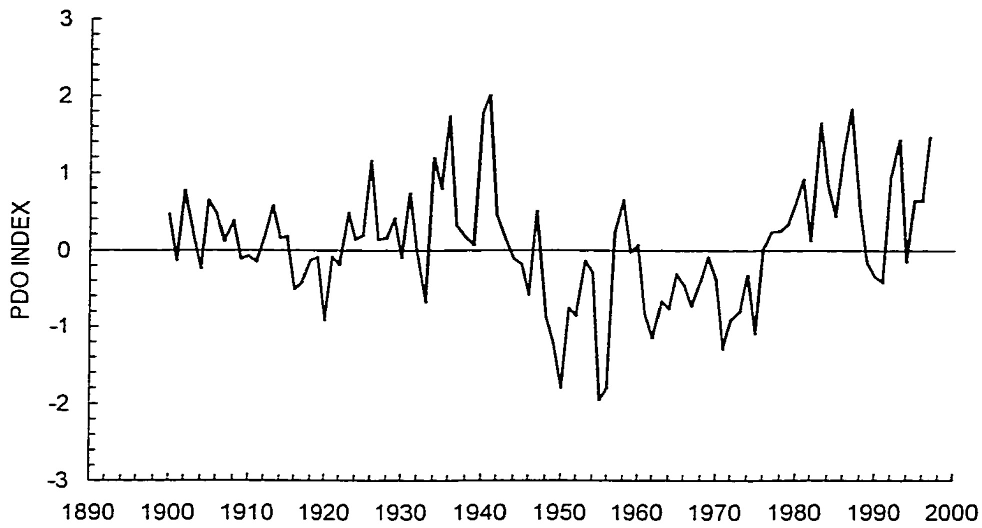

Figure 3.3. Annual time series of the Pacific Decadal Oscillation (PDO) index (after Mantua et al. 1997).

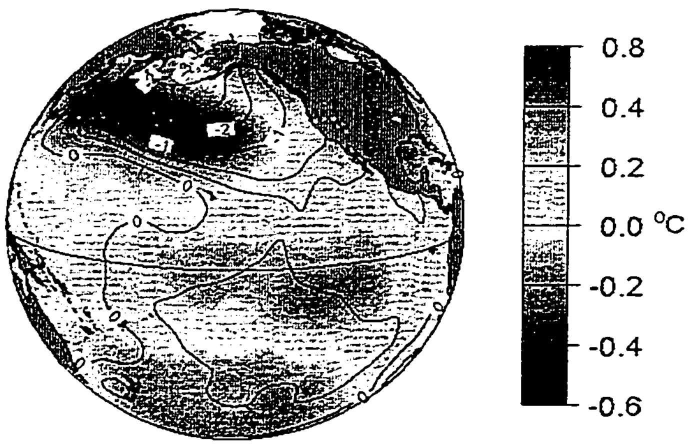

Figure 3.4. Sea surface temperature (shaded) and sea level pressure (contoured) regressed on the PDO index for the period 1900-1992 (after Mantua et al. 1997, Figure 2). Contour interval is 1 mb, negative contours are solid.

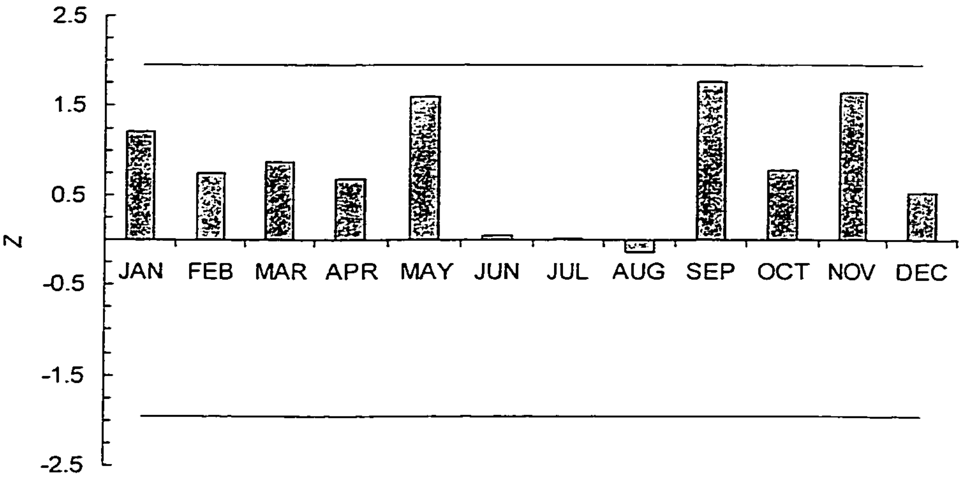

Figure 3.5. Rio Puerco Basin average trend test statistic Z, computed as a weighted mean of 14 gages with contributing areas inside the watershed: $Z=\sum\rho_i Z_i / 14$; where Z_i is the test statistic for individual gages and ρ_i is their Thiessen weight from Table 2.4. Statistically significant trends at the 95% confidence level have $|Z|>1.96$. The sign of Z indicates trend direction. Analyses are for the common period of record (1952-1986).

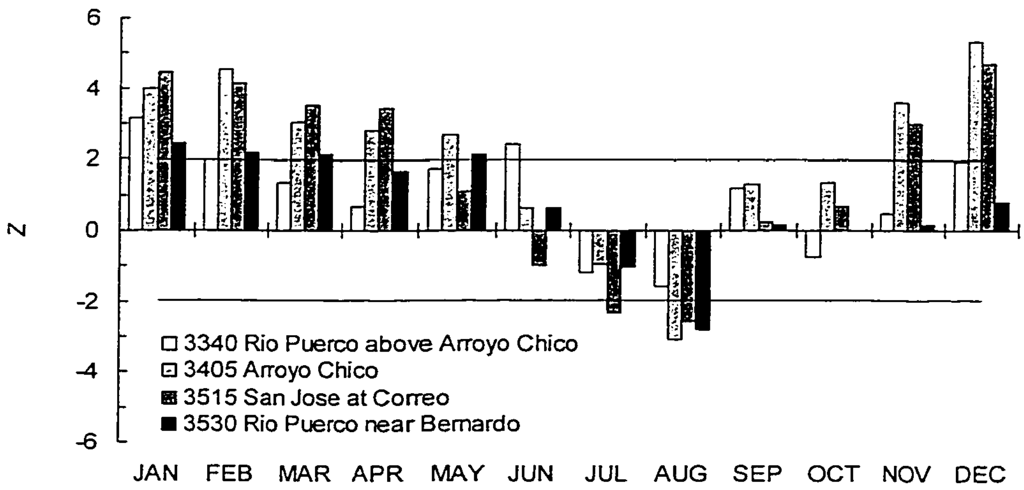

Figure 3.6. Trend test statistics Z for monthly streamflow totals at Rio Puerco main gages. Statistically significant trends at the 95% confidence level have $|Z|>1.96$. The sign of Z indicates trend direction. Analyses are for the common period of record (1952-1986).

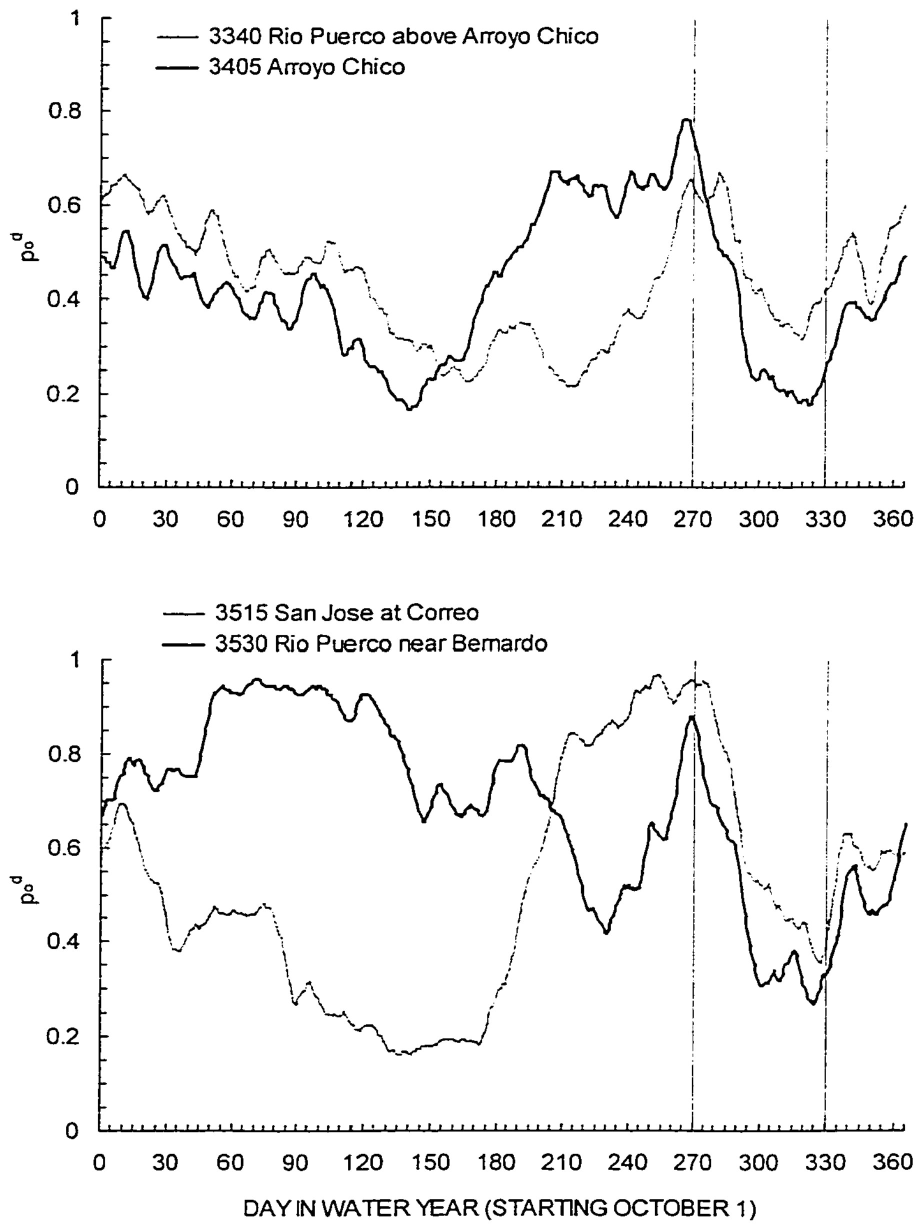

Figure 3.7. The probability of zero flow p_o^d computed for every day of the year d=1, ..., 365 plotted as a 7-day moving average at streamflow gages in the Upper Rio Puerco Basin (top) and Lower Rio Puerco Basin (bottom). The summer high flow period (July-August) is outlined. Results are for the common period of record (1952-1986).

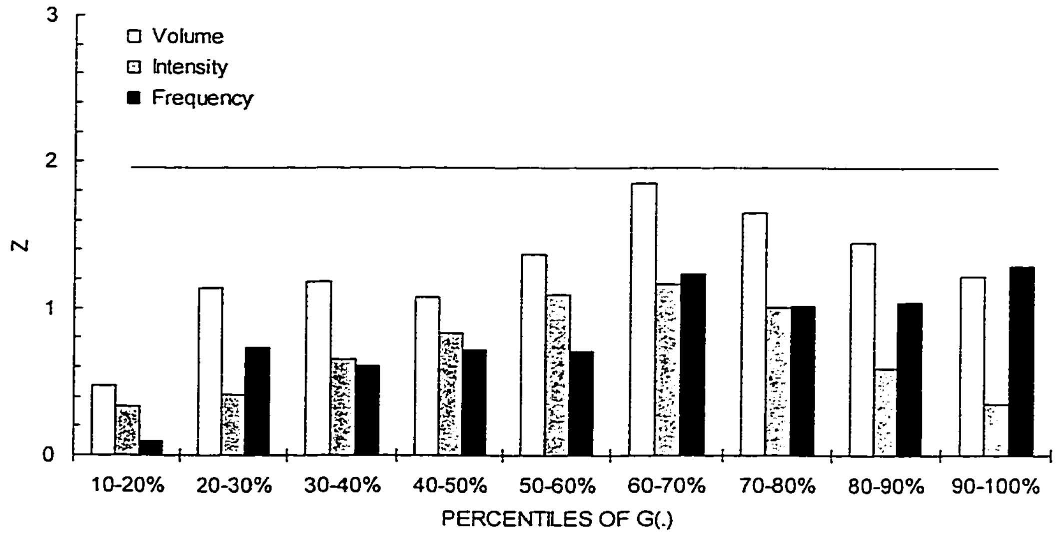

Figure 3.8. The distribution of trends in daily precipitation: number of events (event frequency), average event intensity and total volume by 10% (percentile) classes of the continuous distribution $G^y(x)$ for the common period of record (1952-1986). The average Rio Puerco Basin trend test statistic Z was computed as in Figure 3.5.

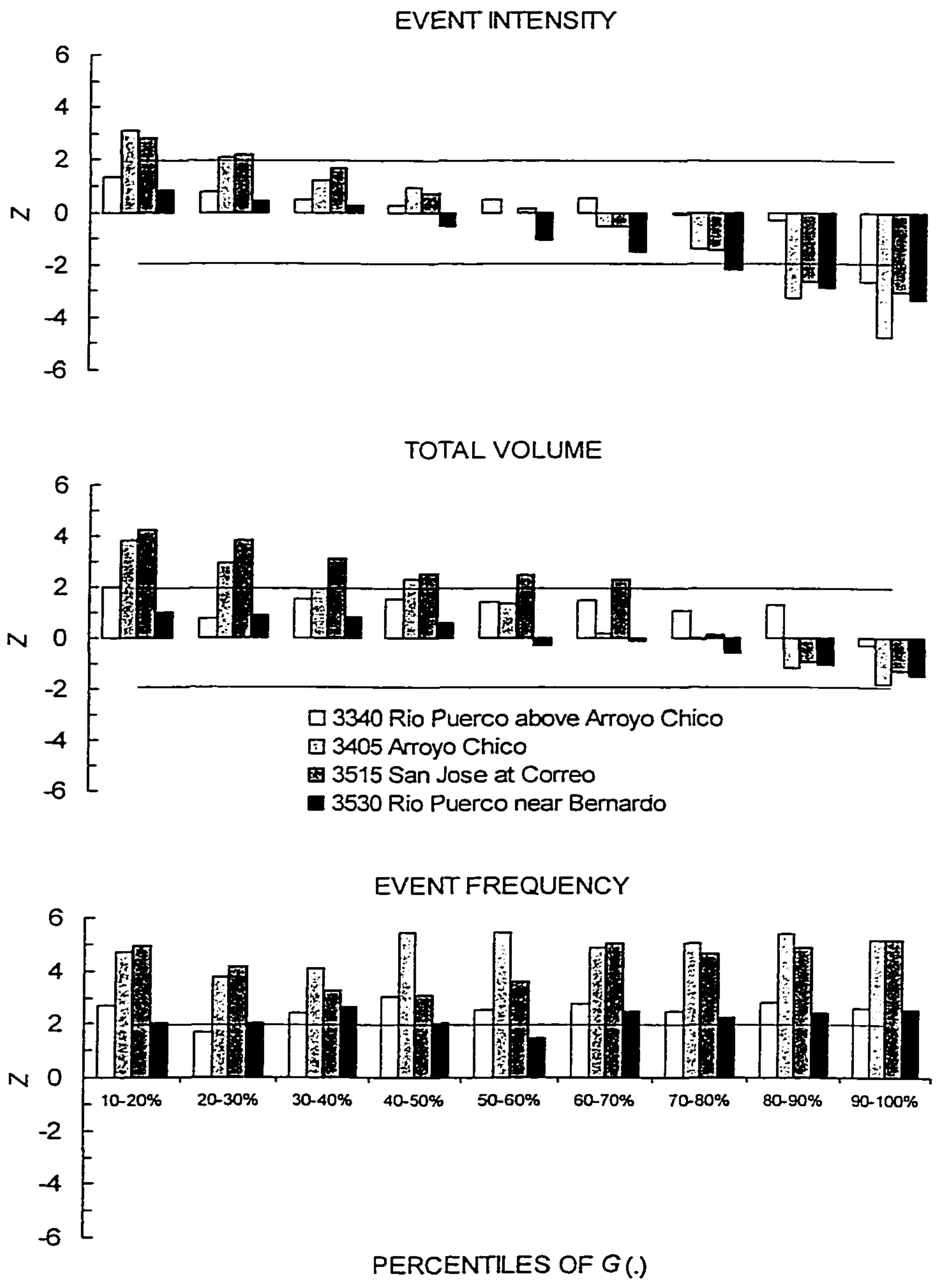

Figure 3.9. The distribution of trends in daily streamflow: average event intensity, total volume and number of events (event frequency) by 10% (percentile) classes of the continuous distribution $G^y(x)$ for the common period of record (1952-1986).

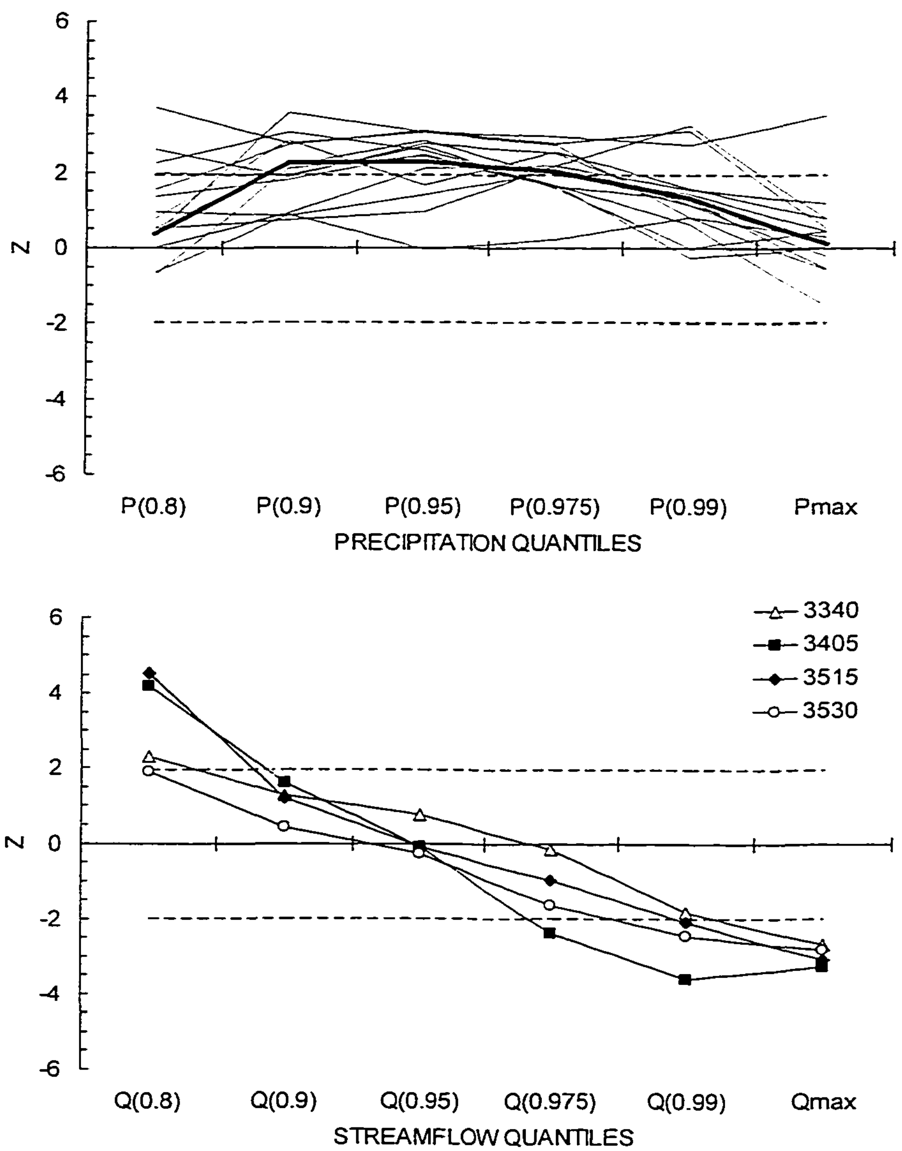

Figure 3.10. Trends in annual precipitation (top) and streamflow (bottom) quantiles of the distribution $F^y(x)$. For precipitation, thin lines represent individual station trends, the black line is the weighted average. Analyses are for the common record (1952-1986).

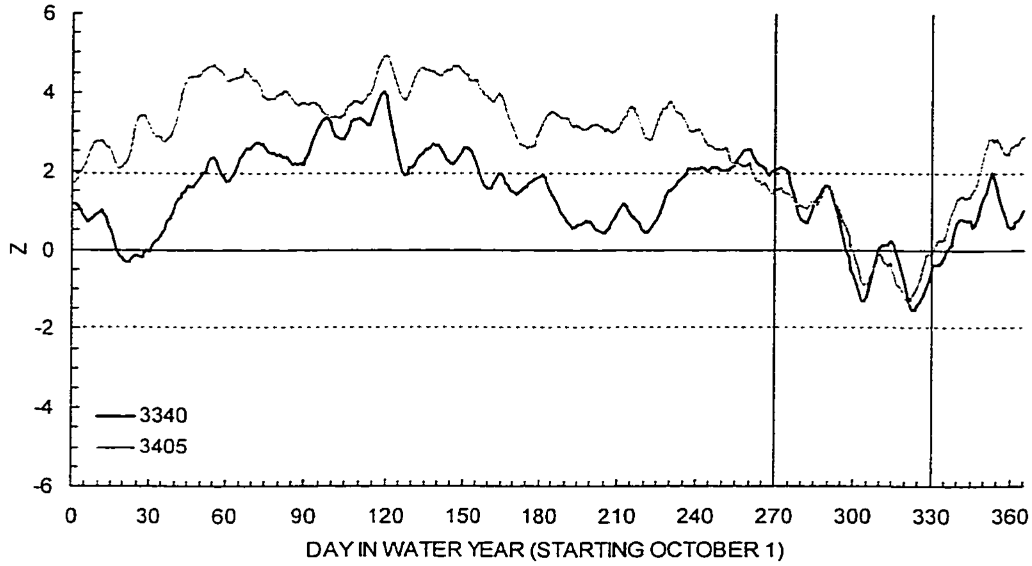

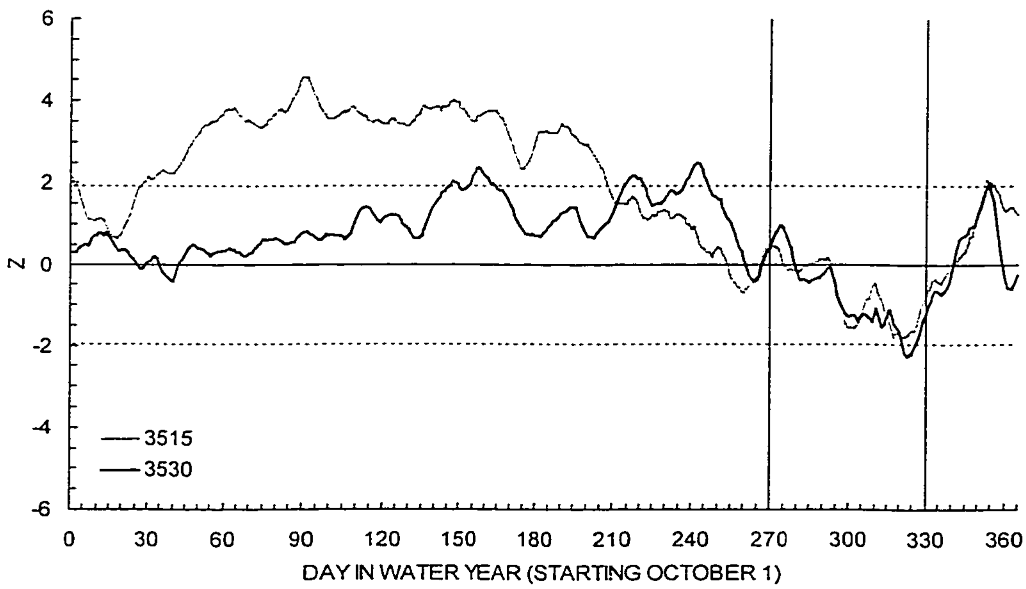

Figure 3.11. Daily streamflow trend test statistic Z for every day of the year at the Upper Rio Puerco gages (top) and Lower Rio Puerco gages (bottom). The summer July-August period is outlined.

4 Precipitation Dynamics

Precipitation is the climatic driving force of large scale erosion in the Rio Puerco Basin. The previous Chapter addressed the importance of trends and shifts in the distribution of daily precipitation in the Basin. Here, the spatial and temporal variability in Rio Puerco daily precipitation at the mesoscale are described and modeled. The primary goal is to develop a stochastic model that will disaggregate annual precipitation into spatially and temporally variable daily precipitation, preserving appropriate statistical properties at all scales involved. Then a conceptual rainfall-runoff model is utilized to transform daily rainfall into daily runoff on a subbasin scale. Subbasin runoff is used as input into the channel erosion model in Chapter 5.

Early studies into the spatial and temporal variability of rainfall focused on the hierarchical structure of rainfall fields and their representation by cluster-point processes (e.g., LeCam 1961, for a review see Foufoula-Georgiou and Georgakakos 1991). More recently, researchers have focused on investigations of statistical self-similarity in spatial rainfall (e.g., Lovejoy and Mandelbrot 1985) and multiscaling departures from it (e.g., Kedem and Chiu 1987, Gupta and Waymire 1990). In order to preserve observed scaling invariance in rainfall (i.e., similarity in the rainfall clustering structure across spatial scales), recent studies have employed the theory of discrete random cascades (introduced by Mandelbrot (1974) as a conceptual basis for fluid turbulence theory). Discrete random cascades are especially amenable to rainfall because they allow for clustering, intermittency and large variability in data, while preserving their scaling invariance and multifractal behavior (e.g., Gupta and Waymire 1993, Over and Gupta 1994).

The aim of this Chapter is threefold. First, to examine whether spatial rainfall data over the Rio Puerco region from NEXRAD (Next Generation Weather Radar) on a daily timescale exhibit scaling invariance and can be modeled using the discrete random cascade theory. In the temporal domain, the applicability of the random cascade theory is examined in the context of regional daily rainfall sequences in wet and dry seasons in the Rio Puerco Basin. Second, parameters of the intermittent random cascade model are estimated for both spatial and temporal rainfall, and related to large scale forcing in the form of a regional average rain rate and seasonal rainfall. Using this information, a Rainfall Modeling System (RMS) is designed that disaggregates annual rainfall over the Rio Puerco Basin into a sequence of stochastic spatial daily rainfall fields using (*a*) a combination of a linear dependence disaggregation model, and (*b*) temporal and (*c*) spatial discrete random cascade models. Finally, (*d*) a conceptual lumped rainfall-runoff model is developed for transforming rainfall into daily runoff on a subbasin scale. This model is calibrated and verified with long-term streamflow statistics.

4.1 Random Cascade Model Theory

Details of the discrete random cascade theory, in particular in the context of its application to rainfall, are presented in Gupta and Waymire (1993), Over and Gupta (1994), Over (1995), Over and Gupta (1996). The theoretical development is not repeated here, only the necessary basics are reviewed, and the most important and relevant properties of random cascades are presented. Special attention is devoted to parameter estimation of the intermittent random cascade model.

4.1.1 Basic Construction

Discrete random cascades distribute mass on successive regular subdivisions of a d-dimensional cube. A schematic of this division with d=2 is shown in Figure 4.1. The initial cube, with length scale L_0, is subdivided at each level into b equal parts, where $b \geq 2^d$ is called the branching number. The i-th subcube after n levels of subdivision is denoted Δ^i_n (there are i=1, ..., b^n subcubes at level n). The length scale of the subcube Δ^i_n is denoted L_n, and the *dimensionless spatial scale* is defined as:

$$\lambda_n = L_n / L_0 = b^{-n/d} \tag{4.1}$$

The distribution of mass through different levels on this cube occurs as follows. First the initial cube is assigned (at level n=0) a nonrandom initial density R_0; i.e., an initial mass $R_0 L_0^d$. The subcubes Δ^i_1, i=1, 2,..., b after the first subdivision (at level n=1) are assigned the density $R_0 W_1(i)$; i.e., mass $R_0 L_1^d W_1(i)$, where W are independent and identically distributed (iid) random variables - the *cascade generator*. This multiplicative process continues through all levels n of the cascade, so that the mass in subcube Δ^i_n is:

$$\mu_n(\Delta^i_n) = R_0 L_n^d \prod_{j=1}^{n} W_j(i) = R_0 L_0^d b^{-n} \prod_{j=1}^{n} W_j(i), \qquad \text{for } i = 1,2,\ldots,b^n \tag{4.2}$$

The distribution of W is non-negative with E[W]=1, so that mass is on the average conserved at all levels in the random cascade development. This is an important statistical property of canonical cascades (Mandelbrot 1974).

The cascade limit mass μ_∞ is obtained as $n \rightarrow \infty$, and is considered degenerate if the total mass is zero with probability 1. Nondegeneracy of μ_∞ depends on the distribution of W and it requires that the condition E[W]=1 be satisfied. The limit mass in a subcube $\mu_\infty(\Delta_n^i)$ is shown to satisfy a basic recursion relation (e.g., Over and Gupta 1996):

$$\mu_\infty(\Delta_n^i) = \mu_n(\Delta_n^i)\, Z_\infty(i), \qquad \text{for } i = 1, 2, \ldots, b^n \tag{4.3}$$

where Z_∞ are iid random variables, distributed as

$$Z_\infty = \mu_\infty(\Delta_0)/\mu_0(\Delta_0) = \mu_\infty(\Delta_0)/R_0 L_0^d \tag{4.4}$$

for all i and n. The property E[W]=1 together with (4.3) and (4.4) result in E[Z]=1 in nondegenerate cascades. Most noteworthy is that (4.3) shows that the cascade limit mass $\mu_\infty(\Delta_n^i)$ is given by the product of a large scale, low-frequency component $\mu_n(\Delta_n^i)$ and a subcube scale, high frequency component $Z_\infty(i)$. The latter term represents subcube scale variability at each level of cascade development.

4.1.2 Moment Scaling

Random cascades exhibit moment scaling behavior from which properties of the cascade generator W can be estimated. Sample spatial moments are defined as:

$$M_n(q) = \sum_{i=1}^{b^n} \mu_\infty^q(\Delta_n^i) \tag{4.5}$$

here moment order $q \geq 0$ (for q=0, only nonzero limit masses are included in the sum). For large n, the sample moments should converge to the ensemble moments. However, because the ensemble moments diverge to infinity or converge to zero as $n \rightarrow \infty$, the (rate of) convergence/divergence of the moments with scale is considered instead. In a random cascade, the ensemble moments are shown to be a log-log linear function of the scale of resolution λ_n (e.g., Over 1995). The slope of this scaling relationship is known as the Mandelbrot-Kahane-Peyriere (MKP) function (Mandelbrot 1974, Kahane and Peyriere 1976):

$$\chi_b(q) = 1 - q + \log_b \mathrm{E}[W^q] \tag{4.6}$$

The MKP function contains important information about the distribution of the cascade generator W, and thus determines the scaling properties of rainfall.

The slope of the sample moment scaling relationship can be defined as:

$$\tau(q) = \lim_{\lambda_n \to 0} \frac{\log M_n(q)}{-\log \lambda_n} \tag{4.7}$$

It is shown that for large n (as $\lambda_n \to 0$) and for a specific range of q, slopes of the moment scaling relationships for sample and ensemble moments converge (e.g., Over 1995); i.e.,

$$\tau(q) = d\chi_b(q) \tag{4.8}$$

In data analysis, the scaling of the sample moments in Equation (4.7) is used to estimate the $\tau(q)$ function (determine the MKP function) and the distribution of the cascade generator, from which parameters of the cascade model can be inferred.

4.1.3 Intermittent Model

So far no restriction has been placed on the character of the random variable W, except $\mathrm{E}[W]=1$. However, for intermittent rainfall data (in both temporal and spatial domains) it is desirable that a nonzero probability that $W=0$ exists. For this purpose an *intermittent model* for the cascade generator W is described here (after Over 1995).

In this case W is written as a composite generator:

$$W = BY \tag{4.9}$$

where B is an intermittency generator of the so-called β-model and Y is a strictly positive random variable. The β-model divides the domain into rainy and nonrainy fractions based on the following probabilities:

$$P(B=0)=1-b^{-\beta} \qquad \text{and} \qquad P(B=b^{\beta})=b^{-\beta} \tag{4.10}$$

where β is a parameter and E[B]=1. By itself, the β-model does not allow for variability in the positive part of the large scale component of the limit mass $\mu_n(\Delta'_n)$ (at every level n it assumes a nonrandom value equal $R_0 L_n^d b^{\beta n} = R_0 L_0^d b^{-n(1+\beta)}$, see Equation (4.2)). Variability in the positive part of the limit mass is obtained from the second element in the composite generator: Y. The distribution of Y is arbitrary, but it has to be positive and E[Y]=1. For rainfall modeling, good results have been obtained with Y lognormal (Over and Gupta 1996), and this is the model chosen here. Consider $Y=b^{\gamma+\sigma X}$, where X is a normal N(0,1) random variable. The condition E[Y]=1 gives

$$Y=b^{-\sigma^2 \ln b/2+\sigma X} \tag{4.11}$$

where σ^2 (variance of Y) is a parameter. The composite generator W is then distributed as:

$$P(W=0)=1-b^{-\beta} \qquad \text{and} \qquad P(W=b^{\beta}Y=b^{\beta-\sigma^2 \ln b/2+\sigma X})=b^{-\beta} \tag{4.12}$$

with two model parameters: β and σ^2.

The MKP function of W is (Over 1995):

$$\chi_b(q)=(\beta-1)(q-1)+\frac{\sigma^2 \ln b}{2}(q^2-q) \tag{4.13}$$

The two basic properties of any MKP function are: (1) it is convex, and (2) $\chi_b(1)=0$ (Over 1995). Furthermore, for the cascade to be nondegenerate the derivative $\chi_b^{(1)}<0$

(Over 1995). For large σ, this requirement may not be satisfied, leading to degenerate cascades. The range of moments q for which Equation (4.8) holds in nondegenerate cascades is given by the half-open interval $[0, q_c/2)$ when $q_c \leq 2$, and for q in at least the closed interval $[0,1]$ when $q_c > 2$. The latter condition leads to the requirement that

$$\beta < 1 - \sigma^2 \ln b \tag{4.14}$$

in nondegenerate cascades (Over 1995, Over and Gupta 1996).

4.1.4 Estimation of the Cascade Generator

The two parameters of the discrete random cascade model, β and σ^2, are estimated from the MKP function. The parameter β describes the growth of nonrainy segments in the modeled domain. Theoretically, $0 \leq \beta \leq 1$, and larger β implies a faster rate of growth of nonrainy segments, leading to a larger fraction of nonrainy areas. The parameter σ^2 describes the variance of the positive, rainy segments. It reflects the curvature of the (convex) MKP function in (4.13). Theoretically, $\sigma^2 \geq 0$, and higher σ^2 leads to a higher spatial variability in rainfall. Both parameters are conveniently estimated from the MKP function, or rather from the $\tau(q)$ function, which is estimated from the data-derived moment scaling relationship in Equation (4.7).

Taking $\sigma^2=0$, allows the estimation of the intermittency parameter β from the linear segment of the MKP function in (4.13): $\chi_b(q) = 1 - \beta$. Using (4.8), an estimate of β at $q=0$ is then:

$$\hat{\beta} = 1 - \frac{\tau(q)}{d} \tag{4.15}$$

For other ways of estimating β see Over (1995). Positive variance in $\boldsymbol{Y}$ corresponds to the curvature in the MKP function (the second term in (4.13)). Taking a second derivative of the MKP function gives $\chi_b^{(2)}(q) = \sigma^2 \ln b$. Using (4.8), the parameter σ^2 can then be estimated as:

$$\hat{\sigma}^2 = \frac{\tau^{(2)}(q)}{d \ln b} \tag{4.16}$$

Derivatives of $\tau(q)$ are generally obtained by numerical differentiation (e.g., Over and Gupta 1994, 1996). It is noteworthy that both parameters can in principle be estimated at any q.

4.2 Application to Spatial Rainfall Fields

In applying the above theory of random cascades to spatial rainfall fields we take d=2 and b=4 (as in Figure 4.1). R_0 is the initial density: the average rain rate (intensity) over the domain $L_0 \times L_0$. The limit mass $\mu_\infty(\Delta^i_n)$ represents the volume of precipitated water on the i-th box (grid) at level n with size $L_n \times L_n$, and $\mu_\infty(\Delta_0)$ represents the total volume over the domain $L_0 \times L_0$. Considering Equation (4.4), the distribution of the spatial average rain rate R' is given by:

$$R' = \mu_\infty(\Delta_0) / L_0^2 = R_0 Z_\infty \tag{4.17}$$

Because E[Z]=1, then E[R']=R_0, which shows that the canonical random cascade development conserves mass on the average, and R_0 is the expected value of the spatial average rain rate.

In practical application, we assume rainfall data on a square grid with number of cells equal to $K \times K$. Note that $K=2^N$, where N is the data level of the cascade. Rainfall on each cell of the grid is taken to be the limit mass $\mu_\infty(\Delta^i_N)$ for the i-th box at level N. Masses at levels $n=N, N-1, N-2, \ldots, 1, 0$, are then computed by summing over all relevant cells, moments of order q are determined by Equation (4.5), and linear regression is performed on log $M_n(q)$ versus -log λ_n in order to obtain the $\tau(q)$ function in Equation (4.7). The linearity of moment scaling is a good first test of the applicability of the random cascade theory to data. From the $\tau(q)$ function, cascade parameters β and σ^2 can then be estimated using (4.15) and (4.16).

In this section, daily spatial precipitation over the Rio Puerco Basin is analyzed. First, the data are described. Second, a trial period is used to test the fit and performance of the random cascade model in spatial rainfall field generation. Finally, the parameters of the spatial random cascade model are estimated and their relation to large-scale forcing in the form of a regional average precipitation rate for the Rio Puerco Basin is examined.

4.2.1 NEXRAD DATA

For the spatial analyses in this study, radar-derived precipitation from the Next Generation Weather Radar (NEXRAD) system of the NWS was used (NOWrad™). NEXRAD data have wide temporal and spatial coverage in the U.S., and are increasingly being used for hydrologic studies (e.g., Fan et al. 1996, and others). The NEXRAD weather surveillance Doppler radar measures the backscatter power of transmitted electromagnetic waves that is related to radar reflectivity Z. Precipitation R is commonly estimated from so-called Z-R relationships that relate radar reflectivity and ground precipitation in a power law form: $R = aZ^b$, where a and b are calibrated parameters (e.g., Smith 1992).

The chosen study region is a square region from UTM coordinates 4018207 (N) to 3794207 (S), and from 363970 (E) to 139970 (W) that covers the Rio Puerco Basin (e.g.

see Figure 4.4). Precipitation data were resampled onto a 1750×1750 meter grid (this is the minimal length of the NEXRAD grid at Albuquerque latitude). The analyzed region then had 128×128 cells, with a total side length of 224,000 m. In the context of the random cascade model application: K=128, the data level of the cascade is N=7, the length scale L_0=224,000 m, and L_N=1750 m.

Gridded rainfall data were obtained from the Global Hydrology Resource Center (GHRC) in the form of *daily total rainfall*. The GHRC daily total rainfall is obtained by converting radar reflectivity obtained every 15 minutes into a 24-hour accumulation (from 00:00 to 23:59) using the *Z-R* relationship proposed by Woodley et al. (1975). The daily rainfall totals are then binned into 12 ranges shown in Table 4.1. In this study, each grid was assigned the median precipitation value from its range. The first, trace range 0-2.5 mm was assigned zero precipitation, because daily precipitation totals at the cell scale in this range do not contribute significantly to runoff in the semiarid conditions of the Rio Puerco Basin (and thus to any appreciable channel erosion). The highest category with precipitation greater than 127 mm was assigned the lower limit 127 mm.

NEXRAD data for the period October 26, 1995, to September 30, 1998 were available and used in this study; that is a total of 1071 daily scans. Out of this total, 644 had nonzero effective rain fields (60.13%), with an average regional rainfall of 1.55 mm and recorded regional maximum equal 29.72 mm. A comparison between NEXRAD cell precipitation and daily records at 11 precipitation gages contained within the Rio Puerco study area was conducted with moderate success. An average linear correlation coefficient r=0.435 was obtained for the period 10/26/95 to 12/31/97 (798 days); best correspondence between radar data and observations was at the (most reliable)

Albuquerque gage r=0.52. However, such data comparisons are difficult to make, because of (1) the error in the Z-R relationship used to estimate precipitation from reflectivity, (2) the time shift between (morning) daily observations taken at gages without continuous recorders (i.e., most gages in the Rio Puerco) and 24 hour radar data, and (3) subgrid variability that may still be present at the app. 2×2 km grid size in radar data.

4.2.2 Model Testing and Generation

A 13-day test period was chosen to examine the applicability of the random cascade model to Rio Puerco spatial rainfall data (June 3, 1997 to June 15, 1997). During this period a large storm occurred on June 7, followed by a smaller storm on June 12. First, moment scaling functions and cascade parameters were estimated from radar data. With these parameters subsequent random spatial fields were then generated. Moment scaling properties and other descriptive statistics of the generated fields were compared to observations, and the ability of the random cascade model to recover important statistical properties of spatial rainfall was examined.

Using (4.15), the estimate of β was evaluated at q=0:

$$\hat{\beta} = 1 - \frac{\tau(0)}{2} \tag{4.18}$$

It was found that this estimate best represented the nonrainy fraction of generated fields as well as the mean spatial rainfall. It is also evident from (4.18) that for 2-dimensional fields without zero rainfall, β=0 and $\tau(q=0)$=2. Using (4.16), the estimate of σ^2 was evaluated by numerical differentiation of the $\tau(q)$ function between q=1 and q=2:

$$\hat{\sigma}^2 = \frac{\tau^{(2)}(1;2)}{2\ln 4} \tag{4.19}$$

The sequence of both parameters β and σ^2, and the mean regional rainfall R for the test period, are shown in Figure 4.2. It is evident from this figure that the intermittency parameter β and the average rainfall R for the region are inversely related; i.e., highly intermittent fields (β>>0) have lower R. On the other hand, variability of highly intermittent fields seems to be lower (lower σ^2). Also notice that June 11 and June 14 were days with no recorded rain; i.e., β=1, σ^2=0 and R=0.

The main purpose of using the random cascade model in this study is for the generation of spatial daily rainfall fields. Therefore, it was necessary to test the ability of the model to reproduce mean rainfall and cascade model parameters in generation. For this purpose, parameters β and σ^2 estimated for each day in the test period and the regional average rainfall R were used as initial input parameters to generate 100 random fields for every day, from which the model parameters were recomputed and compared with input values. The results listed in Table 4.2 show that the random cascade model preserves very well the two parameters of the model as well as the initial rain intensity. Figure 4.3 shows plots of the observed and generated cascade parameters from Table 4.2. The fit to β is excellent, whereas σ^2 is slightly underestimated in generated data with higher variability.

Two days were chosen to show a more detailed comparison of an observed and a randomly chosen generated rainfall field: the high rainfall day June 7 and a lower rainfall day June 15. The respective observed and generated rainfall fields are shown in Figures 4.4 and 4.5. Although there is no reason for the fields to be visually comparable, one criticism of the random cascade model is evident from the figures: the "blockiness" in the generated rainfall fields that results from the cascading of mass on a regular square grid. This feature is less important in this study, where generated daily rainfall is accumulated on a subbasin scale of order 100-1000 times the cell size; however, for fully distributed rainfall-runoff modeling this feature may present a problem. Despite the "blockiness", the statistics of the generated fields and the observed ones are remarkably similar.

The histograms, moment scaling relationships and $\tau(q)$ functions of the observed and generated rainfall fields are shown in Figure 4.6. The log-log linearity of the moment scaling relationship for both days shows that the random cascade model is well applicable to Rio Puerco daily rainfall data. For June 7, the $\tau(q)$ functions of observations and generated data are essentially identical, and there is only slight deviation for $q>2$ for June 15. For the high rainfall day, observed $\beta=0.008$ and generated $\beta=0.003$, and the value of $\tau(q=0)$ is close to 2. For the lower rainfall day, observed $\beta=0.172$ and generated $\beta=0.155$, and the value of $\tau(q=0)$ is less than 2. The convexity of the $\tau(q)$ function gives the estimate of σ^2, which was $\sigma^2=0.027$ for observed and $\sigma^2=0.03$ for generated data on June 7, and $\sigma^2=0.075$ for observed and $\sigma^2=0.05$ for generated data on June 15. Mean regional rainfall was also well preserved in both cases: observed $R=23.33$ mm and generated $R=24.06$ mm on June 7, and observed $R=2.67$ mm and generated $R=2.93$ mm on June 15.

4.2.3 Parameter Estimation and Large Scale Forcing

Using Equations (4.18) and (4.19) parameters β and σ^2 were estimated for the complete period of Rio Puerco NEXRAD data. Here, the relationship between these parameters and large-scale forcing in the form of the regional average rainfall is examined. The dependence of cascade parameters on large-scale forcing is important because it provides a connection between the atmospheric dynamics and the observed scaling structure of rainfall fields (Over and Gupta 1994, 1996). It also allows us to estimate the cascade parameters given mean daily rainfall, which will be employed in the generation of rainfall.

There were 644 scans with rainy fractions in the Rio Puerco NEXRAD data set for which β and σ^2 were estimated and the regional average rainfall R computed. Figure 4.7 shows the dependency of β on R in the form suggested by Over and Gupta (1996):

$$\beta_t = \log\left(\frac{R_t}{R_{\max}}\right)^s \tag{4.20}$$

where the constants s=-0.219 and R_{max}=12 mm/day for Rio Puerco data (the R^2 of the fit was equal 0.973). Here R_{max} is a maximum regional average rainfall with a positive nonrainy fraction that is observed on the average in the data; i.e., for $R > R_{max}$, $\beta=0$.

Over and Gupta (1996) investigated the above relationship for GARP (Global Atmospheric Research Program) Atlantic Tropical Experiment (GATE) instantaneous scans of radar-derived rainfall taken every 15 minutes over the tropical (eastern) Atlantic in the summer of 1974 (the experiment lasted for two 19-day phases: Phase I from June 28 to July 16 and Phase II from July 28 to August 15; and the rainfall was averaged over 4×4 km pixels). Interestingly, they found values of the scaling exponent s not much different from this analysis: s=-0.179 Phase I and s=-0.195 Phase II, despite the difference in the nature of the scans (instantaneous versus daily accumulation). It has also been suggested that the relationship in (4.20) should hold only for a single type of large scale forcing (Over and Gupta 1994). The results here indicate that the relationship may hold for a mixture of storm types and synoptic forcings in the Rio Puerco region.

It also seems from Figure 4.7 that the variability in spatial rainfall increases with decreasing R and increasing β. This is confirmed in Figure 4.8 where the spatial coefficient of variation is shown computed from rainfall mass at the fine grid scale including nonrainy fractions. As the sparsity of the spatial fields increases (β increases), the variability in R increases exponentially. Similar results have also been obtained by Over and Gupta (1994) for the GATE scans.

Finally, Figure 4.9 shows the estimated cascade parameter σ^2 for Rio Puerco data. Here the relationship with R is less evident. There seem to be two opposing tendencies in the data. At small R, the rainfall fields are sparse and the variability in (positive) rainfall intensities is low. This variability increases with R. However, for large R, R>3 mm (β<0.13), the rainfall fields become "full" and their relative variability again decreases. In light of the relationship in Figure 4.9, an average parameter σ^2 is used for cascade generation for all R, σ^2=0.043. Also note that because of estimation error, in some cases σ^2<0. These values were not used in computing mean σ^2. Note that the condition in (4.14) implies that given variability σ^2=0.043, the random cascades will be nondegenerate for β<0.94. Fields with β>0.94 should therefore be treated with caution. Interestingly, the instantaneous GATE scans also lacked a good relationship between σ^2 and R, but their relative variability was larger, average σ^2=0.1 (Over and Gupta 1996).

4.2.4 Summary

The application of the random cascade model to spatial rainfall data obtained by radar in the Rio Puerco Basin was presented in this section. The results show that the random cascade model is suited for modeling daily rainfall totals for the Rio Puerco region.

Results point to the existence of a temporal invariance in the relationship between large-scale forcing and the spatial rainfall pattern (Over and Gupta 1994) that results in a good relationship between the cascade parameter β and the regional average rainfall R in the Rio Puerco Basin. This formulation in Equation (4.20), together with the mean parameter σ^2, will be used in determining the cascade parameters and daily rainfall field generation given the time series of regional average rainfall R. The estimation of R is the subject of the next section.

4.3 Application to Daily Regional Precipitation

In order to describe the space-time evolution of rainfall fields it is necessary to extend the spatial random cascade model described in the previous section into the temporal domain. One possibility is to let the cascade generator evolve as a continuous time stochastic process (Over and Gupta 1996). That is, allow the cascade generator to be dependent in time. In this study, the temporal daily time step is too large for Taylor's (space-time substitution) hypothesis to hold, and it is generally sufficient to consider the generators independent in time. However, some larger scale temporal dependency needs to be considered. The option chosen here is to model the temporal evolution of the regional average rainfall R and use the large scale forcing function in Equation (4.20) to compute the spatial cascade parameter β on a daily basis. Daily precipitation modeling can be performed by discrete autoregressive moving average processes (e.g., Chang et al. 1984), but with prohibitively many parameters. Here, the temporal (one-dimensional) extension of the random cascade theory was chosen instead.

In applying random cascades to a time series of daily rainfall, we take d=1 and b=2 without loss of generality. R_0 is the initial density: the average rain rate (intensity) over the domain L_0 (i.e., number of days in season). The limit mass $\mu_\infty(\Delta^i_n)$ represents the volume of precipitated water on the i-th cell with size L_n days, and $\mu_\infty(\Delta_0)$ represents the total volume over the domain L_0. The latter quantity will be called the seasonal precipitation total R_{season}. As in the spatial case, the temporal random cascade preserves mass on the average.

In practical application, we have daily rainfall data for K number of days; i.e., K=L_0. Again, note that K=2^N, where N is the data level of the cascade. Daily rainfall at level N is taken to be the limit mass $\mu_\infty(\Delta^i_N)$. Masses at levels n=N, N-1, N-2, ..., 1, 0, are then computed by summing over all relevant days, moments of order q are determined and the $\tau(q)$ function is estimated in the same manner as described earlier. From the $\tau(q)$ function, cascade parameters β and σ^2 are estimated.

In this section, daily regional average precipitation over the Rio Puerco Basin is analyzed. First, the data are described and a dry and wet season identified. Second, both seasons are used to test the fit and performance of the random cascade model. Third, the parameters of the temporal random cascade model are estimated and their relation to large-scale forcing similar to the spatial case is identified.

4.3.1 NEXRAD AND CLIMATE STATION DATA

For the temporal analyses in this study, a combination of daily NEXRAD and precipitation station data in the Rio Puerco Basin were used. For NEXRAD, these were time series of daily regional average rainfall R for the study region used in spatial analyses for the years 1996 and 1997. Because two years of data are not sufficient for robust estimates of the cascade parameters, climate station data were also analyzed. An arithmetic average regional rainfall R' was computed from 14 precipitation gaging stations (with $\rho>0$ from Table 2.4) for every day of the year for the period 1948-1997. The station daily data were considered spatial averages in the gage area, so daily rainfall intensities less than 2.5 mm were included in the computation of the Rio Puerco Basin average rain rate.

Because of the large seasonality in Rio Puerco precipitation, the year was divided into a dry and wet season. This division was conducted by examining long-term daily precipitation at the Albuquerque gage. Both seasons were taken to be 128 days long, thereby $K=L_0=128$ and $N=7$ in the random cascade context ($L_N=1$ day) for each season. The dry season lasts from February 12 to June 19 (from February 13 in a leap year). The wet season lasts from June 20 to October 25. Therefore, a *model year* in this study is 256 days long. In terms of precipitation volume, these two seasons together constitute on the average almost 80% of the annual rainfall total. Climate station analyses showed that the long-term average dry season precipitation total was 68 mm and wet season 157 mm.

A comparison of the radar-derived and station-derived daily regional average rainfall is shown in Figure 4.10 for 1997, which was an unusually wet year. NEXRAD estimates are in general higher than station-derived estimates because they include mountainous regions with higher precipitation where climate stations are not located. However, for dry years, such as 1996, station-derived estimates were higher (see also Table 4.3). The linear correlation coefficients between NEXRAD and station-derived daily precipitation for the Rio Puerco region were $r=0.85$ (dry season) and $r=0.88$ (wet season) for 1997 and

r=0.65 (dry season) and r=0.89 (wet season) for 1996. This good correlation allows us to use the station-derived regional average rainfall R' as a substitute for NEXRAD-derived R in determining cascade parameter relationships.

4.3.2 Model Testing and Generation

The years 1996 and 1997 for which radar data are available are used to examine the applicability of the random cascade model to Rio Puerco daily rainfall data. As in the spatial case, moment scaling functions and cascade parameters were estimated from radar data. With these parameters subsequent random time series of daily rainfall were generated and moment scaling properties and other descriptive statistics of the generated fields were compared to observations.

Using (4.15), the estimate of β was also evaluated at q=0:

$$\hat{\beta} = 1 - \tau(0) \tag{4.21}$$

For 1-dimensional fields without zero rainfall, β=0 and $\tau(q=0)=1$. Using (4.16), the estimate of σ^2 was evaluated by numerical differentiation of the $\tau(q)$ function between q=1 and q=3:

$$\hat{\sigma}^2 = \frac{\tau^{(2)}(1;3)}{\ln 2} \tag{4.22}$$

The estimates of β and σ^2 and the seasonal precipitation total R_{season} are listed in Table 4.3 for both years and seasons.

The performance of the random cascade model was tested by generating 100 series of mean daily precipitation with the parameters β and σ^2 estimated from NEXRAD data and the total seasonal rainfall R_{season} used as initial input parameters. The results are listed in Table 4.3. The performance of the model is not as good as in the spatial case. However,

R_{season} and β are preserved reasonably well, although σ^2 is generally underestimated in the generated series as well as the maximum daily average rainfall R_{max}. In Figure 4.11 a randomly chosen simulated series is shown with input parameters for the 1997 dry and wet seasons. The input parameters are listed in Table 4.3; the generated series had: β=0.085, σ^2=0.153, R_{dry}=99.6 mm, R_{max}=6.6 mm for the dry season, and β=0.052, σ^2=0.181, R_{wet}=387.4 mm, R_{max}=27.6 mm for the wet season. Considering the low number of parameters, the performance of the random cascade model can be considered good. It is especially noteworthy that the cascading process indirectly preserves a high level of important autocorrelation in the data. For instance, the lag-one autocorrelation coefficient (including zero rainfall) for the 1997 dry season was $r(1)$=0.434 from radar data and $r(1)$=0.439 for the generated series, for the wet season $r(1)$=0.498 from radar data and $r(1)$=0.488 for the generated series. For 1996, similar results were obtained. Furthermore, the "blockiness" seen in spatial field generation is not evident in temporal data.

4.3.3 Parameter Estimation and Large Scale Forcing

Four seasons of NEXRAD data are not sufficient to estimate β and σ^2 and to develop a large scale forcing formula as in the spatial case. For this reason, station-derived daily regional average rainfall R' was used. Using Equations (4.21) and (4.22), parameters β and σ^2 were estimated from station-derived R'. As in the spatial case, the development of a relationship between cascade parameters and the seasonal total precipitation will be employed in the generation of rainfall.

Fifty years of dry and wet season rainfall data were used to estimate the cascade parameters β and σ^2 and to compute the seasonal precipitation total R_{season}. Figure 4.12 shows the dependency of β on R_{season}. It is evident that there is not a significant break in the scaling relationship between the dry and wet seasons. This interesting fact was also examined and confirmed for individual station records (rather than regional averages). The result is that a single large scale forcing relationship can be used for both seasons of the form (Over and Gupta 1996):

$$\beta_t = \log\left(\frac{R'_t}{R'_{\max}}\right)^{s'} \tag{4.23}$$

where the constants s'=-0.231 and R'_{max}=391.7 mm/day for Rio Puerco data (the R^2 of the fit was equal 0.823). Here R'_{max} is a maximum seasonal precipitation total with a positive nonrainy fraction that is observed on the average in the data; i.e., for $R > R'_{max}$, β=0.

Also included in Figure 4.12 are the NEXRAD-derived 1996 and 1997 estimates of β and R_{season}. These points fall along the relationship in (4.23) except for the dry season in 1996, which is notably different. Closer examination of this record shows that in this extremely dry season more than one half of the seasonal total fell in one day. The $\tau(q)$ functions from NEXRAD data are shown in Figure 4.13. Here it is evident that the dry season 1996 exhibits extreme curvature in the $\tau(q)$ function, which is an indication of extreme variability. It can be concluded that for this season, the random cascade model would not be applicable.

The variability of the temporal rainfall fields in the random cascade context, measured by σ^2, is shown in Figure 4.14. As in the spatial case, σ^2 seems independent of the seasonal precipitation total, but is in general higher. The NEXRAD-derived estimates of σ^2 do not deviate from station-derived estimates. The average σ^2 for the dry season was σ^2=0.137 and for the wet season σ^2=0.142. These were the values used in temporal rainfall field generation using the random cascade model in later sections of this study. Also note that the limiting condition in (4.14) implies that fields with β>0.91 should be treated with caution, as they may be degenerate. However, Figure 4.12 shows that this condition rarely occurs in Rio Puerco seasonal precipitation.

4.3.4 Summary

The application of the random cascade model to temporal rainfall data obtained by radar and supplemented by station observations in the Rio Puerco Basin was presented. The results show that the random cascade model is suited for modeling time series of daily regional rainfall for the Rio Puerco region. As in the spatial case, results point to the existence of invariance in the relationship between large-scale forcing and the temporal rainfall pattern that results in a good relationship between the cascade parameter β and the seasonal total precipitation in the Rio Puerco Basin. What remains is the division of annual rainfall into seasonal totals. This is the subject of the next section.

4.4 Disaggregation of Annual Precipitation

Using station-derived daily regional average rainfall for the Rio Puerco region developed in the preceding section, computed seasonal totals are related to the annual total in this section. The task is to disaggregate an independent (annual) series into several (three) dependent (seasonal) subseries while preserving their (1) additivity, (2) variance and covariance structure between seasons, and (3) covariance structure between seasons and the annual series. This is readily accomplished by the simplest disaggregation model: the linear dependence model.

4.4.1 LINEAR DEPENDENCE MODEL

The linear dependence model disaggregates an independent series into dependent subseries while preserving their statistical properties at different levels. It is attributed to Valencia and Schaake (1973) and has the form:

$$\mathbf{Y} = \mathbf{AX} + \mathbf{B}\boldsymbol{\varepsilon} \tag{4.24}$$

where $\mathbf{Y}$ is a dependent vector consisting of seasons, $\mathbf{A}$ is a parameter vector, $\mathbf{X}$ is the independent annual time series, $\mathbf{B}$ is a lower triangular parameter matrix, and ε is a stochastic term vector distributed N(0,1). In the linear dependence model it is assumed that $\mathbf{X}$ and $\mathbf{Y}$ are almost normally distributed, and they are transformed such that their means are E[$\mathbf{X}$]=0 and E[$\mathbf{Y}$]=0 (i.e., the data are transformed to normal and the means of the original series are removed).

Estimates of the parameter matrices are commonly computed using the method of moments, with the following solution (e.g., Salas et al. 1985):

$$\begin{aligned} \hat{\mathbf{A}} &= \mathbf{S}_{YX}\mathbf{S}_{XX}^{-1} \\ \mathbf{D} = \hat{\mathbf{B}}\hat{\mathbf{B}}^{T} &= \mathbf{S}_{YY} - \mathbf{S}_{YX}\mathbf{S}_{XX}^{-1}\mathbf{S}_{XY} \end{aligned} \tag{4.25}$$

where $\mathbf{S}$ are covariance matrices. If $\mathbf{B}$ is a lower triangular matrix and $\mathbf{D}$ is a positive definite or a positive semi-definite matrix, then there is a unique solution to the individual elements of $\mathbf{B}$ (e.g., Lane 1979):

$$
\begin{aligned}
&b_{11} = \sqrt{d_{11}} \\
&b_{21} = d_{12} / \sqrt{d_{11}} \qquad b_{22} = \sqrt{d_{22} - b_{21}^2} \\
&b_{31} = d_{13} / \sqrt{d_{11}} \qquad b_{32} = (d_{32} - b_{21}b_{31}) / b_{22} \qquad b_{33} = \sqrt{d_{33} - b_{31}^2 - b_{32}^2}
\end{aligned}
\tag{4.26}
$$

Extensions of the linear dependence model allow for the preservation of the seasonal covariances between years. In this study, annual precipitation is considered independent in time and the model is used in its simplest form. It is also important to note that the linear dependence model preserves autocorrelation indirectly (Salas et al. 1985).

4.4.2 Parameter Estimation

The station-derived series of daily regional average rainfall R' for the Rio Puerco Basin were used to compute the dry and wet season totals and the annual total rainfall P for the period 1948-1997. These were then standardized to zero mean by subtracting averages. It was verified that the variables do not deviate significantly from the assumption of normality. The three parameter vector **Y** then consists of the dry season total y_1, the wet season total y_2, and the remaining precipitation volume y_3 that satisfies additivity to the annual rainfall volume $x=P$. Equation (4.24) can then be written as the following system of equations:

$$
\begin{aligned}
y_1 &= a_1 x + b_{11}\varepsilon_1 \\
y_2 &= a_2 x + b_{21}\varepsilon_1 + b_{22}\varepsilon_2 \\
y_3 &= a_3 x + b_{31}\varepsilon_1 + b_{32}\varepsilon_2 + b_{33}\varepsilon_3
\end{aligned}
\tag{4.27}
$$

where a and b are elements of the parameter matrices, and ε are independent N(0,1) distributed random elements of the stochastic vector. It can readily be shown that the exact additivity of the model ($y_1 + y_2 + y_3 = x$) leads to the following parameter constraints:

$$
\begin{aligned}
&a_1 + a_2 + a_3 = 1 \\
&b_{11} + b_{21} + b_{31} = 0 \\
&b_{22} + b_{32} = 0 \\
&b_{33} = 0
\end{aligned}
\tag{4.28}
$$

Therefore, in this application the linear dependence model has 8 parameters (5 independent parameters), that need to be estimated from data.

Estimation was conducted using Equations (4.25) and (4.26); i.e., the covariances **S** were first computed and the estimator elements of the matrix **A** determined from (4.25). Then the elements of matrix **D** were computed and Equation (4.26) employed to find the estimator elements of matrix **B**. The means of **X** and **Y** and the estimated parameters are listed in Table 4.4.

4.5 Rainfall Modeling

To this point, rainfall description in the Rio Puerco Basin has focused on three stages, going from the small scale to the large scale.

First, the spatial rainfall fields of daily precipitation determined by NEXRAD were analyzed and the spatial random cascade parameters were estimated and linked to the regional average rainfall. Second, the temporal evolution of the daily regional average rainfall was investigated on radar and climate station data. The temporal random cascade parameters were estimated and also linked to large scale forcing in the form of a seasonal precipitation total. Third, the disaggregation of the annual total precipitation in the Rio Puerco region into dry and wet season totals using a linear dependence model was analyzed. The main purpose was to develop a rainfall modeling system that would be able to disaggregate annual total rainfall into daily spatial rainfall fields over the Rio

Puerco Basin, while preserving appropriate statistical properties at all temporal and spatial scales. Here some issues regarding this system are discussed.

4.5.1 Rainfall Modeling System

The rainfall modeling system (RMS) is designed to operate in a stochastic generation mode according to the following schematic:

ANNUAL PRECIPITATION Input time series: P_i [mm], i=1, …, n years
DISAGGREGATION INTO SEASONS *Linear dependence model* Seasonal precipitation totals y_1, y_2 [mm], i=1, …, n are obtained Equation (4.27), Parameters from Table 4.4
DAILY REGIONAL AVERAGE RAINFALL *Temporal random cascade model* Daily mean rainfall series for dry season R_j, j=1, …, 128 days are obtained Daily mean rainfall series for wet season R_j, j=129, …, 256 days are obtained Equation (4.23) for β, σ^2=0.137 (dry season), σ^2=0.142 (wet season)
SPATIAL RAINFALL FIELDS *Spatial random cascade model* Daily spatial rainfall for region R_{kj}, for j=1, …, 256, k=1, …, 128×128 cells Equation (4.20) for β, σ^2=0.043

Given an annual average precipitation P and a desired coefficient of variation, actual annual precipitation values P_i are drawn from a normal distribution for the desired generation length in years (commonly n=100 years).

For each year i, the (standardized) annual total is disaggregated using the linear dependence model and the dry and wet season rainfall totals are computed (their averages from Table 4.4 are added to obtain the actual value).

The formula in (4.23) is then used to determine the β parameter of the temporal random cascade model (average σ^2 is used for each season) and the model is used to generate limit masses $\mu_\infty(\Delta_n^i)$ on the grid j=1, ..., K, for the dry and wet seasons separately. In generation, the following recursion formula is utilized:

$$\mu_{n+1}(\Delta_{n+1}^i) = \mu_n(\Delta_n^i)\frac{1}{2}W_{n+1}^i \tag{4.29}$$

where W is the intermittent random cascade generator. According to suggestions by Over and Gupta (1994), the limit mass is estimated as:

$$\mu_\infty(\Delta_n^i) \cong \mu_{N+M}(\Delta_n^i) \tag{4.30}$$

where N is the data level of the cascade (N=7) and M is the level of the subgrid cascade that represents subgrid scale variability. It is another random cascade generated with the same parameters and with $\mu_N(\Delta_n^i)$ as the input mass. Here M=3 was chosen (this gives us a limit mass at the scale of 3 hours, which is approximately the length of summer convective rainfall in the Rio Puerco region). The end result of the temporal cascade model is a series of daily regional average rainfall R_j, j=1, ..., 128 for the dry season and R_j, j=129, ..., 256 for the wet season.

The final step is to generate the spatial daily rainfall fields using the spatial extension of the random cascade model. First the formula in (4.20) is used to determine the β parameter of the spatial random cascade model (average σ^2 is again used). The model is used to generate limit masses $\mu_\infty(\Delta'_n)$ on the (2-dimensional) grid j=1, ..., K, for all days. The recursion formula used in generation is:

$$\mu_{n+1}(\Delta'_{n+1}) = \mu_n(\Delta'_n)\frac{1}{4}W'_{n+1} \tag{4.31}$$

In this case, the limit mass is estimated as:

$$\mu_\infty(\Delta'_n) \cong \mu_N(\Delta'_n) \tag{4.32}$$

where N is the data level of the cascade (N=7). Subgrid scale variability is not considered (M=0), because for convective rainfall, the size of a convective cell on the order of 2 km will constitute the minimum scale below which the cascade structure generally no longer holds (Over and Gupta 1994, Over 1995). The end result of the spatial cascade model is a set of daily spatial rainfall fields R, for all days j in both the dry and wet seasons, and for all years of generation i. Spatially distributed daily rainfall can then be aggregated over subbasins in the Rio Puerco, and daily runoff computed.

4.5.2 RMS Testing

Extensive testing of the RMS was carried out in the course of this study. Of particular interest is the ability of the model to preserve the annual rainfall total P, its variability and autocorrelation (or lack thereof), throughout the temporal and spatial disaggregation. Also of interest is the preservation of the seasonal totals and their statistical properties. An example of the performance of the RMS is presented in this section.

In this example an input series of annual rainfall totals P was generated for the Rio Puerco region from a normal distribution with $\overline{P} = 300$ mm and coefficient of variation C_v=0.25 (approximate long-term statistics from data), of length n=100 years. Figure 4.15 shows the input and RMS simulated series of P. There is close correspondence between the two series. It is also apparent that the stochastic elements in each RMS step result in an increase in the variability of P. Figure 4.16 shows input and simulated values of P plotted versus each other. There is no evident trend in the scatter. In actuality, the slope of the linear regression between input and RMS simulated P was statistically not significantly different from 1, with r=0.69.

The statistics at each level of the RMS are presented in Table 4.5. This table shows that the RMS does an excellent job at preserving mean precipitation at all stages (annual as well as seasonal). Also evident is that the temporal cascade model increases the variance in simulated rainfall. Note that the coefficient of variation of P increases from 0.23 to 0.33 after the temporal cascade model and remains equal to 0.32 after the spatial cascade model (this increase in variance is spread through both dry and wet seasons).

In rainfall-runoff modeling, annual maxima are also of interest. In the above example, the mean annual daily rainfall maximum (i.e., a spatial average over the Rio Puerco region) was 5.2 mm in the dry season and 8.6 mm in the wet season from 100 years of simulation. At the same time, the mean annual daily rainfall maximum at the grid scale (i.e., maximum precipitation simulated at the 1750×1750 meter cell per year in the studied region) was an incredible 193.7 mm in the dry season and 259.1 mm in the wet season. Maximum 1-day precipitation events recorded at the climate stations in the Rio Puerco Basin are on the order of 50-100 mm (see Table 2.4). This disparity is not a shortcoming of the RMS; rather, it shows that the great spatial variability in Rio Puerco rainfall cannot be well captured by the sparse network of rainfall gages. This is also true for most other regions of the world.

The performance of the RMS model in testing was considered very good. The small amount of parameters (12 independent parameters) makes it a very robust method of connecting large scale climate forcing (in the form of an annual precipitation total) with the small convective cell scale variability in daily rainfall. Of course in the context of the random cascade theory, the RMS is as good as the theory is in reproducing temporal and spatial rainfall fields. One example: the spatial cascade model produces rainfall independently on land surface properties; i.e., it is not possible at this stage to produce an elevation gradient in rainfall (as in Figure 2.8) - as this would require that the cascade generator not be independent in space. This may be an avenue for further research. Some other open issues with random cascades, such as the choice of the branching number, can be found in detail elsewhere (Over 1995, Over and Gupta 1996). The main use of the RMS in this study is in rainfall-runoff modeling: in reproducing the temporal and spatial variability in daily runoff in the Rio Puerco main stream that is essential to erosion dynamics.

4.6 Rainfall-Runoff Transformation

The transformation from spatially and temporally variable rainfall to runoff on a daily timescale in the Rio Puerco Basin is conducted with the use of a simple parsimonious conceptual lumped rainfall-runoff model developed in this section. The model is applied at a subbasin scale of order 10^2-10^3 km^2. It is used to simulate daily runoff from Rio Puerco subbasins delineated in Chapter 2, which is the driving input into the channel erosion model described in Chapter 5.

Conceptual lumped rainfall-runoff models are used widely in hydrology, especially in conditions with inadequate watershed and hydroclimate data and in cases where long-term continuous simulations are desired (e.g., Gan et al. 1997, Loumagne et al. 1996, Schreider et al. 1996). The main premise of conceptual lumped hydrologic models is that the basin is a homogeneous unit in which the physical processes that affect the rainfall-runoff transformation (i.e., evapotranspiration, overland flow, channelized flow, etc.) can be lumped into simple input-output functions. This conceptualization is often done on the basis of unit hydrographs and/or reservoir analogies. In this study the latter approach is chosen. A linear reservoir is used to transform effective rainfall into streamflow on a daily basis. Effective rainfall is computed as a nonlinear function of basin rainfall. It is related to basin soil properties and calibrated to satisfy the long-term average runoff volume. Although the lack of data makes proper model calibration and verification impossible, results indicate that this simple model is an adequate representation of the hydrologic response in the Rio Puerco Basin. In this section, the model and calibration of its parameters are described.

4.6.1 Model Description

The *conceptual lumped rainfall-runoff model* developed here contains two elements: (1) a nonlinear transformation function of basin-wide daily rainfall into daily effective rainfall; i.e., rainfall that directly results in basin runoff; and (2) a linear reservoir inflow-outflow model that conceptualizes the basin as a reservoir and determines the outflow; i.e., runoff from the basin. In its concept the model is similar to many other simple conceptual hydrologic models (e.g., Gan et al. 1997, Post and Jakeman 1996, and many others).

The transformation of rainfall into *effective rainfall* is generally dependent on two main factors: the intensity of rainfall and losses (infiltration, evaporation, etc). Here, effective daily rainfall intensity r_e is a nonlinear function of basin-averaged daily rainfall intensity r (provided by RMS):

$$r_e = c\,r \tag{4.33}$$

where c is a runoff coefficient (c<1) such that

$$\begin{aligned} c &= 0 && \text{for } r \le r_{\min} \\ c &= a + b\,r && \text{for } r > r_{\min} \end{aligned} \tag{4.34}$$

The above formulation is based on the argument that rainfall intensity below a threshold $r_{\min}$ does not produce runoff, and that the fraction of rainfall above the threshold observed as runoff increases with the intensity of rainfall. The parameters a and b are calibrated to ensure that for a given season (or calibration period) the total effective rainfall is equal to total measured runoff. On a daily basis, autocorrelation in c is a result of autocorrelation in the daily rainfall intensity r. The advantage of this approach is that the parameters a and b have a straightforward interpretation (which is important in transferring the model between ungaged basins of different sizes; see also Schreider et al. 1996). The disadvantage is that this approach neglects autocorrelation present in c as a result of the antecedent storage of water in the soil column. In developing the rainfall-runoff model, approaches were tested that account for antecedent conditions through an autocorrelated basin wetness index (Post and Jakeman 1996). This addition improved slightly the performance of the model (in particular in simulating the peaks of hydrographs). However, the addition of another storage-related parameter was not desirable, especially because of the difficulty in transferring that parameter across basins.

The basin component that transfers effective rainfall into runoff is the *linear reservoir*, which lumps all physical rainfall-runoff processes into a simple linear relation between the outflow from a reservoir (basin) Q and its storage S:

$$Q = \frac{1}{k} S \tag{4.35}$$

where k is a storage parameter. The basin is conceptualized to behave as a reservoir: an input-output system in which continuity applies:

$$I(t) - Q(t) = \frac{dS}{dt} \tag{4.36}$$

where the input, output and storage are a function of time t. From (4.35) and (4.36):

$$I(t) - Q(t) = k\frac{dQ}{dt} \tag{4.37}$$

The single parameter of the linear reservoir model is k, which conceptually describes the average time that an input wave takes to travel through the reservoir/basin. Larger k means a longer response time. Experiments were also carried out with cascades of linear reservoirs in series. However, in all analyzed cases, the single reservoir provided best results, especially in preserving the attenuation of the runoff hydrograph.

In the present context, the model is discretized on a daily time step (in connection with the RMS). Therefore, the storage parameter k is in days, Q and I are in m^3/day and S is in m^3. The discretization scheme used to solve Equation (4.37) is:

$$Q_t = \frac{I_t + Q_{t-1}(k/\Delta t - 1/2)}{k/\Delta t + 1/2} \tag{4.38}$$

Given daily streamflow data Q and effective precipitation totals I for a given basin, the parameter k can be calibrated using Equation (4.38). Effective daily precipitation totals are connected with effective rainfall intensity as:

$$I = 10^3\, r_e\, A \tag{4.39}$$

where A is the basin area in km^2 and r_e is the basin-averaged effective rainfall intensity in mm from Equation (4.33).

In general, the rainfall-runoff model has three parameter (a, b and k) and it was applied separately to the dry and wet seasons in the Rio Puerco Basin.

4.6.2 Example Calibration

Calibration of the developed rainfall-runoff model in the Rio Puerco Basin is difficult because of the lack of adequate data. Three steps are described here for parameter calibration/estimation.

First, the runoff coefficient relations were tested in the Upper Rio Puerco Basin and seasonal differences were explored. There is good reason to expect different hydrologic response in the two seasons in the Upper Rio Puerco Basin, where the dry (winter and spring) season brings a large percentage of snowmelt runoff from the mountainous regions (in other parts of the Rio Puerco this fraction is not significant). For this purpose, an Upper Rio Puerco Basin-wide average daily rainfall intensity was computed for the period 1961-1996 from the Cuba and Torreon stations (area weighted) and compared with daily runoff at the Rio Puerco above Arroyo Chico gage (3340) on a seasonal basis. The resulting seasonal runoff coefficients for every year are shown in Figure 4.17. The different hydrologic response between the dry and wet seasons in the Upper Rio Puerco Basin is evident. The dry season generally has a higher (mean c=0.078) but variable seasonal runoff coefficient. On the other hand, the wet season has a lower (mean c=0.02) and much less variable seasonal runoff coefficient. In addition, in both cases it is evident that the seasonal runoff coefficient increases with increasing seasonal rainfall. This gives credence to the formulation for the daily runoff coefficient relation in Equation (4.34).

Second, NEXRAD rainfall data for the Upper Rio Puerco Basin and daily streamflow at gage 3340 were used to calibrate the rainfall-runoff model. Unfortunately, only 1997 has concurrent radar estimates of rainfall and observations of streamflow available for calibration. Year 1996 was dry and not suitable for calibration (e.g., Gan et al. 1997). There are two connected steps in the calibration. First is the determination of the parameters a and b for effective rainfall. Let us choose a reference rainfall intensity r^* at which c=c^*. Then

$$\begin{aligned} a &= \frac{c^*}{1 - r^* / r_{\min}} \\ b &= -\frac{a}{r_{\min}} \end{aligned} \tag{4.40}$$

The reference rainfall intensity is arbitrarily taken r^*=10 mm in this study. Then calibration proceeds on the reference runoff coefficient c^* and minimum rainfall intensity $r_{\min}$ which fully determine model parameters a and b. Note that if $r_{\min}$=0, then

$$\begin{aligned} a &= 0 \\ b &= \frac{c^*}{r^*} \end{aligned} \tag{4.41}$$

Second is the determination of the storage parameter k for the linear reservoir model using Equations (4.38) and (4.39). All three parameters are calibrated to maximize the fraction of the variance explained by the model, or model efficiency defined as:

$$E = 1 - \frac{\sum (Q_{sim} - Q)^2}{\sum (Q - \bar{Q})^2} \tag{4.42}$$

where Q are observations and Q_{sim} is simulated streamflow, and to maintain a seasonal water balance:

$$\sum_{t=1}^{n} I_t = \sum_{t=1}^{n} Q_{sim\,t} \tag{4.43}$$

where n=128 for both seasons.

Figure 4.18 shows the wet season calibration with resulting c^*=0.0034, $r_{\min}$=0 mm (a=0, b=0.00034), k=0.858 days and model efficiency E=0.671. The seasonal runoff coefficient was lower than average: c=0.0059 and maximum daily basin-wide rainfall intensity was $r_{\max}$=38.8 mm. The fit is good, especially regarding the time to peak and the quick recession of the hydrographs; less so regarding the peak values themselves (seasonal volumes are preserved exactly through (4.43)). Figure 4.19 shows the dry season calibration. In this case the runoff coefficient formulation in (4.34) did not give good results and a constant seasonal runoff coefficient c=0.1088 was used instead. The estimated linear reservoir parameter k=5.55 days reflects longer hydrograph recession. Maximum daily basin-wide rainfall intensity was $r_{\max}$=7.6 mm, and model efficiency was E=0.455. The fit in this case is not as good; it is evident that the simple model cannot fully account for the complexity of the hydrologic response in the Upper Rio Puerco Basin winter-spring season. However, in both seasons, given the simplicity of the rainfall-runoff model, the results are satisfactory.

Third, generated spatial rainfall fields using RMS for the three independent gaged basins: Rio Puerco above Arroyo Chico, Arroyo Chico and Rio San Jose (Subbasin 4, see Figure 2.3), were used to verify the model and re-calibrate the parameters to other Rio Puerco subbasins.

4.6.3 Calibration For Long-Term Statistics

In order to transfer the model parameters between Rio Puerco subbasins, a calibration was performed with the aim to preserve two long-term statistical properties of streamflow records at gages 3340, 3405 and 3515 (independent basins): the long-term average annual runoff volume $\overline{Q}$ and the probability of zero daily flow p_o. As concurrent measurements of streamflow and radar data are not available for these basins, this was done by generating spatial rainfall with the RMS and adjusting rainfall-runoff model parameters in order to preserve $\overline{Q}$ and p_o at all three gages.

The common period of record 1952-1986 (n=35 years) was chosen as the reference period. The RMS model year consists of 256 days in the period February 12-October 25 (February 13 in a leap year). The average annual runoff in this period at the gages was: $\overline{Q}$=11.33 mil m^3/yr (3340), $\overline{Q}$=17.74 mil m^3/yr (3405) and $\overline{Q}$=9.35 mil m^3/yr (3515). The model year period contains on the average 93% of annual runoff measured at gages 3340 and 3405 and 89.7% at gage 3515 (see Table 2.7). The average annual probability of zero daily flow was p_o^y=0.432 (3340), p_o^y=0.427 (3405) and p_o^y=0.515 (3515). Average annual rainfall over the Rio Puerco Basin in the common record was P=280 mm, with a coefficient of variation equal to 0.23. With these rainfall parameters as input, series of 35 years of daily spatial rainfall were generated using RMS, aggregated over the

Upper Rio Puerco, Arroyo Chico and Rio San Jose watersheds (see Figure 2.3), and daily runoff at gages 3340, 3405 and 3515 was computed. A trial-and-error analysis was employed to find the best set of parameters that preserve $\overline{Q}$ and p_o.

It was found that in order to preserve p_o, the parameter $r_{\min}$=0; i.e., a=0, in all subbasins. Furthermore, it was found that modeling results were more sensitive to the parameter b than to k. Therefore k=1 day was used in all cases except for the wet season in the Upper Rio Puerco watershed where k=5 days was used (see radar calibration example). From generated data, the average calibrated parameters b were found to be b=0.0125 (3340), b=0.0073 (3405), b=0.0036 (3515). Notice the large difference from the radar calibration example for the 1997 wet season in the Upper Rio Puerco Basin. This shows the disadvantage of using one year of data for calibration, which in this case happens to be unseasonably wet.

The applicability of the rainfall-runoff model to individual Rio Puerco subbasins is limited by the parameter b. This parameter governs the transfer of rainfall to effective rainfall based on intensity alone. However, vegetation and soil properties also play an important role. For this reason, a relationship between the parameter b and the basin-averaged fraction of area with very low infiltration soils F derived from the STATSGO Database for the Rio Puerco Basin was developed. Data for the three calibration basin are plotted in Figure 4.20 together with a fitted function of the form:

$$b\,r^* = 0.9723\ F^{2.1167} \tag{4.44}$$

The parameter r^*=10 mm. The parameter F was estimated for every Rio Puerco subbasin and is reported in Chapter 2, Tables 2.1 and 2.2 (it ranges from 0.1 to 0.55). The choice of the function in (4.44) is quite arbitrary - a number of lines can be fitted through three points. Higher values of F mean less infiltration and greater basin runoff. This in turn requires a greater effective rainfall intensity and thus larger b. Most important is that Equation (4.44) allows the use of a varying rainfall-runoff parameter b throughout the Rio Puerco, based on subbasin soil properties.

The average annual runoff $\overline{Q}$ was preserved exactly in calibration and the resulting average annual probability of zero flow was p_o^y=0.575 (3340), p_o^y=0.543 (3405) and p_o^y=0.542 (3515). In general the rainfall-runoff model overestimates the average number of zero flow days in a year. Because the spatial random cascade generator is independent in space, there is no statistical difference between individual subbasins in the intermittency of daily rainfall. This results in similar values of average p_o. The rainfall-runoff model preserves well annual streamflow maxima.

In summary, the rainfall-runoff model is applied in this study as follows:

(1) Daily spatial rainfall generated by RMS is accumulated over each of the 25 Rio Puerco subbasins (Figure 2.3) and the average daily subbasin rainfall intensity r is computed. The parameter b is computed for each subbasin using Equations (4.44) and (4.41). Then the subbasin effective rainfall intensity r_e is computed using (4.33) and (4.34), and the total subbasin effective daily rainfall volume I is determined from Equation (4.39).

(2) The linear reservoir model is then employed to compute daily streamflow Q from each subbasin. The storage parameter is k=1 day for the wet season in all Rio Puerco subbasins. Dry seasons in the Middle and Lower Rio Puerco Basins are also modeled with k=1 day (Subbasins 1 to 10 and 1* to 9*, Figure 2.3), while the Upper Rio Puerco Basin is modeled with k=5 days and a constant runoff coefficient c=0.08 (Subbasins 10 to

13 and 10* to 12*, Figure 2.3). The constant runoff coefficient is the average data-derived estimate from Section 4.6.2.

In conjunction with the RMS, the rainfall-runoff model provides the required spatially and temporally variable streamflow inputs on a daily timescale from tributary subbasins: Q_t, t=1, ..., 13 and main stream subbasins Q_m, m=1, ..., 12, which are used in Chapter 5 for long-term erosion modeling.

Table 4.1. Precipitation ranges for the GHRC daily total rainfall accumulation and the median precipitation value assigned to each grid in this study. Note that Level 1 precipitation; i.e., range 0-25.mm, was assigned zero precipitation; and Level 12 precipitation; i.e., range > 127 mm, was assigned the lower limit 127 mm value in this study.

GHRC Level	Range [mm]	Median precipitation [mm]
1	0 - 2.5	0
2	2.5 - 5.1	3.8
3	5.1 - 10.2	7.7
4	10.2 - 15.2	12.7
5	15.2 - 20.3	17.8
6	20.3 - 25.4	22.9
7	25.4 - 38.1	31.8
8	38.1 - 50.8	44.5
9	50.8 - 76.2	63.5
10	76.2 - 101.6	88.9
11	101.6 - 127	114.3
12	> 127	127

Table 4.2. Comparison of random cascade parameters for the spatial model estimated from observations in the test period June 3, 1997 - June 15, 1997, and from generated data. For each day, 100 spatial fields were generated and the simulation mean is listed together with its coefficient of variation (in parentheses).

Day in June 1997	β	β Generated	σ^2	σ^2 Generated	R [mm]	R Generated [mm]
5	0.205	0.206 (0.14)	0.059	0.050 (0.26)	1.40	1.53 (0.46)
6	0.042	0.044 (0.29)	0.043	0.040 (0.15)	5.06	4.93 (0.24)
7	0.008	0.008 (0.55)	0.027	0.026 (0.15)	23.33	23.46 (0.16)
8	0.037	0.036 (0.27)	0.046	0.042 (0.19)	10.50	10.19 (0.21)
9	0.320	0.334 (0.16)	0.032	0.029 (0.29)	0.35	0.34 (0.53)
10	0.799	0.778 (0.11)	0.008	0.008 (0.65)	0.002	0.004 (0.79)
11	1		0		0	
12	0.125	0.129 (0.18)	0.074	0.061 (0.16)	3.37	3.35 (0.38)
13	0.143	0.146 (0.17)	0.050	0.044 (0.20)	2.07	2.05 (0.34)
14	1		0		0	
15	0.172	0.175 (0.13)	0.075	0.062 (0.21)	2.67	2.76 (0.37)

Table 4.3. Comparison of random cascade parameters for the temporal model estimated for the 1996 and 1997 dry and wet season NEXRAD radar data, generated series and station-derived data. For each season, 100 daily rainfall fields were generated and the simulation mean is listed together with its coefficient of variation (in parentheses). R_{season} gives the seasonal precipitation total and R_{max} gives the daily maximum recorded or generated in every season.

Seasons:	DRY 1996	WET 1996	DRY 1997	WET 1997
NEXRAD				
β	0.115	0.030	0.113	0.051
σ^2	0.174	0.100	0.157	0.155
R_{season} [mm]	9.2	126.5	140.4	363.7
R_{max} [mm]	5.2	6.4	23.3	29.7
GENERATED				
β	0.126 (0.53)	0.031 (1.01)	0.124 (0.52)	0.051 (0.75)
σ^2	0.118 (0.34)	0.082 (0.35)	0.110 (0.36)	0.111 (0.34)
R_{season} [mm]	9.2 (0.45)	126.5 (0.27)	139.5 (0.43)	364.3 (0.37)
R_{max} [mm]	0.6 (0.56)	4.1 (0.38)	8.6 (0.56)	16.6 (0.49)
CLIM. STATION				
β	0.347	0.064	0.143	0.087
σ^2	0.136	0.119	0.116	0.191
R_{season} [mm]	23.8	212.9	117.8	228.3
R_{max} [mm]	3.7	12.6	11.9	26.8

Table 4.4. Parameters of the linear dependence disaggregation model estimated for Rio Puerco from the period 1948-1997.

MEAN	
Annual total, x [mm]	289.52
Dry season, y_1 [mm]	67.78
Wet season, y_2 [mm]	157.29
y_3 [mm]	64.45
PARAMETERS	
a_1	0.249007
a_2	0.458085
a_3	0.292908
b_{11}	22.24251
b_{21}	-20.43860
b_{31}	-1.80391
b_{22}	21.50586
b_{32}	-21.50586

Table 4.5. An example of the performance of the RMS with input parameters P=300 mm, coefficient of variation C_v=0.25 and n=100 years. Precipitation values are averages in milimeters. $R_{d,w}$ are seasonal totals. R_{max} after the temporal cascade is the mean of the maximum observed spatially averaged daily precipitation in each season. R_{max} after the spatial cascade is the mean of the maximum observed cell rainfall in the studied domain in each season.

ANNUAL SERIES GENERATION	AFTER DISAGGREGATION	AFTER TEMPORAL CASCADE	AFTER SPATIAL CASCADE
$P = 303.0$ $C_v = 0.23$ $r(1) = 0.07$	$P = 303.2$ $C_v = 0.23$ $r(1) = 0.08$	$P = 310.0$ $C_v = 0.33$ $r(1) = -0.11$	$P = 309.9$ $C_v = 0.32$ $r(1) = -0.11$
Seasons :	$R_d = 70.4$ (0.41)* $R_w = 162.9$ (0.26)	$R_d = 70.3$ (0.64)* $R_w = 169.9$ (0.45)	$R_d = 70.2$ (0.63)* $R_w = 169.8$ (0.44)
Maxima :		$R_{d,max} = 5.2$ (0.60) $R_{w,max} = 8.6$ (0.48)	$R_{d,max} = 193.7$ (0.27) $R_{w,max} = 259.1$ (0.28)

* Coefficient of variation of the estimate.

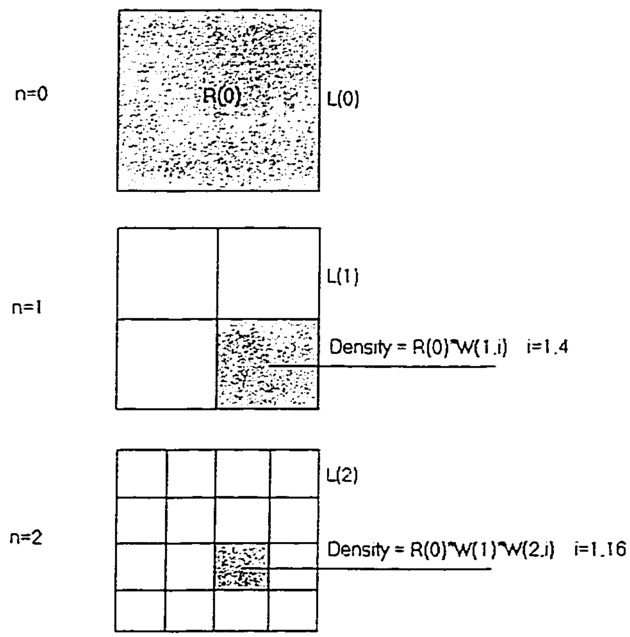

Figure 4.1. Schematic of a two-dimensional random cascade with branching number *b*=4.

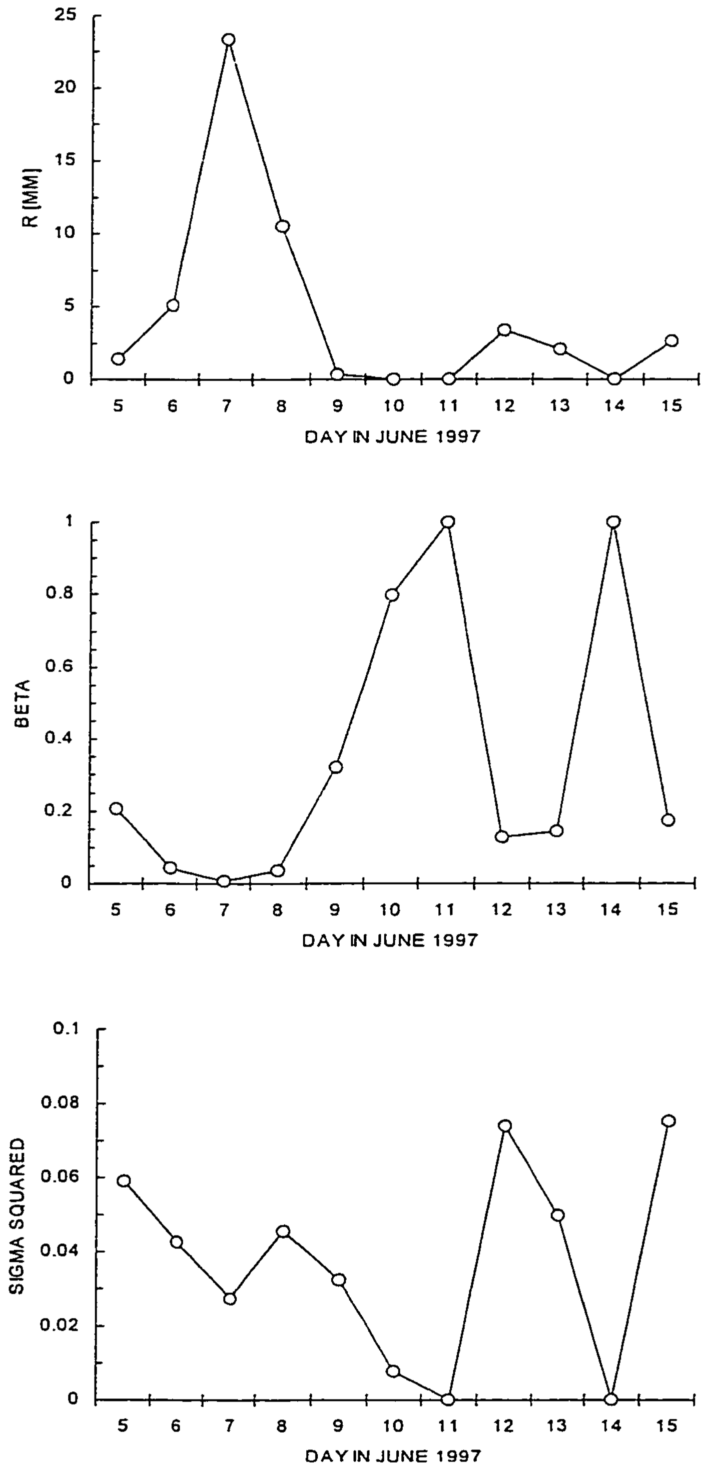

Figure 4.2. Mean spatial rain rate R and parameters β and σ^2 of the spatial random cascade model estimated for the test period June 3, 1997 - June 15, 1997.

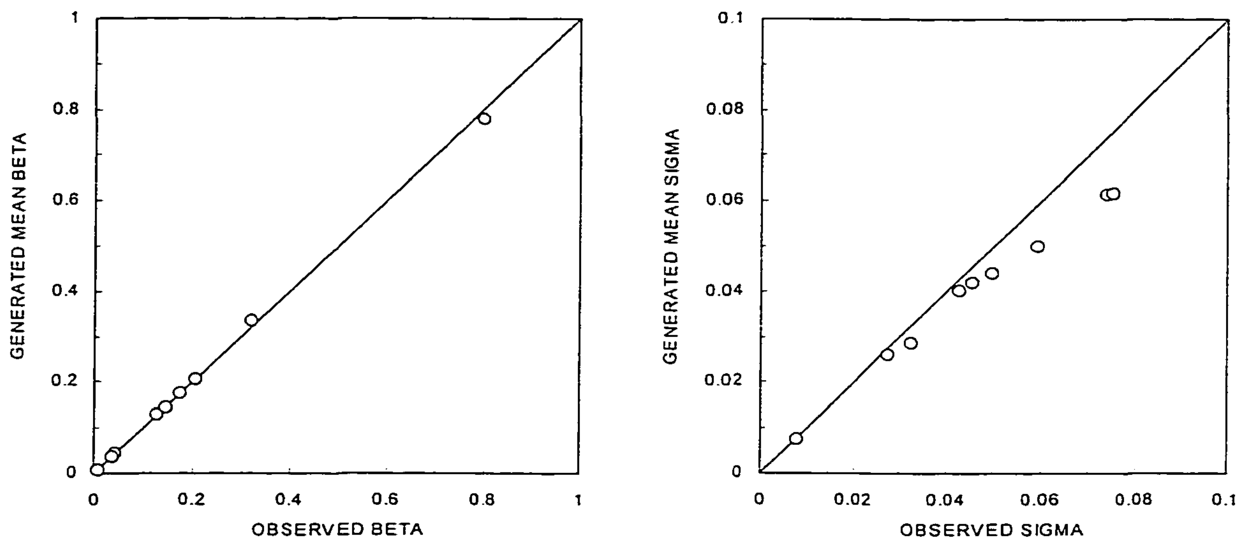

Figure 4.3. Comparison of data-derived estimates of β and σ^2 with generated values using the random cascade model for the test period June 3 - June 15, 1997. Generated values are means computed from 100 realizations of the random cascade model.

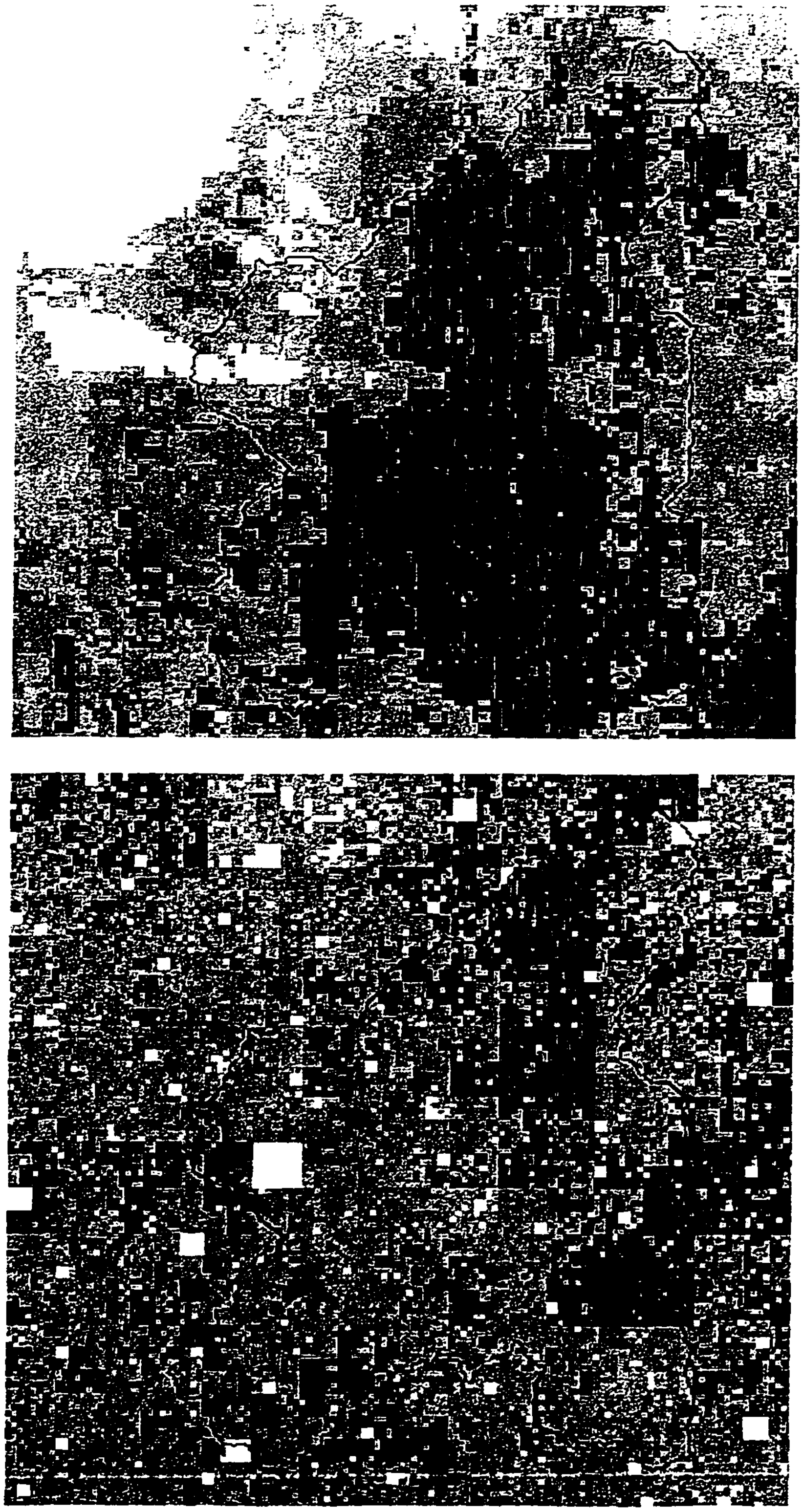

Figure 4.4. Observed (top) and a randomly chosen generated scan (bottom) with parameters identical to those estimated from observations for June 7, 1997. Rainfall data are grouped into categories according to the GHRC standard in Table 4.1. Darker colors indicate higher rainfall intensity.

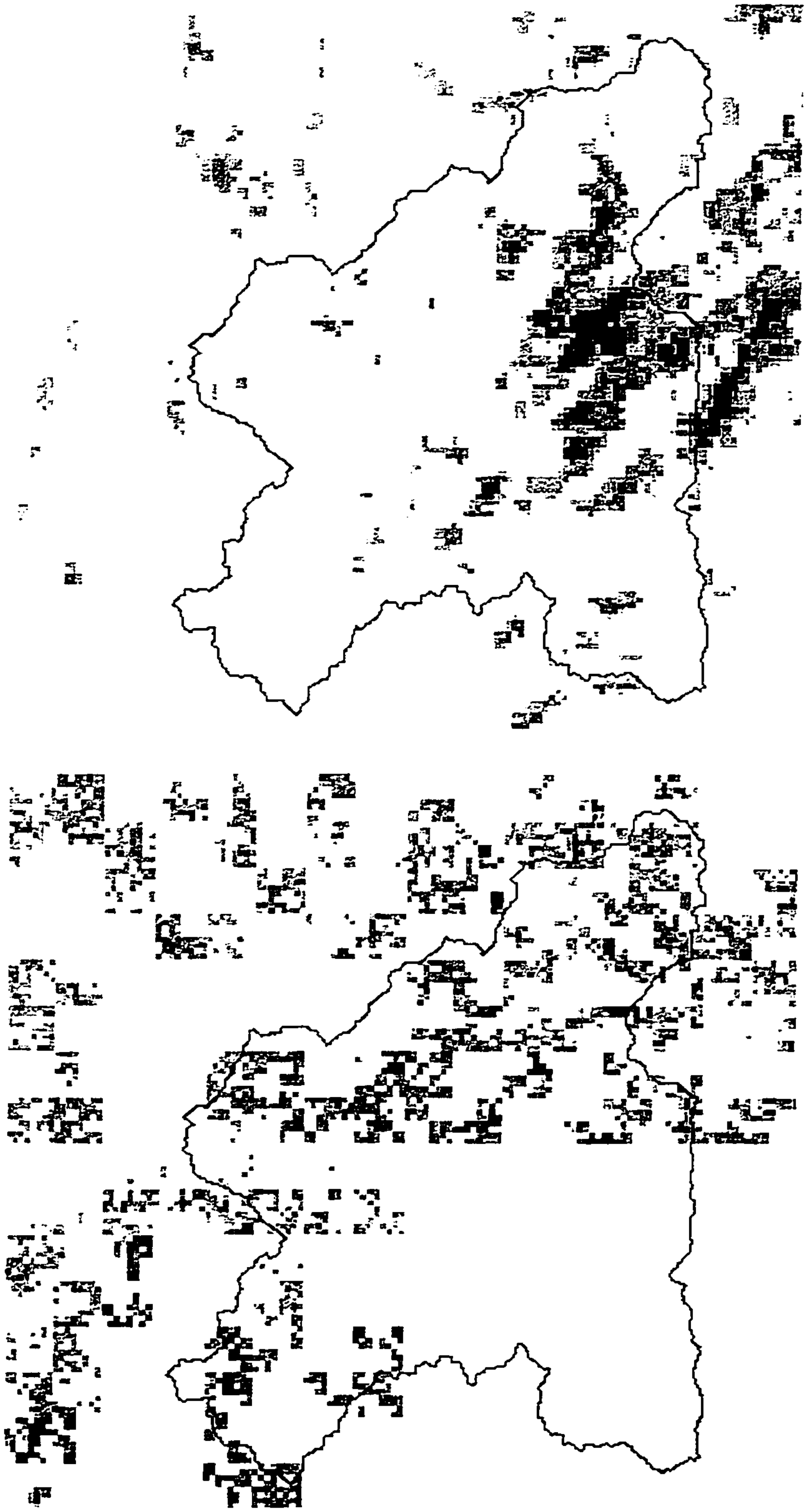

Figure 4.5. Observed (top) and a randomly chosen generated scan (bottom) with parameters identical to those estimated from observations for June 15, 1997. Rainfall data are grouped into categories according to the GHRC standard in Table 4.1. Darker colors indicate higher rainfall intensity.

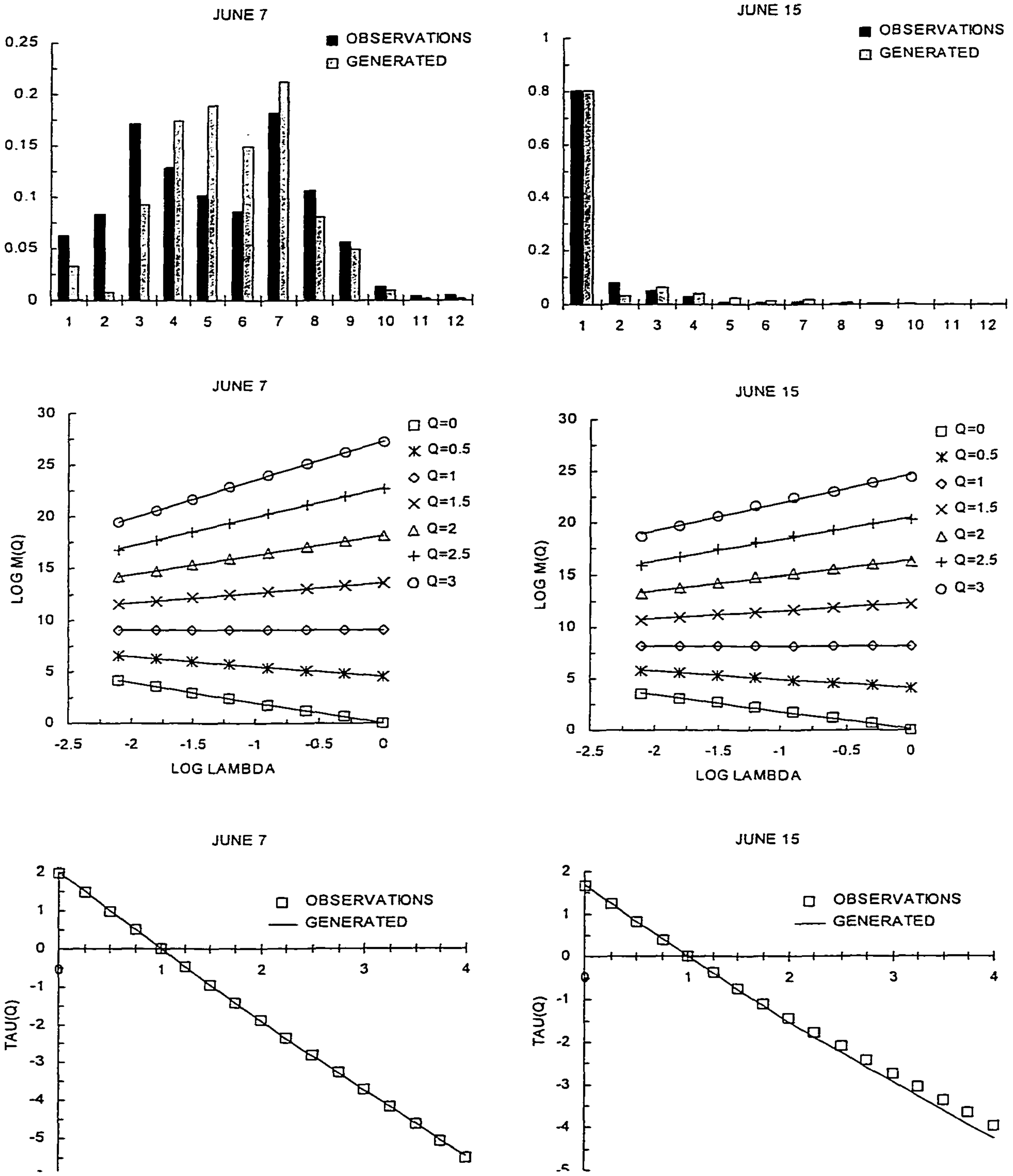

Figure 4.6. Examples of the data-derived and generated histograms (top), moment scaling relationships (center) and $\tau(q)$ functions (bottom) for two spatial scans - June 7 and June 15, 1997.

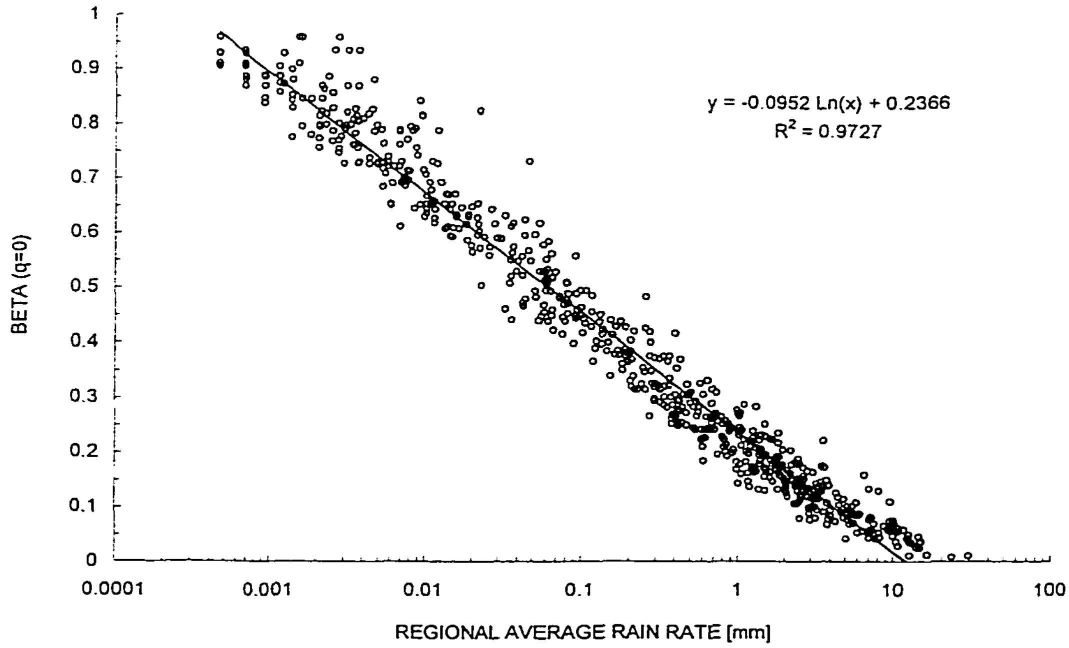

Figure 4.7. The dependency of the spatial cascade parameter β on the spatial average rain rate R for Rio Puerco NEXRAD data, the so-called large scale forcing relationship.

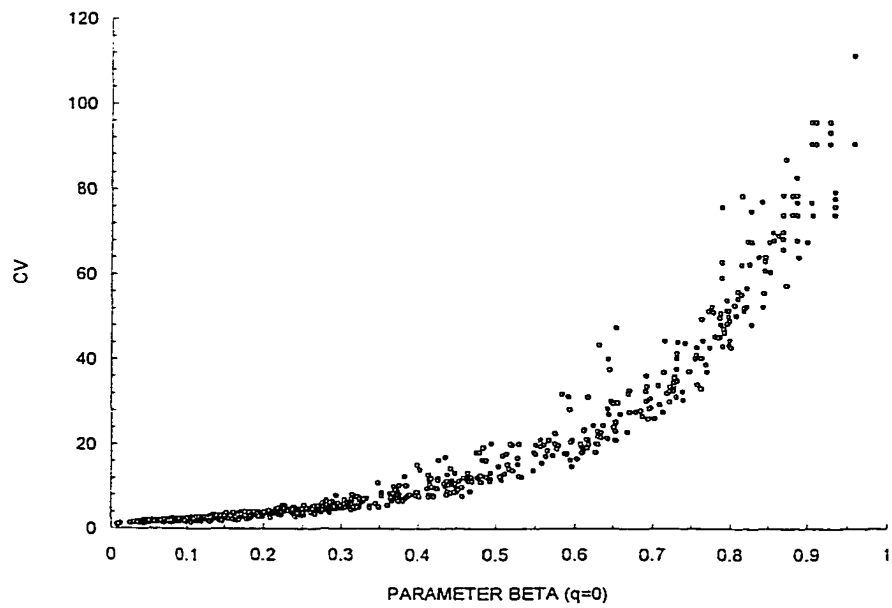

Figure 4.8. The spatial coefficient of variation of rainfall mass at the fine NEXRAD grid scale (1750×1750 m) as a function of the cascade parameter β.

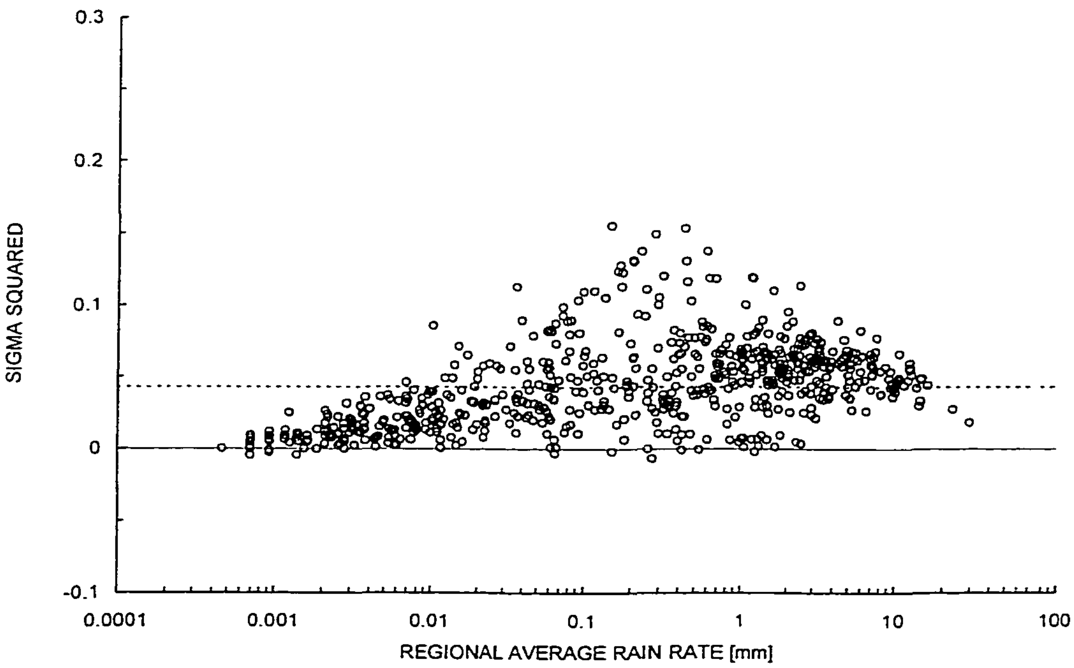

Figure 4.9. The spatial cascade parameter σ^2 estimated from Rio Puerco NEXRAD data. The dashed line shows the average σ^2=0.043, computed only for $\sigma^2 \geq 0$.

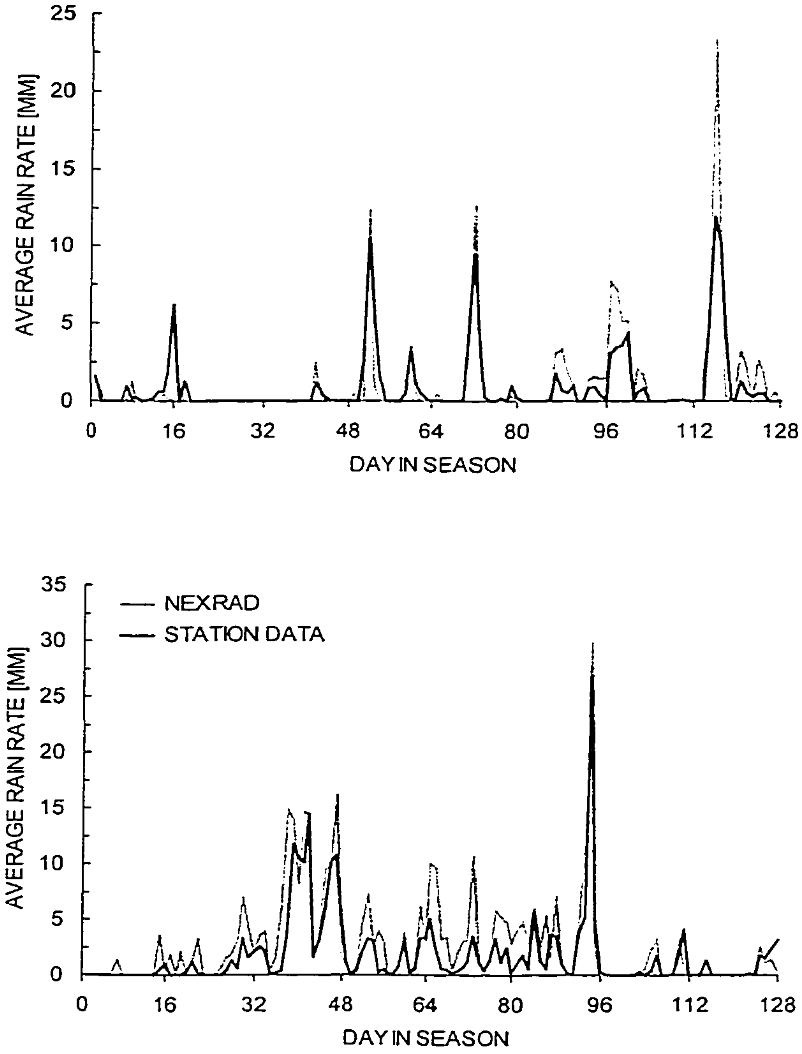

Figure 4.10. Comparison of radar-derived and station-derived average spatial rainfall rate for the Rio Puerco region for the 1997 dry season (top) and wet season (bottom).

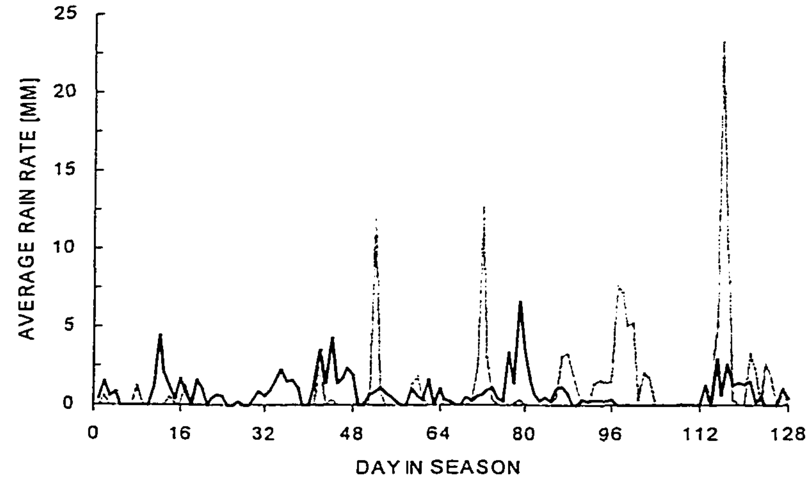

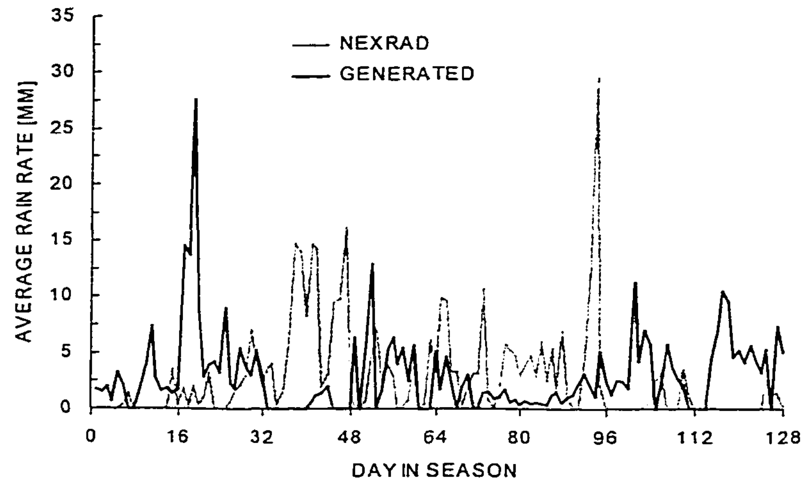

Figure 4.11. Example of radar-derived and randomly chosen generated average daily rainfall series for the Rio Puerco region with parameters estimated from the 1997 dry season (top) and wet season (bottom).

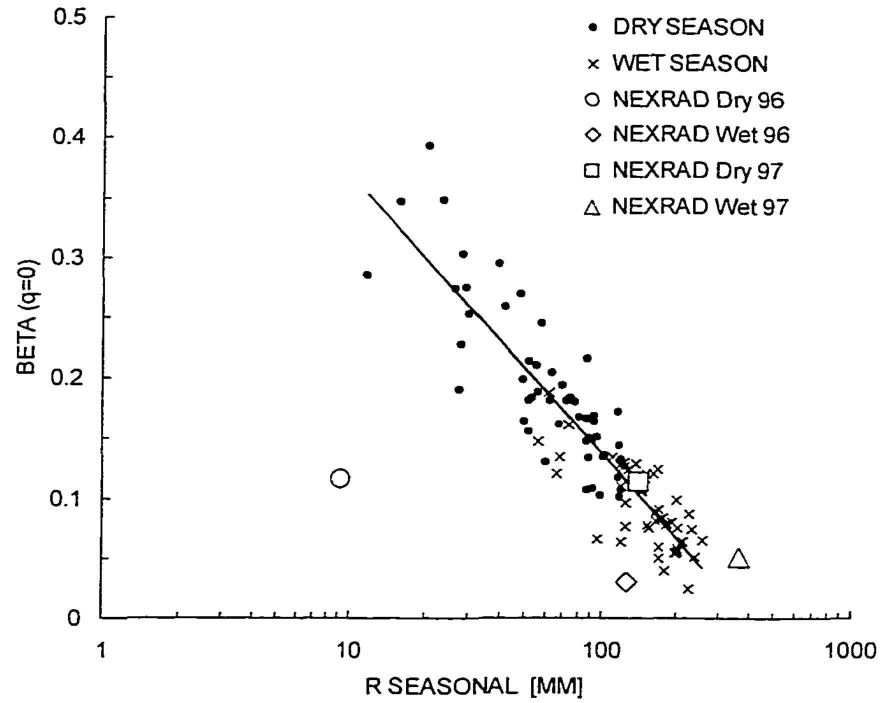

Figure 4.12. Relationship between the random cascade parameter β and the seasonal precipitation total R_{season} estimated from station-derived average daily precipitation for the Rio Puerco for the period 1948-1997. Large markers indicate NEXRAD-estimated values.

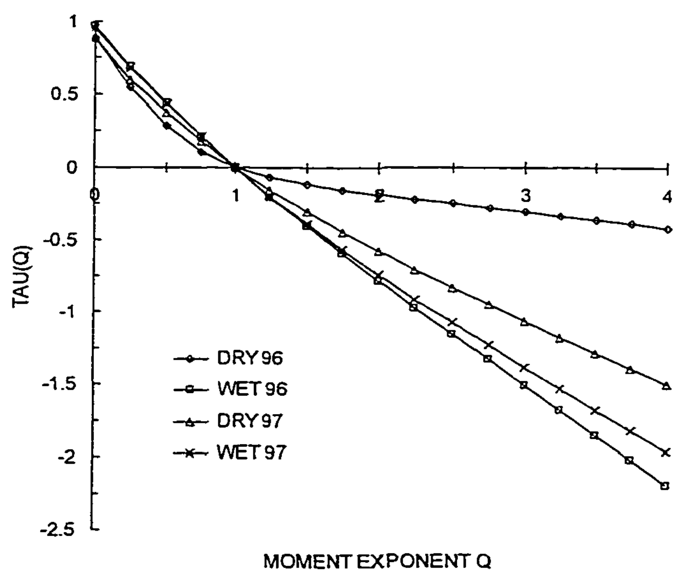

Figure 4.13. Estimated $\tau(q)$ functions for NEXRAD data 1996 and 1997 dry and wet seasons.

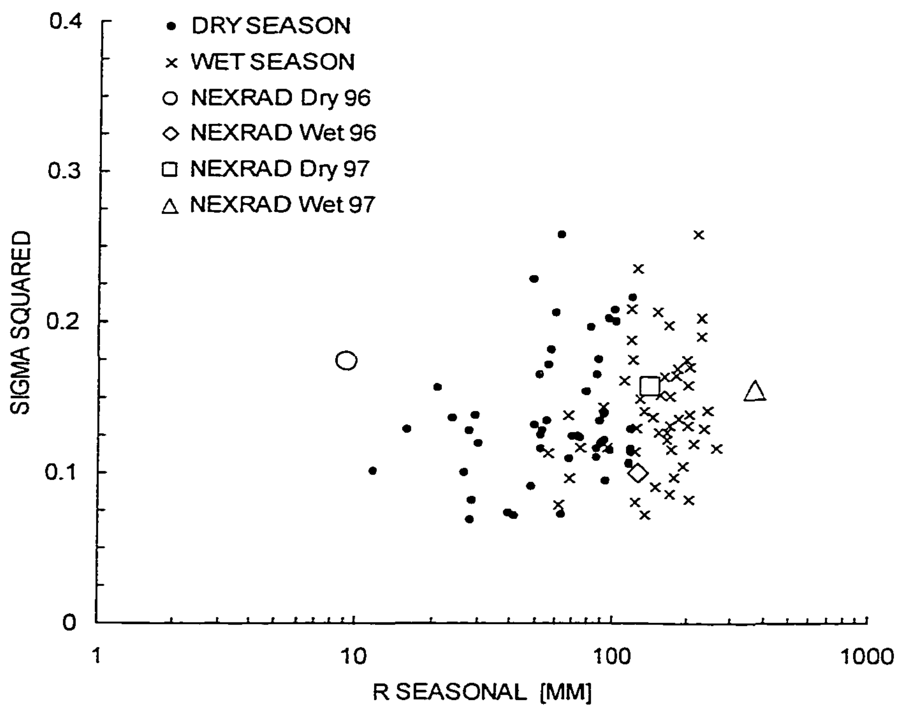

Figure 4.14. Relationship between the random cascade parameter σ^2 and the seasonal precipitation total R_{season} estimated from station-derived average daily precipitation for the Rio Puerco for the period 1948-1997. Large markers indicate NEXRAD-estimated values.

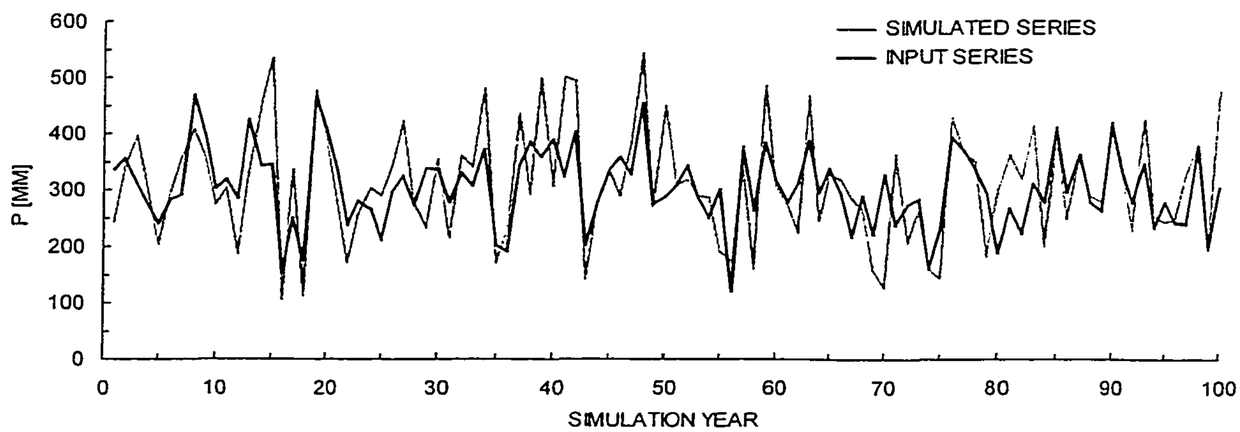

. **Figure 4.15.** Example of an input series and RMS-simulated series of Rio Puerco annual precipitation with mean P=300 mm, and coefficient of variation C_v=0.25.

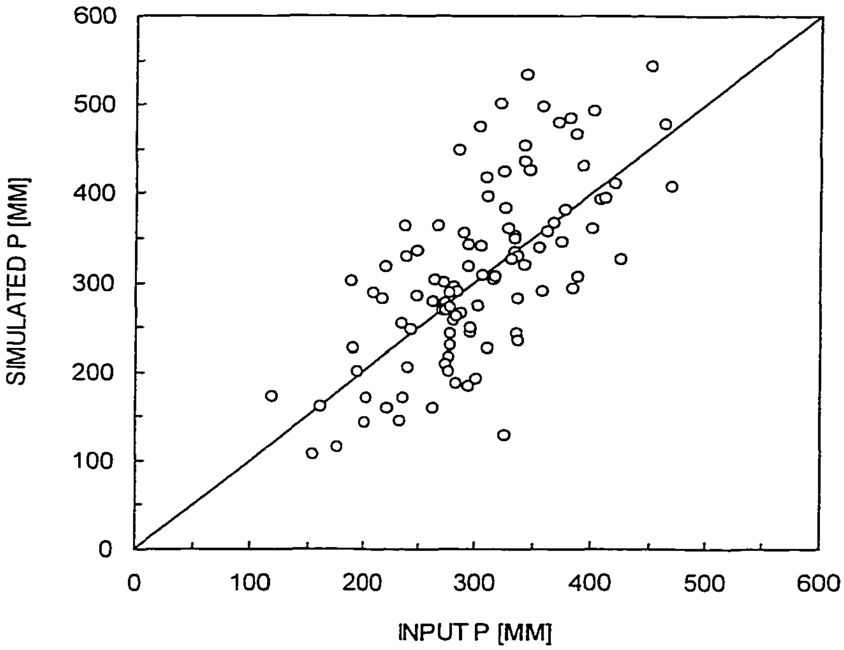

Figure 4.16. Relationship between input and simulated annual precipitation totals *P* for the case in Figure 4.15.

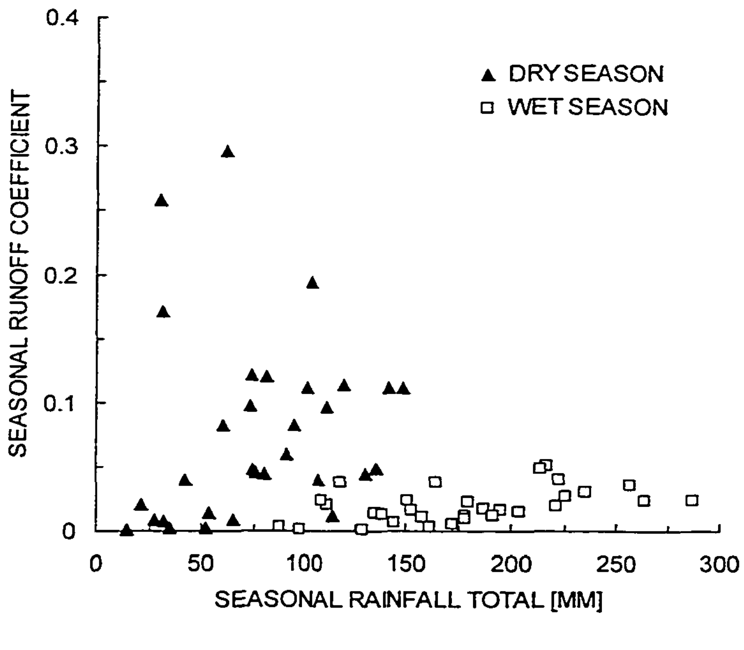

Figure 4.17. Seasonal runoff coefficient for the Upper Rio Puerco Basin computed from climate station data (Torreon and Cuba) and gage 3340 for the period 1961-1996 (5 years with more than 30 days of daily rainfall and/or streamflow estimated or missing were not included in the analysis).

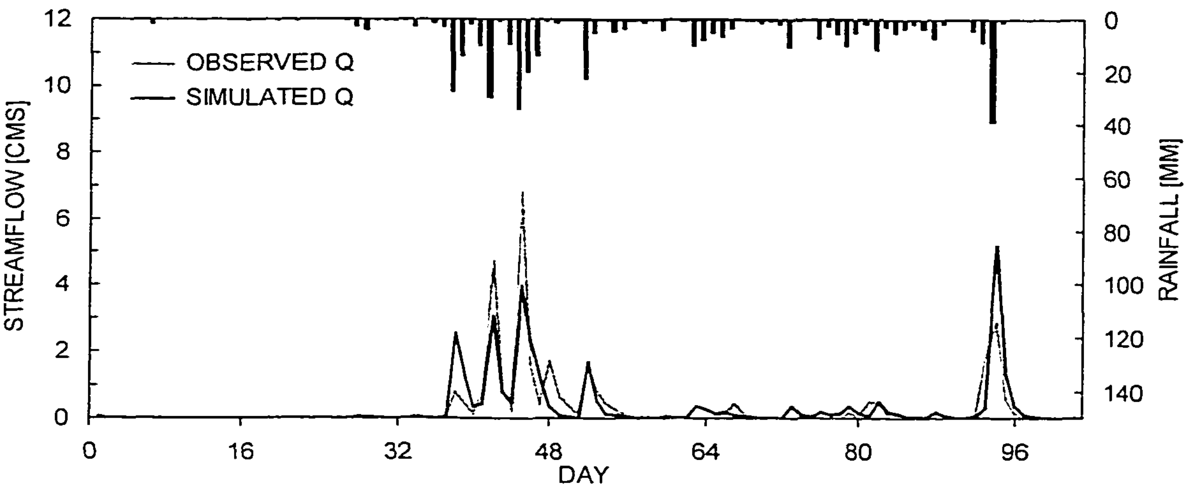

Figure 4.18. Calibration of the rainfall-runoff model for the wet season 1997. Only 103 days (out of 128) with data are available. Rainfall is effective rainfall obtained with c^*=0.0034 and r_{min}=0 mm. The calibrated linear reservoir parameter k=0.858 days.

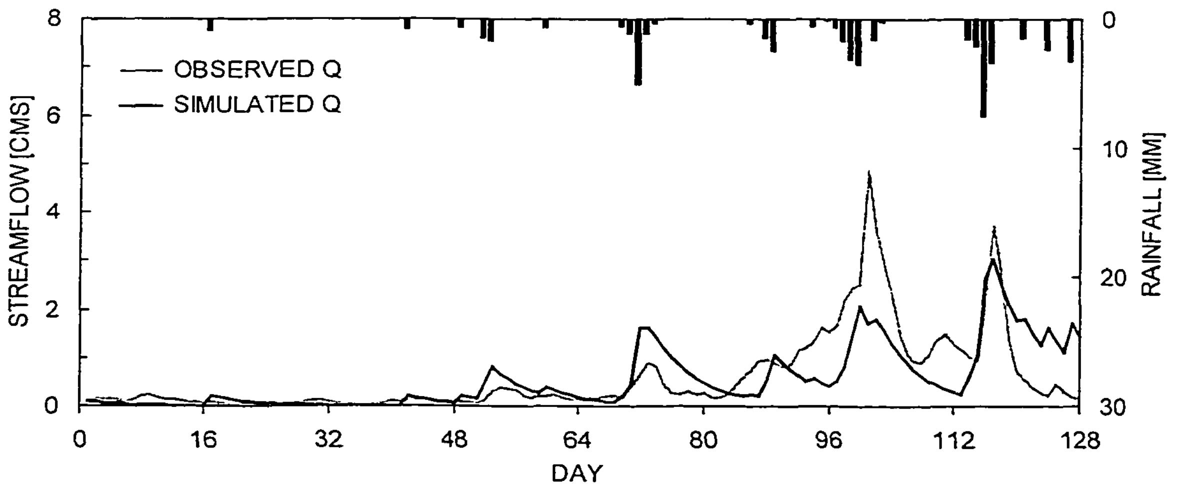

Figure 4.19. Calibration of the rainfall-runoff model for the dry season 1997. Rainfall is effective rainfall obtained with a constant runoff coefficient c=0.1088. The calibrated linear reservoir parameter is k=5.55 days.

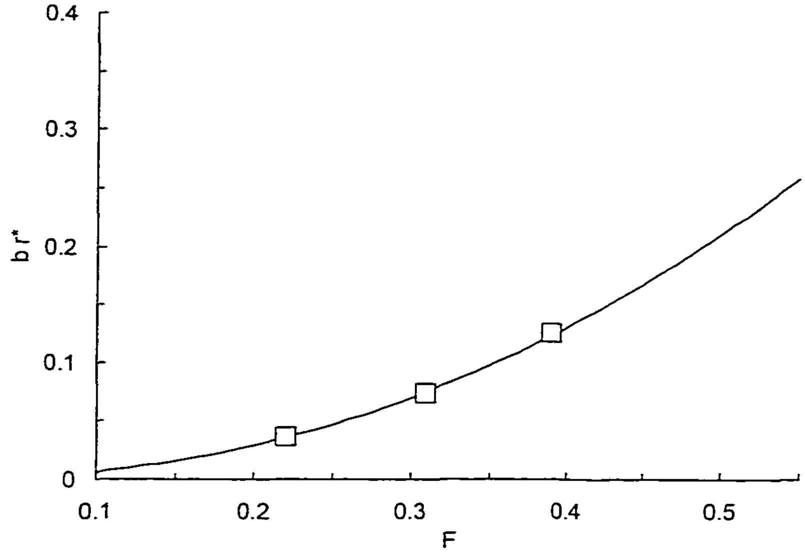

Figure 4.20. Relationship between the soil infiltrability parameter F and the rainfall-runoff model parameter $c^* = b\, r^*$. Markers give the San Jose, Arroyo Chico and Upper Rio Puerco Basin data (from left to right).

5 Erosion Modeling

Numerous experimental flume and modeling studies of aggradation and degradation have been reported in the hydraulic research literature. They are mostly applied to very specific and/or small scale problems, such as changes in braided river morphology (Germanoski and Schumm 1993), small gully morphology (Sidorchuk and Sidorchuk 1998), sediment overloading (Soni et al. 1980, Park and Jain 1986), water withdrawal (Kerssens and van Urk 1984), analyses of the transient nature of sediment waves and unsteadiness of flow (Ponce et al. 1979, Morse and Townsend 1989, Bhallamudi and Chaudry 1991, Yen et al. 1992), and model comparisons and improvements (Jaramillo and Jain 1984, Lu and Shen 1984, Correia et al. 1992, Saiedi 1997, Habersack 1998). Most modeling studies of erosion and deposition in river basins concentrate on short-term or event-based conditions (e.g., Wiele et al. 1996) or on small watershed scales in a distributed form (e.g., Smith et al. 1995).

Modeling studies of channel change similar in the spatial and temporal scale to this study were used to study the effects of water management scenarios on the Missouri River (Holly and Karim 1986), controlled outflow downstream of the Cochiti Dam on the Rio Grande River (Mengis 1981), hydroclimate variability on the extension of a river network and basin denudation rates (Tucker and Slingerland 1997), channel type on the magnitude, type and timescales of channel adjustment (Howard et al. 1994). However, modeling analyses generally concentrate on perennial streams, and analyses of ephemeral streams (e.g., Renard and Laursen 1975, Ruff et al. 1986, Topping 1997) are infrequent because of the complexity involved and the lack of data.

Mathematical models of alluvial streams route water and sediment through channels with erodible beds. In general, there are four elements that need to be considered in channel erosion modeling: (1) conservation of momentum (energy) for streamflow; (2) water and sediment continuity; (3) channel resistance; and (4) sediment transport (e.g., Dawdy and Vanoni 1986). In terms of model structure, it is necessary to select the (*a*) dimensionality of the model; (*b*) steadiness of flow; (*c*) coupling of water and sediment relations; and (*d*) solution scheme. The degree of complexity and detail in the elements and structure of the final model should depend on the temporal and spatial scale of the problem that is being solved, as well as on the properties of the modeled watershed and river system.

Numerous channel erosion models are currently used in engineering practice and scientific investigations (HEC-6: HEC 1977; IALLUVIAL: Karim and Kennedy 1982; FLUVIAL: Chang 1982; GSTARS: Molinas and Yang 1984; KINEROS: Smith et al. 1995; CHILD: Tucker and Slingerland 1997; and many others). For a good review see IACWD (1988). However, none of these models are well suited to simulate long-term channel erosion under highly variable precipitation and resulting ephemeral and intermittent flow conditions such as occur in the Rio Puerco Basin. For this reason a new channel erosion model, ERMO, is developed in this study in Section 5.2 with three important characteristics: (1) a hydraulic routine based on water continuity and a sediment routine based on transport-capacity-driven sediment continuity; (2) few governing parameters, which allows for a clear interpretation of the causes and effects of channel change; and (3) adaptability to ephemeral and intermittent flow conditions and connection to the RMS and rainfall-runoff modeling systems described in Chapter 4.

The long timescale and large spatial scale of application govern ERMO structure: the model is one-dimensional with changes to width allowed; steady at the daily timescale; the water and sediment relations are fully decoupled; and a finite difference solution method is used. The accuracy of sediment transport is essential. ERMO uses a Rio Puerco data-derived bedload sediment rating curve (Section 5.1) to determine sediment transport rates. The model is used to study the longitudinal distribution of channel change and cross-sectional erosion profiles (Section 5.3.2), the influence of streamflow (Section 5.3.3) and streambed infiltration (Section 5.3.4) on maximum deposition and erosion depths and erosion dynamics in general, and the effect of a changing climate (Section 5.4) on channel erosion in the Rio Puerco main stream.

In addition to modeling long-term channel change, a short-term analysis is conducted to study erosion dynamics in the vicinity of tributary junctions (Section 5.5). This task is accomplished by another model developed here - the aggradation/degradation model GRAD. This model contains additional elements to ERMO: a conservation of energy equation for streamflow; a channel resistance formulation; and a theoretical bedload sediment transport relation.

Channel erosion modeling on the Rio Puerco in this Chapter emphasizes the dynamic nature of channel change in the stream system; in particular, the roles played by the spatial and temporal variability of rainfall and runoff, extremely wet years/events, and transmission losses.

5.1 Rio Puerco Sediment Load

Rio Puerco is known for extremely high sediment loads. Instantaneous suspended sediment concentrations exceeding 20% in volume have been observed (e.g., Nordin 1963). These hyperconcentrations rate the Rio Puerco among the world's top sediment-carrying streams. Because of the high sediment load and the noncohesive nature of the sand-sized bed and bank material, the Rio Puerco is subject to considerable and rapid channel changes. In this section, suspended sediment transport is analyzed from available data and the amount of bedload is estimated. A sediment rating curve is developed for use in the channel erosion model.

5.1.1 Data and Sediment Sources

Analyses of sediment transport in the Rio Puerco have been few. Most notable is the work of Nordin (1963), who studied the effects of high suspended sediment concentrations on particle settling velocities and the transport of sands in the vicinity of the Bernardo gage (3530). Other analyses were generally concerned with the long-term sediment balance, trends and/or delivery to the Rio Grande River (e.g., Gellis 1991, Gorbach et al. 1996). A crucial problem was (and is) the lack of good quality data. Only streamflow gaging stations 3340, 3405 and 3530 have sufficiently long records of point measurements of sediment in suspension that are used to infer daily average sediment concentration. At present only gages 3340 and 3530 are in operation.

In the past, daily samples were collected by an observer, with additional samples taken at irregular intervals (during more intense runoff events) by USGS professional staff. In 1981, an automatic suspended sediment sampler was installed at gage 3340 and in 1995 at gage 3530 on the Rio Puerco main stream. Average daily suspended sediment concentrations in mg/l are evaluated according to standard USGS procedures (Edwards and Glyson 1988). Daily streamflow and sediment concentration data are available from the WATSTORE Database (webserver.cr.usgs.gov/sediment/content.html). According to the data provider, data quality is considered generally to be fair to good. In this study, data up to 1995 (inclusive) were analyzed. Table 5.1 gives the record periods and the lengths of records of the three analyzed gages.

According to Happ (1948) and others, sources of sediment in the Rio Puerco are mainly from the bed and banks of the channel system (40%), tributary contribution (30%) and overland flow and minor gully erosion (30%). In the headwater basins, sheetwash is generally the primary sediment source (Leopold et al. 1966). The average annual suspended sediment load measured at the outlet of the Basin is about 3.46 million T/yr, or 1.31 million m^3/yr. This amounts to about 60-80% of the total sediment load of the Rio Grande River downstream.

5.1.2 Suspended Load

Because of the abundance of fine (silt and clay) sediment in the Rio Puerco Basin, most of the sediment in transport is in suspension; i.e., not in contact with the streambed. USGS analyses of the particle size of suspended sediment at the Bernardo gage from the period 1986-1992 give d_{50}=0.002 mm (coarse clay) and d_{90}=0.023 mm (medium silt). This means that bed material, with D_{50}=0.125 mm and D_{10}=0.0625 mm (see Chapter 2), is rarely in suspension.

Some properties of suspended sediment records at gages 3340, 3405 and 3530 are listed in Table 5.1. In these analyses, only days with measured sediment concentration $C>0$ were included; estimated values were discarded. Note that the average daily sediment concentration is greatest at the Bernardo gage (3530). The recorded average daily maximum is also greatest here, C=269,000 mg/l. The Bernardo gage has the longest (37.2 years) and most reliable (least estimated values) record.

There are four elements that affect sediment transport in a stream: (1) hydraulic properties of flowing water (e.g., velocity, depth, turbulence); (2) channel properties (e.g., channel slope, planform structure, geology); (3) sediment properties (e.g., particle size, distribution, cohesion); and (4) the availability of sediment. In the Rio Puerco, there is abundant sediment supply and sediment transport is driven by transport capacity. Under transport-capacity-driven conditions, a sediment rating curve lumps the hydraulic, channel and sediment properties into a simple sediment load-discharge relationship at a single cross section.

Here daily sediment rating curves were developed for the analyzed gaging stations. Specific suspended sediment discharge q_s was related to specific water discharge q in the form:

$$q_s = a\, q^b \tag{5.1}$$

where q_s and q are in m^2/s, and a and b are parameters. To avoid spurious correlation, the determination of a and b was conducted by linear regression on volumetric sediment concentration C_v rather than sediment discharge (Julien 1995):

$$C_v = \frac{q_s}{q} = a\, q^{b-1} \tag{5.2}$$

where C_v is $C_v = C$ mg/l / (10^6 G) and G is the specific gravity of sediment (G=2.65).

Figure 5.1 shows the suspended sediment rating curves for stations 3340, 3405 and 3530. In determining specific discharge, each cross section was assumed to be rectangular, with the following representative channel width: 3340 W=25 m (Elliott 1979), 3405 W=15 m (measured by Molnar), and 3530 W=7 m (measured by Molnar). The data points in the figure are averages of 50 individual sorted measurements. It is noteworthy that although there are significant differences in the sediment rating curves at lower q, the curves seem to converge for q>0.1 m^2/s. The Bernardo gage is used as the representative site in this study with the widest range of q, and the relationship developed for gage 3530 is used to describe the suspended sediment rating curve in the Rio Puerco main stream system:

$$q_s = 0.0356\, q^{1.2098} \tag{5.3}$$

with R^2=0.6829 (least squares regression on log-transformed data was used). Figure 5.2 shows the scaling of the variance of C_v with q at gages on the Rio Puerco main stream. It appears that the variability of sediment concentration for q<0.1 m^2/s is quite random, whereas for q>0.1 m^2/s there is a notable increase in variability with increasing q. This again points to the fact that suspended sediment transport is capacity limited in Rio Puerco conditions.

An advantage in hyperconcentrated flows is also that point samples (taken by the automated sampler) are generally better representative of a vertically averaged sediment concentration profile than in less concentrated flows. This is because suspended sediment is more uniformly distributed in the streamflow profile as a result of the decrease in sediment settling velocity in hyperconcentrated flows (Nordin and Dempster 1963, Nordin 1963).

5.1.3 Bedload

In the Rio Puerco, there are no continuous measurements of bedload available, so it is necessary to employ the suspended sediment rating curve in estimating bedload. The transport rate of *bedload*; i.e., material that is in immediate contact with the streambed and is transported by saltating and rolling, is generally less than that of suspended load. If we take the fraction of total load q_t transported in suspension to be equal to

$$\frac{q_s}{q_t} = B \tag{5.4}$$

with $0<B<1$, then bedload q_b is proportional to suspended load as

$$q_b = \gamma q_s \qquad \text{where} \qquad \gamma = \frac{1-B}{B} \tag{5.5}$$

with $\gamma>0$ being the *bedload parameter*.

Theoretical and empirical analyses show that the parameter B is a function of hydraulic as well as sediment properties. For example, Figure 5.3 shows B as a function of the ratio of bed shear velocity to sediment settling velocity u^*/ω according to the theoretical developments of Van Rijn (1984b) together with data of Guy et al. (1966) from flume experiments. As the ratio u^*/ω increases and/or the sediment size decreases, there is more sediment in suspension, causing an increase in B. Notice that for $u^*/\omega>6$, B approaches 1 (i.e., almost all sediment is in suspension). I determined the ratio u^*/ω for the Bernardo gage assuming normal flow conditions, channel bed slope S=0.0012 and channel bed surface roughness equal n=0.02 (Mannings coefficient), as follows. Average bed shear velocity for normal uniform flow can be estimated as:

$$u_* = \sqrt{g\, y_n\, S} \tag{5.6}$$

with normal depth y_n equal

$$y_n = \left[\frac{nq}{S^{0.5}}\right]^{3/5} \tag{5.7}$$

and the settling velocity in sediment laden flow ω is approximately equal to (Richardson and Zaki 1954, Cheng 1997):

$$\omega = (1 - C_v)^k\, \omega_c \tag{5.8}$$

where k is a parameter k>1. In (5.8) ω_c is the sediment particle settling velocity in clear water estimated for a particular representative particle size d_s from (Julien 1995):

$$\omega_c = \frac{8\nu}{d_s}\left(\sqrt{1 + 0.0139\, d_*^{\,3}} - 1\right) \tag{5.9}$$

where ν is the kinematic viscosity ($\nu = 1 \times 10^{-6}$ m^2/s for 20°C water) and d_* is a dimensionless particle diameter:

$$d_* = d_s\left[\frac{(G-1)g}{\nu^2}\right]^{1/3} \tag{5.10}$$

Taking k=8 (an estimate for the highly sediment-loaded rivers in China, Yang 1996) and $d_s = d_{90}$=0.023 mm for the Rio Puerco suspended sediment, we get the relationship between $u*/\omega$ and q shown in Figure 5.4. It is evident that $u*/\omega >> 6$, and then according to Figure 5.3 B is assumed to be equal to 0.95 and γ=0.053. This means that in the Rio Puerco, bedload constitutes only about 5% of the total sediment load. Other analyses also confirm that the Rio Puerco bedload does not exceed 10% of the total load (Gorbach et al. 1996).

It is also noteworthy that in sediment-laden flows settling velocity is considerably smaller than in clear water. Nordin (1963) argued that in the Rio Puerco, extremely high suspended sediment concentrations decrease settling velocities and affect the vertical distribution of flow velocity, dampen turbulence of flow and can result in an increased ability of the flow to carry sand-sized particles. These issues of the hydraulics of hyperconcentrated flow are an important avenue for further research.

5.2 Development of the Erosion Model ERMO

The Erosion Model ERMO is designed to simulate changes in channel depth and width in an ephemeral stream system driven by spatially and temporally variable runoff on long, decadal timescales. ERMO models channel change in the main stream (trunk) of the river system driven by the sediment transporting capacity of the stream: it is assumed that there is abundant supply of sediment available. ERMO is a one-dimensional model that consists of fully decoupled hydraulic and sediment components solved by an explicit finite difference method. The model is one dimensional, but allows for changes in channel width.

In ERMO, sediment transport is modeled by the bedload sediment rating curve that is developed for Rio Puerco conditions (Section 5.1.3). Armoring and the separation of sediment load into size fractions were not considered in ERMO, because they are not widely present and/or their effect on long-term channel dynamics is insignificant. In terms of the water component, ERMO is driven by hydrographs consisting of steady state daily flows. Daily runoff is simulated at the outlet of each Rio Puerco subbasin according to the procedure in Chapter 4, and it is the driving input into ERMO. The model simulation runs in general consist of n=100 years.

Although ERMO is simpler than most of its counterparts in hydrologic literature (e.g., IACWD 1988), together with RMS it is specifically designed to model long-term channel evolution in environments with high spatial and temporal variability in runoff. This makes it a new and unique tool for the quantification of channel change and behavior under climate change and variability in arid environments. In this section, the individual elements of ERMO are presented.

5.2.1 Stream System Schematization

The main stream of the Rio Puerco is schematized as a system of reaches shown in Figure 5.5. As discussed in Chapter 2, there are 13 tributaries to the main stream: 12 are side tributaries and one is the headwater tributary. Details, such as tributary drainage areas, slopes, etc. can be found in Chapter 2. Each tributary contributes daily streamflow to the main stream at the point of the tributary node. The main stream is further divided into 12 subbasins, which drain directly to the main stream. The contribution of these subbasins to the main stream is lateral daily streamflow distributed uniformly throughout the length of the subbasin main stream section.

ERMO is a one-dimensional model: the length between individual channel nodes is the length along the streamline and accounts for sinuosity in individual reaches. The reaches are further divided into computational elements - links with length Δx. The choice of Δx is important - it is determined by the transient nature of streambed changes.

In essence, Δx is the representative length that a streambed disturbance will travel in one day. Detailed analyses of the transient nature of streambed changes downstream of tributaries on the Rio Puerco described in the short-term simulations in Section 5.5 and experimental flume analyses of Yen et al. (1992) show that a representative length Δx=500 m is appropriate for analyses at the daily timescale with ERMO. This spatial scale is used throughout the analysis.

The Rio Puerco main stream is divided into a system with 428 links and 429 nodes. The links and nodes are numbered in the upstream direction from the outlet. Therefore, the outlet node i=1 and the top node i=n=429. The total length of the schematized main stream of the Rio Puerco is then L=214 km. The elevation of each node z_i is determined from DEM analyses. The channel cross section is assumed to be rectangular with channel width W_i assigned to each node. No separation between a main channel and floodplain section is made. It is assumed that in long-term simulations, the role of the floodplain in water conveyance is negligible compared to the main channel.

5.2.2 Water Routine

In ERMO, water is routed down the main stream of the Rio Puerco as a succession of steady state - daily flows - provided by RMS and the rainfall-runoff model in Chapter 4. The hydraulic, or water routine, in ERMO consists of the steady state one-dimensional equation of continuity for water:

$$\frac{\partial Q}{\partial x} + q_l - q_{\inf} = 0 \qquad (5.11)$$

where Q is daily streamflow in the main stream, q_l is lateral daily inflow into the main stream and $q_{\inf}$ is the infiltration (transmission) loss along the main stream. Equation (5.11) is discretized between nodes i and i+1 as:

$$Q_i = Q_{i+1} + Q_t + \Delta x\, q_l - \Delta x\, q_{\inf} \tag{5.12}$$

where Q_t is a tributary inflow (t=1, ..., 13) if node i+1 is a tributary node, otherwise Q_t=0. The lateral inflow into the main stream is computed as:

$$q_l = \frac{Q_m}{L_m} \tag{5.13}$$

where m=1, ..., 12 are the individual main stream subbasins, each producing daily runoff Q_m along the main stream segment with length L_m. The transmission loss is computed as:

$$q_{\inf} = f\,\overline{W} \tag{5.14}$$

where f is an infiltration rate into the streambed and $\overline{W}$ is the average channel width of the link equal $\overline{W} = 0.5\,(W_i + W_{i+1})$. The assumption in ERMO is that f represent a *steady-state infiltration rate* that is constant throughout the main stream irrespective of location, streamflow, antecedent moisture conditions and alluvium storage. The infiltration rate f is a crucial parameter in ERMO. In cases of low flow, f can be large enough to infiltrate all flow before reaching the outlet. This situation is often observed in the Rio Puerco Basin. Estimates of f from point measurements in the Basin described in Chapter 2 indicate extremely high infiltration losses. However, it is expected that a stream-wide value of f in ERMO will be considerably less than the point measurements of field saturated hydraulic conductivity. The importance of f will be explored in detail in Section 5.3.4.

The daily streamflow profile is computed from the top node in the downstream direction $i=n, \ldots, 1$, gradually adding lateral inflow and tributary inputs and subtracting infiltration loss. The boundary condition at the top node is given by the headwater tributary discharge ($t=13$):

$$Q_n = Q_{t=13} \tag{5.15}$$

Specific discharge is used as input into the sediment routine of ERMO, so specific discharge is computed for every node as:

$$q_i = \frac{Q_i}{W_i} \qquad \text{for } i = 1,\ldots,n \tag{5.16}$$

The water routine is fully decoupled from the sediment routine and is executed first for every day of the simulation. Required daily inputs provided by RMS and the rainfall-runoff model are tributary inflows Q_t, $t=1, \ldots, 13$ and main stream subbasin inflows Q_m, $m=1, \ldots, 12$.

5.2.3 Sediment Routine

Subsequent to the computation of the streamflow profile with the water routine of ERMO, the sediment routine is executed. This routine consists of computing the sediment transport capacity and evaluating the sediment continuity equation:

$$W\frac{\partial q_b}{\partial x} + (1-p)W\frac{\partial z}{\partial t} = 0 \tag{5.17}$$

Here, p is the porosity of the bed sediment deposits and z is the channel bed elevation. From the sediment continuity equation it is evident that aggradation/degradation of the channel is a result of an imbalance in the bedload sediment transport capacity in the link. In ERMO the supply of sediment is only from the bed and banks of the main stream or from tributary inflows. It is assumed that sheet flow (i.e., unchannelized lateral inflow into the main stream) does not supply the channel with significant bedload sized material. An explicit finite difference approximation used to solve the differential equation in (5.17) is briefly described below.

The (spatial) gradient in sediment transport capacity in link i is approximated as:

$$\frac{\partial q_b}{\partial x}_i = \frac{\Delta q_b}{\Delta x}_i = \frac{1}{\Delta x}(q_{b(i)} - q_{b\,(i+1)} - q_{b\,t}) \tag{5.18}$$

where $q_{b\,(i)}$ is the output of sediment at node i (i.e., bottom of link i), $q_{b\,(i+1)}$ is the input of sediment at node i+1 (i.e., input from the upstream link i+1), and q_{bt} is the input of sediment from tributary t if i+1 is a tributary node, otherwise q_{bt}=0. All bedload sediment transport capacities q_b are computed using Equations (5.3) and (5.5):

$$q_{b\,i} = \gamma\, 0.0356\, q_i^{\;1.2098} \tag{5.19}$$

Special cases are tributary sediment inflows which are assumed to follow the same sediment transport relation as the main stream, thus:

$$q_{b\,t} = \gamma\, 0.0356\, (\frac{Q_t}{W_t})^{1.2098} \tag{5.20}$$

Tributary channel widths W_t are a required input into the channel erosion model. Estimated and/or measured widths for the 13 tributaries are presented in Chapter 2 (Table 2.2).

The (temporal) gradient in channel bed elevation in link i using Equation (5.17) and (5.18) is then:

$$\Delta z_i = -\frac{\Delta t}{1-p}\frac{\Delta q_b}{\Delta x}_i \tag{5.21}$$

where Δt is the simulation time step: Δt=1 day. Tests with Δt<1 day were performed but the effects on the magnitude of channel aggradation/degradation were found to be insignificant. Porosity p depends on the specific weight of the sediment deposits. For sand-sized material coarser than 0.1 mm, the specific dry weight of a sediment mixture remains practically constant: γ_{md}=14.75 kN/m^3 (the specific weight of solid particles γ_s=26 kN/m^3). The porosity of sand material is then $p = 1 - \gamma_{md} / \gamma_s = 0.43$ (Julien 1995, p. 246). As a result of the consolidation of bed material and exposure to air, γ_{md} can vary in time. However, for the purposes of this study a constant value p=0.43 was used.

For the solution of (5.21) the following explicit finite difference scheme is used:

$$z_i^{N+1} = z_i^N + \frac{1}{2}(\Delta z_i + \Delta z_{i-1}) \tag{5.22}$$

where z_i^N is the channel bed elevation at node i at time level N and z_i^{N+1} is the channel bed elevation at node i at time level N+1 (Pickup 1977, Saiedi 1997, and others). Equation (5.22) is solved in the upstream direction for every node i=1, ..., n. The solutions for the bottom and top nodes are:

$$z_1^{N+1} = z_1^N + \Delta z_1 \qquad\qquad z_n^{N+1} = z_n^N + \Delta z_{n-1} \tag{5.23}$$

Using (5.22) and (5.23), the new channel bed elevation is computed for every node in the stream system.

An integral part of the sediment routine is the redistribution of sediment mass in situations where there is a negative slope between nodes; i.e., where $z_i^{N+1} > z_{i+1}^{N+1}$ (this case can occur with rapid erosion at tributary junctions). The redistribution is accomplished by distributing sediment in the longitudinal direction between affected links (fully satisfying sediment continuity) in sweeps, such that the limiting condition $z_i^{N+1} = z_{i+1}^{N+1}$ is achieved for all nodes downstream and/or upstream of the disturbance.

Up to this point channel changes were assumed only in the vertical z direction. However, ERMO allows for changes in channel width, which require corrections to Δz.

5.2.4 Channel Width Changes

Two-dimensional analyses of bed deformation simulate channel width changes based on lateral sediment fluxes and bank stability (e.g., Darby and Thorne 1996). In one-dimensional models changes in channel width are often computed as linear or nonlinear functions of changes in channel depth (e.g., IACWD 1988), or determined based on the principle of minimization of stream power (e.g., Chang 1982). The first approach is chosen here, as I believe that the principle of minimum stream power is not well applicable to conditions of rapid channel changes in ephemeral flow conditions and is more suitable for gradually varied flow conditions and perennial rivers that exhibit some level of geomorphic equilibrium.

In ERMO, channel width changes are applied to every link of the stream system according to the schematic shown in Figure 5.6. The general principle is that the cross-sectional area is adjusted so that the widening/narrowing of the cross section balances the change in Δz (area A is identical to area B in the figure). Here Δz is the uncorrected vertical channel change computed in the sediment routine and Δz' is the corrected new vertical channel change. The redistribution of sediment mass is parametrized by a single *width parameter*, h. Notice from Figure 5.6 that the new channel link width is equal to

$$W' = W + \Delta W \tag{5.24}$$

and

$$\Delta W = -2h\Delta z \tag{5.25}$$

so that in the erosional phase when $\Delta z<0$, $\Delta W>0$, and vice versa for the depositional phase. In other words, the channel widens in the erosional phase and becomes narrower in the depositional phase. The new corrected vertical channel change $\Delta z'$ then becomes:

$$\Delta z' = \frac{W}{W+\Delta W}\Delta z \tag{5.26}$$

The sign of ΔW (erosional or depositional phase) determines whether the corrected vertical channel change $\Delta z'$ will be greater or smaller than Δz. The above described procedure is applied to every link i of the main stream system. First ΔW is computed from Equation (5.25) and then the correction to Δz is made according to Equation (5.26). While the finite difference scheme in Equations (5.22) and (5.23) is used to determine z_i^{N+1}, the following forward finite difference scheme is used for changes in channel width:

$$W_i^{N+1} = W_i^N + \Delta W_i \tag{5.27}$$

for i=1, ..., n-1. Here W_i^N is the channel width at node i at time level N and W_i^{N+1} is the channel width at node i at time level N+1. The solution for the top node is:

$$W_n^{N+1} = W_n^N + \Delta W_{n-1} \tag{5.28}$$

Using (5.27) and (5.28), the new channel width is computed for every node in the stream system.

It is noteworthy that although the above finite difference solution for width does not provide exact sediment continuity, it does provides a negative feedback process between changes in channel depth and channel width observed in nature. For example, in highly erosive links the channel widens in the downstream section thereby decreasing sediment transport capacity and slowing further erosion, whereas the opposite is true in depositional reaches.

The so-called width parameter h is essentially the fraction of the change in channel depth Δz that is applied to the change in channel width ΔW. From (5.25):

$$h = -\frac{\Delta W}{2\,\Delta z} \tag{5.29}$$

In some modeling applications it is assumed that ΔW=-Δz, so h=0.5 (see IACWD 1988). Here, it is hypothesized that channel changes are distributed evenly across the whole wetted perimeter of the (rectangular) channel cross section. Then ΔW=-2Δz, and h=1. In the Rio Puerco, there are insignificant differences in the bed material between bed and banks, and it can be assumed that the noncohesive banks will erode at a rate similar to the bed of the channels. The sensitivity of ERMO modeling results to the parameter h will be shown later.

5.2.5 Summary

The accuracy of ERMO-predicted channel change is largely dependent on the accuracy of the sediment transport relation used. The model is based on the assumption that aggradation and degradation of the channel bed are a result of the variability in the sediment transport capacity of bedload; i.e., sand-sized material that is transported in contact with the streambed (Ponce et al. 1979, Habersack 1998). Suspended load is assumed to remain in suspension and is transported out of the system. In the Rio Puerco, the fraction of total load transported as bedload is small, and the parameter γ describing this fraction is an important model parameter. The sources of bedload sediment supply in the ERMO model are two: (1) the stream bed and banks, and (2) sediment supply from tributaries.

In links between tributaries, the bedload sediment transport capacity is satisfied exclusively by the stream bed and banks. In these links there may be lateral inflow of water directly into the main stream (see Equation (5.13)), but this unconcentrated flow is assumed only to carry wash load that is not deposited on the streambed and adds to the suspended sediment material in the main stream. The same assumption is made regarding sediment supply from random bank mass failure in the process of channel widening. On the other hand, the supply of bedload by tributaries is computed using the same sediment transport relation as for the main stream. As the Rio Puerco is relatively homogeneous regarding sediment type and supply this is not a bad assumption. However, generally there are differences in sediment rating curves between subbasins that are a result of sediment supply and type, vegetation, geology, etc. Where it is possible, these differences should be accounted for and parametrized.

ERMO does not account for streambed armoring; i.e., a process by which selective sediment transport leaves a pavement of coarser particles on the channel bed (e.g., Yang 1996). The development of an armored layer decreases the rate of degradation (e.g., Bennet and Nordin 1977, Karim and Kennedy 1982, Karim and Holly 1985, Dawdy and Vanoni 1986). Generally, the process of armoring is particular to gravel bed streams, although the ephemeral nature of flow may impede their development even there (Reid and Laronne 1995). In the Rio Puerco ephemeral and sand bed stream system armoring does not play a major role in the long-term erosion dynamics. It is true that clay impregnates the sand bed with receding flow to a depth of about 20 cm (Nordin and

Dempster 1963, Nordin 1963) and eventually creates a dry and hardened armor coating (the author observed occasional intermittent 2-3 cm thick layers of silt in the sandy channel alluvium). However, this layer is quickly eroded or covered by sand-sized sediment during flow events.

Because of the homogeneous and noncohesive nature of Rio Puerco alluvial sediment, the effect of the separation of sediment load into size fractions on sediment transport (van Niekerk et al. 1992) and the effect of selective transport on downstream fining (Hoey and Ferguson 1994, Cui et al. 1996) were not considered. The role of these processes in long-term simulations in the Rio Puerco environment is likely to be minor (e.g., Holly and Karim 1986).

In summary, the three primary parameters of ERMO are: the (*a*) bedload parameter γ, (*b*) infiltration parameter f, and (*c*) width parameter h. The parameter f can be calibrated (as shall be seen in the subsequent section), whereas the remaining two parameters were estimated (γ=0.053, h=1) from known sediment relations and/or observations.

5.3 Current Climate Analysis

The first modeling task with ERMO is to analyze the spatial and temporal pattern of the erosion dynamics in the Rio Puerco main stream for the *current climate* conditions; i.e., present level of annual precipitation. The current climate analysis described in this section will focus on five main topics: (1) Calibration of the infiltration parameter. (2) Study of the spatial and temporal evolution of erosion on the main stream. (3) The influence of the magnitude of annual streamflow on erosion dynamics. (4) The influence of streambed infiltration on erosion dynamics. (5) Discussion of parameter effects.

5.3.1 CALIBRATION

Calibration of ERMO for the current climate consists of the calibration of the infiltration parameter f for the current level of annual precipitation. This is accomplished by generating daily streamflow inputs at all Rio Puerco 13 tributaries and 12 main stream subbasins: RMS was used to generate 20 runs of daily streamflow inputs, each consisting of n=100 years. The current climate precipitation scenario has: P=280 mm and coefficient of variation C_v=0.23 (statistics for the common record, for RMS details see Chapter 4). For each of the 20 runs, a trial and error method was employed to calibrate the infiltration parameter f such that the average annual runoff at the outlet of the Basin was 35.9 mil m^3/year, which is the observed amount at Bernardo (gage 3530) adjusted for the shorter 256 day model year in RMS.

In the current climate scenario, the remaining parameters in ERMO were h=1.0 and γ=0.053. The initial conditions in the channel system were given by the channel bed elevations at individual nodes extracted from DEM analyses of the Basin described in Chapter 2, and by the initial main stream channel widths, which were taken to be W_i=15 m, for all i=1, .., n. This is an average conveyance width based on the author's own measurement/estimation of the Rio Puerco main stream and data of Elliott (1979). All simulation runs in this study begin with the same initial conditions so that intercomparisons can readily be made.

Tables 5.2 and 5.3 summarize the main results. In Table 5.2, the calibrated infiltration parameter f is given for every run together with the cumulative volume of channel change V in 100 years of simulation. The parameter f varies between 0.33 and 1.01 cm/hr, with an average f=0.65 cm/hr. Negative V means that after 100 years of simulation, the Rio Puerco river system had overall degraded relative to the initial conditions. The opposite is true for $V>0$. Table 5.2 shows that the Rio Puerco is on the average in an aggradational mode; mean V=0.854 mil m^3 in 100 years. Figure 5.7 shows the relationship between f and V. To maintain the same long-term average runoff at Bernardo, high values of the infiltration rate f mean a greater downstream streamflow loss in the main stream and therefore more aggradation. Although this general behavior is expected, the high (linear) correlation between f and V is quite remarkable. It is also interesting to note that for $f>0.45$ cm/hr, the Rio Puerco main stream would be on the average in a depositional mode, while for $f<0.45$ cm/hr, overall erosion would prevail. The issue of streambed infiltration will be explored further in subsequent analyses. For now it is important to note that the intermittent nature of streamflow in the Rio Puerco does in the long term promote general aggradation.

Table 5.2 also lists maximum simulated depths of aggradation and degradation in the main stream. There are two principal variables of interest here: one is the maximum channel change within the 100-year simulation (i.e., maximum channel change from initial conditions), the other is the maximum annual channel change (i.e., maximum channel change within one year). Results in Table 5.2 show that the average maximum 100-year aggradation depth was Δz_{max}=1.66 m and degradation depth was Δz_{max}=3.79 m. This shows that despite an average depositional regime occurring in the Rio Puerco main stream, degradation is generally more dramatic than aggradation. As will be subsequently shown, maximum degradation generally occurs downstream of large tributaries, whereas maximum aggradation generally occurs at the downstream end of long channel reaches without tributaries and with low lateral inflow. It is also interesting to note that the variability of the maximum 100-year degradation rate in-between runs is very low, indicating that the maximum erosion depth may be a function of other variables, such as the longitudinal streamflow profile, in addition to streamflow. The annual erosion maxima on the other hand are quite variable and also of substantial magnitude. The average annual erosion maximum was Δz_{max}=1.16 m, which means that almost a third of the 100-year maximum can occur in one year. This is a very important finding which points to the importance of extremely wet years in channel erosion.

Finally, Table 5.2 also gives the maximum 100-year changes in channel width ΔW. The average maximum channel narrowing was ΔW_{max}=3.23 m, whereas the average maximum channel widening was ΔW_{max}=9.03 m. Figure 5.8 shows a comparison of maximum 100-year changes in channel depth and width. The figure shows that maximum channel deposition and narrowing are better (linearly) related (r^2=0.921), while the scatter is greater for maximum channel erosion and widening (r^2=0.606). This confirms that channel erosion is the more dynamic process with larger variability.

Statistics of streamflow, the driving force of erosion, are given in Table 5.3. To adequately represent the spatial distribution of erosion in the Rio Puerco main stream it is vital that the statistics of simulated streamflow contributions at the 4 main streamflow gages compare well with observations. Again two variables are of importance here: the average annual runoff Q, which represents long-term runoff conditions, and the average annual maximum daily flow Q_p, which represents short-term response. The results for Q are very satisfactory: at gage 3515 the average Q from simulations was Q=9.63 mil m^3/yr compared to Q=9.35 mil m^3/yr observed; at gage 3405 Q=18.3 mil m^3/yr compared to Q=17.74 mil m^3/yr observed and at gage 3340 Q=8.95 mil m^3/yr compared to Q=11.33

mil m^3/yr observed. At gage 3530 the simulated and observed averages were identical because they were used for calibration. For peak flow, the RMS generally overestimates the average annual maxima: at gage 3530 Q_p=79.6 m^3/s compared to Q_p=54.3 m^3/s observed; at gage 3515 Q_p=18.4 m^3/s compared to Q_p=20.0 m^3/s observed; at gage 3405 Q_p=34.1 m^3/s compared to Q_p=37.7 m^3/s observed; at gage 3340 Q_p=29.3 m^3/s compared to Q_p=13.8 m^3/s observed. Poorest results are for the Upper Rio Puerco Basin (3340), where the model underestimates the average annual runoff slightly but overestimates the average annual maxima considerably. However, this basin is modeled as an aggregate of 6 individual subbasins that constitute the Upper Rio Puerco Basin, connected with a section of the Rio Puerco main stream. Therefore, considering the simplicity of the individual models concerned, ERMO in conjunction with RMS and the rainfall-runoff model perform very well in preserving the spatial variability in long-term statistics of daily streamflow.

5.3.2 Erosion Profile Examples

The current climate calibration showed that rates of erosion and channel widening are generally much higher than the rates of deposition and channel narrowing. At the same time, the Rio Puerco main stream is on the average in an aggradational phase, meaning that the slower but continuous process of channel aggradation is more dominant in the long-term than the rapid but intermittent process of channel erosion. In addition to this general behavior, it is also important to understand the spatial and temporal distribution of aggradation and degradation throughout the main stream. In this section, two representative example runs are shown in detail in order to discuss the simulated erosion profiles and the dynamics of erosion.

First is the aggradational Run 5 (Figure 5.9 top). The term aggradational refers to the fact that after 100 years of simulation, the total change in volume of the channel system during this run was positive; i.e., the system was overall in a depositional mode. Second is the degradational Run 18 (Figure 5.9 bottom). Here the total change in volume of the channel system after 100 years was negative; i.e., the system was overall in an erosional mode. The calibrated infiltration parameter was f=0.58 cm/hr for Run 5 and f=0.42 cm/hr for Run 18. Figure 5.9 illustrates well the difference in erosional and depositional behavior in the Rio Puerco main stream. The depositional regime is continuous and gradual, interrupted irregularly by rapid erosional events that correspond to particularly wet years. This is precisely the geomorphologic behavior and evolution that is observed in many semiarid stream systems in the U.S. Southwest (e.g., Cooke and Reeves 1976).

The longitudinal distribution of vertical channel change Δz is shown in Figure 5.10 for both runs after 50 and 100 years of simulation. The general behavior very accurately simulates hypothesized channel change in ephemeral streams (Thornes 1977). Erosion occurs immediately downstream of major tributaries and gradually extends in the downstream direction. Aggradation is present throughout the entire stream system, but highest accumulations are found in long stream reaches without appreciable tributary inflows and/or low lateral streamflow contributions. The most active tributary junctions in general were Arroyo Chico, Salado Creek and Rio San Jose (in that order), and occasionally the Arroyo Hondo and Arroyo Chijuilla junctions in the Upper Rio Puerco Basin. From Figure 5.10 it appears that locations on the main stream where two tributaries join in close vicinity (e.g., Salado Creek and Arroyo Cuervo) are most prone to extended erosion.

The longitudinal distribution of channel width is shown in Figure 5.11. There is a dramatic increase in width downstream of major tributaries. This fact is also confirmed by the author's own observations on the Rio Puerco, especially downstream of the Arroyo Chico junction. Another interesting observation is that although there is large downstream variability in width as a result of tributary effects, an overall general channel narrowing in the downstream direction is also evident. This was true for most of the simulation runs. Extremely high variability in channel width in ephemeral streams was also observed by Leopold et al. (1966). In contrast to most perennial rivers, a general decrease in channel width downstream is common in ephemeral streams and was observed on the Rio Puerco (e.g. Elliott 1979) and other semiarid streams in the U.S. Southwest region (e.g., Cooke and Reeves 1976).

The temporal evolution of channel change downstream of a tributary is illustrated on an example of the Rio Puerco main stream and Arroyo Chico junction in Figure 5.12. At the tributary, rapid erosion response to increased streamflow from the tributary and gradual aggradation in periods of lower flow are evident, while just upstream of the tributary, gradual aggradation occurs. The upstream reach is part of a subbasin with very low lateral streamflow contributions and few tributaries. Infiltration here is of sufficient magnitude to cause a considerable loss in sediment transporting capacity and in some cases eliminate all streamflow in the reach. Note also the progression of degradation downstream: after about 20 years of simulation, the overall change in channel depth 2 km below the tributary is greater than at the tributary itself. Furthermore, the interannual variability of channel change caused by fluctuating inflows from the tributary is largely diminished.

Changes in channel depth are accompanied by changes in channel width. Figure 5.13 shows the width of the main stream channel at the Arroyo Chico junction. Just downstream of the tributary (-0.5 km) the channel widens from the initial width of 15 m to about 22 m after about 15 years of simulation, and thereafter fluctuates around that level. This effect of initial conditions is also evident in channel depth where the first 15 years show rapid degradation followed by less dramatic and persistent channel changes. Further downstream interannual variability in channel width diminishes.

Figures 5.14 and 5.15 show more examples of the temporal evolution of channel depth and width changes for the Rio Puerco main stream at the Rio San Jose tributary for Runs 5 and 18. Erosion activity downstream of the Rio San Jose is considerably lower than downstream of the Arroyo Chico because of the lower annual runoff and also lower peak flows. However, the temporal evolution exhibits the same signatures: rapid degradation and channel widening in wet years followed by longer periods of aggradation and channel narrowing in sequences of drier years.

5.3.3 Influence of Streamflow

From previous analyses it is evident that streamflow variability is the primary factor in the erosion dynamics of the Rio Puerco main stream. In this section the relationship between streamflow, sediment transport and erosion on the annual timescale is investigated in greater detail. Runs 5 and 18 are again used as examples of current climate behavior.

Previous analyses showed that calibrated for the current climate, the Rio Puerco Basin is on the average in an aggradation phase. However, large variability in the annual volume of channel change related to variability in streamflow was found (e.g., Figure 5.9). In Figure 5.16 the annual volume of channel change V is plotted versus annual streamflow Q at the Basin outlet (gage 3530). For both runs these graphs show a region of low Q in which $V>0$ is independent of Q. The annual volume of channel change then changes to degradation mode ($V<0$) and decreases rapidly with increasing Q: at the annual time scale, extremely wet years produce substantial erosion along the entire main stream. In wet years lateral streamflow contributions to the main stream are commonly larger than the infiltration losses, therefore erosion occurs along main stream reaches (where generally only aggradation occurs in drier years) as well as at tributary junctions.

Simulated maximum annual depths of degradation and aggradation are also well related to annual streamflow (Figure 5.17). The variability in both maximum annual degradation and aggradation depths increases with increasing streamflow. Downstream of tributaries the main stream can degrade over 1 m in a wet year just as a result of the natural spatial and temporal variability in streamflow contributions. It also appears from Figure 5.17 that there is an upper limit to the maximum aggradation rate quite independent of discharge magnitude. In fact, it is the spatial variability in streamflow contributions from the tributaries and main stream that influence both aggradation and degradation dynamics (as shall be shown in Chapter 6). It seems that aggradation in particular responds strongly to this spatial variability in streamflow.

An interesting question in the sediment balance and erosion dynamics remains the identification of sediment sources. In particular it is of interest to know what percentage of bedload transported out of the Rio Puerco stream system comes from the streambed. This is investigated on an annual basis in Figure 5.18 for the example runs. ERMO simulations show that peaks in sediment transport are associated with large channel degradation. In the wettest year, 40.9% of the bedload was supplied by the streambed in Run 5 and 41.0% in Run 18. The average streambed contribution to bedload from all 20 simulation runs was 38.4% in the peak year (ranged from 29.4% to 47.9%). According to ERMO modeling results, for the 5 wettest years in every run, over 30% of the bedload transported out of the Rio Puerco came from the streambed. For moderate flow years, the percentage supplied from the streambed was less than 30%. These results indicate that although sheetwash may be a primary source of sediment in the headwater basins (Leopold et al. 1966), the bed and banks are an equally important supply of bed material load in the main channel system.

5.3.4 Streambed Infiltration

Infiltration into the streambed is an important parameter affecting erosion dynamics. A stream-wide average steady state infiltration rate f should be smaller than point measurements of infiltration (Chapter 2) because it includes the effects of groundwater storage, high suspended sediment, variability in the permeability of the alluvium, etc. Rather than looking at the infiltration rate itself, it is more interesting to study the volume of transmission loss.

If we take subbasin runoff Q_{sb} to be the annual runoff total from all 25 Rio Puerco tributary and main stream subbasins simulated by RMS and Q to be the annual runoff at the outlet of the Rio Puerco Basin from ERMO (i.e., including the infiltration losses through *f*), we can define the following annual streamflow effectiveness ratio *m*:

$$m = \frac{Q_{sb}}{Q} = \frac{\sum_{i=1}^{25} Q_i}{Q} \tag{5.30}$$

This ratio is an indicator of annual streamflow loss into the streambed. Note that if f=0, m=1, and if f>0, m>1. Results of ERMO analyses show that *m* is exponentially related to annual streamflow *Q* (Figure 5.19). In dry years, the amount of streamflow loss is a large percentage of total streamflow, while in wet years this percentage decreases (there is much less interannual variability in the amount of streamflow loss due to infiltration than in annual streamflow itself). In fact in dry years it is common for m>2; i.e., less than 50% of the observed streamflow in the Rio Puerco main stream makes it to the Basin outlet on an annual basis.

The average annual effectiveness ratio for Run 5 was m=1.89 and the average annual transmission loss in the Rio Puerco main stream was 21.7 mil m^3/yr. For Run 18, these values were m=1.69 and 17.2 mil m^3/yr. (Notice that the simulated average annual transmission loss for the entire main stream is 4-5 times greater than the minimum estimate of annual streamflow loss (4.02 mil m^3/yr) in the Middle and Lower Rio Puerco from Chapter 2.) The simulated average annual transmission loss of 0.101 mil m^3/yr per kilometer of channel (Run 5) and 0.08 mil m^3/yr per kilometer (Run 18) is of similar magnitude to other streams in the U.S. Southwest (e.g., 0.26 mil m^3/yr per km in Tucson Basin, Arizona, Burkham 1970).

Streambed infiltration also affects maximum erosion and deposition rates. Figure 5.20 shows the maximum 100-year erosion and deposition depths as a function of *f* in the current climate calibration. It is quite clear that while the maximum erosion rate is independent of f (it is driven by streamflow), the maximum deposition rate shows a good (linear) relationship with f (it is driven by infiltration). Based on Figure 5.20 it can also be hypothesized that for a sufficiently large infiltration rate, the extreme rates of erosion and deposition will converge.

In the Rio Puerco, the storage of water in the alluvium cannot be estimated because of the lack of data. In ERMO the alluvium storage capacity is considered infinite and the infiltration rate is steady. However, in reality the alluvium storage capacity is variable in space and, when capacity is reached, the infiltration rate into the streambed should decrease. It is likely that in the Rio Puerco, where the groundwater level is deep and the alluvial sediment appears to be homogeneous to great depths, the effects of alluvium storage capacity are not great. However, these factors should be parametrized where possible.

5.3.5 Summary

Two main conclusions can be made from the long-term channel erosion modeling results presented here. First, erosion generally is rapid in both space and time and mostly results from extremely wet years/seasons/events. Second, deposition generally is slow but occurs continuously as a result of the loss in sediment transport capacity (in space) and extended periods of low flow (in time). So, although rates of erosion are generally greater than rates of deposition in the short-term, deposition is the dominant process in the long-term. Current climate simulation in the Rio Puerco shows that the main stream is overall in a depositional phase.

It is also necessary to evaluate the influence of the main ERMO parameters, γ and h, on modeling results. Although a comprehensive parameter sensitivity analysis was not conducted, two examples are shown here in which the parameters γ and h were varied towards a more erosion-prone situation.

The first case tests the effect of the width parameter: h=0.5 (i.e., channel width response is less than in the original scenario). This case may resemble more cohesive and/or vegetated banks of the main stream, and it is expected that it will intensify the rate of vertical channel change. The second case tests the effect of the bedload parameter: γ=0.087 (i.e., bedload sediment transport is increased to 8% of total load, B=0.92). This case resembles a condition of higher sand-sized sediment transporting capacity, and it is expected that it will also intensify the rate of vertical and horizontal channel change. Experimental results show that arroyo widening increases with increasing bedload sediment transport (Meyer 1986). With the new parameters, all 20 runs of the current climate scenario were used to recalibrate the infiltration parameter f as in previous analyses.

Runs 5 and 18 are again used as examples. The cumulative volume of channel change is compared to the original scenario (h=1, γ=0.053) in Figure 5.21. It appears that the channel change volume is not significantly affected by changing the width parameter. However, increasing bedload transport caused a considerable increase in erosion and deposition activity in the main stream. Figure 5.22 shows the cumulative volume of channel change after 100 years for all 20 simulated runs. It is also evident that the effect of the channel width parameter on the total volume of channel change is less significant than the effect of bedload transport. Increased overall deposition with increasing γ is mainly a result of higher sediment supply from tributaries.

An example of the temporal erosion dynamics at the Arroyo Chico junction is shown in Figure 5.23 for Run 5. Notice that because of smaller changes to channel width for h=0.5, vertical erosion in this scenario is considerably greater than in the original case. However, after about 40 years, channel widths converge to the same average value in all three scenarios. Increased supply of sediment to the main stream from the Arroyo Chico tributary for the case γ=0.087 manifests itself by increased rates of aggradation downstream of the tributary (Figure 5.23).

Figure 5.24 summarizes the maximum annual depth changes in the two scenarios compared to the original one. The conclusion is that going from h=1 to h=0.5 slightly decreases annual aggradation rates, but increases annual degradation rates. From all runs, the average annual Δz_{max} went from 0.64 m to 0.6 m (aggradation) and 1.16 m to 1.34 m (degradation). On the other hand going from γ=0.053 to γ=0.087 considerably increases both annual degradation and aggradation rates. From all runs, the average annual Δz_{max} went from 0.64 m to 1.55 m (aggradation) and 1.16 m to 1.63 m (degradation).

The results of this parameter analysis can be summarized in two statements: (1) The erosion dynamics in the Rio Puerco main stream are more sensitive to the bedload parameter γ. Increasing the amount of sediment transported as bedload results in both increased rates of deposition (result of higher sediment supply from tributaries) and erosion (result of higher sediment transporting capacity). (2) The width parameter h particularly affects the spatial distribution of channel width and depth changes. "Slowing" down width changes by decreasing h results in increased vertical degradation.

These changes are manifested mostly downstream of tributaries where simulated width changes are most severe.

5.4 Changing Climate Scenario

Historical, archeological and dendrochronological records in the Rio Puerco Basin indicate long-term variability in regional climate. Analyses of hydroclimatic trends in Chapter 3 of this study show a strong connection between Rio Puerco annual precipitation and reccurring large scale climatic anomalies in the Northern Pacific. This changing environment will affect erosion dynamics in the Rio Puerco.

The effect of changing climate on erosion dynamics was analyzed by taking three climate modes. Each climate mode was represented by an average annual precipitation total P: (1) *dry climate* P=200 mm, (2) *current climate* P=280 mm and (3) *wet climate* P=400 mm. In the subsequent analyses, an increase in wetness (i.e., an increase in P), is also associated with an increase in the probability of extreme rainfall and runoff events, due to the nature of RMS (Chapter 4). For each climate mode, 20 runs with given average P, coefficient of variation C_v=0.23 and n=100 years were generated with RMS. The ERMO infiltration parameter was constant for all climate modes and equal to the average calibrated f for the current climate condition f=0.654 cm/hr (see Table 5.2). The width parameter h=1 and the bedload parameter γ=0.053.

5.4.1 Streamflow and Sediment Transport

Changing climate affects erosion through changes in runoff. Average annual runoff at the main Rio Puerco gages for the changing climate scenario is listed in Table 5.4

together with average annual maximum daily flows. There is a marked increase in both variables going from the dry to the wet climate. In the wet climate mode, the average annual runoff at the outlet of the Basin was 55.61 mil m^3/yr (23.39 mil m^3/yr in the dry climate) with an average annual daily peak flow of 109 m^3/s (62.7 m^3/s in the dry climate).

Associated with streamflow is variability in sediment transport. Table 5.4 gives the simulated average annual bedload and total load amounts at the outlet of the Basin. Simulations show that in the current climate mode, suspended sediment output from the Basin is on the average 1.48 mil m^3/yr, which compares very well with observations at the Bernardo gage (1.31 mil m^3/yr from Table 5.1). Simulated average total sediment load varies between 1.01 and 2.53 mil m^3/yr going from the dry to the wet climate. This is an increase of about 150% in sediment supply to the Rio Grande River. Clearly, climate variability can have major impacts on the sediment balance of the Rio Grande River downstream of Rio Puerco.

In summary, simulations show that a shift towards a wetter climate in terms of annual precipitation and annual extremes will lead to a considerable increase in annual streamflow as well as peak flows and thereby to a considerable increase in sediment output from the Rio Puerco Basin.

5.4.2 Erosion Dynamics

Changes in sediment transport will strongly affect the erosion dynamics in a changing climate. Analyses under the changing climate scenario all showed generally the same spatial and temporal distribution of erosion along the Rio Puerco main stream, and the same response to increased streamflow, infiltration, etc. So, erosion profiles, general streamflow and infiltration effects are not repeated here. However, the rates of channel change varied systematically with changing climate. Therefore, we concentrate here on the main signatures of changing climate: on overall main stream volume change and extreme rates of channel change.

Figure 5.25 shows the cumulative volume of channel change V after 100 years of simulation for all runs in each climate mode. Several interesting features are apparent from this figure. First, within each climate mode, V decreases sharply with increasing streamflow; i.e., there is more overall degradation with increasing streamflow. Runs with higher than average annual streamflow within a climate mode have more precipitation and/or higher precipitation intensity falling on Rio Puerco subbasins, although the average annual regional precipitation remains the same. The intensity of precipitation and resulting runoff events is also the reason why a wetter climate run with low average Q will show more aggradation than a drier climate run with high average Q, the latter case on the average having more intense rainfall and runoff events leading to more intense erosion episodes.

Second, in addition to trends in V within each climate mode, there is an apparent downward trend in the average cumulative volume of channel change (also average annual channel change) going from the dry to the wet climate (Table 5.4). This analysis points to the fact that moving towards a wetter climate results in (1) less overall aggradation and (2) increased variability in erosion response. In fact, it appears from Figure 5.25 that for regional average annual precipitation P>400 mm, the Rio Puerco main stream may be on the average in a quasi equilibrium or even overall degradational state in terms of total volume of channel change. This result has very serious implications for understanding the effects of sustained climate change in the Rio Puerco Basin.

In addition to the above trends in the overall volume of channel change, it is also interesting to look at extreme rates of aggradation and degradation under a changing climate (Table 5.4). Figure 5.26 shows the maximum100-year vertical channel change for all runs in each climate mode. This figure clearly shows that both maximum degradation and aggradation depths increase with increasing streamflow. However, maximum aggradation depths increase at a faster rate. As the climate becomes wetter and more extreme, the maximum depths of deposition become similar in magnitude to depths of erosion. This fact was confirmed by probabilistic analyses of annual rates of channel change discussed in Chapter 6.

In conclusion it is important to note, that this analysis assumes that changing climate in the Rio Puerco region will not affect the spatial and temporal distribution of precipitation, or its variability as defined in the RMS spatial and temporal random cascade models and the linear dependence disaggregation model. Although it is likely that some changes to the distribution of precipitation could occur under a changing climate, they are at this time impossible to predict or quantify. Furthermore, changes in climate would also likely affect vegetation in the Basin and thereby the rainfall-runoff transformation function. The effects of these factors are hypothetical and are not included in the ERMO analysis.

In summary, ERMO simulation shows that moving towards a wetter climate in the Rio Puerco Basin results in (*a*) increased extremes of aggradation and degradation depths, (*b*) overall degradation being the prevailing process in long-term channel change and (*c*) increased variability in the erosion dynamics.

5.5 Short-Term Erosion Modeling

In addition to the channel response to spatially and temporally variable streamflow modeled by ERMO, a short-term erosion analysis was conducted to study the detailed channel response to threshold-dominated processes, in particular in the vicinity of tributaries. For this purpose a new aggradation/degradation model GRAD was built.

GRAD is a one-dimensional iteratively coupled steady-state flow model. It is built on the basis of ERMO, but various parts and concepts of other alluvial models have been utilized in the development and application of its improved hydraulic routine. Iterative coupling, issues related to spatially varied flow and the numerical solution of differential equations were based on the model IALLUVIAL. The backwater calculations in the energy conservation equation were adopted from the river analysis system model HEC-RAS (US Army Corps 1995). Added to these elements of GRAD was a sand-type sediment transport relation applicable to Rio Puerco conditions. Although GRAD is a more detailed model than ERMO, it is not suitable for long-term simulations because of the numerical complexity and instability associated with these. Its application here is exclusively in short-term investigations.

The Rio Puerco main stream system is also schematized into a system of links and nodes as specified in ERMO. The channel is rectangular with width W. Changes to channel width at the short timescale of simulation are not allowed. The initial condition is given by the streambed elevations along the main stream.

5.5.1 GRAD Model Description

The governing equations used in GRAD for describing water and sediment motion are three. First is the hydraulic routine, which consists of the one-dimensional steady-state equation of flow continuity:

$$\frac{\partial Q}{\partial x} + q_l - q_{\inf} = 0 \tag{5.31}$$

where Q is daily streamflow, q_l is lateral daily inflow and $q_{\inf}$ is the infiltration loss along the main stream, and the flow specific energy equation in its integral form:

$$\frac{\partial E}{\partial x} = S_0 - S_f^{'} \tag{5.32}$$

where E is specific energy $E = y + \alpha v^2 / 2g$ at a cross section, with y being depth of flow, α the energy correction factor and v the average flow velocity. The terms on the right hand side are the channel bed slope S_0 and the friction slope S'_f, which represents the head loss term in the energy equation. As in ERMO, the flow equations are steady at the daily timescale. Longer hydrographs are constructed as sequences of steady daily flows.

Second is the sediment transport routine, which consists of the one-dimensional unsteady sediment continuity equation:

$$\frac{\partial Q_b}{\partial x} + (1 - p)W\frac{\partial z}{\partial t} - q_t = 0 \tag{5.33}$$

where Q_b is the bedload sediment flux, p is porosity of the bed material, W is channel width, $\partial z / \partial t$ is the change in channel bed elevation in time, and q_t is the (point) specific sediment discharge from tributaries into the main stream. Equation (5.33) assumes that bedload sediment concentration is constant in time and that channel changes are only in the vertical direction. To solve the above system of differential equations, two additional relations are needed: a flow resistance equation to determine the head loss term:

$$v = \frac{1}{n} R_h^{2/3} S_f^{1/2} \tag{5.34}$$

where R_h is the hydraulic radius, and n is the Manning roughness coefficient; and a one-dimensional sediment transport equation for bedload of the form:

$$Q_b = f(y, v, d_s, \ldots) \tag{5.35}$$

where $f(.)$ represents a function of fluid and sediment properties.

The flow continuity Equation (5.31) is discretized as in ERMO, Equation (5.12). The energy equation is discretized between two successive computational nodes i and i+1:

$$z_{i+1} + y_{i+1} + \alpha_{i+1} \frac{v_{i+1}^2}{2g} = z_i + y_i + \alpha_i \frac{v_i^2}{2g} + h_e \tag{5.36}$$

where z is the channel bed elevation at the node and h_e is the head loss term which consists of energy loss due to friction with the streambed and channel contraction/expansion:

$$h_e = \Delta x S_f + C_l \left| \alpha_{i+1} \frac{v_{i+1}^2}{2g} - \alpha_i \frac{v_i^2}{2g} \right| \tag{5.37}$$

where C_l is the contraction/expansion loss coefficient between nodes i and i+1. In the rectangular conveyance channel of the Rio Puerco main stream, flow velocity is assumed to be uniformly distributed and the energy correction coefficients are $\alpha_i = 1$ for i=1, ..., n. The coefficient C_l in GRAD is linearly interpolated between 0 and 0.1 (for contraction) or 0 and 0.3 (for expansion) based on the change in channel width between successive nodes $|W_{i+1} - W_i|$ for i=1, ..., n, where the maximum value is assigned to the maximum change in channel width at each time step of computation. The solution to

(5.36) is known as the backwater curve, and it proceeds in an upstream sweep. A predictor-corrector standard-step method is used to compute the backwater curve from the downstream node i=1, where the boundary condition is given by the normal depth at that node:

$$y_1 = \left[\frac{nQ_1}{W_1 S_1^{0.5}}\right]^{3/5} \tag{5.38}$$

Subcritical flow is assumed; if supercritical flow is encountered, flow depth is set to critical. The backwater solution uses the average friction slope between successive nodes. The solution procedure is taken from HEC-RAS and is discussed in detail in U.S. Army Corps of Engineers (1995).

The sediment continuity Equation (5.33) is discretized using a standard four-point finite difference scheme, where the time and space derivatives are replaced by the following approximations:

$$\frac{\partial z}{\partial t} = \frac{\Delta z_j}{\Delta t} = \frac{1}{\Delta t}\left[\varphi(z_{i+1}^{N+1} - z_{i+1}^{N}) + (1-\varphi)(z_i^{N+1} - z_i^{N})\right] \tag{5.39}$$

$$\frac{\partial Q_b}{\partial x} = \frac{\Delta Q_{b\,j}}{\Delta x} = \frac{1}{\Delta x}\left[\theta(Q_{b\,i+1}^{N+1} - Q_{b\,i}^{N+1}) + (1-\theta)(Q_{b\,i+1}^{N} - Q_{b\,i}^{N})\right] \tag{5.40}$$

where the subscript i denotes nodes in space, j denotes the link between i and i+1, and superscript N denotes steps in time, φ is the space weighting factor and θ is the time weighting factor. GRAD generally uses a scheme centered in both space φ=0.5 and time θ=0.5, unless numerical instability requires that θ≥0.5 (e.g., Lyn and Goodwin 1985, Saiedi 1997). Equation (5.33) can be written as:

$$\Delta z_j = -\frac{\Delta t}{(1-p)W}\left[\frac{\Delta Q_{b\,j}}{\Delta x} + q_t\right] \tag{5.41}$$

where q_t is a specific sediment discharge from a tributary if $i+1$ is a tributary node, q_t=0 otherwise. The solution is found in a downstream sweep from the top node $i=n$: gradients in bedload ΔQ_{b_j} are found for every link using (5.40), q_t is added at tributary nodes and Δz_j is computed from (5.41). Then the new bed elevations z^{N+1} are determined using (5.39).

The hydraulic and sediment relations are coupled, in the sense that changes in hydraulic conditions affect sediment transport capacity and determine changes to streambed elevations, which in turn affect the hydraulic conditions. In a coupled solution to the discretized differential equations, the hydraulic and sediment governing equations are solved simultaneously, whereas in a decoupled solution they are solved separately, which is numerically simpler and faster. In most practical cases the use of decoupled approaches to channel modeling is justified because of different timescales in the motion of sediment and water (e.g., Cui et al. 1996, Saiedi 1997). However, because of the great spatial variability in streamflow in the Rio Puerco, coupling in some form is desirable. GRAD uses the method of iterative coupling, by which the hydraulic and sediment relations are repeatedly solved in sequence until they converge on a correct streambed elevation (e.g., Karim and Kennedy 1982, Holly and Karim 1986).

The physical coupling of hydraulics and sediment transport occurs through the sediment transport process described conceptually in Equation (5.35). Sediment transport is assumed to be transport capacity (as opposed to supply) limited. Specific bedload sediment discharge in GRAD is computed by the method of Van Rijn (1984a), developed and calibrated for sand bed channels (with representative particle diameter between 0.2 and 2 mm).

$$q_b = 0.053\sqrt{(G-1)g}\ D_{50}^{\ 1.5}\ \frac{T^{2.1}}{D_*^{\ 0.3}} \qquad (5.42)$$

where D_{50} is the median bed material particle diameter and D_* is the dimensionless particle diameter for bed material computed as (5.10). The physically-based, but empirically calibrated method is based on a dimensionless transport stage parameter T which expresses the mobility of particles in terms of the stage of movement relative to the critical stage for the initiation of motion (Van Rijn, 1984a):

$$T = \frac{u_*^{'2} - u_{*cr}^{\ 2}}{u_{*cr}^{\ 2}} \qquad (5.43)$$

where $u_*^{'}$ is bed shear velocity related to grains and u_{*cr} is the critical bed shear velocity for initiation of motion. The bed shear velocity related to grains is defined as (Van Rijn 1984a):

$$u_*^{'} = v\sqrt{g}\,/\,C' \qquad (5.44)$$

where C' is a Chezy roughness coefficient due to grain roughness (Van Rijn 1984a):

$$C' = 18\ \log\left[\frac{12\,R_b}{3\,D_{90}}\right] \qquad (5.45)$$

where R_b is the hydraulic radius related to the bed, and $3D_{90}$ is the effective roughness height of a movable plane bed. Bed shear velocity related to grains is the effective shear velocity that contributes to sediment transport, and is only a part of the overall bed shear velocity u_*. The overall Chezy roughness coefficient C due to grain and bed form drag is $C<C'$, and as a result $u_* > u_*^{'}$ (see Van Rijn 1984a). The critical bed shear velocity is taken from the “Shields diagram” for incipient motion (e.g., Julien 1995, Yang 1996). The bedload sediment transport equation was calibrated on 130 flume experiments and verified on 524 flume experimental data and 3 field data sets, with satisfactory results (Van Rijn 1984a).

5.5.2 Examples of Tributary Effects

Sediment transport in the GRAD model is based on a critical threshold for incipient motion through the transport stage parameter, the hydraulics of flow (in particular flow depth and velocity) and the local channel bed slope. Therefore, GRAD can model detailed channel change resulting from the variability in the hydraulics of flow and channel bed slope that the ERMO model (which is based on water continuity in terms of mass only) cannot. These conditions occur especially at tributary junctions. In this section examples of aggradation and degradation downstream of a tributary junction are illustrated.

The influx of sediment from a tributary is computed by determining the sediment transport capacity under normal flow conditions at the tributary outlet using the same sediment transport relation as for the main stream. It is hypothesized that the tributary geometry and slope at the confluence reflects the long term sediment contribution rate from the watershed.

The example shown here takes a segment of the Rio Puerco main stream at the junction with Arroyo Chico. The channel bed slope in this section of the Rio Puerco is S=0.0038 m/m (Chapter 2, Table 2.1). The main stream channel width is assumed constant at W=15 m, as in ERMO analyses. The infiltration rate into the streambed is f=6.5 cm/hr, which is the average of point measurements taken at the closest Guadalupe cross section (Chapter 2, Table 2.10). Channel bed slope in the Arroyo Chico tributary is

S=0.0036 m/m (Chapter 2, Table 2.2) and channel width is W=15 m, as in ERMO analyses. Other GRAD parameters were: n=0.03, Δx=50 m, Δt=60 s, p=0.43, φ=0.5, θ=0.5, and the bed sediment particle diameters were D_{50}=0.125 mm and D_{90}=0.325 mm (Chapter 2).

To illustrate degradation downstream of a tributary junction, the following streamflow scenario is shown: the main stream segment is carrying Q=13.8 m^3/s, which is the mean annual maximum daily flow for gage 3340, for a period of t=4 days in sequence. The first t=2 days, the tributary is adding another (a) Q_t = 5 m^3/s, (b) Q_t = 13.8 m^3/s, (c) Q_t = 37.7 m^3/s (case (c) is the mean annual maximum daily flow for gage 3405). These streamflow scenarios in general represent extreme runoff situations in the stream segment.

Simulated channel change after the first two days is shown in Figure 5.27 and after the remaining days 3 and 4 in Figure 5.28. It is clear that rapid degradation occurs with tributary inflow. Up to 0.5 m of degradation was simulated just downstream of the tributary junction after two days of the highest flow conditions. It is interesting that up to 0.3 m of aggradation was simulated upstream of the tributary as a result of the backwater effects reaching up the main stream during the passage of the tributary wave. After the flow from the tributary ceased, the eroded profile begins to smoothen: sediment is gradually removed from steep slopes and deposited downstream. The inflection point between aggradation and degradation also shifts slowly upstream. Continued high streamflow in the main stream segment would gradually lead to aggradation reaching almost the pre-incision level. However, this is a hypothetical scenario, and situations where the main stream at this location carries such high streamflow for an extended period of time and at the same time the Arroyo Chico tributary is dry do not generally occur.

Also shown in Figures 5.27 and 5.28 is the spatial step used in ERMO analyses, Δx=500 m. In ERMO this value was chosen to represent the velocity of a degradation wave in one day. GRAD simulations show that this value well represents the transient nature of degradation waves in the Rio Puerco main stream downstream of tributaries.

In summary, the presented example shows that: (1) Rapid erosion is simulated at tributary junctions where the sediment transport capacity downstream of the confluence is higher than the supply of sediment. This region of erosion gradually extends in the downstream direction. (2) A longitudinal redistribution of sediment occurs in the vicinity of tributary junctions, in particular in periods of no tributary inflow. The latter point is well supported by observations of ephemeral streams where breaks in longitudinal profiles were found to be quickly removed by degradation processes (Schumm 1961) and is at the heart of the hypothesis of intrinsic thresholds in arroyo formation (Schumm and Hadley 1957). Although infiltration into the streambed results in general aggradation, this effects is not so clear in this example, because of extremely high streamflow.

These encouraging results support long-term ERMO analyses and show the importance of spatial variability in runoff in ephemeral stream systems. However, the results do not imply that degradation always occurs downstream of tributaries. It is always the balance of sediment supply and transporting capacity of streamflow that determines the outcome. These issues will be addressed in Chapter 6.

5.5.3 Simulated Sediment Transport

Perhaps the most crucial element in channel erosion modeling is the choice of the sediment transport equation (e.g., Dawdy and Vanoni 1986). In this section GRAD-simulated sediment transport using Van Rijn's (1984a) bedload formula is discussed for the example cases and for the Bernardo gage at the outlet of the Basin.

For the Rio Puerco bed material particle diameters we get $D_{*} = 3.16$ (from 5.10). The critical bed shear velocity for this sediment size according to Van Rijn (1984a) is:

$$u_{*cr}^{2} = \frac{0.24}{D_{*}}(G-1)g\,D_{50} \tag{5.46}$$

which gives $u_{*cr} = 0.012$ m/s. In the above example with no tributary inflow, Chezy grain roughness is C'=69.2 m$^{0.5}$s in the main stream link and the resulting bed shear velocity related to grains is $u_{*}' = 0.067$ m/s. With tributary inflows Q_t>0, u_{*}' increases. As a result, the transport stage parameter T for all high flow example cases was T>100, indicating strong upper flow regime (Van Rijn, 1984c). Simulated bedload transport in the main stream for the case of no tributary inflow was Q_b=193 m^3/day, and it varied between 365 m^3/day (Q_t=5 m^3/s) and 2,943 m^3/day (Q_t=37.7 m^3/s) for the cases with tributary inflow.

To compare these transport rates with the bedload sediment rating curve developed for the Rio Puerco and used in the ERMO model, we look at sediment transport at the Bernardo gage. Here, the channel width is approximately W=7 m, average channel bed slope for main stream Subbasin 1* is S=0.0015 (Table 2.1), and the bed material is the same as for the example cases above. Overall channel roughness was chosen n=0.03; i.e., the overall Chezy roughness coefficient is

$$C = R_h^{1/6} / n \tag{5.47}$$

and flow was assumed normal. The crucial issue is to separate grain roughness and drag due to bed forms in the overall roughness term C, and to determine the effective bed shear velocity (i.e., grain velocity), for bedload sediment transport (Van Rijn 1984a). An example of estimated annual bedload transport at the Bernardo gage for varying discharge Q is shown in Figure 5.29 for two cases: (1) Grain shear velocity; i.e., the case where C' is computed from Equation (5.45) and bed shear velocity due to grains is a small fraction of overall bed shear velocity $u_*' << u_*$. (2) Total shear velocity; i.e., the case where $C'=C$ computed from Equation (5.47). Here it is assumed that the overall shear velocity is identical to bed shear velocity due to grains $u_*' = u_*$, meaning that total bed shear stress is available for sediment transport and bed form drag is neglected.

Figure 5.29 is constructed in such a way that every chosen streamflow Q is assumed to last for n days in the model year ensuring that the annual streamflow is always 35.9 mil m^3/yr. (For example, Q=15 m^3/s would have to last for n=27.7 days.) The annual bedload transport Q_b is computed based on this. It is clear from this figure that the original Van Rijn's formula, case (1), underestimates annual bedload in the Rio Puerco by a factor of 10 (for high flows). On the other hand, neglecting bed form drag gives approximately the same annual bedload rate as ERMO simulations. Although this analysis is very simplified, it illustrates the importance of bed form drag on sediment transport. In the upper flow regime, the streambed typically consists of antidunes, or standing waves, which are in phase with the free surface waves. It has been shown that these bedforms can and do exert strong influences on sediment transport in the Rio Puerco (e.g. Nordin 1963).

Table 5.1. Suspended sediment concentration data at three streamflow gaging stations with automated pumping sediment samplers. Record periods are according to water years from the WATSTORE Database. N_{tot} is the total number of days in the period excluding days with estimated values of sediment concentration. N_{rec} is the number of days with a measured sediment concentration $C>0$. Average daily Q and C are computed only for days with $C>0$. C_v is sediment concentration by volume.

Gaging Station	**3340**	**3405**	**3530**
Record period/s	1955-56, 81-89, 91-95	1955-56, 78-86	1955-89, 91-95
N_{rec} [days]	3146	2719	4803
N_{tot} [days]	4544	2993	13567
Record length [yr]	12.5	8.2	37.2
Daily Q [m^3/s]			
Average	0.725	0.608	3.029
Maximum	31.4	30.9	142
Daily C [mg/l]			
Average	24,792	15,110	62,167
Maximum	214,000	201,000	269,000
Daily C_v [m^3/m^3]			
Average	0.0094	0.0057	0.023
Maximum	0.081	0.076	0.102
Average annual susp. sediment load			
L [T/yr]	0.683 (10^6)	0.948 (10^6)	3.46 (10^6)
L [m^3/yr]	0.258 (10^6)	0.358 (10^6)	1.31 (10^6)

Table 5.2. ERMO calibration for the current climate. V is the cumulative volume of channel change after 100 years from initial conditions. Maximum rates of channel change are: (1) Δz_{max} is (a) the maximum vertical channel change from the initial conditions during the 100-year simulation, and in parentheses (b) the maximum annual vertical channel change (i.e., vertical channel change that occurred in one year) ; and (2) ΔW_{max} is the maximum change in channel width from the initial conditions during the 100-year simulation.

Run	f [cm/hr]	V [mil m^3]	Δz_{max} Aggradation [m]	Δz_{max} Degradation [m]	ΔW_{max} Narrowing [m]	ΔW_{max} Widening [m]
1	0.39	-0.2	1.12 (0.54)	3.51 (0.77)	2.23	7.86
2	1.01	2.198	2.23 (0.65)	3.63 (0.69)	4.46	8.42
3	0.83	1.218	2.06 (0.9)	4.46 (1.74)	3.65	11.06
4	0.75	1.486	1.85 (0.4)	4.13 (0.65)	3.71	9.56
5	0.58	0.447	1.53 (0.55)	3.8 (0.98)	3.07	8.85
6	0.43	-0.243	1.29 (0.83)	3.8 (1.14)	2.31	8.98
7	0.68	1.199	1.74 (0.61)	3.64 (0.84)	3.49	8.7
8	0.86	1.568	1.93 (0.71)	4.23 (1.6)	3.87	10.42
9	1.01	2.415	2.29 (0.64)	3.47 (0.99)	4.59	8.36
10	0.54	0.475	1.42 (0.58)	3.94 (1.03)	2.85	8.82
11	0.67	1.069	1.65 (0.64)	3.92 (2.16)	3.31	10.33
12	0.68	0.916	1.91 (0.82)	3.88 (1.08)	3.22	8.87
13	0.33	-0.578	0.96 (0.29)	3.87 (1.19)	1.92	8.78
14	0.75	1.253	2.15 (1.1)	3.57 (1.24)	3.64	9.7
15	0.53	0.295	1.39 (0.8)	3.59 (2.2)	2.78	9.46
16	0.76	1.282	1.79 (0.75)	3.71 (0.62)	3.58	8.42
17	0.54	0.472	1.41 (0.49)	3.6 (1.42)	2.83	8.2
18	0.42	-0.226	1.12 (0.58)	3.88 (1.35)	2.25	8.95
19	0.55	0.601	1.5 (0.34)	3.5 (0.79)	3.0	8.3
20	0.76	1.435	1.91 (0.54)	3.57 (0.7)	3.83	8.61
Average	0.654	0.854	1.66 (0.64)	3.79 (1.16)	3.23	9.03
St. Dev.	0.193	0.811	0.39 (0.19)	0.26 (0.47)	0.73	0.82
Coeff. Var.	0.295	0.950	0.231 (0.304)	0.07 (0.405)	0.224	0.091
Minimum	0.33	-0.578	0.96 (0.29)	3.47 (0.62)	1.92	7.86
Maximum	1.01	2.415	2.29 (1.1)	4.46 (2.2)	4.59	11.06

Table 5.3. ERMO calibration for the current climate conditions: streamflow results. Q is the long-term average annual runoff for each run at the main streamflow gages. Q_p (in parentheses) is the average annual maximum daily flow at each gage. Note that at Bernardo (gage 3530), Q was calibrated to be equal to the long-term average (35.9 mil m^3/yr) in all runs.

Run	**3530** Q [mil m^3/yr] Q_p [m^3/s]	**3515** Q [mil m^3/yr] Q_p [m^3/s]	**3405** Q [mil m^3/yr] Q_p [m^3/s]	**3340** Q [mil m^3/yr] Q_p [m^3/s]
1	35.9 (66.8)	8.66 (16.5)	16.4 (31.0)	8.52 (24.4)
2	35.9 (87.7)	10.6 (19.3)	20.6 (40.2)	9.41 (33.3)
3	35.9 (83.5)	10.2 (19.9)	19.3 (35.1)	9.2 (27.4)
4	35.9 (82.5)	10.1 (19.0)	19.1 (33.5)	9.01 (32.1)
5	35.9 (76.4)	9.69 (18.2)	17.8 (31.1)	8.57 (28.0)
6	35.9 (80.5)	8.52 (16.0)	16.7 (34.4)	8.93 (30.6)
7	35.9 (81.5)	9.79 (19.4)	18.9 (36.7)	8.86 (28.7)
8	35.9 (90.7)	9.9 (18.4)	20.0 (39.2)	9.48 (32.6)
9	35.9 (79.4)	11.0 (19.5)	20.6 (34.4)	8.99 (28.6)
10	35.9 (81.9)	9.35 (19.3)	17.7 (35.0)	8.4 (28.1)
11	35.9 (77.4)	10.0 (19.2)	18.6 (34.5)	9.06 (32.0)
12	35.9 (86.2)	9.83 (19.2)	18.6 (35.3)	8.57 (31.6)
13	35.9 (63.4)	8.5 (15.7)	15.3 (26.1)	8.68 (24.4)
14	35.9 (85.9)	9.69 (19.3)	19.3 (36.6)	9.49 (30.2)
15	35.9 (81.7)	9.49 (19.2)	17.0 (30.0)	8.95 (30.5)
16	35.9 (81.1)	10.1 (21.3)	19.0 (34.2)	9.21 (29.3)
17	35.9 (72.3)	9.23 (16.7)	17.6 (32.6)	8.54 (26.6)
18	35.9 (73.7)	8.94 (19.1)	16.4 (30.9)	8.6 (25.9)
19	35.9 (77.9)	9.43 (17.0)	17.7 (33.9)	8.84 (28.4)
20	35.9 (82.0)	9.58 (16.4)	19.6 (37.3)	9.71 (33.6)
Average	35.9 (79.6)	9.63 (18.4)	18.3 (34.1)	8.95 (29.3)
St. Dev.	(6.68)	0.66 (1.51)	1.47 (3.26)	0.37 (2.77)
Coeff. Var.	(0.084)	0.068 (0.082)	0.08 (0.096)	0.042 (0.094)
Minimum	(63.4)	8.5 (15.7)	15.3 (26.1)	8.4 (24.4)
Maximum	(90.7)	11.0 (21.3)	20.6 (40.2)	9.71 (33.6)

Table 5.4. Results of changing climate on streamflow, sediment transport and erosion. Climate precipitation scenarios were modeled with RMS given annual rainfall P (each scenario contained 20 runs) and C_v=0.23, n=100 years. ERMO parameters were f=0.654 cm/hr, h=1, γ=0.053. Q is average annual streamflow and Q_p is average annual maximum daily flow at a given gage. Q_b is average annual bedload and Q_t average annual total load at Bernardo. V is the average cumulative volume of channel change after 100 years of simulation. Δz_{max} is the average 100-year and annual maximum vertical channel change and ΔW_{max} is the average 100-year maximum change in channel width.

VARIABLES:	DRY CLIMATE (P=200 mm)		CURRENT CLIMATE (P=280 mm)		WET CLIMATE (P=400 mm)	
STREAMFLOW	Q	Q_p	Q	Q_p	Q	Q_p
Q [mil m^3/yr] and Q_p [m^3/s]						
3530 (Bernardo)	23.39	62.7	35.62	79.6	55.61	109
3515 (San Jose near Correo)	6.64	14.7	9.63	18.4	14.5	24.9
3405 (Arroyo Chico)	12.64	26.9	18.3	34.1	27.5	46.8
3340 (Rio Puerco a. A. Chico)	5.98	22.5	8.9	29.3	13.1	39.3
SEDIMENT TRANSPORT						
Q_b [mil m^3/yr] at 3530	0.051		0.079		0.127	
Q_t [mil m^3/yr] at 3530	1.01		1.56		2.53	
EROSION and DEPOSITION						
V [mil m^3]	1.026		0.921		0.266	
Δz_{max} aggradation [m] 100-year	1.25 (0.05)*		1.85 (0.28)*		2.62 (0.21)*	
Δz_{max} degradation [m] 100-year	3.46 (0.09)		3.74 (0.1)		3.93 (0.1)	
ΔW_{max} narrowing [m] 100-year	2.49 (0.05)		3.28 (0.03)		4.06 (0.17)	
ΔW_{max} widening [m] 100-year	8.2 (0.09)		8.97 (0.11)		9.65 (0.14)	
Δz_{max} aggradation [m] annual	0.50 (0.37)		0.63 (0.28)		1.09 (0.52)	
Δz_{max} degradation [m] annual	0.92 (0.37)		1.14 (0.41)		1.35 (0.26)	

* The term in parentheses is the coefficient of variation of the estimates.

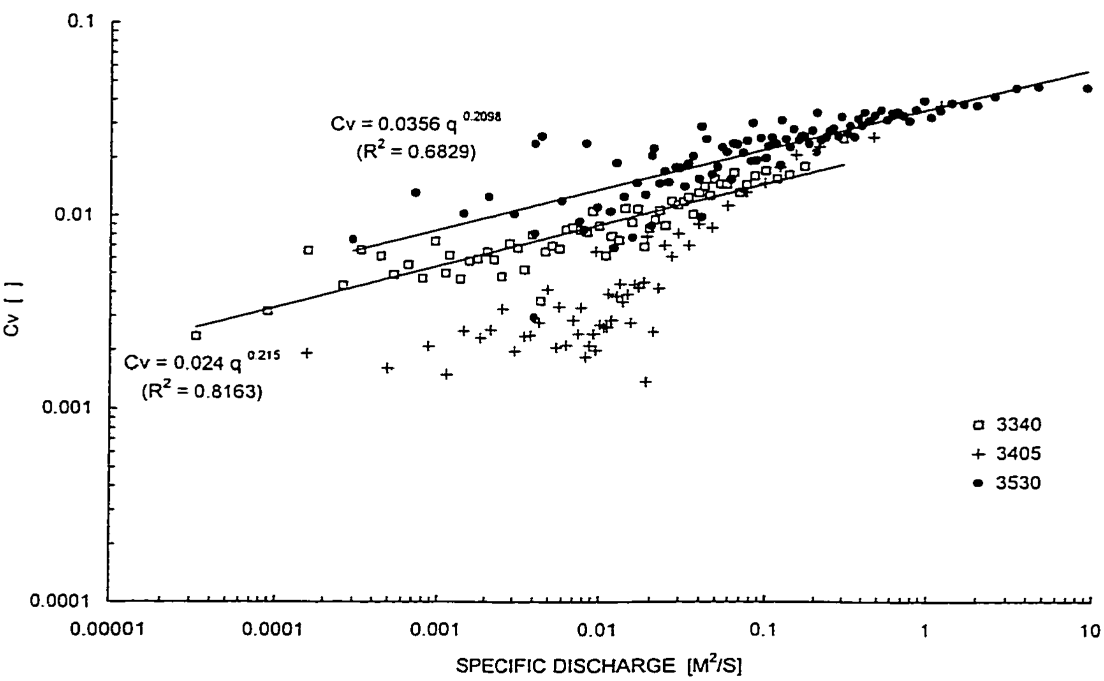

Figure 5.1. Daily suspended sediment rating curves for the Rio Puerco gages 3340, 3405 and 3530. Data were binned into classes with 50 points, and averages are plotted. Linear regression on log-transformed data is shown for the Rio Puerco main stream gages 3340 and 3530.

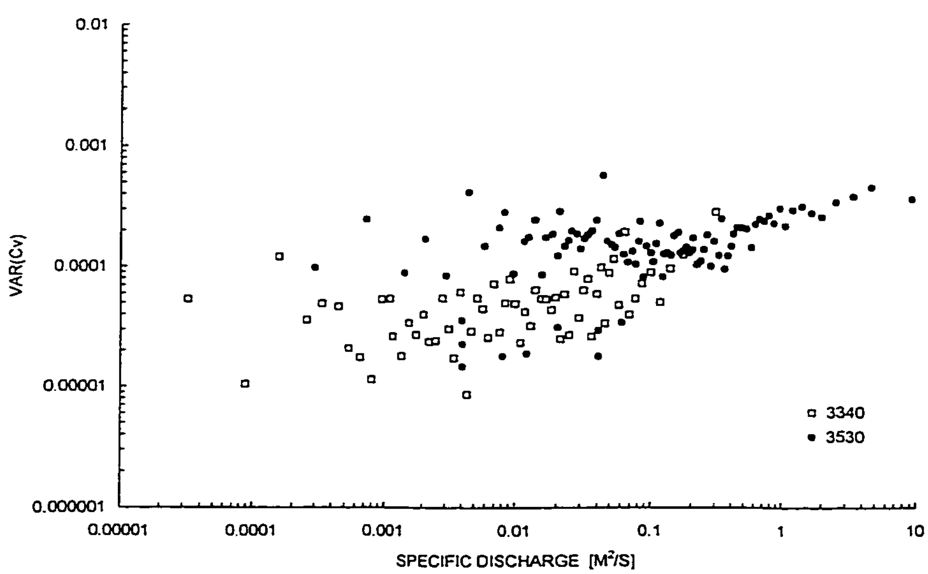

Figure 5.2. Scaling of the variance of volumetric suspended sediment concentration for gaging stations 3340 and 3530 on the Rio Puerco main stream. Each point is the unbiased variance of 50 measurements.

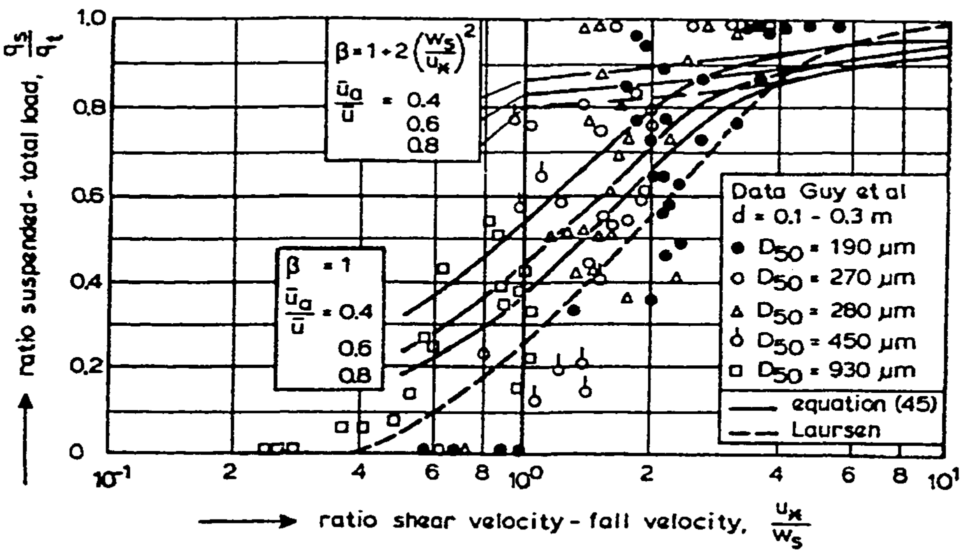

Figure 5.3. Ratio of suspended load to total load according to the theory of Van Rijn (1984b), with data from Guy et al. (1966).

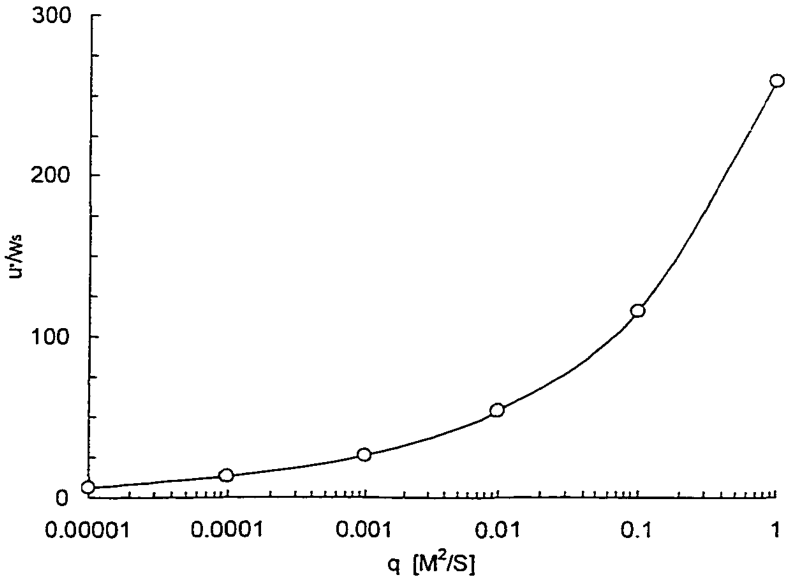

Figure 5.4. Relationship between specific discharge and the ratio u^*/ω estimated for the Bernardo gaging station.

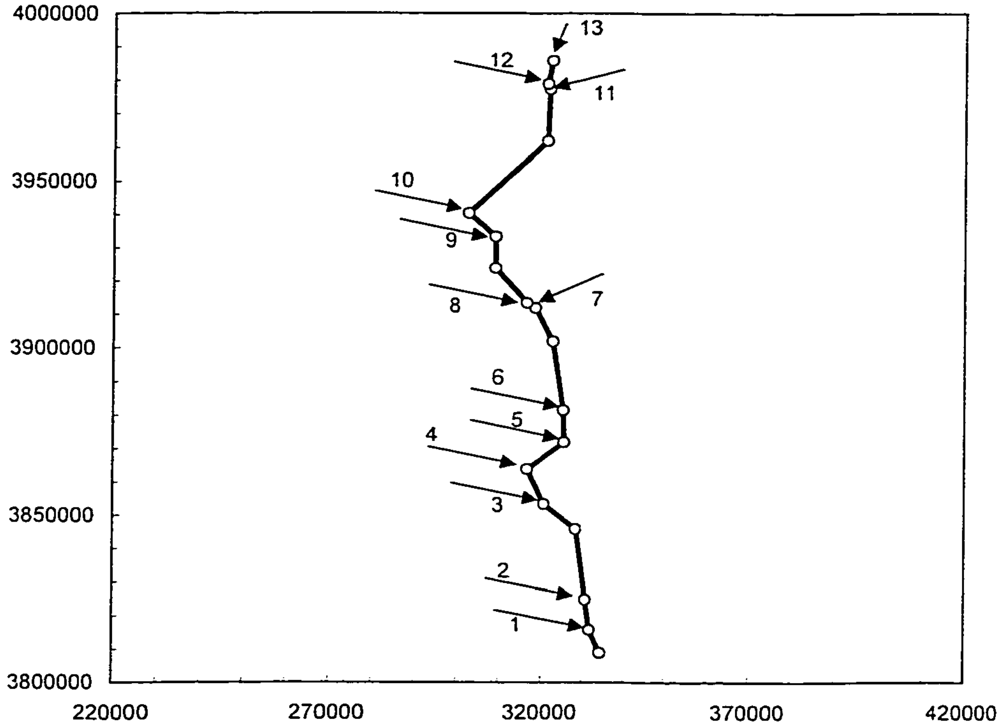

Figure 5.5. Schematic of the Rio Puerco main stream, with 13 tributaries (1-12 are side tributaries and 13 is the headwater tributary) and 17 internal links in between nodes. The internal links correspond to 12 main stream subbasins delineated in Chapter 2 (Figure 2.3). The x and y axes are in UTM coordinates [m].

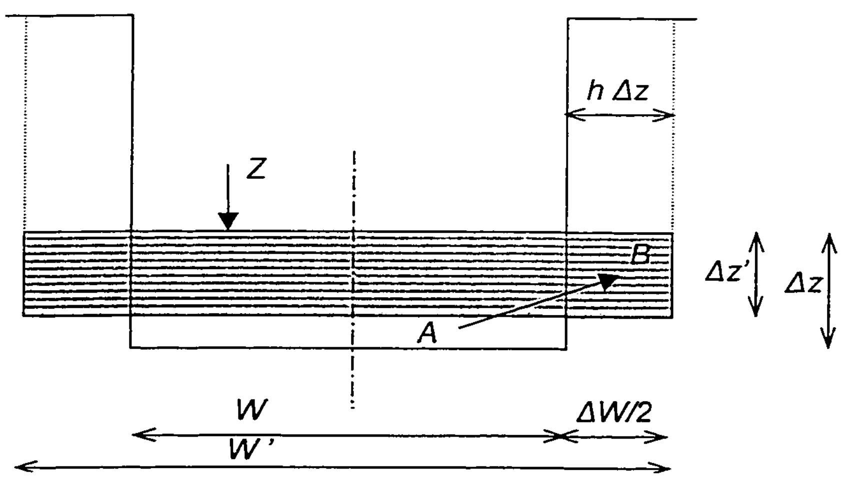

Figure 5.6. Schematic of channel width changes in ERMO. Redistribution occurs between cross-sectional areas A and B.

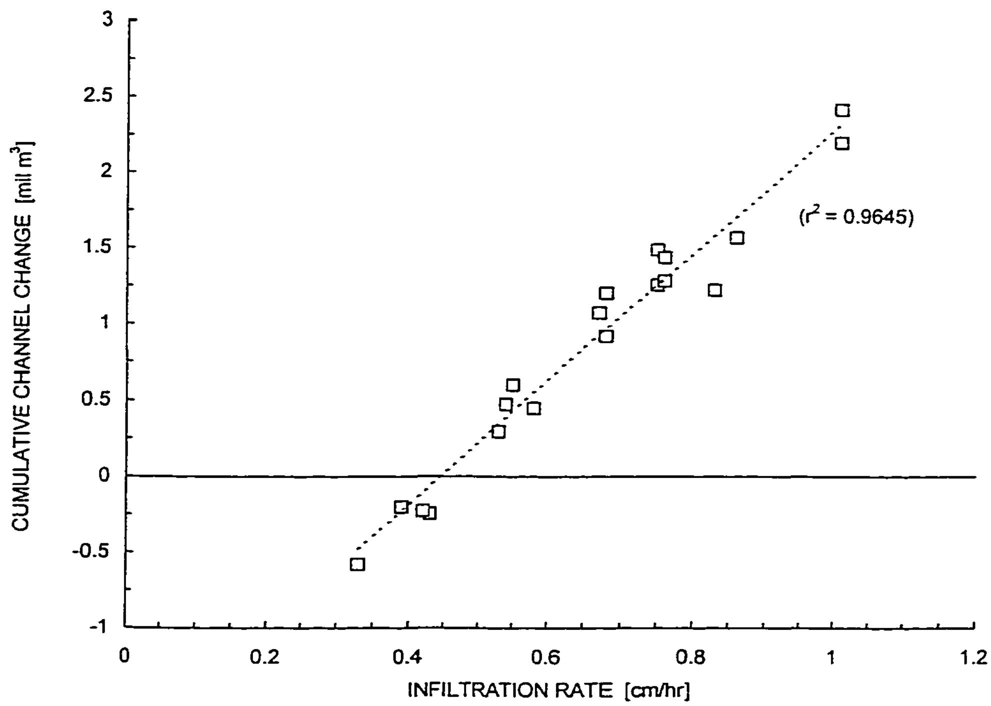

Figure 5.7. Cumulative volume of channel change V after 100 years of simulation for 20 runs of the current climate calibration as a function of the infiltration parameter f. The parameter f was calibrated to ensure that the long-term average annual runoff at the outlet of the Basin was 35.9 mil m^3/yr in all runs.

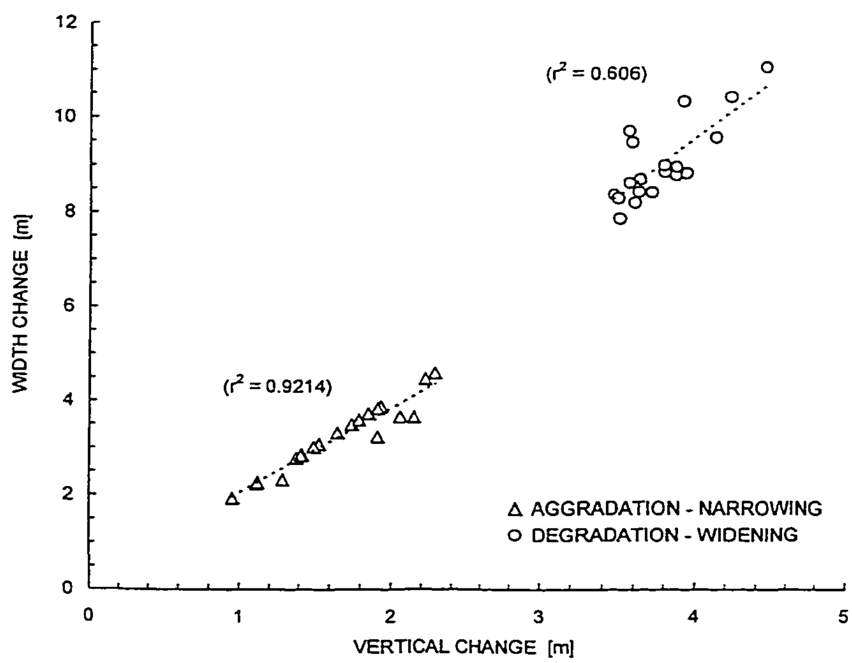

Figure 5.8. Comparison of the maximum 100-year channel depth and width change for the current climate scenario.

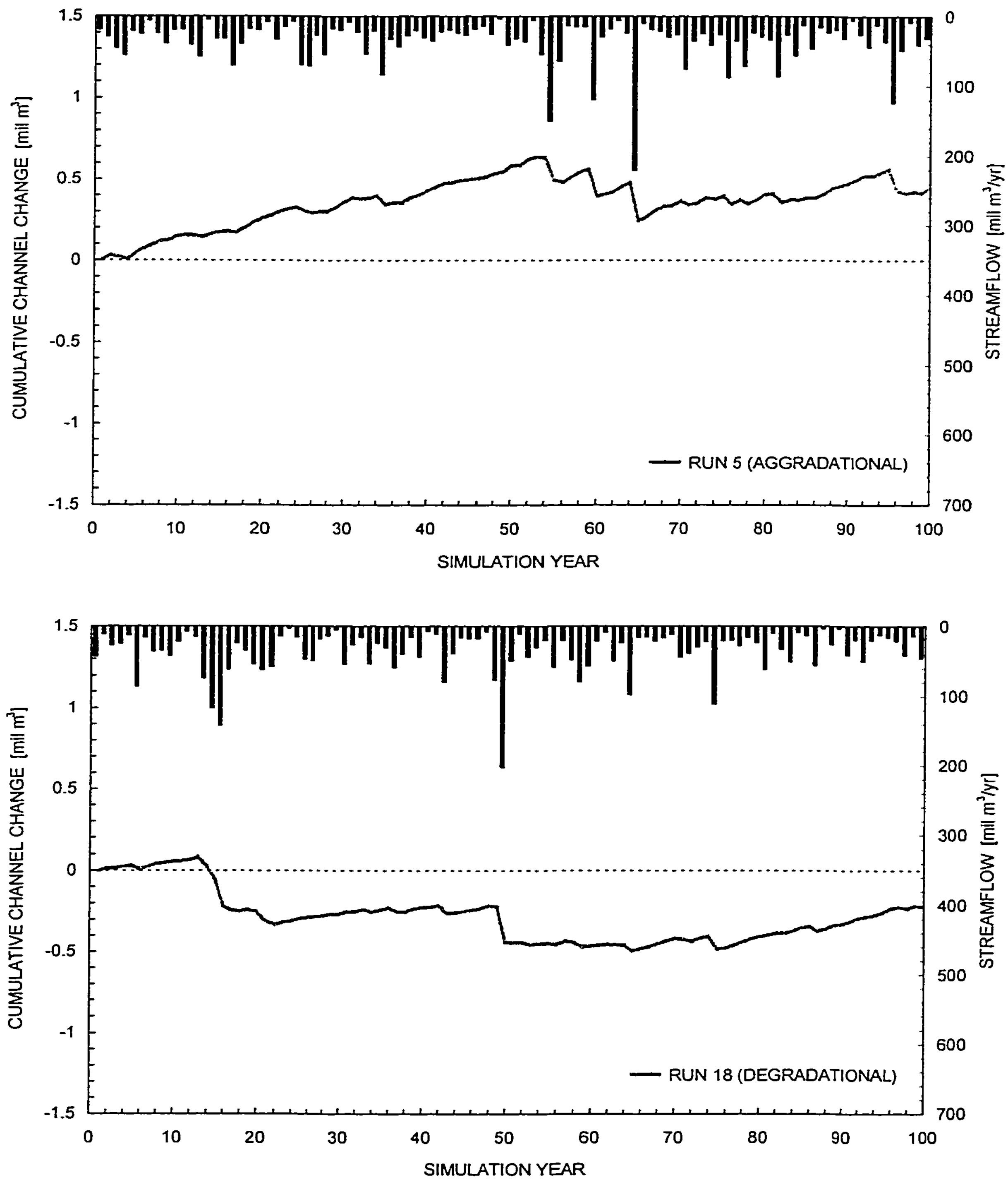

Figure 5.9. Cumulative change in channel volume from initial conditions for the current climate scenario for the aggradational Run 5 (top) and degradational Run 18 (bottom). If we neglect changes in channel width, a change in channel depth of 0.1 m throughout the whole Rio Puerco main stream would result in a change in channel volume of ΔV=0.321 mil m^3. Streamflow is the annual runoff at Bernardo.

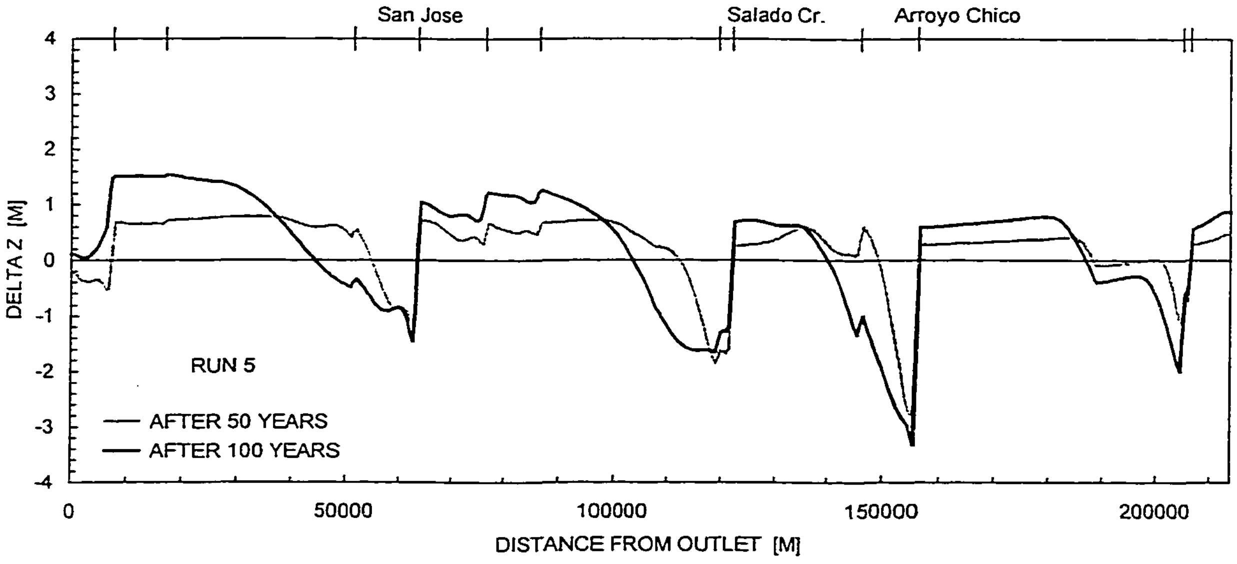

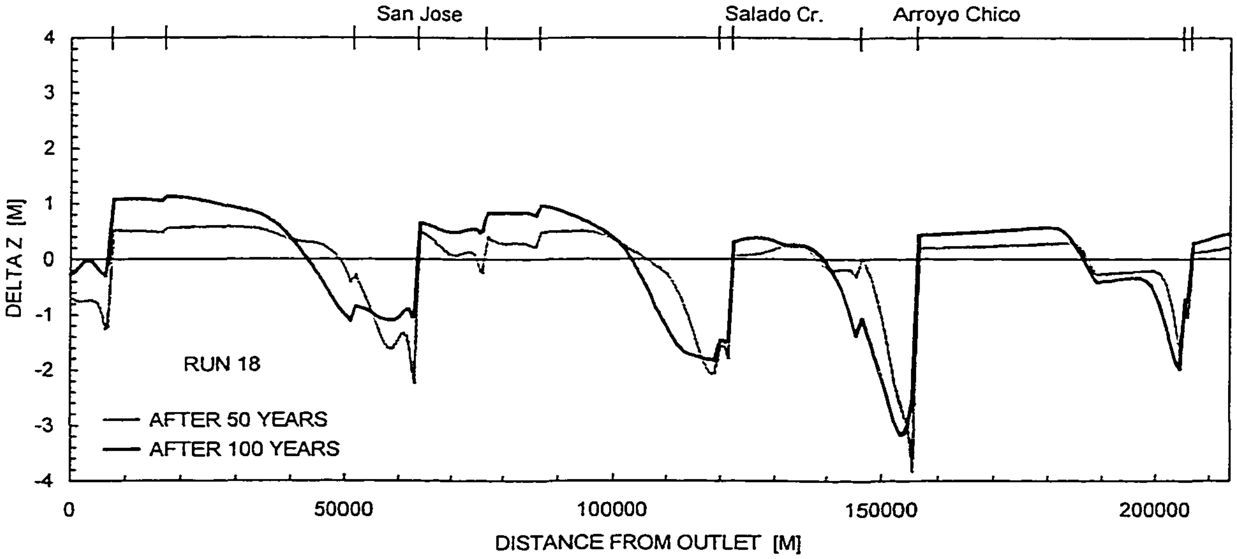

Figure 5.10. Longitudinal distribution of vertical channel change from initial conditions in the Rio Puerco for Run 5 (top) and Run 18 (bottom). The locations of all tributaries are shown on top axis of graphs (three most active tributaries are named).

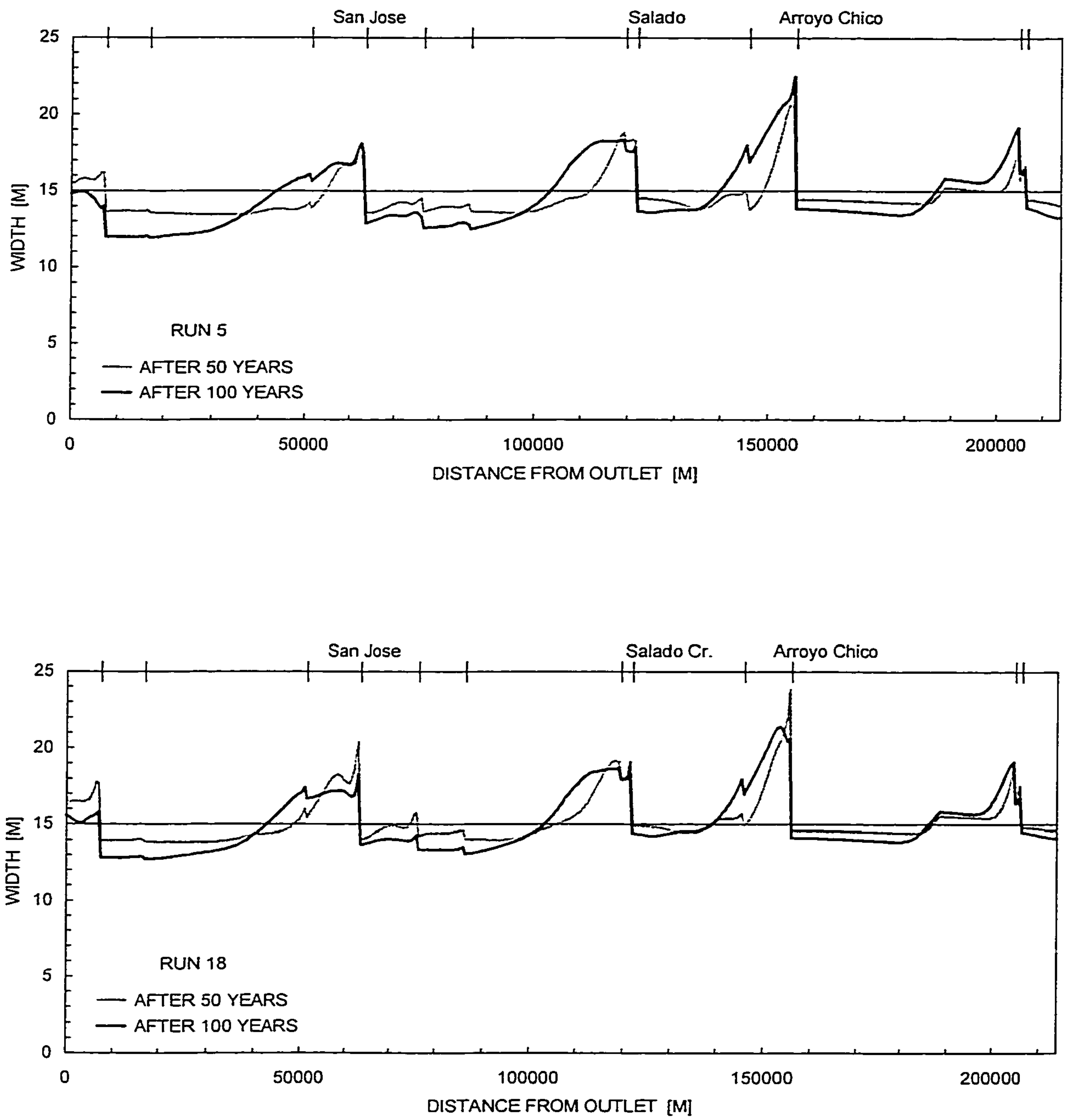

Figure 5.11. Longitudinal distribution of change in channel width from initial conditions in the Rio Puerco for Run 5 (top) and Run 18 (bottom). The locations of all tributaries are shown on top axis of graphs (three most active tributaries are named).

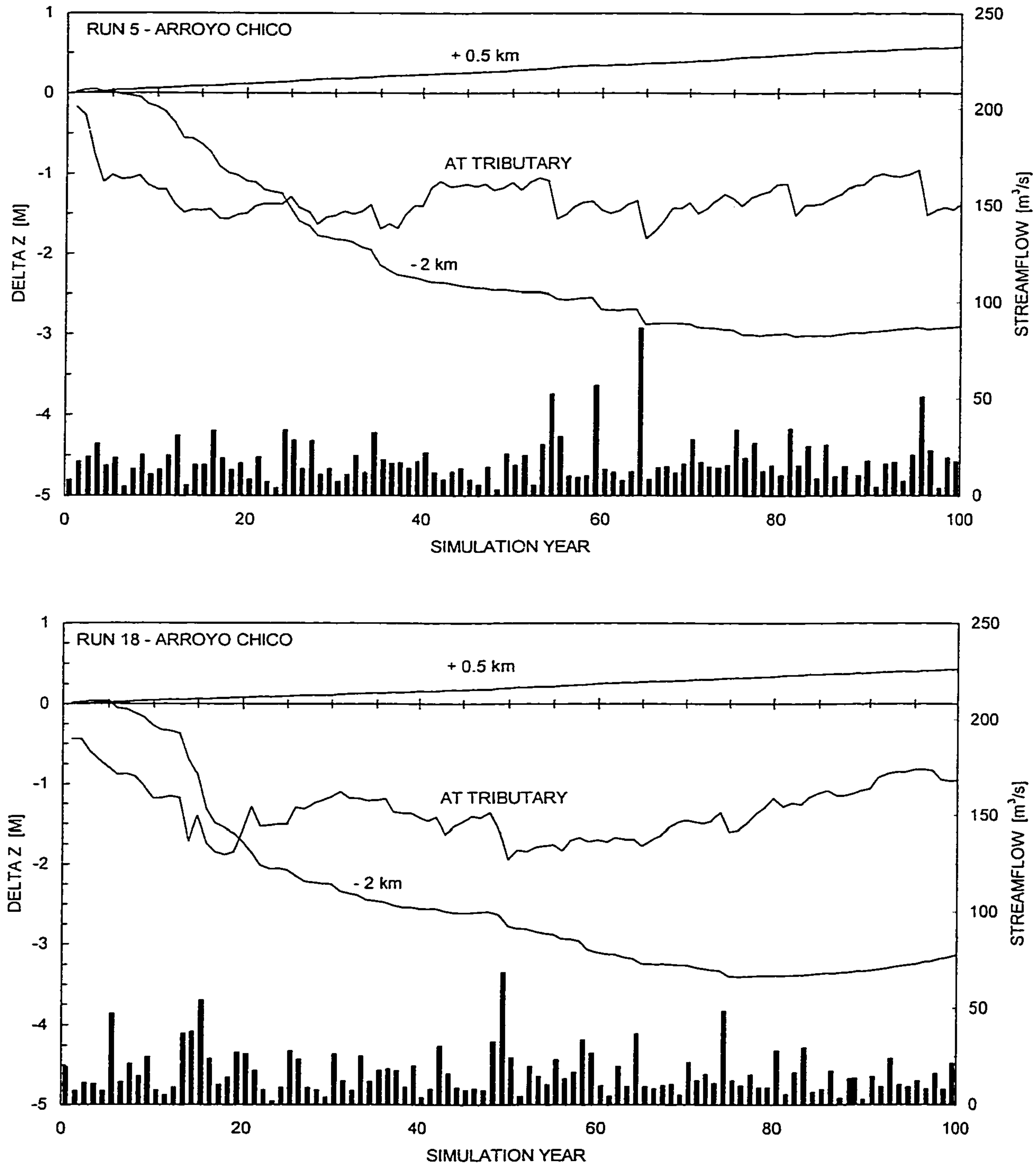

Figure 5.12. Change in channel depth from initial conditions on the Rio Puerco main stream at the Arroyo Chico tributary and two locations upstream (+0.5 km) and downstream (-2 km) of the junction for Run 5 (top) and Run 18 (bottom). Streamflow is the annual runoff simulated at the Arroyo Chico tributary.

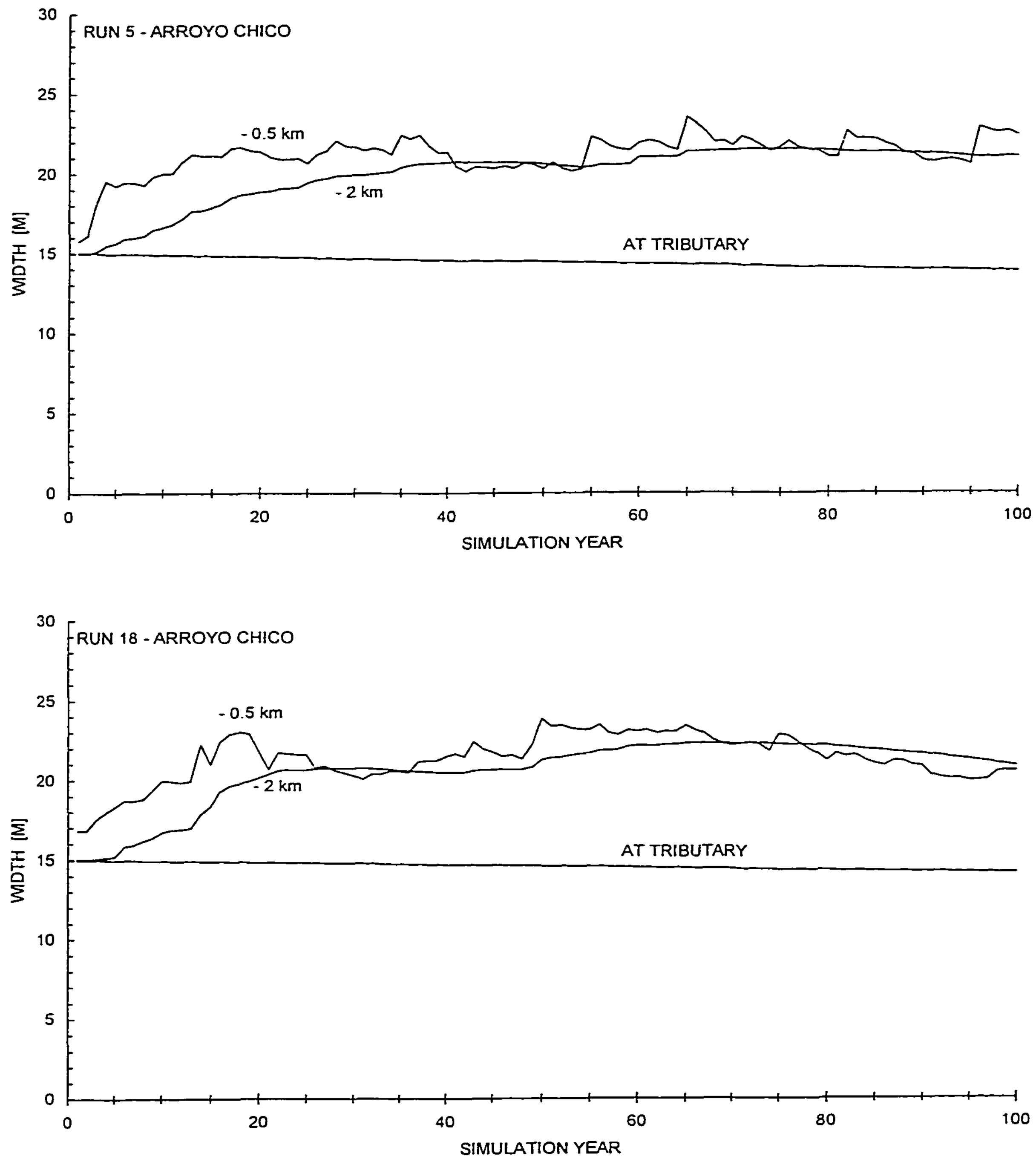

Figure 5.13. Channel width on the Rio Puerco main stream at the Arroyo Chico tributary and two locations downstream (-0.5 km and -2 km) of the junction for Run 5 (top) and Run 18 (bottom). The initial main stream channel width was W=15 m.

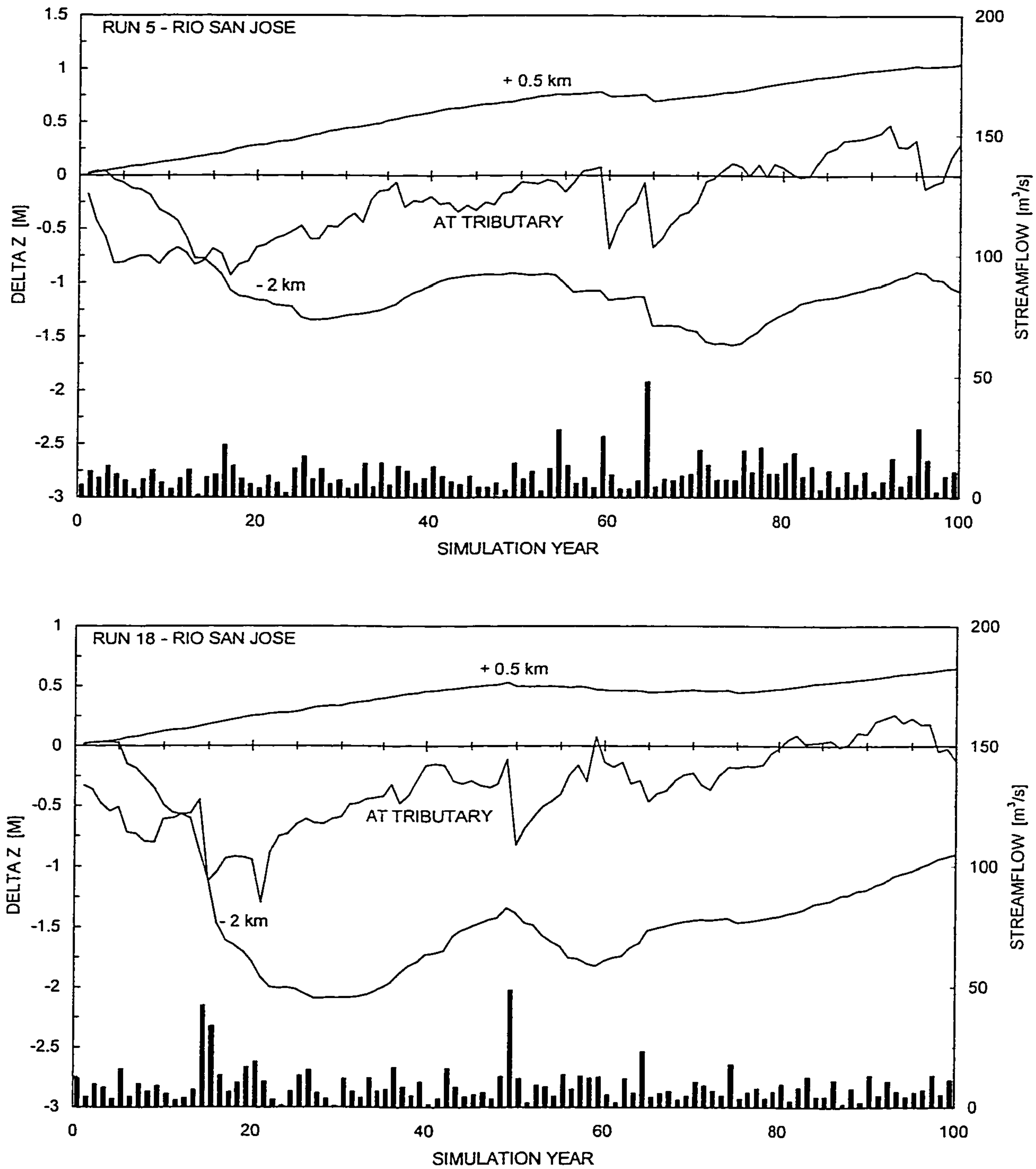

Figure 5.14. Change in channel depth from initial conditions on the Rio Puerco main stream at the San Jose tributary and two locations upstream (+0.5 km) and downstream (-2 km) of the junction for Run 5 (top) and Run 18 (bottom). Streamflow is the annual runoff simulated at the San Jose Correo tributary.

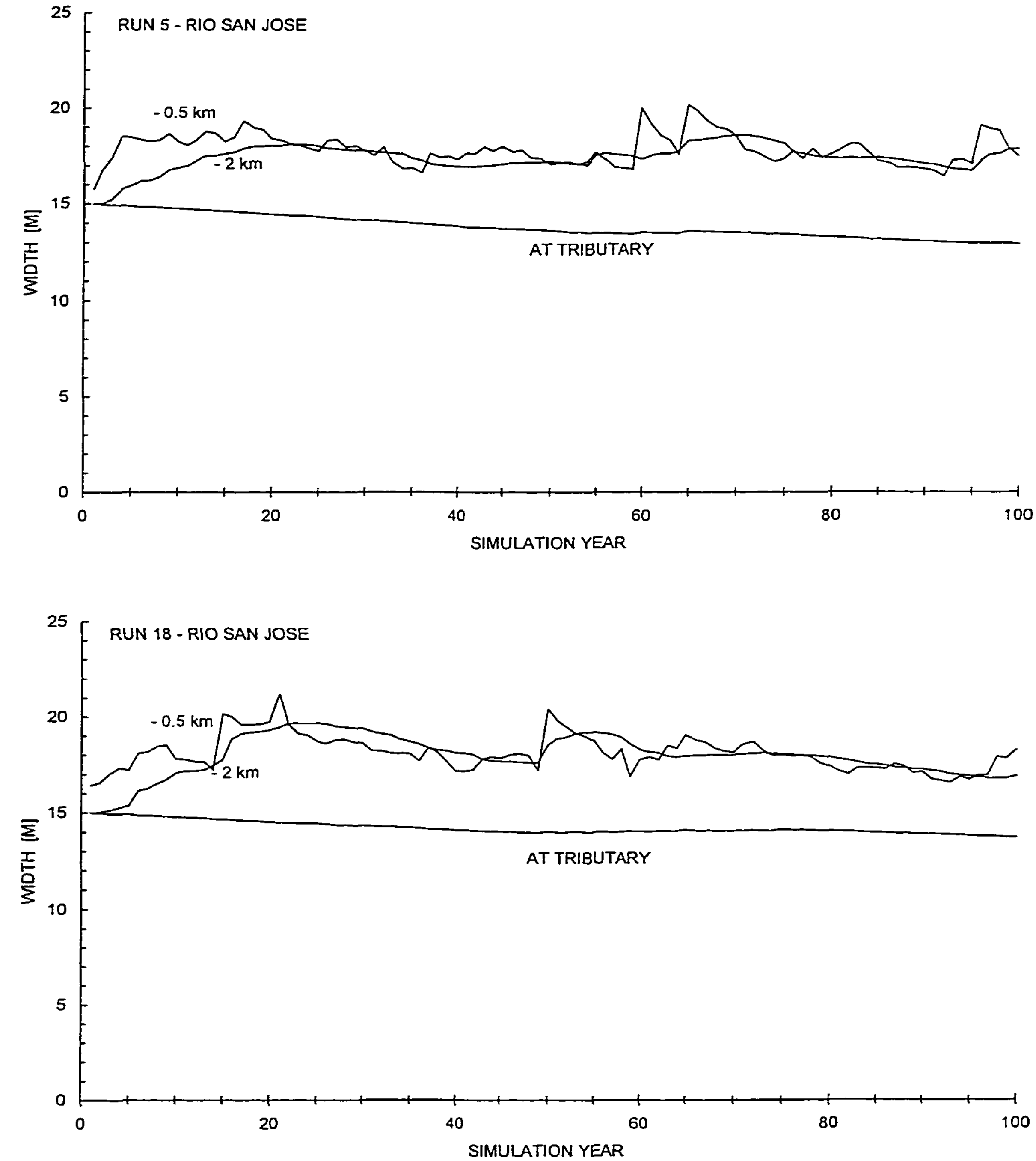

Figure 5.15. Channel width on the Rio Puerco main stream at the Rio San Jose tributary and two locations downstream (-0.5 km and -2 km) of the junction for Run 5 (top) and Run 18 (bottom). The initial main stream channel width was W=15 m.

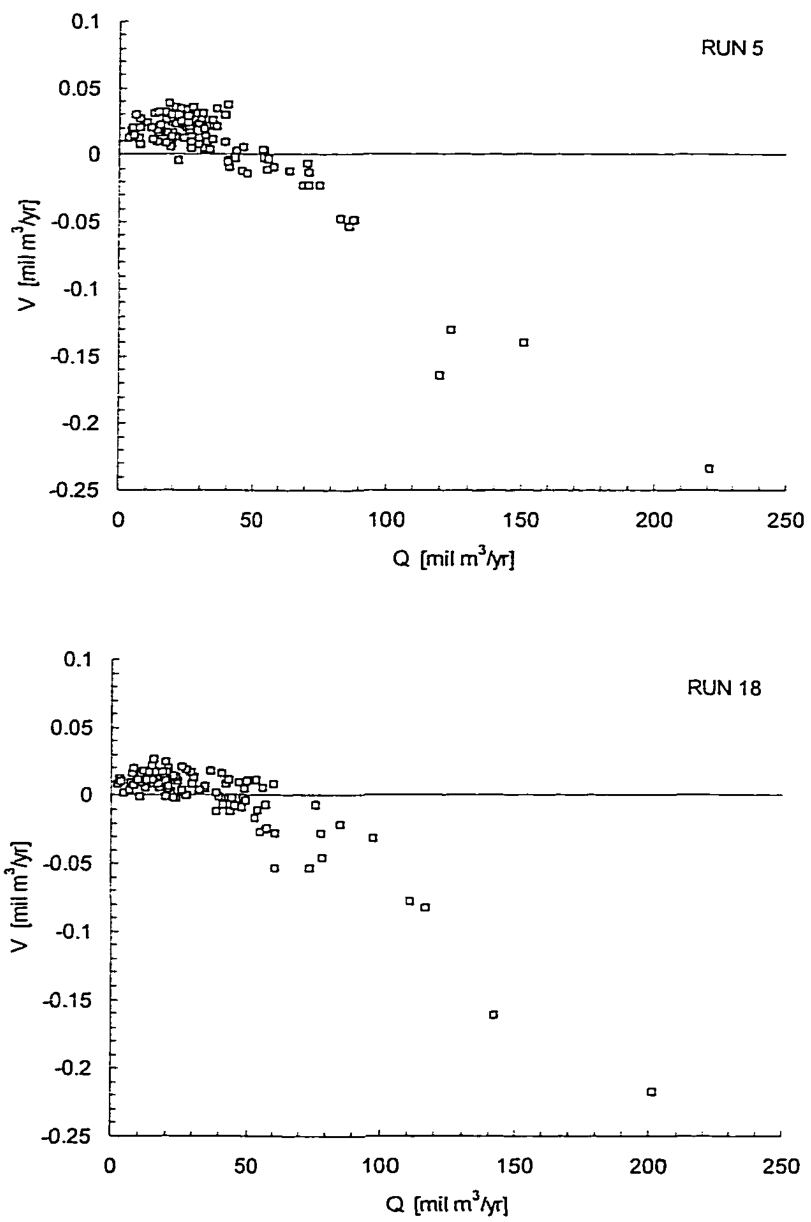

Figure 5.16. Annual volume of channel change as a function of annual streamflow at the outlet of the Rio Puerco Basin in Run 5 (top) and Run 18 (bottom).

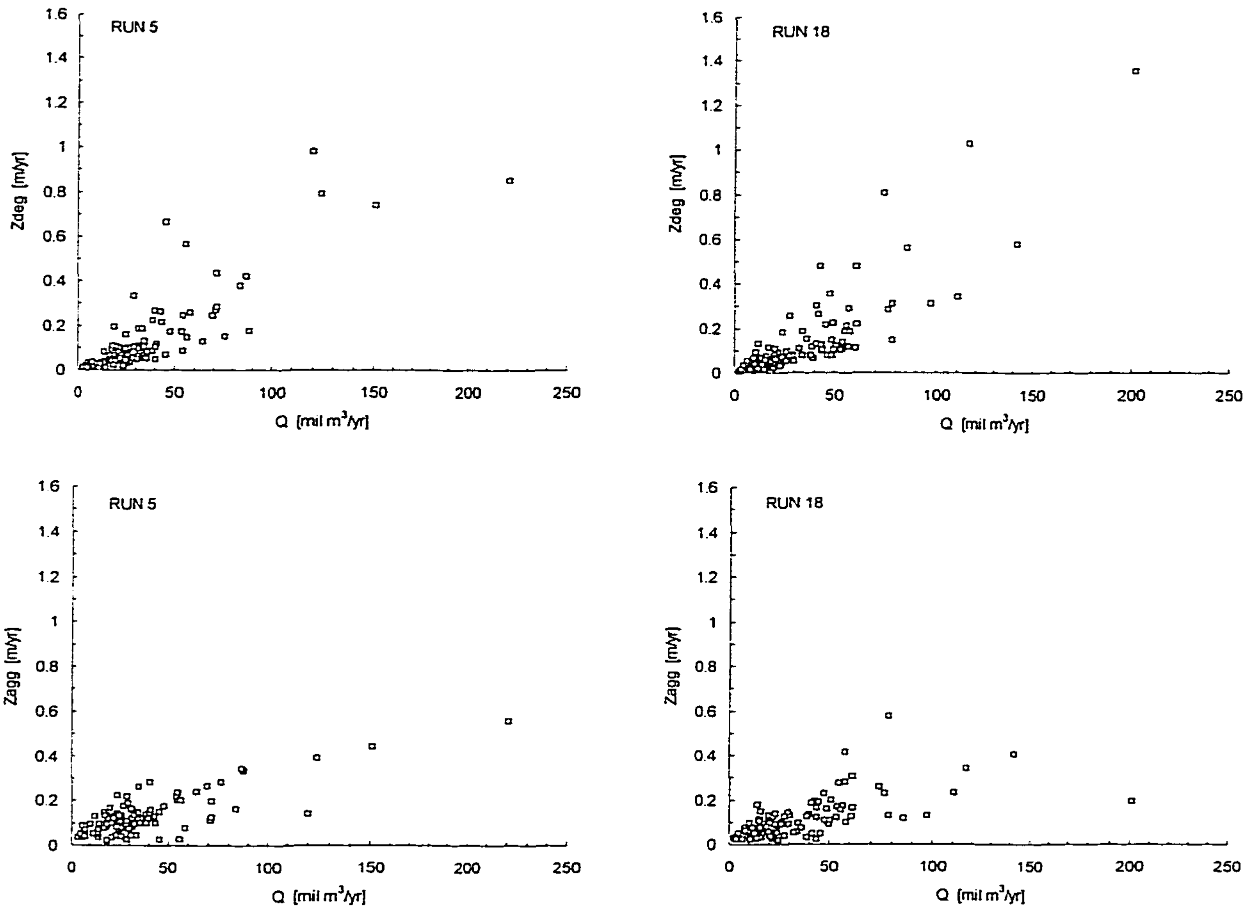

Figure 5.17. Maximum annual degradation (top) and aggradation (bottom) depths in 100 years as a function of annual streamflow at the Basin outlet for Run 5 and Run 18 of the current climate scenario.

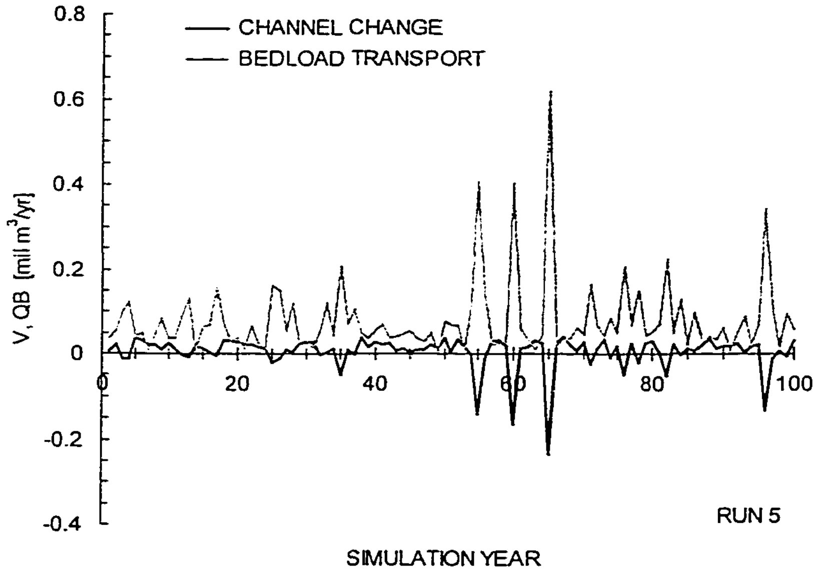

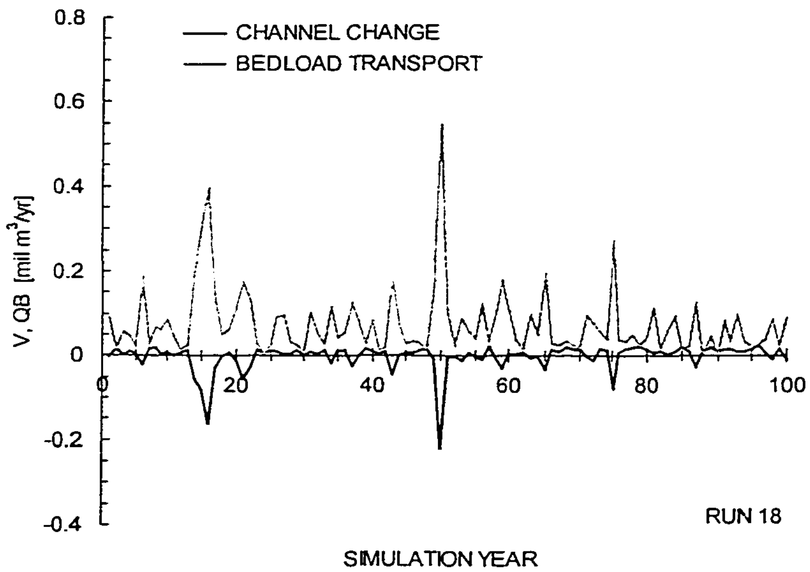

Figure 5.18. Annual channel change V and bedload sediment transport Q_b for Run 5 (top) and Run 18 (bottom).

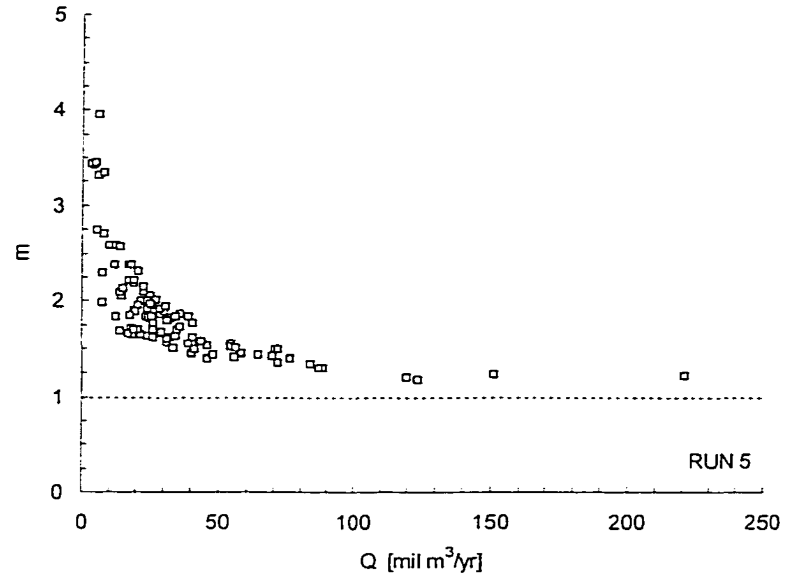

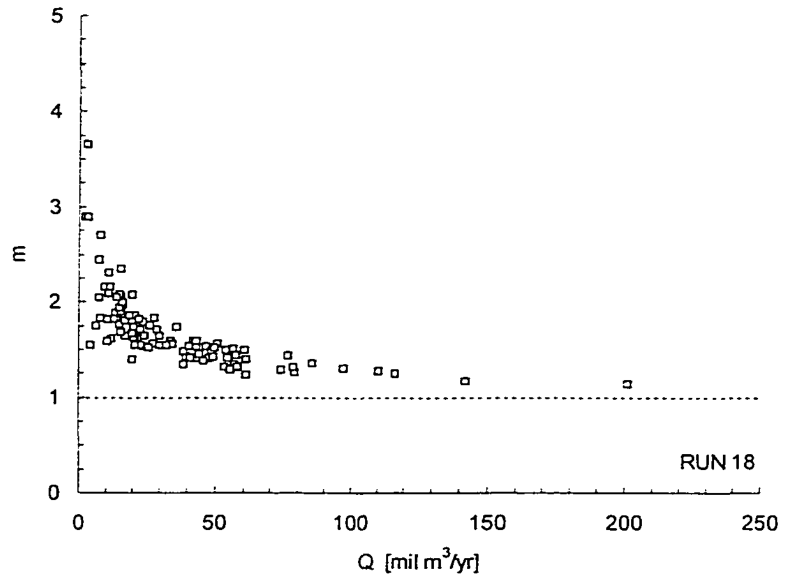

Figure 5.19. The annual streamflow effectiveness ratio *m* (subbasin runoff to total simulated runoff) as a function of annual streamflow at the Basin outlet.

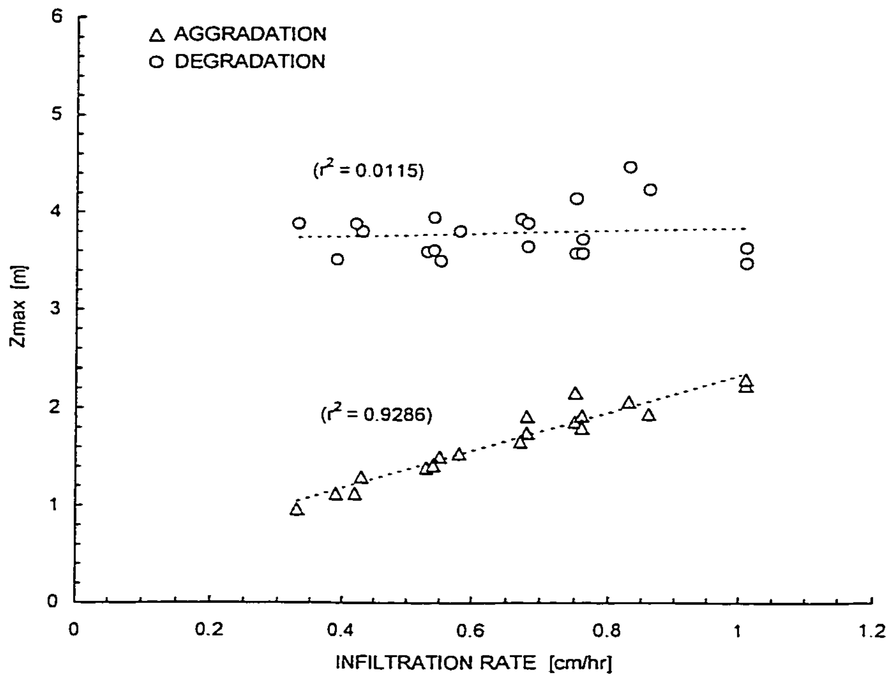

Figure 5.20. Maximum 100-year channel depth change as a function of streambed infiltration for the current climate scenario.

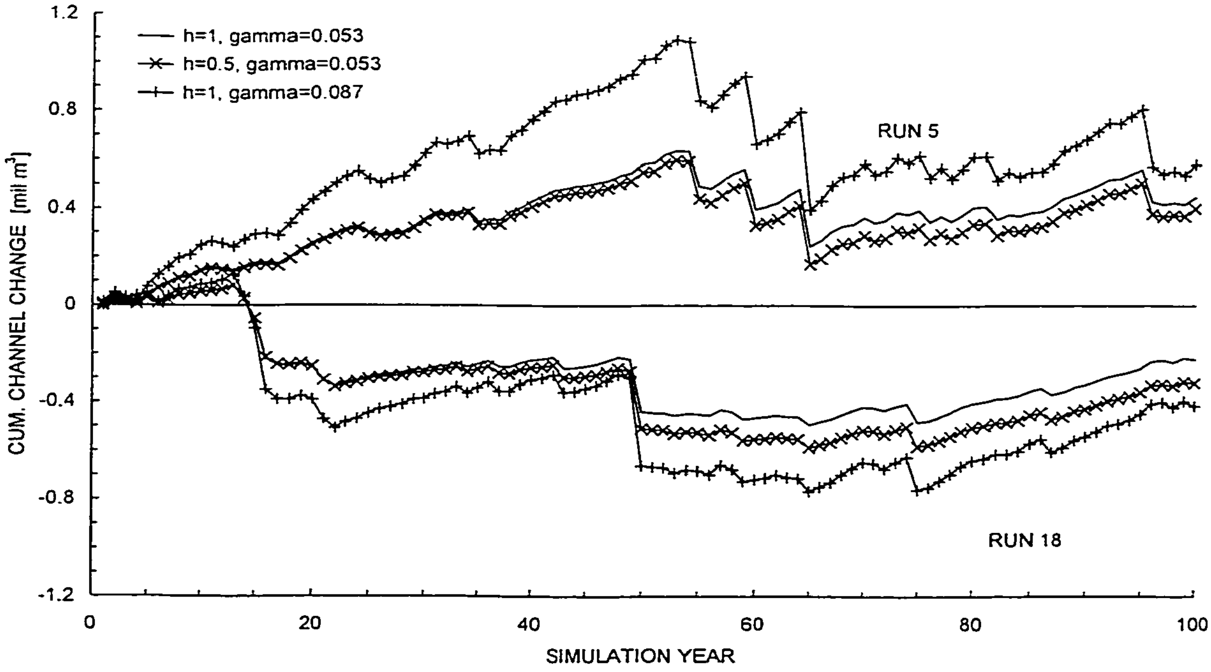

Figure 5.21. Cumulative volume of channel change for three different ERMO parameter combinations for the current climate scenario.

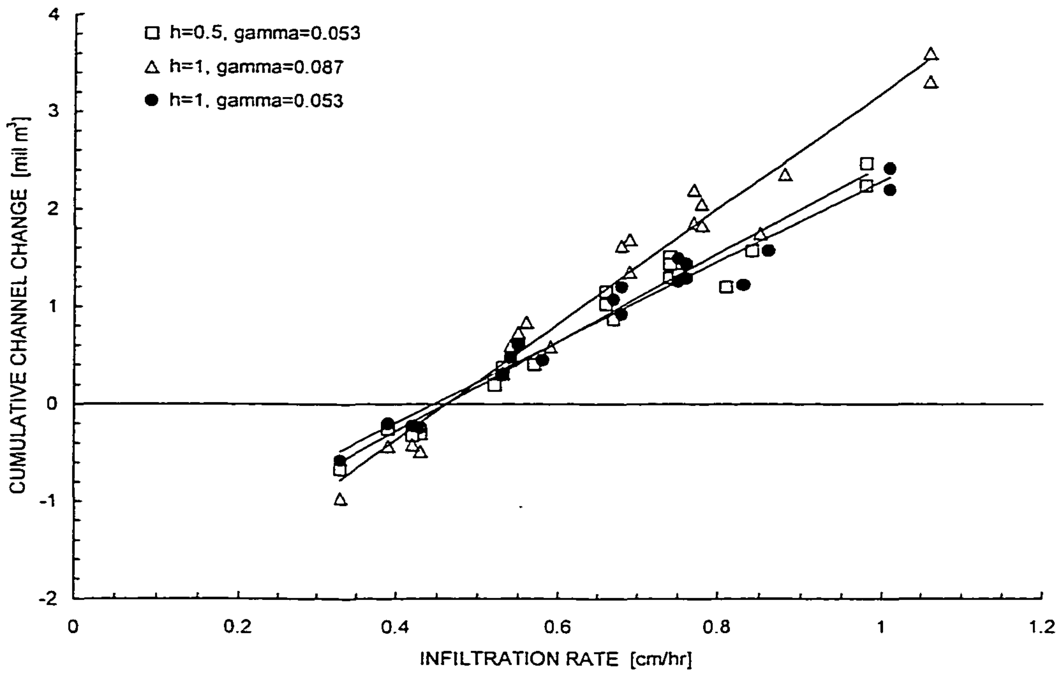

Figure 5.22. Cumulative volume of channel change after 100 years of simulation as a function of the infiltration rate for three different combinations of ERMO parameters for the current climate scenario. The parameter *f* is calibrated to maintain the long-term average annual runoff at Bernardo (35.9 mil m^3/yr).

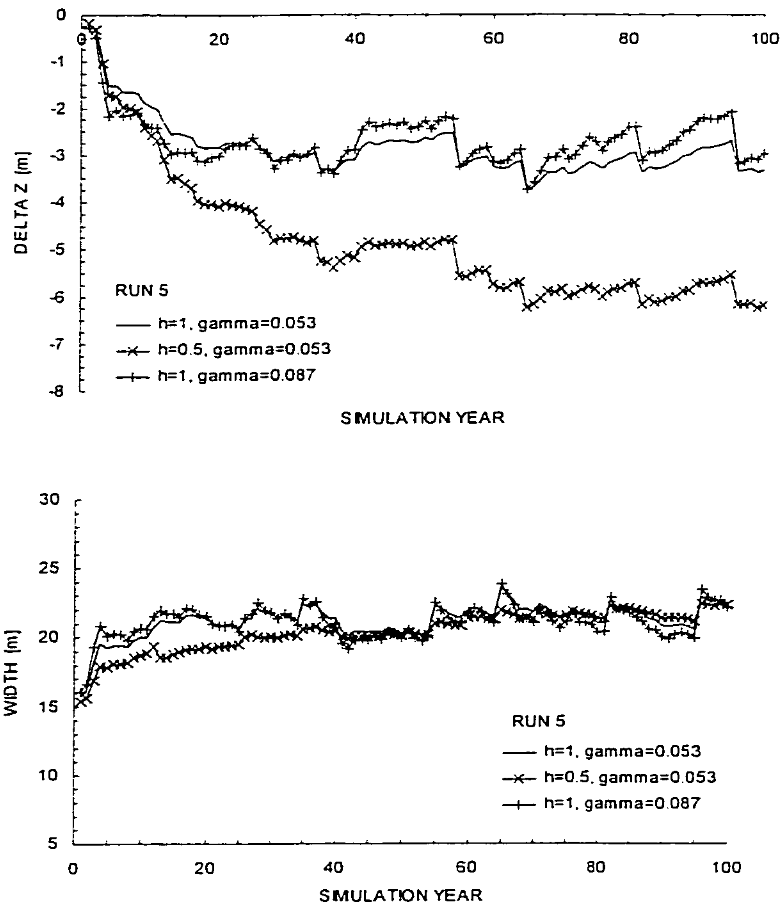

Figure 5.23. Changes in channel depth and width for three different ERMO parameter combinations for Run 5 on the Rio Puerco main stream 0.5 km downstream of the Arroyo Chico junction.

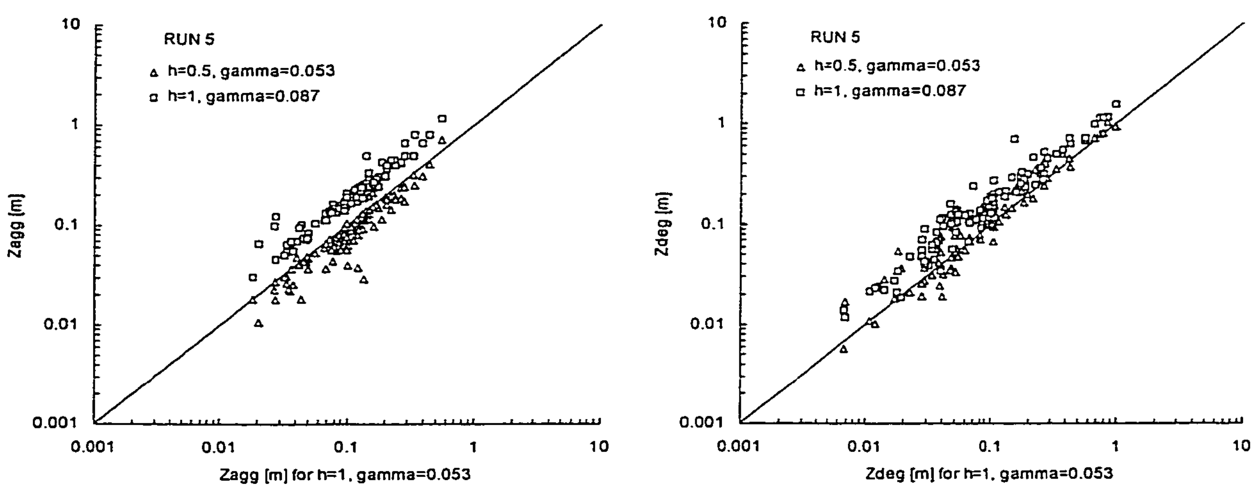

Figure 5.24. Comparing maximum annual aggradation (left) and degradation (right) depths for Run 5 for different ERMO parameter combinations with the original scenario.

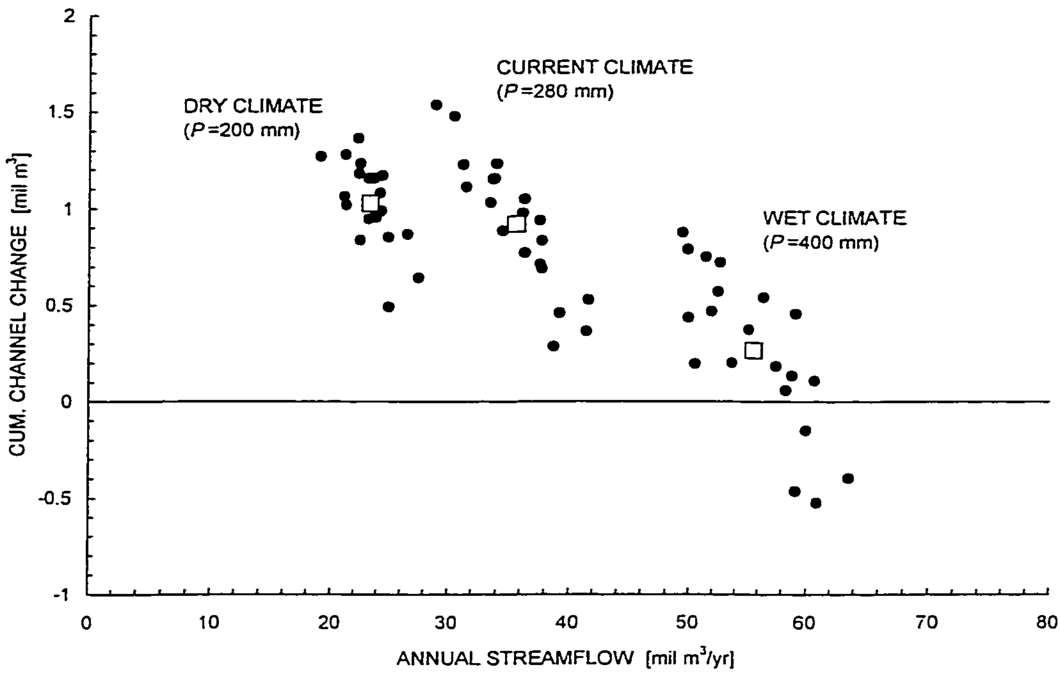

Figure 5.25. Cumulative volume of Rio Puerco channel change in a changing climate as a function of average annual streamflow at the Basin outlet. The open squares are averages of annual streamflow and channel change volume for each climate mode.

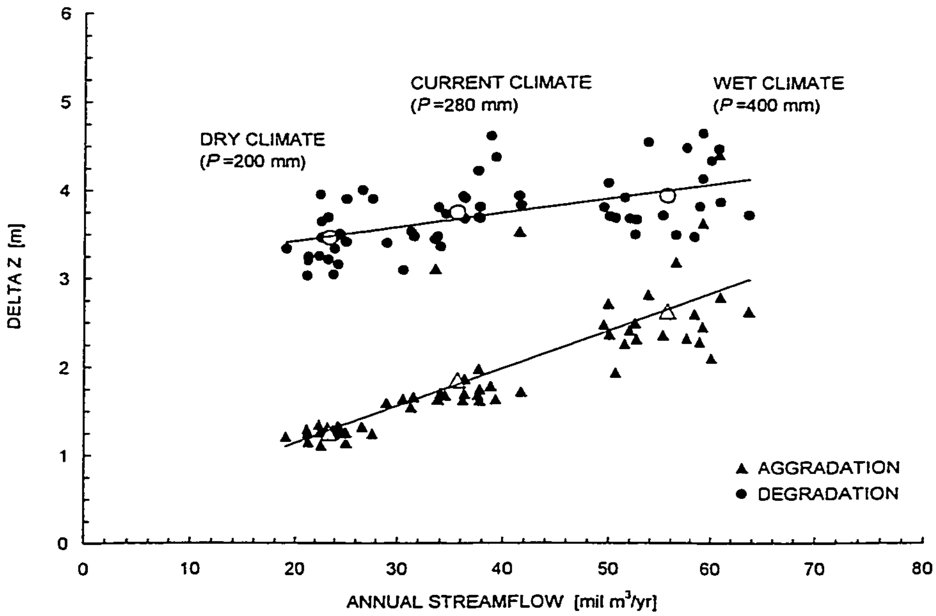

Figure 5.26. The 100-year maximum vertical Rio Puerco channel change in a changing climate as a function of average annual streamflow at the Basin outlet. Open markers are averages of annual streamflow and maximum erosion and deposition depths for each climate mode.

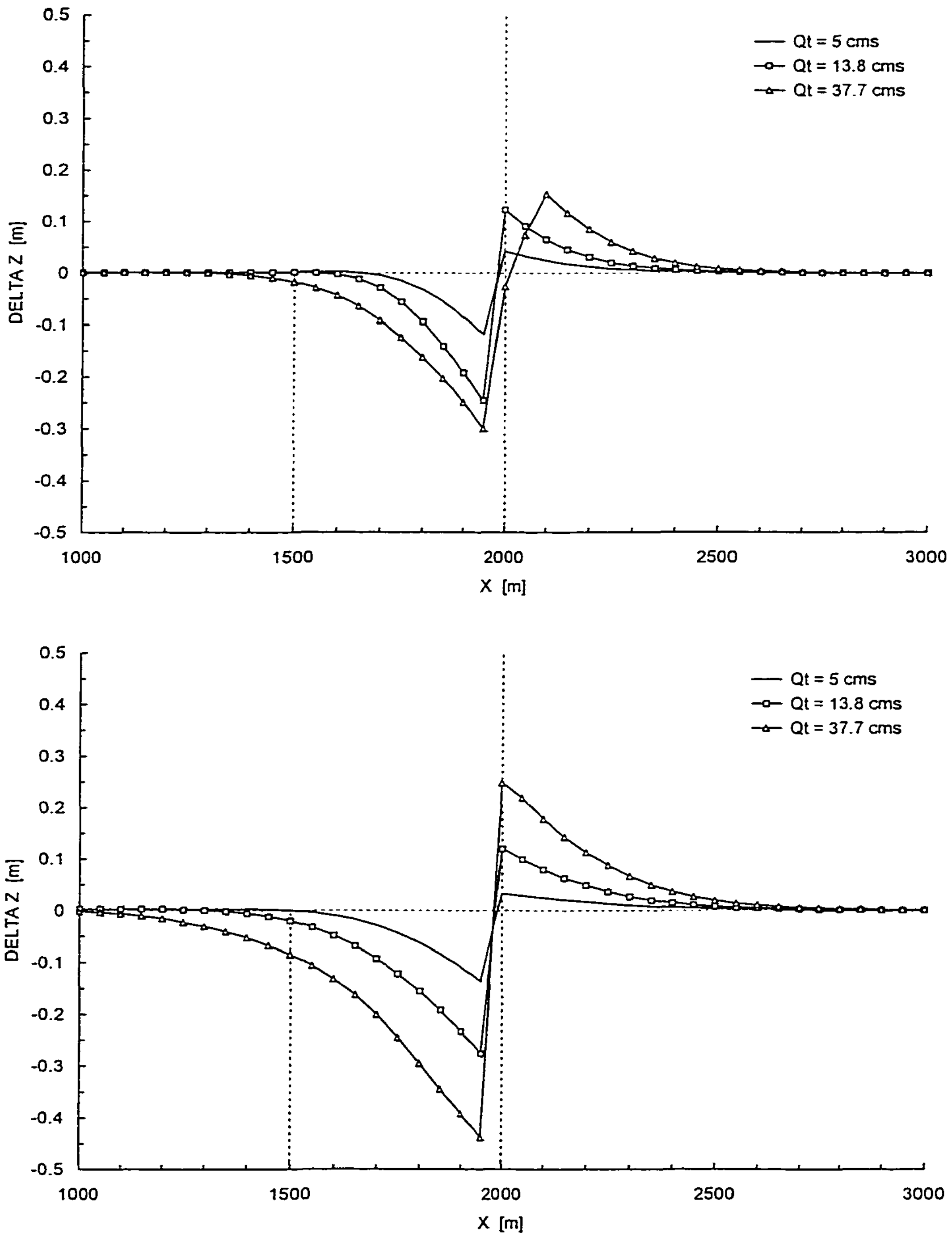

Figure 5.27. Channel change simulated by GRAD after t=1 day (top) and t=2 days (bottom) with main stream Q=13.8 m^3/s and different tributary inflows Q_t.

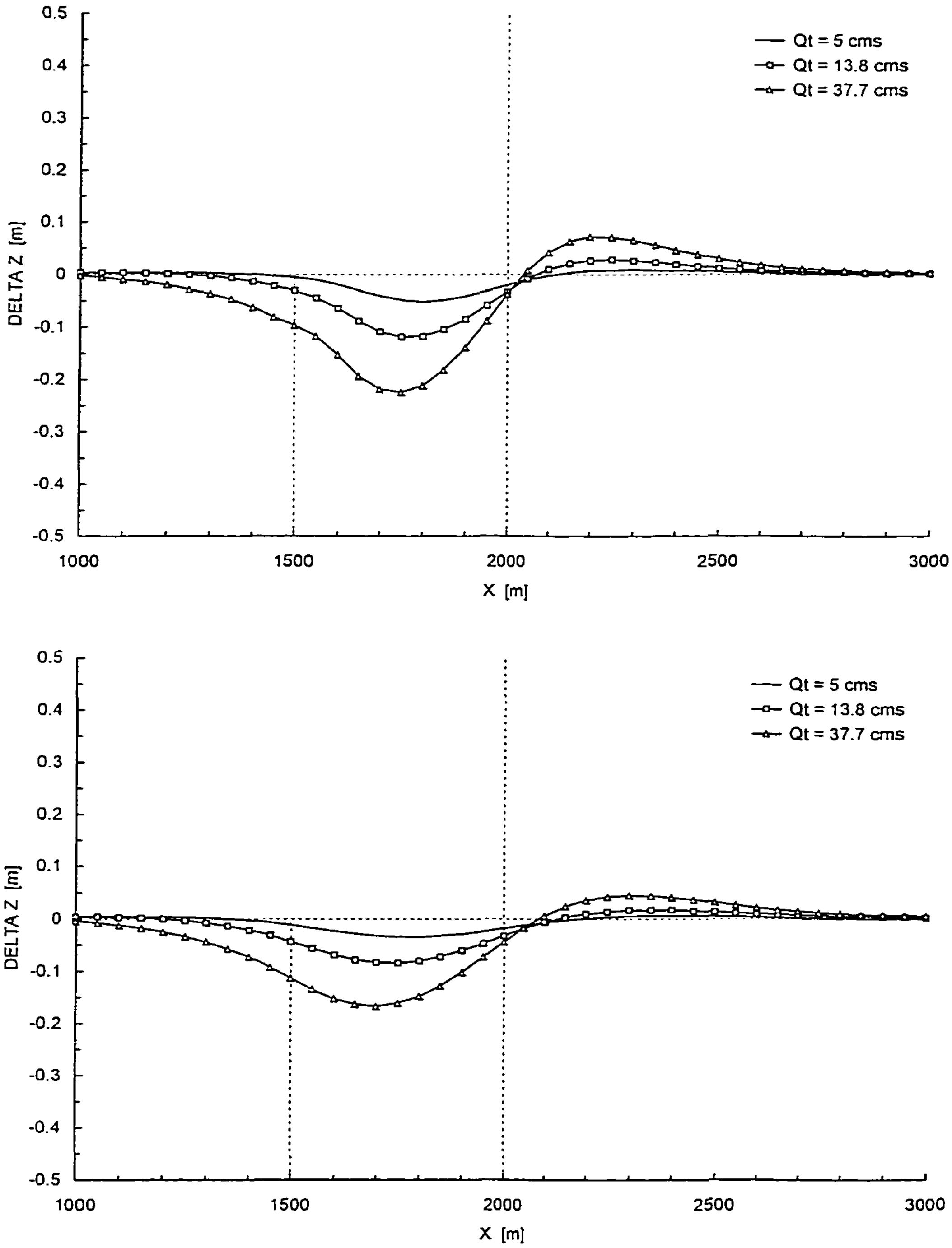

Figure 5.28. Channel change simulated by GRAD after t=3 days (top) and t=4 days (bottom) with main stream Q=13.8 m^3/s. Tributary inflows in days 3 and 4 were Q_t=0.

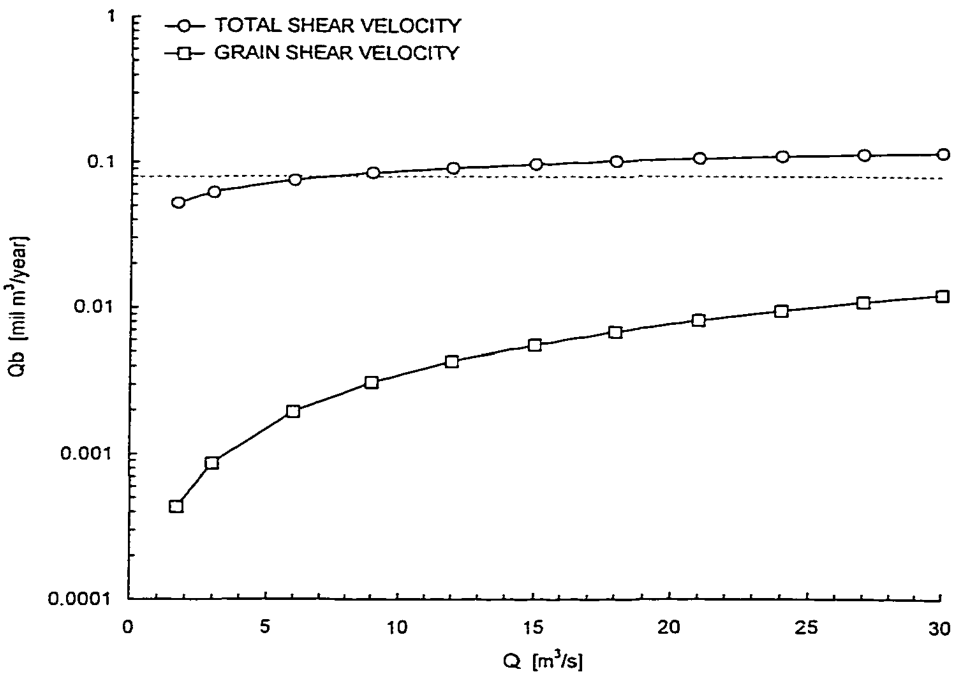

Figure 5.29. Annual bedload transport computed according to Van Rijn (1984a) for the outlet of the Rio Puerco Basin at Bernardo. Grain shear velocity is the sediment transport condition where bed form drag is not neglected. Total shear velocity is the sediment transport condition where bed form drag is neglected. ERMO-simulated bedload transport for the current climate scenario was 0.079 mil m^3/yr (dashed line).

6 DISCUSSION

The investigation of trends in hydroclimatic variables and the modeling of channel change under stochastic spatially and temporally variable rainfall in the Rio Puerco Basin in this study quantify important features of the erosion dynamics in the river system. In this Chapter the most important aspects of the investigations are discussed. Particular attention is devoted to the spatial pattern and magnitude of erosion, the issue of sediment supply, and to the effect of climate variability on channel change. The most important assumptions in the ERMO model are reviewed and some possible directions for further research are outlined.

6.1 HYDROCLIMATIC TRENDS

Because the Rio Puerco is such a large contributor of sediment to the Rio Grande, there are concerns about sedimentation and water quality in the Elephant Butte Reservoir and the Rio Grande downstream of the Rio Puerco. For this reason, investigations of trends in the water and sediment supply of the Rio Puerco are of great interest to land and water resources managers.

Since 1928 numerous sediment control plans in the Rio Puerco have been under investigation and some small scale projects (mostly sediment trapping reservoirs) have been built in the Upper Rio Puerco watershed by the Bureau of Land Management. A recent study by the Bureau of Reclamation does not recommend major investment in sediment control in the Basin at this time, and calls for an expansion of the data-collecting activities in the Basin (Gorbach et al. 1996).

Extreme runoff events transport the majority of suspended sediment. Therefore, the decreasing trend in annual maximum streamflow observed at Rio Puerco gages affects total sediment transport. This may help explain the decreasing trend in annual suspended sediment concentrations observed at Bernardo, Arroyo Chico and Rio Puerco above Arroyo Chico gages in addition to arguments of arroyo evolution and changes in land management (Gellis 1991, Gellis et al. 1991). Floodplain alluviation, attributed to a decrease in flood magnitude and frequency, has also been observed in the Paria River Basin in Utah and Arizona in the period 1940-1980 (Graf et al. 1991) and in the Little Colorado River in Arizona since 1940 (Hereford 1984).

6.2 Spatial Pattern of Erosion

As mentioned earlier, one of the new advances in channel erosion modeling in this study is the use of stochastically generated spatially and temporally distributed rainfall. To my knowledge, at the spatial and temporal scales studied here, there has been a comparable study of basin-wide erosion modeling with stochastic rainfall in the temporal domain (Tucker and Bras 2000), but none in the spatial domain. The stochastic analysis in this study provided spatial patterns of erosion remarkably similar to those observed in ephemeral streams.

For instance, the qualitative assessment of erosional and depositional behavior in ephemeral streams according to Thornes (1977) is shown in Figure 6.1. Notice the similarity in longitudinal erosion profiles between Figure 6.1 and ERMO modeling results in Figure 5.10. Erosion generally occurs immediately downstream of tributary confluences and deposition further downstream. Another example is from a comprehensive data collection experiment on the Arroyo de los Frijoles, in northern New Mexico (Leopold et al. 1966). Figure 6.2 (bottom) shows the distribution of erosion and deposition in the main stream measured by scour chains in the streambed for the period 1958-1962. Observations also show degradation downstream of the three main tributaries and general aggradation elsewhere in the stream. Leopold et al. (1996) conclude that depth of scour is well related to streamflow and that general aggradation in the river system is the dominant process. These findings are in very good agreement with the Rio Puerco erosion modeling in this study.

One of the main results of this analysis was the dominant occurrence of erosion downstream of tributaries. However, it is not implied that degradation always occurs downstream of tributaries in ephemeral streams. A tributary may carry high sediment loads, and if the channel below the confluence is not able to transport the added sediment load because of its hydraulic characteristics, deposition will occur. A recent study of flood flows from the Little Colorado River into the Colorado River showed aggradation below the confluence for this reason (Wiele et al. 1996). Nonetheless, degradation below tributaries is not uncommon, and is related to the relative streamflow and sediment contributions from the tributary and main stream, transmission losses, and channel characteristics.

A simple exercise can illustrate the dynamic behavior of erosion or deposition with the sediment rating curve used in ERMO. Let us a take a main stream link immediately downstream of a tributary. The width of the link is W_u at the upstream end and W_d at the downstream end, and streamflow is Q_u and Q_d, respectively. The tributary enters the main stream link at the upstream end, and has width and streamflow W_t and Q_t. Now let us consider the sediment balance in this link by computing the gradient in sediment transport:

$$\Delta Q_s = Q_{sd} - Q_{su} \tag{6.1}$$

where, using the sediment rating curve from Equations (5.1) and (5.5), the sediment flux out of the link (downstream) is:

$$Q_{sd} = \gamma a \left[\frac{Q_u}{W_d} + \frac{Q_t}{W_d} \right]^b W_d \tag{6.2}$$

and the sediment flux into the link (upstream) is:

$$Q_{su} = \gamma a \left[\frac{Q_u}{W_u} \right]^b W_u + \gamma a \left[\frac{Q_t}{W_t} \right]^b W_t \qquad 6.3)$$

Then the sediment balance is given by:

$$\frac{\Delta Q_s}{\gamma a} = (Q_u + Q_t)^b W_d^{\,1-b} - Q_u^{\,b} W_u^{\,1-b} - Q_t^{\,b} W_t^{\,1-b} \tag{6.4}$$

In this equation, the effect of streambed infiltration in the link was neglected and the tributary and link use the same sediment rating curve. The sign of the sediment balance term on the left-hand side of Equation (6.4) determines the nature of channel change in the link:

$$\begin{array}{ll} \text{if } \Delta Q_s > 0 & \text{erosion} \\ \text{if } \Delta Q_s < 0 & \text{deposition} \end{array} \tag{6.5}$$

It is evident from Equation (6.4) that the exponent b of the sediment rating curve is the crucial parameter that determines whether erosion or deposition will occur downstream of a tributary. However, also important are the link and tributary channel geometry and streamflow.

Let us take an example in which $W_u = W_t = W_d = W$. Then Equation (6.4) becomes:

$$\frac{\Delta Q_s}{\gamma a W} = (Q_u + Q_t)^b - Q_u{}^b - Q_t{}^b \tag{6.6}$$

So in this special case,

$$\begin{array}{lll} \text{for } b > 1 & \Delta Q_s > 0 & \text{erosion} \\ \text{for } b < 1 & \Delta Q_s < 0 & \text{deposition} \end{array} \tag{6.7}$$

Therefore, in the Rio Puerco (and in most river systems where b>1) erosion will occur regardless of streamflow downstream of a junction of two streams with equal width. The erosion depth will generally depend on the difference between streamflow magnitudes in the streams. This fact has also been observed experimentally (Mosley 1976).

However, generally in nature

$$\begin{array}{l} W_t < W_u, W_d \\ W_d > W_u \end{array} \tag{6.8}$$

Let us therefore look at the erosion dynamics under these general conditions. In this example, the link represents general high flow conditions downstream of the Arroyo Chico tributary. The upstream inflow into the link is given by the average annual maximum daily streamflow at Rio Puerco above Arroyo Chico: Q_u=13.78 m^3/s (Table 2.9). The tributary inflow varies between 0 and 38 m^3/s, which is the average annual maximum daily streamflow at Arroyo Chico. The upstream width of the link is W_u=15 m. Figure 6.3 shows the results for variable width downstream (top left), for variable tributary width (top right) and both variable width downstream and at the tributary (bottom). Note that in this figure the vertical axis is $-\Delta Q_s / \gamma a$, so negative values indicate erosion and positive values indicate deposition.

The example shows that with a widening channel downstream two features appear. First, the amount of erosion decreases with widening of the channel. Second, for low streamflow inputs from the tributary, there may be aggradation downstream of the tributary. The example of a variable tributary width also reveals interesting features. Given the same sediment rating curve, a narrower tributary means more sediment supply to the link (for the same streamflow). It is evident that with a decreasing tributary width, aggradation may occur in the link downstream of the tributary. This sediment overloading condition will happen mostly for high tributary flows. A combination of the above conditions is shown in the bottom graph in Figure 6.3, and it illustrates that (*a*) where two channels of equal width join, erosion will generally occur; (*b*) where the tributary supplies more sediment and the main link widens downstream, both deposition (for low flow and high flow) and erosion (for moderate flow) may occur; (*c*) where the tributary sediment supply is excessive and/or the main link widens downstream excessively, deposition will generally occur downstream of a tributary.

The latter point is also illustrated in short-term GRAD simulations of the high flow condition in the Rio Puerco main stream and Arroyo Chico for sediment overloading in Figure 6.4 (see Section 5.5.2 for model details). In this scenario, the Arroyo Chico channel was assumed to be steep (S=0.008 m/m), thereby sediment supply to the main stream was high, causing a cone of deposition at the tributary mouth. After two days flow from the tributary ceased and the cone began to dissipate. Sediment overloading has been studied intensively in experimental flumes (e.g., Soni et al. 1980).

The above examples show the complex and dynamic response that occurs downstream of tributaries, in particular in ephemeral streams where streamflow and sediment supply can vary greatly between main stream and tributary and where channel geometries are quite unpredictable.

Although ERMO-simulated longitudinal erosion profiles of the Rio Puerco main stream exhibit similarities with other ephemeral streams, it is, at this time, impossible to make direct comparisons with Rio Puerco observations. There is insufficient spatial and temporal information about the initial conditions and evolution in terms of channel geometry, the extent and location of geologic controls along the main stream, etc., to make such comparisons. In fact, the purpose of ERMO simulation in this study was not to exactly "fit" Rio Puerco conditions, but rather to model expected channel behavior. Very few replicate surveys of cross sections have been conducted, considering the length of the main stream. An example of a cross section on the Lower Rio Puerco is shown in Figure 6.5. There is clear evidence of channel aggradation and narrowing in this reach (in addition to lateral migration). The main channel aggraded about 3 m and narrowed by about 20 m in 60 years. Assuming that this cross section is representative of general behavior in Rio Puerco main stream Subbasins 2* and 3* (Chapter 2), as it is located about 40 km upstream of Bernardo, ERMO results are encouraging, because they generally predict aggradation and channel narrowing in this section of the Lower Rio Puerco (Figure 5.10 and 5.11). However, this point measurement cannot be used as a validation of the ERMO model. Ongoing detailed geologic and geomorphologic mapping of the Rio Puerco main stream may in the future permit more detailed analyses based on which comparisons with Rio Puerco observations can be made.

6.3 Maximum Rates of Channel Change

One of the water and erosion management goals of this study was to provide estimates of the maximum annual erosion and deposition depths on the Rio Puerco. To answer this question a frequency analysis was performed on the maximum annual aggradation and degradation depths simulated by ERMO from 100-year simulations for the three different climate modes studied.

The probability distribution function of the exponential model was fitted to simulated maximum annual erosion and deposition depths using the method of moments. Other extreme value models were also tested. The cumulative distribution function of the exponential distribution is:

$$F(x) = 1 - e^{-\beta(x-\xi)} \tag{6.9}$$

from which values of x with nonexceedance probability p are determined:

$$F(x) = P(X \leq x) = p \tag{6.10}$$

The moment estimators of the parameters of the exponential models are:

$$\begin{aligned} \beta &= \sqrt{\frac{1}{\sigma_x^2}} \\ \xi &= \mu_x - \frac{1}{\beta} \end{aligned} \tag{6.11}$$

where σ_x is the unbiased sample standard deviation and μ_x is the sample mean of x.

In Figure 6.6, maximum annual aggradation and degradation depths are shown together with the fitted exponential model in the form of Equation (6.9) for all three climate modes. Data are plotted according to Weibull's plotting position: $p = 1 - i/(n+1)$, where i is the order of the series sorted in descending manner and n is the number of runs in each climate mode (n=20). Quantiles with nonexceedance probabilities p=0.5 and p=0.95 extracted from the exponential model are listed in Table 6.1 for all climate modes.

Looking at the mean values (p=0.5), results show that the maximum annual degradation depth in 100 years is Δz_{max}=1.0 m in the current climate and Δz_{max}=1.24 m in the wet climate. For maximum aggradation depths these values are Δz_{max}=0.57 m for the current climate and Δz_{max}=0.91 m for the wet climate. However, looking at the quantile exceeded with 5% probability (p=0.95), the maximum annual degradation depth in the wet climate is Δz_{max}=2.05 m, whereas the maximum annual aggradation depth is Δz_{max}=2.22 m. These results show that with increasing wetness (i.e., more annual precipitation and runoff, as well as more extreme events), the annual maximum depths of aggradation and degradation will become very similar in magnitude.

How do these rates compare with historical observations of the Rio Puerco? In a review of erosion in the Basin, Tuan (1966) reports average annual erosion rates in about 100 years to be approximately 0.6 m at La Ventana and 0.2 m at San Luis - both locations are in the Upper Rio Puerco Basin. Leopold et al. (1966) report a maximum scour of up to 0.4 m in one event on the Arroyo de los Frijoles near the Rio Puerco. These values correspond quite well with ERMO simulations.

However, although the erosion and deposition response at the annual timescale is of comparable magnitude to scant Rio Puerco observations, the ERMO model did not predict the massive arroyo trenching that apparently reached about 11-13 m in the Upper

Rio Puerco Basin between 1850 and 1964 (Tuan 1966). ERMO predicted that maximum degradation depths in 100 years were on the order of 3-7 m (depending on the studied climate and sediment transport scenario) and were not widespread. In the Lower Rio Puerco, ERMO predicted that maximum aggradation depths in 100 years were on the order of 1-4 m. Observations show the recent alluvium depth to be about 3-6 m in this stream section (Heath 1983). So it appears that ERMO simulations under constant variability in climate do not provide sequences of extremely wet and/or dry years that could initiate the extraordinary erosion and deposition comparable to the historical arroyo formation period.

6.4 Long-Term Variability and Climate Change

Long-term climate variability in the Rio Puerco region is well illustrated on a reconstruction of climate from tree-ring chronologies in the Malpais area by Grissino-Meyer (1995). In Figure 6.7 a 2,129 year reconstructed sequence of (smoothed) standardized annual rainfall is shown. The time series shows sequences of generally above normal rainfall in A.D. 81-257, 521-660, 1024-1398 and 1791-1992, and below normal rainfall in A.D. 258-520, 661-1023 and 1399-1790. It is noteworthy that the current wet period is the longest and largest in the record. Estimated periods of arroyo incision (e.g., 1250-1325, 1880-1900 in Elliott et al. 1999) in the Rio Puerco do not coincide conclusively with wet or dry periods in the reconstructed climate record. Spectral analyses of the reconstructed climate record gave periods of 16.5, 20, 25, 30, 79 and 426 years (Grissino-Meyer 1995). It has been noted in Chapter 3 that the significant

79 year period approximately coincides with a 50-70 year cycle found in the PDO climate anomaly in the Northern Pacific (Minobe 1997).

Perhaps the most detailed large (basin) scale and long-term drainage basin response modeling to climate variability was conducted recently by Tucker and Slingerland (1997). The authors study how the extent of the channel network and erosion in the watershed are controlled by thresholds for overland flow erosion. They simulate a rapid extension of the river network caused by an increase in runoff (rainfall) intensity (or a decrease in vegetative cover) followed by aggradation in the stream system as a result of the large sediment supply from upstream, and later repeated degradation as the sediment supply tapers off. A decrease in runoff intensity (or more resistant surface) leads to a retraction of the active channel network. Cyclic changes in runoff intensity are shown to produce aggradation and degradation cycles observed in nature. The results underscore the importance of the temporal variability in runoff. Also accented are the complex relationship between hillslope and channel processes, and the important role of first-order channels (and therefore drainage density) in supplying sediment to the river network. Although the model does not account well for asynchronicity of flow throughout a river network where drainage area and streamflow magnitude are not well related (such as the Rio Puerco), the modeling results are very interesting.

Clearly, climate (i.e., precipitation) variability plays an important role in Rio Puerco channel dynamics. It has been argued that an increase in precipitation variability generally increases erosion (Tucker and Bras 2000). Based on simulations in this study it also appears that an increase in precipitation magnitude, accompanied by an increase in extreme rainfall events, would increase the probability of large and extensive degradation in the Rio Puerco Basin. The decadal scale variability in precipitation caused by North Pacific climate anomalies likely plays an important role in the cyclic nature of aggradation and degradation in the river system.

6.5 Review of Assumptions

It is worthwhile to review the assumptions and simplifications made in the channel erosion modeling in this study, as these influence the results and may be avenues for further research and improvements in the future.

Sediment transport is instrumental to channel change. In ERMO, sediment transport is governed by a simple sediment rating curve for the main stream as well as tributaries. Because of this, simulations cannot fully account for the spatial distribution of sediment type and availability: it is assumed that supply is not limited. In the Rio Puerco context, it may be interesting to analyze basin-wide sediment supply and adjust the sediment rating curves to account for variable sediment supply. Another improvement to the rating curves would be to include additional variables, such as slope, sediment size, indexes of vegetation cover, geology, etc., in their formulation. Results are also affected by the choice of the drainage area threshold in identifying subbasins. Finer resolution may provide a more detailed description of the erosion dynamics. It is also important to note that in this study Rio Puerco erosion profiles are simulated without any controls on channel change, such as geology, roads, stream stabilization works, etc., because these are not well mapped in the Basin and/or their effects are difficult to quantify. Continuing mapping in the Basin may provide data to parametrize these effects in the future.

The infiltration rate into the streambed f is an important ERMO parameter, because transmission losses along the entire Rio Puerco main stream can be more than 50% of mean annual runoff at Bernardo. In ERMO, the parameter f is constant in time and space, and most importantly, the storage capacity of the alluvium is assumed to be infinite. This assumption was based on the fact that the regional water table is reported to be more than 20 m below the surface in the Lower Rio Puerco and even deeper in the Middle and Upper Rio Puerco reaches (Heath 1983). The depth of the alluvial fill with homogeneous sandy material is great and so the storage capacity of the subsurface reservoir was not considered limiting to the subsurface flux of water from the streambed. Nevertheless, perched water tables and geological controls may exist, and accounting for the storage capacity of the alluvium would be a significant improvement to the ERMO model. This is, however, contingent upon the availability of detailed geological information required to parameterize the alluvial fill, which is not available at the present time.

The one-dimensional nature of the ERMO model does not allow for a full description of lateral channel movement and meandering. The effective channel in the Rio Puerco is assumed to be rectangular and channel widening in ERMO is based on a simple linear redistribution of sediment mass. In reality, bank erosion in the Rio Puerco and many arroyos in the U.S. Southwest is a complex process with significant piping and mass wasting processes. Piping is the subsurface erosion initiated by percolating waters which remove solid particles and produce tubular underground conduits (Bryan and Jones 1997). It was beyond the scope of this study to model these processes in detail, but their effect on channel width changes may be significant in the short term. Vegetation also controls channel widening by stabilizing the floodplain. The growth of salt cedar in the floodplain in recent decades not only decreased the conveyance of channels but likely also limited changes in channel width. These factors were not considered in ERMO. Including the effects of vegetation and the role of the floodplain on the long-term erosion dynamics in ephemeral streams would be a significant improvement and should be an avenue for further research.

The ERMO model operates on a steady-state basis at the daily timescale. The average time for a flood wave to travel along the Middle and Lower Rio Puerco is approximately 36 hours (Heath 1983), so it appears that the daily steady-state assumption is appropriate. However, because the travel time of flood waves along the entire length of the Rio Puerco is generally more than one day, correlation between daily streamflow at Bernardo and upstream gages is maximum at lag k=1 day. Because of the daily steady-state assumption, these correlations are generally maximum at lag k=0 in ERMO. Nevertheless, the maximum correlation coefficients are notably similar for both observations and simulated data (about r=0.5), and the spatial and temporal correlations are well preserved by the random cascade model for rainfall described in Chapter 4. In terms of spatial correlation, in the context of the spatial random cascade model it may also be of interest to explore and include the effect of land surface topography on generated rainfall fields.

Analyses with varying climate in Chapter 5 equate an increase in wetness with increasing annual precipitation. It is important to note that in the context of the random cascade model in Chapter 4, an increase in regional annual precipitation brings with it a proportional increase in the probability of extreme daily rainfall events. However, analyses of hydroclimatic trends in this study showed that substantial shifts in the distributions of daily rainfall events are not related to changes in annual precipitation in a simple manner. For instance, increases in annual precipitation were not accompanied by increases in annual maximum rainfall events but rainfall with moderate intensity. Further research should be directed toward investigations of the relationship between shifts in rainfall distributions and climate change, as these may be of great consequence to the erosion dynamics in the Rio Puerco Basin. Results in this study indicate that the dramatic arroyo formation episodes in the Rio Puerco may be related to changes in the variability of climate as well as a general increase in wetness. The author intends to pursue this research topic in the future.

6.6 Ongoing Research in the Rio Puerco Basin

This study is part of a larger investigation of the Rio Puerco Basin conducted by the United States Geological Survey and associated agencies. Ongoing research activities in the Basin are presented at *Rio Puerco Online* (climchange.cr.usgs.gov/rio_puerco). The reader is referred to the web page for more up-dated information.

Some of the ongoing research and data-collecting activities are especially pertinent to the topic of this study. Sediment yield is measured by sediment traps and small dams at a small basin scale in the Arroyo Chavez experimental watershed (in the Arroyo Chico subbasin). Other quantities measured are sheet wash erosion, eolian transport of sand, rainfall, runoff and sediment transport. At the Arroyo Chavez watershed, distributed hydrological modeling was conducted by the author to investigate the role of the valley floor on the amount of hillslope infiltration and the location of piping and drainage network extension. Long-term rates of sediment generation and erosion were measured by cosmogenic isotopes (^{10}Be and ^{26}Al) at several sites in the Basin. From these analyses, the time frames of arroyo cutting and infilling are being inferred. Alluvial sediments are also dated by ^{14}C to determine deposition rates as well as long-term cycles in channel aggradation. A thorough geological mapping project in the Basin is also underway, together with mapping of sections of the Rio Puerco main stream with remotely sensed data.

Table 6.1. Maximum annual aggradation and degradation depths Δz_{max} (in 100 years) for nonexceedance probabilities p=0.5 and p=0.95 (modeled with the exponential distribution) under the changing climate scenario.

Channel change	DRY CLIMATE (P=200 mm)	CURRENT CLIMATE (P=280 mm)	WET CLIMATE (P=400 mm)
AGGRADATION			
$\Delta z_{max}(p=0.5)$ [m]	0.45	0.57	0.91
$\Delta z_{max}(p=0.95)$ [m]	0.88	0.98	2.22
DEGRADATION			
$\Delta z_{max}(p=0.5)$ [m]	0.81	1.0	1.24
$\Delta z_{max}(p=0.95)$ [m]	1.6	2.06	2.05

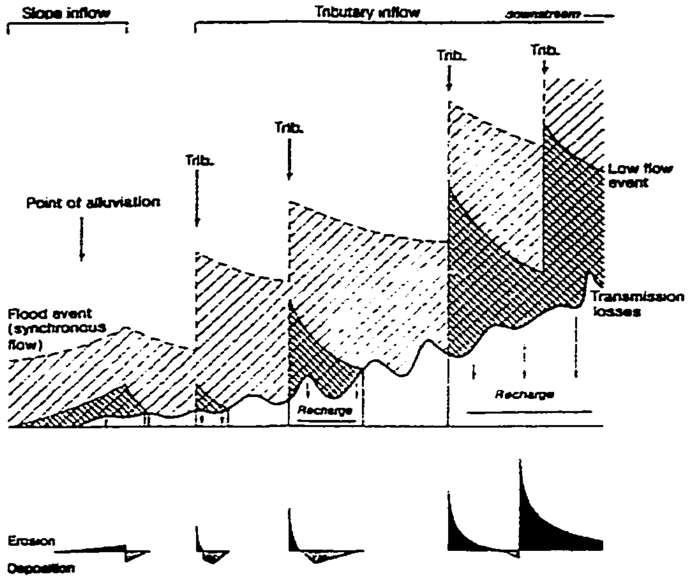

Figure 6.1. Schematic representation of transmission losses, tributary inflows, and resulting erosional processes for two different streamflow magnitudes: low flow and flood event in an ephemeral stream (after Thornes 1977).

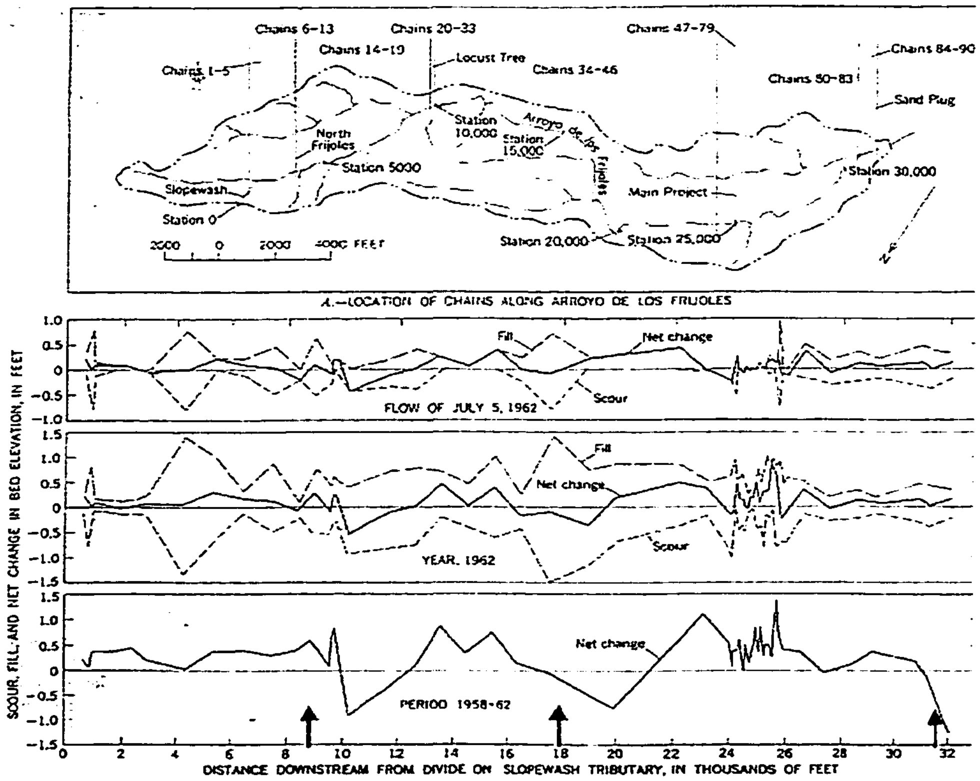

Figure 6.2. Scour and fill in the Arroyo de los Frijoles main stream, New Mexico, for the period 1958-1962 (after Leopold et al. 1966, Figure 158). Arrows indicate locations of three main tributaries to the main stream.

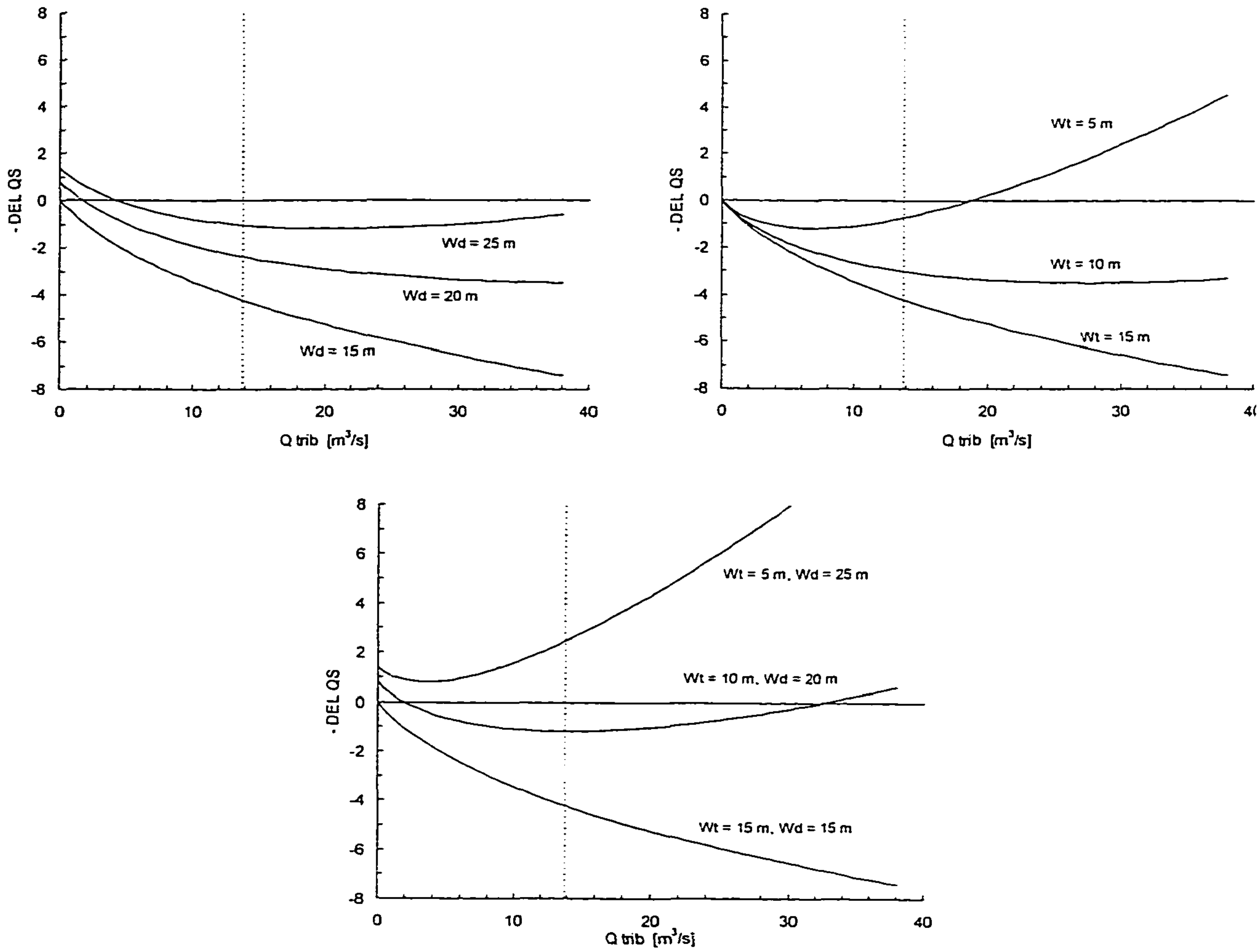

Figure 6.3. Illustration of aggradation/degradation behavior in a main stream link downstream of a tributary (positive -ΔQ_s indicates deposition, negative indicates erosion). Inflow into the link is Q_u=13.78 m^3/s; the width upstream is W_u=15 m. Q_t is tributary inflow upstream. Graphs illustrate the effect of variable width downstream (top left), variable tributary width - i.e., variable sediment supply from tributary (top right), and both situations combined (bottom).

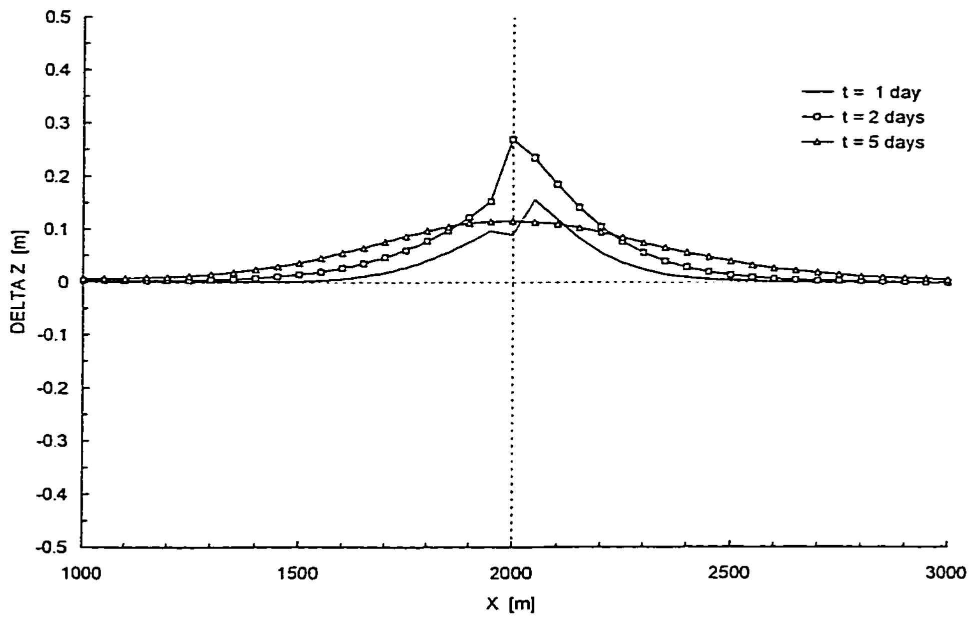

Figure 6.4. GRAD simulation of main stream (vertical) aggradation at the Arroyo Chico tributary confluence by sediment overloading. Flow in main stream and tributary is identical Q=13.78 m^3/s for two days. For the next three days only the main stream is flowing.

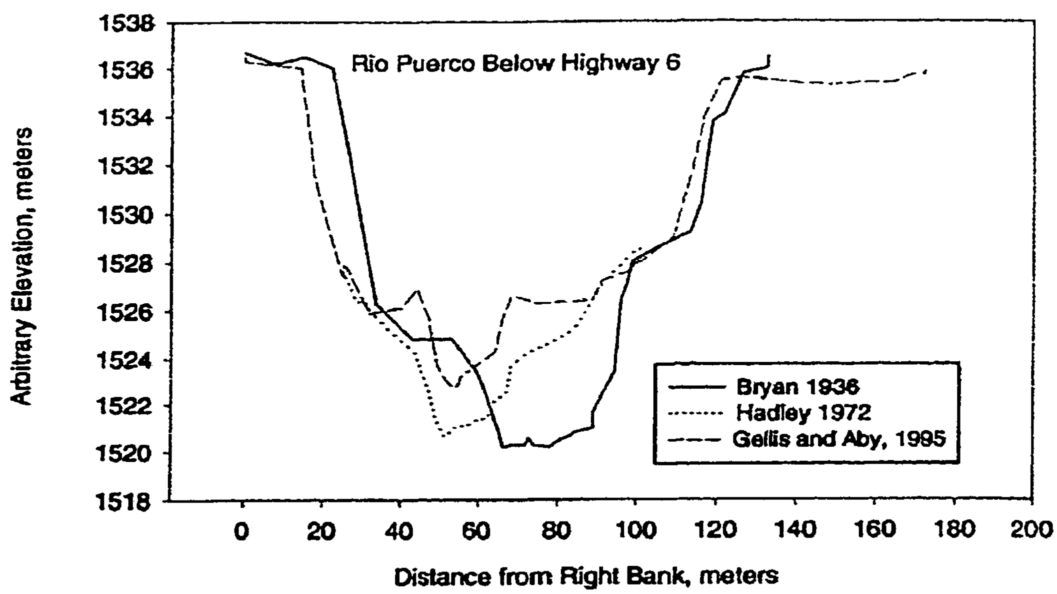

Figure 6.5. Replicate surveys of cross section 31 on the Lower Rio Puerco between 1936 and 1995 (Gellis 2000, personal communication).

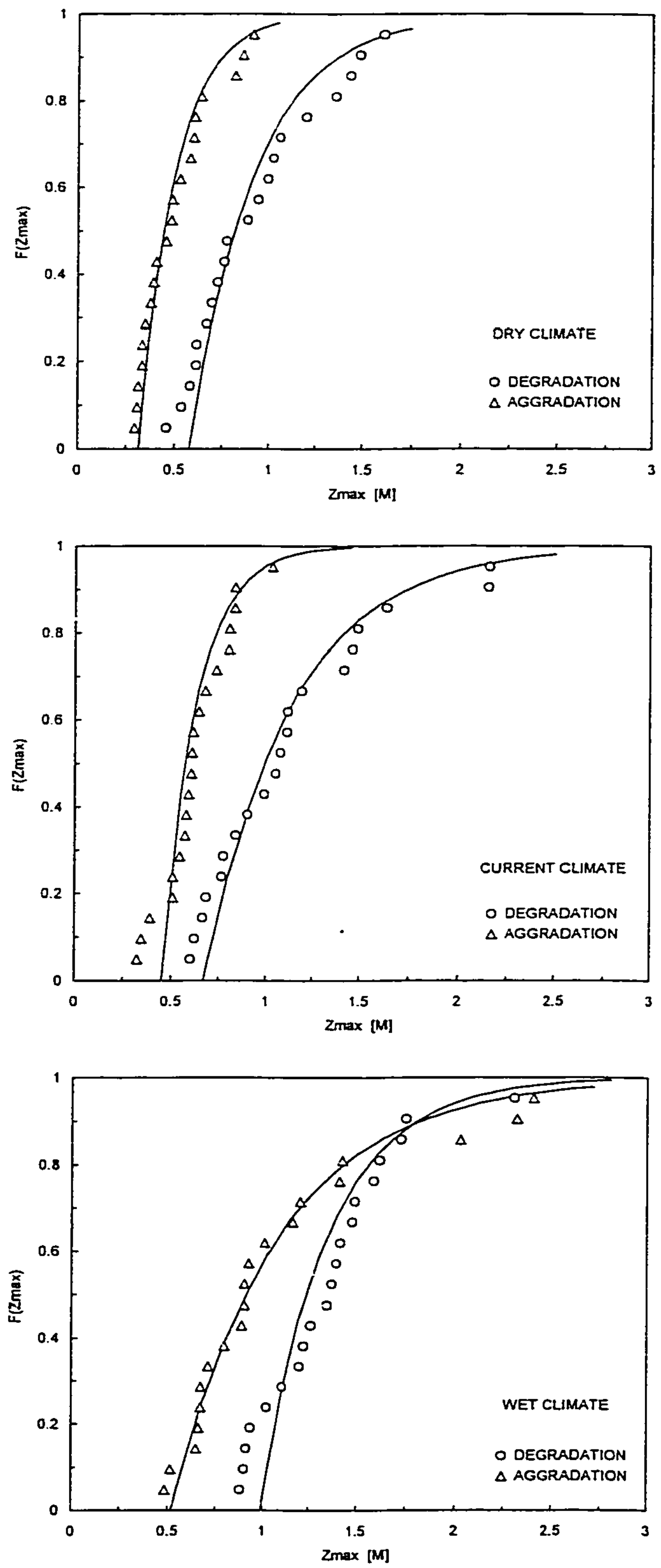

Figure 6.6. Frequency analysis of maximum annual aggradation and degradation depths from 100 years of simulation for the dry (top), current (center) and wet (bottom) climate modes.

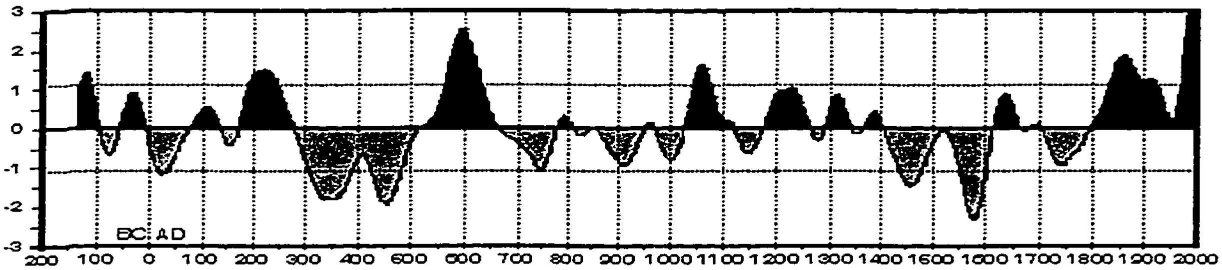

Figure 6.7. Reconstructed record of standardized annual (July-July) precipitation in the Malpais region in the Rio San Jose watershed from dendrochronological records shown as a 100-year smoothing spline (after Grissino-Meyer 1995, Figure 3.10). The vertical axis is in units of standard deviation.

7 Conclusions

The goal of this study was to examine the long-term erosional behavior of an ephemeral stream, the Rio Puerco in New Mexico, driven by spatially and temporally distributed rainfall and runoff. The original contribution of this study to the understanding of the erosion dynamics in ephemeral streams lies in the utilization of the stochastic nature of temporal and spatial precipitation in modeling channel change. This approach quantifies the connections between precipitation dynamics and erosion dynamics, thereby providing a useful tool for the study of the effects of climate variability and change on channel adjustment. In this Chapter the main results and conclusions are summarized.

The main conclusions of the hydroclimatic trends analyses in Chapter 3 are:

(1) A significant increasing trend in Rio Puerco annual precipitation in the period 1948-1997 is observed. This increase results from increases in non-summer precipitation, in particular in the frequency and intensity of moderate rainfall events, but maximum annual rainfall events remain unaffected. There is a strong connection between long-term trends in Rio Puerco precipitation and sea surface temperature anomalies in the Northern Pacific which may provide a better predictive capability for rainfall.

(2) Annual maximum rainfall events are producing progressively lower annual maximum runoff events in the last 50 years. This is indicative of alluviation in the channel and floodplain of the Rio Puerco (supported by observations) as well as possible changes in vegetative cover in the Basin.

Analyses of precipitation dynamics in Chapter 4 result in the development of a rainfall modeling system and rainfall-runoff model that produce the spatial and temporal distribution of daily rainfall at the regional scale and daily runoff at the Rio Puerco subbasin scale. The main conclusion of the daily rainfall radar data and streamflow analyses is:

(3) The spatial and temporal variability and scaling invariance of daily rainfall are well preserved by the discrete random cascade model. Parameters of the model can be related to large scale forcing in the form of a regional average rain rate (spatial cascade) and a seasonal rainfall total (temporal cascade). Together with the conceptual linear reservoir rainfall-runoff model, the system generates Rio Puerco subbasin runoff on a daily timescale at the same time preserving long-term streamflow statistics at the seasonal and annual timescales.

Modeling erosion dynamics in Chapter 5 is central to this study. Using stochastic, spatially and temporally distributed runoff at the subbasin scale, channel behavior is simulated in the Rio Puerco main stream with the following main findings:

(4) Degradation in the river system is generally more rapid than aggradation. However, although degradation is the dominant process in the short-term in response to extremely wet years and/or events, aggradation is a gradual process that dominates erosion dynamics in the long-term.

(5) The areas of most active erosion are generally tributary confluences because of high spatial variability in streamflow. Infiltration into the streambed is responsible for gradual deposition throughout the ephemeral stream, in particular in reaches without appreciable lateral streamflow contributions: the infiltration rate is an important model parameter. Simulated channel width is highly variable in space and shows a general narrowing in the downstream direction.

(6) In the current climate (average annual rainfall P=280 mm), the Rio Puerco is in a general aggradation phase. Moving towards a wetter climate with more intense rainfall increases general degradation and increases both maximum depths of erosion as well as deposition. In 100 years, the maximum annual degradation depth in a wet climate (P=400 mm) is about 1.2 m on the average (2.1 m exceeded with probability 5%), while in a dry climate (P=200 mm) the maximum annual degradation depth is only 0.8 m on the average (1.6 m exceeded with probability 5%). These rates compare well with observations of annual channel change on the Rio Puerco. Total annual sediment output from the Rio Puerco increased on the average by 150% moving from a dry to a wet climate.

(7) The ERMO model underpredicts the recent massive arroyo formation episode (on the order of 11-13 m degradation in the Upper Rio Puerco Basin). Simulated maximum degradation depths in 100 years were on the order of 3-7 m and were not widespread. In the Lower Rio Puerco, simulated maximum aggradation depths in 100 years were on the order of 1-4 m.

REFERENCES

Antevs, E., 1952: Arroyo cutting and filling. *J. Geology*, 60, 375-385.

Antevs, E., 1954: Climate of New Mexico during the last glacio-pluvial. *J. Geology*, 62, 182-191.

Bailey, R. W., 1935: Epicycles of erosion in the valleys of the Colorado Plateau province. *J. Geology*, 43, 337-355.

Balling, R. C., and S. G. Wells, 1990: Historical rainfall patterns and arroyo activity within the Zuni River drainage basin, New Mexico. *Ann. Assoc. Amer. Geog.*, 80(4), 603-617.

Bennett, J. P., and C. F. Nordin, 1977: Simulation of sediment transport and armoring. *Hydrol. Sciences Bull.*, 22(4), 555-569.

Bhallamudi, S. M., and M. H. Chaudry, 1991: Numerical modeling of aggradation and degradation in alluvial channels. *J. Hydraul. Eng.*, 117(9), 1145-1164.

Bouwer, H., 1986: Intake rate - Cylinder infiltrometer. Methods of Soil Analysis, Part 1. Physical and Mineralogical Methods, *Amer. Soc. Agronomy - Soil Sci. Soc. Amer.*, 825-844.

Branson, F. A., and A. Janicki, 1986: Botanic and hydrologic changes on rangelands of the Rio Puerco Basin, New Mexico. *U.S. Geol. Surv. Water-Resources Report*, 86-4021, 23 pp.

Bras, R. L., 1990: *Hydrology, An introduction to hydrologic science*. Addison-Wesley, 643 pp.

Bryan, K., 1925: Date of channel trenching (arroyo cutting) in the arid Southwest. *Science*, 62(1607), 338-344.

Bryan, K., 1928a: Historic evidence on changes in the channel of Rio Puerco, a tributary of the Rio Grande in New Mexico. *J. Geology*, 36, 265-282.

Bryan, K., 1928b: Change in plant association by change in ground water level. *Ecology*, 9(4), 474-478.

Bryan, K., 1940: Erosion in the valleys of the Southwest. *New Mexico Quarterly*, 10(4), 227-232.

Bryan, K., and F. T. McCann, 1937: The Ceja del Rio Puerco - A border feature of the basin and range province in New Mexico, I. Stratigraphy and structure. *J. Geology*, 45(8), 801-828.

Bryan, K., and F. T. McCann, 1938: The Ceja del Rio Puerco - A border feature of the basin and range province in New Mexico, II. Geomorphology. *J. Geology*, 46(1), 1-16.

Bryan, R. B., and J. A. A. Jones, 1997: The significance of soil piping processes, Inventory and prospect. *Geomorphology*, 20, 209-218.

Bull, W. B., 1979: Threshold of critical power in streams. *Geol. Soc. Amer. Bull.*, 90, 453-464.

Burkham, D. E., 1970: Depletion of streamflow by infiltration in the main channels of the Tuscon Basin, Southeastern Arizona. *U.S. Geol. Surv. Water-Supply Paper*, 1929-B, 36 pp.

Cayan, D. R., Dettinger, M. D., Diaz, H. F., and N. E. Graham, 1998: Decadal variability of precipitation over Western North America. *J. Climate*, 11, 3148-3166.

Chang, H. H., 1982: Mathematical model for erodible channels. *J. Hydraul. Div.*, ASCE, 108(HY5), 678-689.

Chang, T. J., Kavvas, M. L., and J. W. Delleur, 1984: Daily precipitation modeling by discrete autoregressive moving average processes. *Water Resour. Res.*, 20(5), 565-580.

Cheng, N., 1997: Effect of concentration on settling velocity of sediment particles. *J. Hydraul. Eng.*, 123(8), 728-731.

Chiew, F. H. S., and T. A. McMahon, 1996: Trends in historical streamflow records. *Regional Hydrological Response to Climate Change*, J. A. A. Jones et al., Ed., Kluwer Academic Publishers, Amsterdam, 63-68.

Chowdhury, J. U., Stedinger, J. R., and L. Lu, 1991: Goodness-of-fit tests for regional generalized extreme value flood distributions. *Water Resour. Res.*, 27(7), 1765-1776.

Cooke, R. U., and R. W. Reeves, 1976: *Arroyos and environmental change in the American South-West*. Clarendon Press, Oxford, 213 pp.

Correia, L. R. P., Krishnappan, B. G., and W. H. Graf, 1992: Fully coupled unsteady mobile boundary flow model. *J. Hydraul. Eng.*, 118(3), 476-494.

Cui, Y., Parker, G. and C. Paola, 1996: Numerical simulation of aggradation and downstream fining. *J. of Hydraul. Res.*, 34(2), 185-204.

Daniel, D. E., 1989: In situ hydraulic conductivity test for compacted clay. *J. Geotech. Eng.*, 115(9), 1205-1226.

Darby, S. E., and C. R. Thorne, 1996: Numerical simulation of widening and bed deformation of straight sand-bed rivers, I. Model development. *J. Hydraul. Eng.*, 122(4), 184-193.

Dawdy, D. R., and V. A. Vanoni, 1986: Modeling alluvial channels. *Water Resour. Res.*, 22(9), 71S-81S.

Dellenbaugh, F. S., 1912: Cross-cutting and retrograding of streambeds. *Science*, 35(904), 656-658.

Dortignac, E. J., 1960: The Rio Puerco - past, present, and future. *Fifth Annual New Mexico Water Conference*, New Mexico State University, 45-51.

Duce, J. T., 1918: The effect of cattle on the erosion of canyon bottoms. *Science*, 47, 450-452.

Edwards, T. K., and G. D. Glyson, 1988: Field methods for measurement of fluvial sediment. *U.S. Geol. Surv. Open-File Report*, 86-531, 118 pp.

Elliott, J. G., 1979: Evolution of large arroyos: The Rio Puerco of New Mexico. M.S. Thesis, Colorado State University, 106 pp.

Elliott, J. G., Gellis, A. C., and S. B. Aby, 1999: Evolution of arroyos: incised channels of the southwestern United States. *Incised River Channels*, S. E. Darby and A. Simon, Eds., John Wiley & Sons Ltd., 153-185.

Euler, R. C., Gumerman, G. J., Karlstrom, T. N. V., Dean, J. S., and R. H. Hevly, 1979: The Colorado Plateaus, Cultural dynamics and paleoenvironment. *Science*, 205(4411), 1089-1101.

Fan, Y., Wood, E. E., Baeck, M. L., and J. A. Smith, 1996: Fractional coverage of rainfall over a grid: Analyses of NEXRAD data over the southern Plains. *Water. Resour. Res.*, 32(9), 2787-2802.

Farquharson, F. A. K., Meigh, J. R., and J. V., Sutcliffe, 1992: Regional flood frequency analysis in arid and semi-arid areas. *J. Hydrol.*, 138, 487-501.

Filliben, J. J., 1975: The probability plot correlation coefficient test for normality. *Technometrics*, 17(1), 111-117.

Finley, R. J., and T. C. Gustavson, 1983: Geomorphic effects of a 10-year storm on a small drainage basin in the Texas Panhandle. *Earth Surf. Processes and Landforms*, 8, 63-77.

Foufoula-Georgiou, E., and K. P. Georgakakos, 1991: Hydrologic advances in space-time precipitation modeling and forecasting. *Recent Advances in the Modeling of Hydrologic Systems*, D. S. Bowles and P. E. O'Connel, Eds., Kluwer, Netherlands, 47-65.

Gan, T. Y., Dlamini, E. M., and G. F. Biftu, 1997: Effects of model complexity and structure, data quality, and objective functions on hydrologic modeling. *J. Hydrol.*, 192, 81-103.

Gee, G. W., and J. W. Bauder, 1979: Particle size analysis by hydrometer: a simplified method for routine textural analysis and a sensitivity test of measured parameters. *Soil Sci. Soc. Am.*, 43, 1004-1007.

Gellis, A., 1988: Decreasing sediment and salt loads in the Colorado River Basin: A response to arroyo evolution. M.S. Thesis, Colorado State University, 178 pp.

Gellis, A., 1991: Decreasing trends of suspended sediment concentrations at selected streamflow stations in New Mexico. *New Mexico Water Resoures Research Institute*, 11, 77-93.

Gellis, A., Hereford, R., Schumm, S. A., and B. R. Hayes, 1991: Channel evolution and hydrologic variations in the Colorado River Basin, Factors influencing sediment and salt loads. *J. Hydrol.*, 124, 317-344.

Germanoski, D. and S. A. Schumm, 1993: Changes in braided river morphology resulting from aggradation and degradation. *J. Geology*, 101, 451-466.

Gershunov, A., and T. P. Barnett, 1998: Interdecadal modulation of ENSO teleconnections. *Bull. Amer. Meteor. Soc.*, 79(12), 2715-2725.

Gorbach, C., Love, D., Piper, S., Davis, R., and A. Cross, 1996: *Rio Puerco sedimentation and water quality study*. U.S. Dept. Interior, Bureau of Reclamation, Preliminary Report.

Graf, J. B., Webb, R. H., and R. Hereford, 1991: Relation of sediment load and floodplain formation to climatic variability, Paria River drainage basin, Utah and Arizona. *Geol. Soc. Amer. Bull.*, 103, 1405-1415.

Graf, W. L., 1979: The development of montane arroyos and gullies. *Earth Surf. Process.*, 4, 1-14.

Gregory, H. E., 1917: Geology of the Navajo country. *U.S. Geol. Surv. Prof. Pap.*, 93, 161 pp.

Grissino-Meyer, H. D., 1995: Tree-ring reconstructions of climate and fire history at El Malpais National Monument, New Mexico. Ph.D. Dissertation, University of Arizona, 250 pp.

Gupta, V. K., and E. C. Waymire, 1990: Multiscaling properties of spatial rainfall and river flow distributions. *J. Geophys. Res.*, 95, 1999-2009.

Gupta, V. K., and E. C. Waymire, 1993: A statistical analysis of mesoscale rainfall as a random cascade. *J. App. Meteorol.*, 32, 251-267.

Guy, H. P., Simons, D. B., and E. V. Richardson, 1966: Summary of alluvial channel data from flume experiments, 1956-1961. *U.S. Geol. Surv. Prof. Pap.*, 462-I.

Habersack, H. M., 1998: Numerical sediment transport models - theoretical and practical aspects. *Modeling Soil Erosion, Sediment Transport and Closely Related Hydrological Processes*, W. Summer et al., Eds., IAHS Publ., 249, 299-308.

Happ, S. C., 1948: *Sedimentation in the Rio Grande Valley, New Mexico*. U.S. Dept. Agriculture, SCS Report.

Heath, D. L., 1983: Flood and recharge relationships of the lower Rio Puerco, New Mexico. *New Mexico Geological Society Guidebook*, 34th Field Conference, 329-337.

Helsel, D. R., and R. M. Hirsch, 1992: Statistical methods in water resources. *Studies in Environmental Science* 49, Elsevier, New York, 522 pp.

Hereford, R., 1984: Climate and ephemeral stream processes, Twentieth Century geomorphology and alluvial stratigraphy of the Little Colorado River, Arizona. *Geol. Soc. Amer. Bull.*, 95, 654-668.

Hirsch, R. M., and J. R. Slack, 1984: A nonparametric trend test for seasonal data with serial dependence. *Water Resour. Res.*, 20(6), 727-732.

Hirsch, R. M., Helsel, D. R., Cohn, T. A., and E. J. Gilroy, 1993: Statistical analysis of hydrologic data. *Handbook of Hydrology*, D. R. Maidment, Ed., McGraw-Hill, Inc., New York, 17.1-17.55.

Hirschboeck, K. K., 1987: Catastrophic flooding and atmospheric circulation anomalies. *Catastrophic flooding*, L. Mayer and D. Nash, Eds., Allen & Unwin, Inc., Winchester, 23-56.

Hoey, T. B. and R. Ferguson, 1994: Numerical simulation of downstream fining by selective transport in gravel bed rivers: Model development and illustration. *Water Resour. Res.*, 30(7), 2251-2260.

Holly, F. M., and M. F. Karim, 1986: Simulation of Missouri River bed degradation. *J. Hydraul. Eng.*, 112(6), 497-517.

Hosking, J. R. M., 1990: L-moments, Analysis and estimation of distributions using linear combinations of order statistics. *J. R. Stat. Soc.*, B, 52(1), 105-124.

Hosking, J. R. M., and J. R. Wallis, 1988: The effect of intersite dependence on regional flood frequency analysis. *Water Resour. Res.*, 24(4), 588-600.

Hosking, J. R. M., and J. R. Wallis, 1993: Some statistics useful in regional frequency analysis. *Water Resour. Res.*, 29(2), 271-281.

Hosking, J. R. M., and J. R. Wallis, 1997: *Regional frequency analysis: an approach based on L-moments*. Cambridge University Press, 224 pp.

Howard, A. D., Dietrich, W. E., and M. A. Seidl, 1994: Modeling fluvial erosion on regional to continental scales. *J. Geophys. Res.*, 99(B7), 13,971-13,986.

Huntington, E., 1914: The climatic factor as illustrated in arid America. *Carnegie Institute Washington*, Publication 192, 341 pp.

Hydrologic Engineering Center (HEC), 1977: *HEC-6 scour and deposition in rivers and reservoirs*. User's manual, US Army Corps of Engineers, Davis.

Interagency Advisory Committee on Water Data (IACWD), 1988: *Twelve selected computer stream sedimentation models developed in the United States*, Shou-shan, Ed., Subcommittee on Sedimentation, Water Resources Publication, 552 pp.

Intergovernmental Panel on Climate Change (IPCC), 1995: *Climate change 1995*, The science of climate change. Cambridge University Press, 572 pp.

Jaramillo, W. F., and S. C. Jain, 1984: Aggradation and degradation of alluvial-channel beds. *J. Hydraul. Eng.*, 110(8), 1072-1085.

Julien, P. Y., 1995: *Erosion and sedimentation*. Cambridge University Press, 280 pp.

Kahane, J. P., and J. Peyriere, 1976: Sur certaines mertingales de Benoit Mandelbrot. *Adv. Math.*, 22, 131-145.

Kahya, E., and J. A. Dracup, 1993: U.S. streamflow patterns in relation to the El Nino/Southern Oscillation. *Water Resour. Res.*, 29(8), 2491-2503.

Karim, M. F., and F. M. Holly, 1985: Armoring and sorting simulation in alluvial rivers. *J. Hydraul. Eng.*, 112(8), 705-715.

Karim, M. F., and J. F. Kennedy, 1982: IALLUVIAL - A computer-based flow and sediment routing model for alluvial streams and its application to the Missouri River. *IIHR Report No. 250*, University of Iowa, 125 pp.

Karl, T. R., Knight, R. W., and N. Plummer, 1995: Trends in high-frequency climate variability in the twentieth century. *Nature*, 377, 217-220.

Karl, T. R., and R. W. Knight, 1998: Secular trends of precipitation amount, frequency, and intensity in the United States. *Bull. Amer. Meteor. Soc.*, 79(2), 231-24 1.

Kedem, B., and L. S. Chiu, 1987: Are rain rate processes self-similar? *Water Resour. Res.*, 23(10), 1816-1818.

Kendall, M. G., 1938: A new measure of rank correlation. *Biometrika*, 30, 81-93.

Keppel, R. V., and A. M. Renard, 1962: Transmission losses in ephemeral stream beds. *J. Hydraul. Div.*, ASCE, 8(HY3), 59-68.

Kerssens, P. J. M., and A. van Urk, 1984: Experimental studies on sedimentation due to water withdrawal. *J. Hydraul. Eng.*, 112(7), 641-656.

Latif, M., and T. P. Barnett, 1994: Causes of decadal climate variability over the North Pacific and North America. *Science*, 266, 634-637.

Landwehr, J. M., Matalas, N. C., and J. R. Wallis, 1980: Quantile estimation with more or less floodlike distributions. *Water Resour. Res.*, 16(3), 547-555.

Lane, W. L., 1979: *Applied stochastic techniques*. Division of Planning Technical Sciences, Eng. Res. Center, U.S. Bureau of Reclamation.

LeCam, L., 1961: A stochastic description of precipitation. *4th Berkeley Symp. on Mathematical Statistics and Probability*, Vol. 3, University of California, Berkeley, 165-186.

Leopold, L. B., 1951: Rainfall intensity: An aspect of climatic variation. *AGU Transactions*, 32(3), 347-357.

Leopold, L. B., and J. P. Miller, 1956: Ephemeral streams, Hydraulic factors and their relation to the drainage net. *U.S. Geol. Surv. Prof. Pap.*, 282-A, 36 pp.

Leopold, L. B., Emmett, W. W., and R. M. Myrick, 1966: Channel and hillslope processes in a semiarid area, New Mexico. *U.S. Geol. Surv. Prof. Pap.*, 352-G, 253 pp.

Lettenmaier, D. P., Wallis, J. R., and E. F. Wood, 1987: Effect of regional heterogeneity on flood frequency estimation. *Water Resour. Res.*, 23(2), 313-323.

Lettenmaier, D. P., Wood, E. F., and J. R. Wallis, 1994: Hydro-climatological trends in the Continental United States, 1948-88. *J. Climate*, 7, 586-607.

Lins, H. F., 1997: Regional streamflow regimes and hydroclimatology of the United States. *Water Resour. Res.*, 33(7), 1655-1667.

Lins, H. F., and J. R. Slack, 1999: Streamflow trends in the United States. *Geophys. Res. Lett.*, 26(2), 227-230.

Loumagne, C., Chkir, N., Normand, M., Ottle, C., and D. Vidal-Madjar, 1996: Introduction of the soil/vegetation/atmosphere continuum in a conceptual rainfall/runoff model. *J. Hydrol. Sc.*, 41(6), 889-902.

Love, D. W., 1986: *A geological perspective of sediment storage and delivery along the Rio Puerco, central New Mexico.* IAHS Publ., 159, 305-353.

Lovejoy, S., and B. B. Mandelbrot, 1985: Fractal properties of rain and a fractal model. *Tellus*, 37A, 209-232.

Lu, J. Y., and H. W. Shen, 1984: Analysis and comparisons of degradation models. *J. Hydraul. Eng.*, 112(4), 281-299.

Lu, L. H., and J. R. Stedinger, 1992: Variance of two- and three-parameter GEV/PWM quantile estimators: formulae, confidence intervals, and a comparison. *J. Hydrol.*, 138(1/2), 247-267.

Lyn, D. A., and P. Goodwin, 1985: Stability of a general Preissmann Scheme. *J. Hydraul. Eng.*, 113(1), 16-28.

Mandelbrot, B. B., 1974: Intermittent turbulence in self-similar cascades: Divergence of high moments and dimension of the carrier. *J. Fluid Mech.*, 62, 331-358.

Mantua, N. J., Hare, S. R., Zhang, Y., Wallace, J. M., and R. C. Francis, 1997: A Pacific interdecadal climate oscillation with impacts on salmon production. *Bull. Amer. Meteor. Soc.*, 78(6), 1069-1079.

Matlock, W. G., 1965: The effect of silt-laden water on infiltration in alluvial channels. Ph.D. Dissertation, University of Arizona, 102 pp.

Melton, M., 1965: The geomorphic and paleoclimatic significance of alluvial deposits in Southern Arizona. *J. Geology*, 73, 1-38.

Mengis, R. C., 1981: Modeling of a transient streambed in the Rio Grande, Cochiti Dam to near Albuquerque, New Mexico. *U.S. Geol. Surv. Open-File Report*, 82-106, 99 pp.

Meyer, D. F., 1986: The significance of sediment transport in arroyo development. Ph.D. Dissertation, Colorado State University, 139 pp.

Miller, J. R., and S. G. Wells, 1986: *Types and processes of short-term sediment and uranium-tailings storage in arroyos: An example from the Rio Puerco of the West, New Mexico.* IAHS Publ., 159, 335-353.

Minobe, S., 1997: A 50-70 year oscillation over the North Pacific and North America. *Geophys. Res. Lett.*, 24(6), 683-686.

Molinas, A., and C. T. Yang, 1984: Computer Program User's Manual for (GSTARS) Generalized Stream Tube Model for alluvial river simulation. U.S. Bureau of Reclamation, Denver, Colorado.

Morse, B., and R. D. Townsend, 1989: Modeling channel bed transients using explicit F-D schemes. *J. Hydraul. Eng.*, 116(11), 1345-1356.

Mosley, M. P., 1976: An experimental study of channel confluences. *J. Geology*, 84, 535-562.

Mualem, Y., and S. Assouline, 1996: Soil sealing, infiltration and runoff. *Runoff and Subsurface Flow of Water in Arid and Semi-Arid Regions*, A. S. Issar and S.D. Roesnick, Eds., Kluwer Academic Publishers, Netherlands, 131-181.

National Research Council NRC, 1991: *Opportunities in the hydrologic sciences*. National Academy Press, Washington, DC, 348 pp.

Nordin, C. F., 1963: A preliminary study of sediment transport parameters, Rio Puerco near Bernardo, New Mexico. *U.S. Geol. Surv. Prof. Pap.*, 462-C, 21 pp.

Nordin, C. F. and G. R. Depmster, 1963: Vertical distribution of velocity and suspended sediment, Middle Rio Grande, New Mexico. *U.S. Geol. Surv. Prof. Pap.*, 462-B, 20 pp.

O'Callaghan, J. F., and D. M. Mark, 1984: The extraction of drainage networks from digital elevation data. *Comput. Vision. Graphics Image Process.*, 28, 328-344.

Over, T. M., 1995: Modeling space-time rainfall at the mesoscale using random cascades. Ph.D. Dissertation, University of Colorado, Boulder.

Over, T. M., and V. K. Gupta, 1994: Statistical analysis of mesoscale rainfall: Dependence of a random cascade generator on large-scale forcing. *J. Appl. Meteorol.*, 33, 1526-1542.

Over, T. M., and V. K. Gupta, 1996: A space-time theory of mesoscale rainfall using random cascades. *J. Geophys. Res.*, 101(D21), 26319-26331.

Park, I., and S. C. Jain, 1986: River-bed profiles with imposed sediment load. *J. Hydraul. Eng.*, 112(4), 267-280.

Patton, P. C., 1973: Gully erosion in the semiarid west. M.S. Thesis, Colorado State University, 129 pp.

Patton, P. C., and S. A. Schumm, 1975: Gully erosion, Northwestern Colorado: A threshold phenomenon. *J. Geology*, 3, 88-90.

Peterson, H. V., 1950: The problem of gulyying in Western valleys. *Applied Sedimentation*, P.D. Trask, Ed., 407-434.

Pickup, G., 1977: Simulation modelling of river channel erosion. *River Channel Changes*, K. J. Gregory, Ed., John Wiley & Sons, 47-60.

Piechota, T. C., and J. A. Dracup, 1996: Drought and regional hydrologic variation in the United States: Associations with the El Nino-Southern Oscillation. *Water Resour. Res.*, 32(5), 1359-1373.

Ponce, V. M., Garcia, J. L., and D. B. Simons, 1979: Modeling alluvial channel bed transients. *J. Hydraul. Div.*, ASCE, 105(HY3), 245-256.

Post, D. A., and A. J. Jakeman, 1996: Relationships between catchment attributes and hydrological response characteristics in small Australian Mountain Ash catchments. *Hydrol. Processes*, 10, 877-892.

Potter, K. W., and D. P. Lettenmaier, 1990: A comparison of regional flood frequency estimation methods using a resampling method. *Water Resour. Res.*, 26(3), 415-424.

Redmond, K. T., and R. W. Koch, 1991: Surface climate and streamflow variability in the western United States and their relationship to large-scale circulation indices. *Water Resour. Res.*, 27(9), 2381-2399.

Reid, I. and B. L. Laronne, 1995: Bed load sediment transport in an ephemeral stream and a comparison with seasonal and perennial counterparts. *Water Resour. Res.*, 31(3), 773-781.

Renard, K. G., and M. Laursen, 1975: Dynamic behavior model of ephemeral streams. *J. Hydraul. Div.*, ASCE, 101(HY5), 511-528.

Rich, J. L., 1911: Recent stream trenching in the semi-arid portion of Southwestern New Mexico, a result of removal of vegetation cover. *Amer. J. Science*, 32(190), 237-245.

Richardson, H. L., 1945: The significance of terraces due to climatic oscillation. *Geol. Magazine*, 82(1), 16-18.

Richardson, J. F., and W. N. Zaki, 1954: Sedimentation and fluidization. *Trans. Inst. Chem. Eng.*, I(31), 35-53.

Ruff, P. F., Dust, D. W., and M. T. Bowers, 1986: Application of HEC-6 to ephemeral streams. *Proceedings of the Fourth Federal Interagency Sedimentation Conference*, Las Vegas, Nevada, 6:85-6:94.

Saiedi, S, 1997: Coupled modeling of alluvial flows. *J. Hydraul. Eng.*, 123(5), 440-446.

Salas, J. D., Delleur, J. W., Yevjevich, V., and W. L. Lane, 1985: *Applied modeling of hydrologic time series*. Water Resources Publications, Littleton, CO, 484 pp.

Schreider, S. Y., Jakeman, A. J., and A. B. Pittock, 1996: Modelling rainfall-runoff from large catchment to basin scale: The Goulburn Valley, Victoria. *Hydrol. Processes*, 10, 863-876.

Schumm, S. A., 1961: Effect of sediment characteristics on erosion and deposition in ephemeral-stream channels. *U.S. Geol. Surv. Prof. Pap.*, 352-C, 70 pp.

Schumm, S. A., 1973: Geomorphic thresholds and complex response of drainage systems. *Fluvial Geomorphology*, M. Morisawa, Ed., 299-310.

Schumm, S. A., 1980: Some applications of the concept of geomorphic thresholds. *Thresholds in Geomorphology*, D. R. Coates and J. D. Vitek, Eds., Allen & Unwin, 473-485.

Schumm, S. A., and R. F. Hadley, 1957: Arroyos and the semiarid cycle of erosion. *Amer. J. Science*, 255, 161-174.

Schumm, S. A., and H. R. Khan, 1972: Experimental study of channel patterns. *Geol. Soc. Amer. Bull.*, 83, 1755-1770.

Searcy, J. K., 1959: Flow-duration curves, Manual of hydrology: Part 2. Low Flow Techniques, *U.S. Geol. Surv. Water-Supply Paper*, 1542-A, 33 pp.

Shepherd, R. G., 1978: Distinction of aggradational and degradational fluvial regimes in valley-fill alluvium, Tapia Canyon, New Mexico. *Fluvial Sedimentology*, A.D. Miall, Ed., Canadian Society of Petroleum Geologists, 277-286.

Sidorchuk, A., and A. Sidorchuk, 1998: Model for estimating gully morphology. *Modeling Soil Erosion, Sediment Transport and Closely Related Hydrological Processes*, W. Summer et al., Eds., IAHS Publ., 249, 333-343.

Smith, J. A., 1992: Precipitation. *Handbook of Hydrology*, D. R. Maidment, Ed., McGraw-Hill, Inc., New York, 3.1-3.47.

Smith, R. E., Goodrich, D. C., Woolhiser, D. A., and C. L. Unkrich, 1995: KINEROS - A kinematic runoff and erosion model. *Computer Models of Watershed Hydrology*, V. P. Singh, Ed., Water Resources Publications, 697-732.

Soni, J. P., Garde, R. J., and K. G. R. Raju, 1980: Aggradation in streams due to overloading. *J. Hydraul. Div.*, ASCE, 106(HY1), 117-132.

Stedinger, J. R., Vogel, R. M., and E. F. Foufoula-Georgiou, 1993: Frequency analysis of extreme events. *Handbook of Hydrology*, D. R. Maidment, Ed., McGraw-Hill, Inc., New York, 18.1-18.66.

Thomas, C. L., 1995: Infiltration and quality of water for two arroyo channels, Albuquerque, New Mexico. *U.S. Geol. Surv. Water-Resources Investigations Report*, 95-4070, 63 pp.

Thornes, J. B., 1977: Channel changes in ephemeral streams: Observations, problems, and models. *River Channel Changes*, K. J. Gregory, Ed., John Wiley & Sons, 317-335.

Thornes, J. B., 1994: Channel processes, evolution, and history. *Geomorphology of Desert Environments*, A. D. Abrahams and A. J. Parsons, Eds., Chapman and Hall, London, 288-317.

Thornthwaite, C. W., Sharpe, C. F., and E. F. Doesch, 1942: *Climate and accelerated erosion in the arid and semiarid Southwest, with special reference to the Polacca Wash drainage basin, Arizona.* Dept. of Agriculture Technical Bulletin 808, 134 pp.

Topping, D. J., 1997: Physics of flow, sediment transport, hydraulic geometry, and channel geomorphic adjustment during flash floods in an ephemeral river, the Paria River, Utah and Arizona. Ph.D. Dissertation, University of Washington, 405 pp.

Tuan, Y., 1966: New Mexican gullies - A critical review and some recent observations. *Assoc. Amer. Geogr. Ann.*, 56, 573-597.

Tucker, G. E., and R. Slingerland, 1997: Drainage responses to climate change. *Water Resour. Res.*, 33(8), 2031-2047.

Tucker, G. E., and R. L. Bras, 2000: A stochastic approach to modeling the role of rainfall variability in drainage basin evolution. *Water Resour. Res.*, in print.

Tucker, G. E., Lancaster, S. T., Gasparini, N. M., and R. L. Bras, 2000: The channel-hillslope integrated landscape development (CHILD) model. *Landscape Erosion and Sedimentation Modeling*, R. S. Harmon and W. W. Doe, Eds., Kluwer, in print.

U.S. Army Corps of Engineers, 1995: *HEC-RAS River Analysis System*, Hydraulic Reference Manual. Hydrologic Data Center, Davis.

Valencia, D. R., and J. C. Schaake, 1973: Disaggregation processes in stochastic hydrology. *Water Resour. Res.*, 9(3), 580-585.

Van Niekerk, A., Vogel, K. R., and R. L. Slingerland, 1992: Routing of heterogeneous sediments over movable bed: Model development. *J. Hydraul. Eng.*, 118(2), 246-261.

Van Rijn, L. C., 1984a: Sediment transport, Part I: Bed load transport. *J. Hydraul. Eng.*, 110(10), 1431-1456.

Van Rijn, L. C., 1984b: Sediment transport, Part II: Suspended load transport. *J. Hydraul. Eng.*, 110(11), 1613-1641.

Van Rijn, L. C., 1984c: Sediment transport, Part III: Bed forms and alluvial roughness. *J. Hydraul. Eng.*, 110(12), 1733-1754.

Vogel, R. M., Thomas, W. O., and T. A. McMahon, 1992: Flood-flow frequency model selection in the Southwestern United States. *J. Water. Resour. Plann. Man.*, 119(3), 353-366.

Vogel, R. M., and I. Wilson, 1996: Probability distribution of annual maximum, mean, and minimum streamflows in the United States. *J. Hydrol. Eng.*, 1(2), 69-76.

Wahl, K. L., 1992: Evaluation of trends in runoff in the western United States. *Proceedings Managing Water Resources During Global Change*, 28th Annual Conf. and Symp., Reno, NV, Amer. Water Resour. Assoc., 701-710.

Waltemeyer, S. D., 1996: Analysis of the magnitude and frequency of peak discharge and maximum observed peak discharge in New Mexico. *U.S. Geol. Surv. Water-Resources Investigations Report*, 96-4112, 79 pp.

Webb, R. H., and J. L. Betancourt, 1990: Climatic variability and flood frequency of the Santa Cruz River, Pima County, Arizona. *U.S. Geol. Surv. Open-File Report*, 90-553, 69 pp.

Wiele, S. M., Graf, J. B., and J. D. Smith, 1996: Sand deposition in the Colorado River in the Grand Canyon from flooding of the Little Colorado River. *Water Resour. Res.*, 32(12), 3579-3596.

Woodley, W. L., Olsen, A. R., Herndon, A., and V. Wiggert, 1975: Comparison of gage and radar methods of convective rain measurement. *J. App. Meteorol.*, 14, 909-928.

Wright Jr., H. E., 1946: Tertiary and Quaternary geology of the lower Rio Puerco area, New Mexico. *Geol. Soc. Amer. Bull.*, 57, 383-456.

Yang, C. T., 1996: *Sediment transport, Theory and practice*. McGraw-Hill, 393 pp.

Yen, C., Chang, S, and H. Lee, 1992: Aggradation-degradation process in alluvial channels. *J. Hydraul. Eng.*, 118(12), 1651-1669.

Zhang, Y., Wallace, J. M., and D. S. Battisti, 1997: ENSO-like interdecadal variability: 1900-93. *J. Climate*, 10, 1004-1020.